Intergrade Joints for Nb$_3$Sn cables of high magnetic field magnets

Vincenzo D'AURIA

École
polytechnique
fédérale
de Lausanne

2022

Contents

Abstract

The objective of this thesis is the development of high-field and high-current joints between Nb_3Sn cables for superconducting coils. The main fields of application are high energy physics (HEP) and thermonuclear fusion. In this thesis, the focus is on Wind&React (WR) HEP dipole magnets and React&Wind (RW) fusion magnets. These two have in common the design strategy of optimizing the superconductor quantity in the turns of the magnet according to the magnetic field intensity, with the main advantage of a cheaper and smaller coil. This technique is called magnet grading. As a consequence, the magnet is formed by different Nb_3Sn cables that have to be connected electrically in series. The joints realize such connections and have to satisfy, in particular, electrical resistance requirements that allow to keep the superconductor temperature under the allowed limit. Nevertheless, the two considered fields of application have different magnet technology and cable, i.e. WR and Rutherford cables for HEP dipole magnets, whereas RW and Cable in Conduit Conductors (CICC) for fusion coils. For this reason, the joint development is split into two parts.

In WR HEP magnets, the joint has to be integrated in the dipole head, which has a curved geometry. The first step was the identification of a suitable splicing technique. In this context, ultrasound welding was identified as potential splicing technique applicable before the magnet heat treatment, whereas diffusion-bonding during it and soldering after the coil reaction. These different solutions were experimentally investigated. Several prototypes were designed, electrically tested in SULTAN to assess their electrical resistance and analyzed through modelling, which helped in the interpretation of the obtained results. In the end, the objective is achieved and two different joints are developed, one based on diffusion-bonding and the other on soldering. The bent diffusion-bonded joint prototype has a resistance of 1.04 nΩ at B=10.9 T, T=5 K and ratio between current and critical current I/I_c=0.63. The soldered joint shows R=0.58 nΩ at B=10.9 T, T=5 K and I/I_c=0.54.

In RW fusion magnets, opposed to WR coils, splicing can occur only after the heat treatment of the cable. Copper diffusion-bonding is proposed as jointing technique, since cleaner and potentially with higher mechanical strength than soldering. The cables to splice are first coated by copper thermal spray to increase the contact between the surfaces to splice. The proposed set-up takes into account the joint manufacture during in-line winding.

A joint prototype was manufactured and tested in SULTAN, demonstrating that the electrical resistance fulfils the requirements (the measured resistance is R=0.48 nΩ at B=8 T, I=63.3 kA and T=5.1 K) and that the operability range of the joint, in terms of current and magnetic field, is wide (at least up to 10.9 T and 63.3 kA). The joint AC losses and behaviour under electromagnetic cyclic loading are illustrated, as such a splice would work in a pulsed fusion machine, the Tokamak. Metallographic analyses of the developed prototype were carried out to provide feedbacks on the joint manufacture.

In both applications, i.e. WR HEP magnets and RW fusion coils, recommendations are given to the magnet designer for the implementation of the developed joints in a superconducting magnet.

Keywords: Nb_3Sn Rutherford cable and CICC, accelerator and fusion magnets, electrical joints, electrical resistance measurements, SULTAN.

Zusammenfassung

Das Ziel dieser Doktorarbeit ist die Entwicklung elektrischer Verbindungen, die aus Nb_3Sn Kabeln bestehen und in hohen magnetischen Feldern von Magneten mit hohem Strom einzusetzen sind. Die Hauptanwendungsbereiche betreffen Hochenergiephysik (HEP) und Kernfusionsreaktoren. Die Schwerpunkte sind insbesondere die sogenannten Wind&React (WR) Dipolmagneten und React&Wind (RW) Fusionsspulen. Die Beiden folgen derselben Entwurfsstrategie dadurch, dass die Menge supraleitenden Materials je nach dem verschiedenen magnetischen Feldniveau in den Windungen der Spule optimiert wird. Die gerade beschriebene Technik wird im Englischen «grading» genannt, was mit «Abstufen» übersetzt werden kann. Dieser Optimierung zufolge besteht der Magnet aus verschiedenen Nb_3Sn-Kabeln, die elektrisch aneinander anzuschliessen sind. Derartige Anschlüsse werden durch die Verbindungen geschaffen und müssen insbesondere die Widerstandsbedingungen erfüllen, welche ermöglichen, die Temperatur des Magneten innerhalb der zumutbaren Grenze zu halten. Die zwei Anwendungsgebiete teilen zwar dieselbe Entwurfsstrategie, aber ihre Magnettechnologie und die Art der Kabel unterscheiden sich. Zu den in dieser Doktorarbeit berücksichtigten HEP-Magnetdipolen gehören nämlich die WR-Wicklungsart und das Rutherford-Kabel an, während die Fusionsspulen die RW-Wicklungsweise und «Cable in Conduit Conductors» (CICC) verwenden. Aus diesem Grund wird die Verbindungsentwicklung in dieser Doktorarbeit in zwei unabhängige Kapitel geteilt.

Bezüglich der HEP-Magneten muss die Verbindung im Dipolkopf, der eine kurvige Gestalt hat, platziert werden. Der erste Schritt war die Identifizierung einer passenden Verbindungstechnik: Ultraschallschweissen als potentielle Verbindungstechnik vor der Magnetwärmebehandlung, Diffusionsschweissen währenddessen und Löten danach. Diese verschiedenen Möglichkeiten sind experimentell untersucht worden. Mehrere Prototypen wurden entworfen und in der SULTAN-Anlage mit dem Ziel getestet, deren elektrischen Widerstand zu messen. Durch die physikalische Modellierung wurden die Testergebnisse ausgewertet. Schlussendlich ist das Doktorarbeitsziel erreicht worden, indem zwei unterschiedliche Verbindungen entwickelt wurden: Die Eine beruht auf Diffusionsschweissen und die Andere auf Löten. Der elektrische Widerstand der durch das Diffusionsschweissen entwickelten Verbindung beträgt 1.04 nΩ bei B=10.9 T, T=5 K und dem Verhältnis zwischen Betriebsstrom und kritischem Strom I/I_c=0.63. Der Widerstand der verlöteten Verbindung ist R=0.58 nΩ bei demselben Feld- und Temperaturwert und bei I/I_c=0.54.

Im Gegensatz zu WR-Magneten kann die Herstellung der Verbindungen bei RW-Fusionsspulen ausschliesslich nach der Wärmebehandlung stattfinden. Diffusionsschweissen wird als Verbindungstechnik vorgeschlagen, da es sauberer und mit einer potentiell höheren mechanischen Festigkeit ist als eine verlötete Verbindung. Die zu schweissenden Kabel werden zuerst einmal mit Kupfer bespritzt, damit die Kontaktoberfläche ausgebaut wird. Der ganze vorgeschlagene Vorgang berücksichtigt, dass die Verbindung während der Wicklung des Magneten hergestellt wird.

Ein Verbindungsprototyp wurde dementsprechend erzeugt und in der SULTAN-Anlage getestet. Dadurch wurde nicht nur belegt, dass der elektrische Widerstand die Voraussetzungen erfüllt (gemessen wurde R=0.48 nΩ bei B=8 T, I=63.3 kA und T=5.1 K), sondern auch, dass die Betriebsreichweite ziemlich breit ist, und zwar mindestens bis zu 10.9 T und 63.3 kA. Die AC-Verluste und das Verbindungsverhalten nach der elektromagnetischen zyklischen

Belastung werden aufgezeigt, da eine derartige Verbindung in einer gepulsten Maschine, dem Tokamak, eingesetzt würde. Metallographische Analysen des entwickelten Prototyps sind durchgeführt worden, damit die Verbindungsfertigung verbessert werden kann.

In beiden Anwendungen, beziehungsweise WR-HEP-Magneten und RW-Fusionsspulen, werden Empfehlungen für die Implementierung der entwickelten Verbindungen in einem supraleitenden Magneten erwähnt.

Stichwörter: Rutherford-Kabel und CICC, Beschleuniger- und Fusionsspulen, elektrische Verbindungen, Widerstandmessungen, SULTAN.

Sommario

L'obiettivo di questa tesi di dottorato consiste nello sviluppo di giunti tra cavi in Nb₃Sn da posizionare in alto campo in magneti superconduttori ad alta corrente. I principali settori di applicazione riguardano la fusione termonucleare e la fisica delle particelle ad alta energia, la quale viene indicata in inglese con l'acronimo HEP ("high energy physics"). In questa tesi, viene fatto riferimento ai magneti di tipo Wind&React (WR) per i dipoli per acceleratori di particelle e alle bobine React&Wind per i magneti da fusione. Le sopracitate applicazioni hanno in comune la strategia di design di scalare il conduttore (in inglese "conductor grading"), ovvero la quantità di materiale superconduttore viene ottimizzata all'interno delle spire della bobina a seconda dell'intensità del campo magnetico. Da quest'ottimizzazione risulta un magnete composto da diversi cavi in Nb₃Sn, i quali devono essere collegati elettricamente in serie. I giunti realizzano tali connessioni e devono soddisfare, in particolare, i requisiti di resistenza elettrica che permettono di mantenere la temperatura del magnete entro il limite di operabilità. Lo sviluppo del giunto è stato diviso in due parti indipendenti in quanto le due applicazioni considerate sono caratterizzate da una diversa tecnologia di avvolgimento della bobina e da un differente tipo di cavo, ovvero la tecnologia WR con cavi Rutherford nei magneti per HEP, mentre la tecnologia RW con cavi "cable in conduit conductor" (CICC) nei magneti da fusione.

Per quanto concerne i magneti RW per HEP formati da cavi Rutherford, il giunto è da integrare nella testa del magnete di tipo dipolo. Tale testa ha una geometria curva. In primo luogo, si è proceduto con l'identificazione di una potenziale tecnica di giuntaggio: la saldatura ad ultrasuoni è applicabile prima del trattamento termico del magnete, la saldatura per diffusione del rame durante esso e la saldatura di metalli riempitivi a basso punto di fusione dopo il trattamento termico della bobina. Queste potenziali soluzioni sono state investigate sperimentalmente. Diversi prototipi sono stati progettati e testati in SULTAN per misurarne la resistenza elettrica. Modelli fisici sono stati sviluppati per l'analisi dei risultati sperimentali ottenuti. Alla fine, l'obiettivo della tesi è stato raggiunto e due diversi tipi di giunto sono stati sviluppati, l'uno basato sulla saldatura per diffusione del rame e l'altro sulla saldatura di metalli riempitivi a basso punto di fusione. Il primo è caratterizzato da una resistenza di 1.04 nΩ a B=10.9 T, T=5 K e rapporto tra corrente operativa e critica I/I_c=0.63, mentre per il secondo è stato misurato R=0.58 nΩ a B=10.9 T, T=5 K e I/I_c=0.54.

Nei magneti RW da fusione, al contrario di quelli WR, il giuntaggio può avvenire solamente in seguito al trattamento termico del cavo superconduttore. Nella tesi, la saldatura per diffusione del rame è proposta come tecnica di giuntaggio, poiché più pulita e potenzialmente con maggiore solidità della saldatura di metalli a basso punto di fusione. Sui cavi da giuntare, viene dapprima depositato rame tramite spruzzatura termica affinché la superficie di contatto sia più estesa. Il procedimento proposto considera l'assemblaggio dei giunti durante l'avvolgimento del magnete.

Un prototipo di giunto è stato fabbricato e testato in SULTAN, dimostrando non solo che la resistenza elettrica soddisfa i requisiti (è stato misurato R=0.48 nΩ a B=8 T, I=63.3 kA e T=5.1 K), ma anche che l'intervallo di operatività del giunto è ampio, cioè fino ad almeno B=10.9 T e I=63.3 kA. Le perdite AC del giunto ed il suo comportamento a carico elettromagnetico ciclico vengono riportati, siccome questo giunto opererebbe in una macchina

pulsata, ovvero in un Tokamak. Analisi metallografiche del prototipo sviluppato sono state condotte per il miglioramento della manifattura del giunto.

Per entrambe le applicazioni, cioè i magneti WR per HEP e quelli RW da fusione, vengono date raccomandazioni per l'implementazione nella bobina dei giunti sviluppati.

Parole chiave: cavi Rutherford e CICC in Nb$_3$Sn, magneti per acceleratori e da fusione, giunti elettrici, misure di resistenza elettrica, SULTAN.

1.   Introduction

Superconductors are materials that exhibit null electrical resistance when cooled below their critical temperature T_c, are exposed to a magnetic field below the critical one, B_c, and carry a current not exceeding the critical current density J_c [1] [2]. The so-called critical surface defines the range of these three parameters within which these particular materials are superconducting (Figure 1.1). Above the critical surface, the material is in normal conducting state and dissipates Ohmic energy when carrying current. A quench is an event in which a thermal runaway occurs because the critical surface is accidentally hit and the dissipated power is higher than the heat removal capability. In both high energy physics (HEP) and thermonuclear fusion, superconducting magnets are a key technology. In relation to HEP research, they allow reducing both the capital expense and the cost of operation with respect to conventional magnet systems based on copper, if one considers also the power supply and the cooling water [3] [4]. Regarding thermonuclear fusion, whose final goal is the electrical power production, superconducting magnets are an enabling technology. In fact, without them, a great amount of the nuclear power would be spent for the cooling of conventional magnets heated up by the Ohmic power. In both HEP and fusion, the cost of the superconducting systems drives the capital cost of the devices.
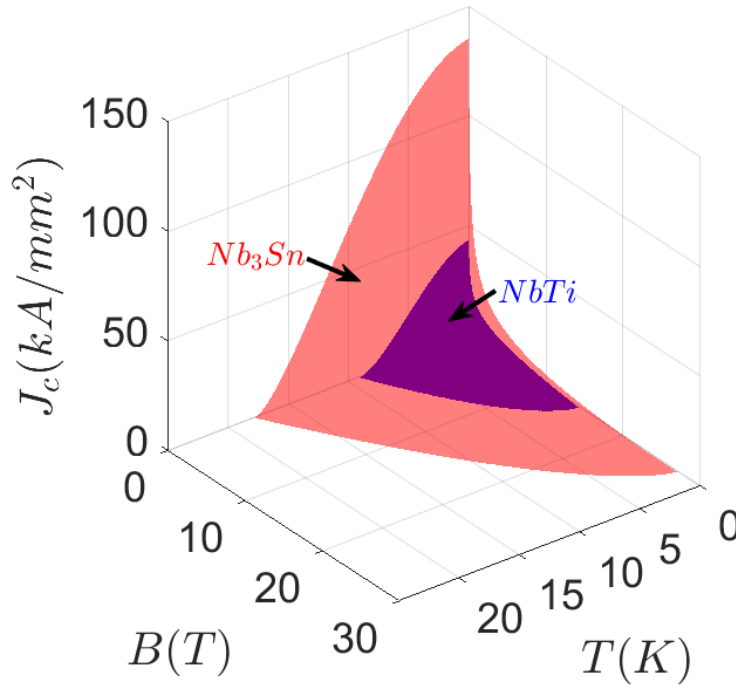

Figure 1.1 *Critical surface of the NbTi and Nb$_3$Sn superconductors.*

1.1 Superconductivity and High Energy Physics

In HEP, the aim is to study collisions between charged particles accelerated up to energies that can reach the level of the ~TeV. Such experiments have allowed scientists to discover fundamental particles and properties of matter, and to develop descriptive models. To reach these high energy levels, circular accelerators [5] make use of electric and magnetic fields that respectively accelerate and control the trajectory of two opposite particle beams, letting them circulate around a ring several times until the required energy is reached. Superconductors can find here application in several systems and forms. For instance in: detectors; power lines; crab cavities, systems that optimize the beam collision angle; quadrupoles, magnets that focus the beam; dipoles, magnets that bend the particles around the circumference; corrector magnets that sharpen the field generated by quadrupoles or dipoles [6] (Figure 1.2). The dipoles are particularly important because the energy of the particles is proportional to the radius of the circumference and the magnetic field of the dipole [7]. On the one hand, increasing the magnetic field of the dipole can allow containing the length of the ring. On the other hand, in the design of an accelerator, one should also consider the energy losses due to the higher synchrotron radiation generated by particles on a lower curvature radius. The maximum field at which dipoles can be designed generally depends on the maturity of the technology and its cost. Key research areas for increasing the magnetic field of the future accelerator magnets are the development of materials with higher B_c, the engineering of dipoles constituted by such materials and the management of higher and higher mechanical stresses due to the increasing Lorentz forces.

The 1232 main dipoles of the Large Hadron Collider (LHC) at the European Organization for Nuclear Research (CERN) have a nominal field of 8.3 T in the bore of the particle beam. They are designed at the limit of the NbTi dipole technology [8]. The maximum collision energy by design of the particle beam is 14 TeV. With its 27 km long ring, LHC represents not only the biggest experimental facility but also the highest energy particle accelerator of the world [9]. Each dipole costs about 1 MCHF, equally divided among conductor, structure and assembly [10]. The conductor material is the alloy NbTi, whose ductility and relatively simple manufacture make it the cheapest and most used Low Temperature Superconductor (LTS) in nowadays magnet applications. An upgrade of LHC, called High Luminosity (HL-LHC), should start operating in 2025 [11]. The upgrade consists in the fivefold increase of the collision rate of the beam with respect to the current LHC design value, which will allow to acquire more data. This goal will be reached by the installation of new quadrupoles, which, providing a field of 12 T, will focus the particle beam more than the present 8 T ones. Moreover, the installation of two 11 T dipoles is also foreseen. From the point of view of the superconductor technology, these facts constitute a push towards innovation. In fact, the passage from 8 T to 11-12 T implies not only a change of the magnetic field intensity, but also a switch of conductor material, magnet manufacture and thus magnet technology. Beyond the technological limits of NbTi, these new magnets are going to be made up of Nb_3Sn and will represent the first magnets based on this material ever used in a particle accelerator. The characteristics of Nb_3Sn will be described in detail in Chapter 2.

By looking further into the future, the European Strategy for Particle Physics [12] is already planning the step after HL-LHC, once this will have reached its discovery potential limits around 2035. The future plans foresee to explore higher collision energies. In particular, one option consists in increasing by one order of magnitude the highest possible collision energy

in LHC, thus reaching 100 TeV, in a new machine called Future Circular Collider (FCC). This target would be reached by digging a new tunnel, 80-100 km long, and installing 4668 dipoles producing 16 T magnetic field. The use of Nb_3Sn instead of NbTi is mandatory. The estimated cost of each dipole ranges between 1.7 and 2.0 MEUR/magnet, already relying on a certain R&D development of such technology [13]. The cost of the only dipole magnet system would then be around 8 GEUR. A second option exploits the already existing ring of LHC, less expensive than FCC. This second option is called High Energy LHC (HE-LHC) and has in common with FCC the development of the Nb_3Sn 16 T dipoles that, in the case of the energy upgrade of LHC, would substitute the 1232 NbTi dipoles. In HE-LHC, the maximum collision energy would be 27 TeV.
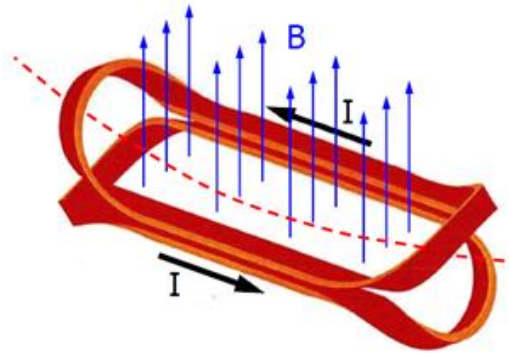

Figure 1.2 *Sketch of a dipole magnet for HEP (taken from* **[6]***).*

1.2 Superconductivity and Thermonuclear Fusion

In a fusion reaction, light nuclei collide against each other forming other nuclei and subatomic particles. During this reaction, part of the mass of the reagents is converted into kinetic energy of the products. The conversion of this into heat and eventually electricity, in a continuous and reliable way, is at the base of the future fusion power plants. The fuel must be kept for long burning periods around 150 million °C. There is no known material able to withstand such a temperature. This means that the fuel must be confined in order to avoid contact with the walls of a reactor. At this temperature level, the state of the matter is plasma. Therefore, it can be confined magnetically. The so-called Magnetic Confinement [14], which constitutes the most pursued confinement method nowadays, builds the link between Thermonuclear fusion and superconductors. As already anticipated in this Chapter, for the high magnetic fields (~1 T and ~10 T as order of magnitudes) and the size of the magnets involved, superconductors are preferred to conventional conductors. Superconductor magnets are not only the solution for the fusion power plants of the future, which will have to economically compete with the other energy sources, but they are also already employed in several large scale superconducting fusion devices, either in operation or in construction phase. Noteworthy examples are Tore Supra and ITER in France, Wendelstein-7 in Germany, T-15 in Russia, SST in India, HT-7 and EAST in China, KSTAR in South Korea, Triam, LHD and JT-60SA in Japan.

Based on the magnetic confinement scheme, several major types of fusion reactor concepts can be distinguished [15]: the Magnetic Mirror, Tokamak, Spherical Tokamak, Reversed Field pinch (RFP), Spheromak, Field Reversed Configuration, and the Stellarator. Among them, Tokamaks [16] are the most diffused and are believed to represent the most promising option. In this magnetic confinement concept, the plasma current creates one of the components of the

magnetic field. This plasma current is inductively generated by the transient magnetic field of the Central Solenoid (CS), one of the main magnet systems of a Tokamak. Based on this inductive mechanism, Tokamaks are pulsed machines. The two other most important magnet systems of a Tokamak are the Toroidal Field coils (TF) and the Poloidal Field coils (PF), as indicated in Figure 1.3 [17].

ITER is the biggest Tokamak and fusion machine worldwide. Its start of operation is foreseen in 2025 [18]. With its 500 MW expected thermal fusion power, ITER aims at demonstrating the feasibility of thermonuclear fusion as an energy source, i.e. proving that it is possible to gain from the fusion reaction significantly more power than the one used to trigger and sustain it. The aimed power gain by ITER, also called "Q factor" [19], is about 10. Detailed information about the ITER magnet system can be found in [20].

Beyond ITER, the next step would be a fusion reactor prototype able to demonstrate the reliable production of electricity. One of such demonstrators is called DEMO [21], the European fusion machine which is being designed within the EUROfusion consortium. Its first plasma is foreseen around 2050 [22]. The aimed electric power is around 500 MW, implying that the thermal power must be around 1600 MW due to the thermodynamic cycle. DEMO will then have all the components of a power plant. The cost of electricity from fusion and the capital cost of the power plant are among the topics that must be addressed. In DEMO, the cost of the superconducting systems can be about one third of the whole machine. In the current DEMO designs, most of the magnets are made up of Nb_3Sn, just like in HE-LHC or FCC. The huge cost of the magnet system warns that, even if it is the enabling technology of fusion, superconductivity can be the insurmountable obstacle of fusion energy as a competitive energy source [23]. As for HEP, R&D is needed to optimize the fusion magnet systems.
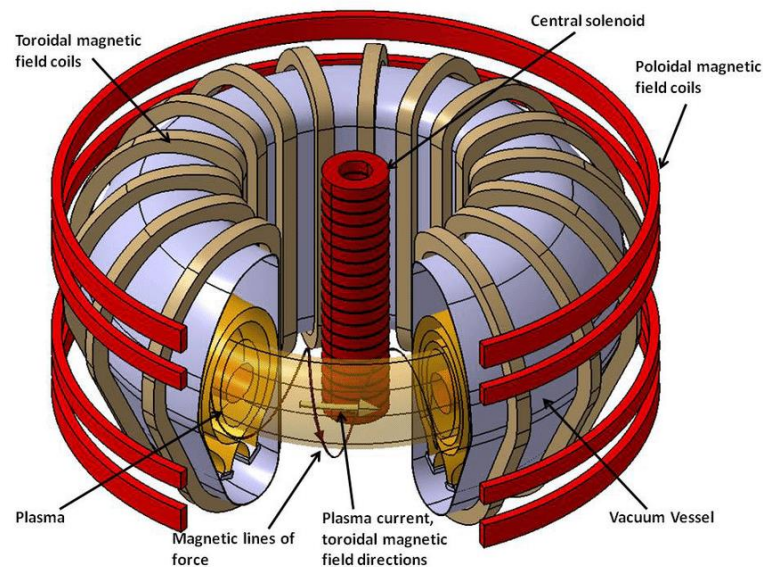

Figure 1.3 *Magnet system components of a Tokamak (taken from* **[17]***).*

2.   Background

2.1. The Nb₃Sn superconducting material

Nb$_3$Sn is an intermetallic compound with A15 crystal structure. Discovered in 1954 by B.T. Matthias et al. [24], it is a type II superconductor belonging to the LTS category and is commercialized in the form of filamentary composite wires (strands). The reduction in filaments with a diameter of the order of magnitude of ~10 μm is for electromagnetic and thermal stability reasons as well as to lower the superconductor magnetization [3]. Several filaments are arranged in a 0.5-2 mm thick wire. The matrix of the wire is usually made of Cu because of its ductility, thermal and electrical conductivity, which gives the composite thermal stability. In applications, the filaments of the wire are twisted to reduce coupling screening currents arising in the composite when transient field variations occur. In general, the only current contribution that is desired in a superconducting wire is the transport current, coming from the power supply.

In the magnet systems of HEP and fusion devices, the superconductor is wound in cable form rather than wire. Such a cable is obtained by twisting several strands in one or multiple stages. With respect to a strand, the winding of a cable has the advantage of a lower coil inductance, important for the charge, discharge and safety of a magnet [3]. The cable transposition is meant to reduce coupling currents among strands and the consequent power deposition in the cable, called AC loss. Moreover, transposed wires favour current balance in the wires of a cable during the coil charge, thus reducing the risk that some strands hit the critical surface by carrying more current than the others. However, in a cable, the performance of the wire is seldom retained. The actual critical current, I_c, of a Nb$_3$Sn cable is often smaller than the sum of the I_c of each strand, due to:

- The cabling process that, by compacting the wires to the desired shape of the cable, may irreversibly damage the filaments of the wires.
- The different strain distribution of the wires of the cable during operation. In fact, the superconducting properties of Nb$_3$Sn depend also on strain. A non-null strain shrinks the critical surface of Nb$_3$Sn [25] [26].

Because of the brittleness of Nb$_3$Sn, strand production and cabling are carried out with ductile precursors of the superconductor [27]. The composite wire contains Nb filaments and Sn. To form Nb$_3$Sn, the cable is heat treated up to a maximum temperature of about 650-700 °C for several days, during which the tin diffuses into niobium, forming Nb$_3$Sn crystals smaller than 200 nm in dimensions. The strand volume increases by a few percent after reaction. Figure 2.1 [28] reports an unreacted cross-section of the three main methods that are currently used to produce the wire: the Bronze method, the Internal-tin (IT) and Powder-in-tube (PIT) [29] [30]:

- In the bronze process, the Sn contained in a bronze matrix diffuses reaching the Nb filaments. A diffusion barrier out of Nb, Ta or V separates the bronze from the copper stabilizer to prevent contamination by Sn.
- In the IT process, the diffusion barrier is present as well. The Sn is not evenly distributed as in the bronze-process but is contained in discretized Sn cores. A stepwise heat treatment is needed to let first the Sn melt (~200 °C), form the bronze to homogenize the Sn around the Nb filaments (~390 °C) and, in the end, form Nb_3Sn.
- The PIT method consists in $NbSn_2$ powder embedded by Nb cans with a Cu tube in between. After a first heat treatment phase in which Nb_6Sn_5 is obtained from the powder, Nb_3Sn is formed.

The fabrication method, the duration and the temperature of the heat treatment influence the superconducting wire properties, in particular:

- The effective size of the filaments. The low Sn content involved in the bronze process often provides smaller filament diameters of the Nb_3Sn filaments (~2-3 μm) than in the other processes (~40-50 μm). In IT and PIT, the Nb elements are usually so close to each other that Nb_3Sn filaments bridging occurs when Sn diffuses, thus bringing to an equivalent filament diameter larger than the one of the precursors. Therefore, the filaments of a bronze-processed wire present better electro-thermal stability and have lower hysteresis losses, i.e. the ones occurring due to the magnetization of type II superconductors.
- The thermal strain of Nb_3Sn at cryogenic temperature. This tends to be lower in bronze-processed wires ($\varepsilon \approx -0.25$ %) than in the IT and PIT processes ($\varepsilon \approx -0.1$ %). This fact is a consequence of the higher thermal expansion coefficient of Cu with respect to Nb_3Sn and of the lower density of the latter one in the strands produced through the bronze process.
- The critical current density J_c. IT and PIT can provide higher J_c, also above 3000 A/mm^2 at 12 T and 4.2 K, because of the higher content of Sn than in the bronze and because of the high density of Nb rods or cans.

The length and the temperature of the heat treatment influence factors such as:

- The level of completeness of the stoichiometric reaction between Sn and Nb. Tin must first diffuse into Cu or bronze to reach Nb. Temperature and time favour this diffusion mechanism and thus J_c increases.
- The size of the Nb_3Sn grains. The grain boundaries serve as flux pinning centres [31], which are important for a high J_c. The temperature and length of the heat treatment decrease the density of grain boundaries and thus J_c.

For the reasons just mentioned, the highest J_c values come from a trade-off in time and temperature of the heat treatment.

Whereas for fusion magnets all three strand production methods are an option, in accelerator magnets IT and PIT wires are generally preferred, as accelerator magnets need higher current densities than fusion magnets.
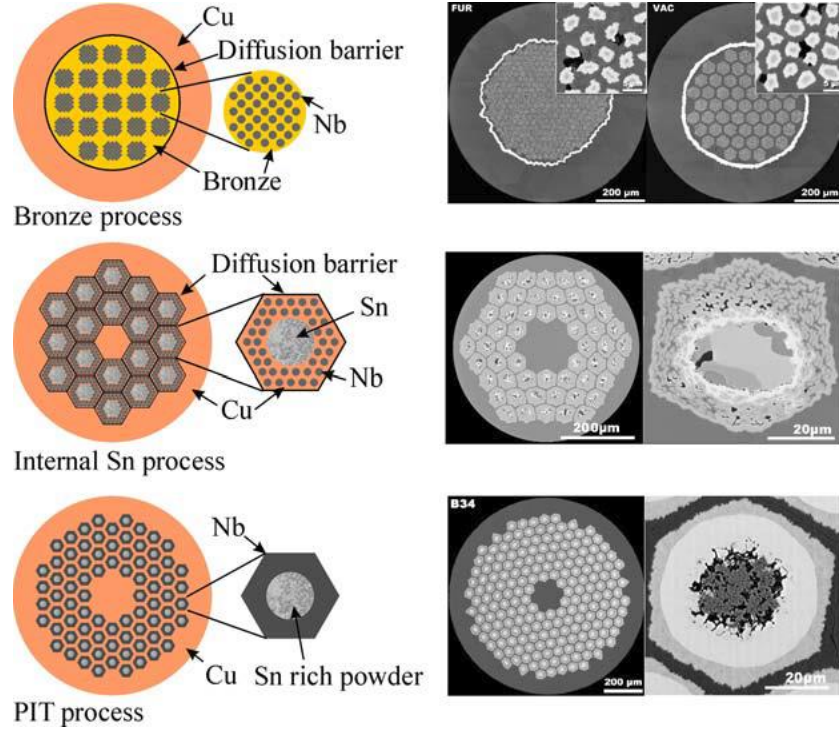
Figure 2.1 *Unreacted cross-section in the three main Nb₃Sn wire production processes: bronze process, Internal-Tin (IT) process and Powder-in-Tube (PIT) process. Taken from* **[28]***.*

2.2. Nb₃Sn conductors in HEP and Thermonuclear fusion

The Rutherford cable is the typical configuration used not only for NbTi but also Nb₃Sn accelerator magnets. It consists in a flat or slightly trapezoidal cable with multiple strands twisted in one stage on two layers (Figure 2.2). Compactness and windability on low bending-radii (~10 mm as order of magnitude) are among its principal characteristics. The former allows reaching a high engineering current density J_e, i.e. the one averaged on the conductor cross-section. In order to wind it on easy bending-radii, the cable has a thickness of about 1-2 mm. Consequently, the geometrical aspect ratio is relatively high, also over 10, since the number of strands required to reach the operating current I_{op} are arranged on the width of the cable. The wires are fully transposed, i.e. each of them has the same inductance. The compaction of the round strands increases the electrical contact among them, thus favouring the possibility of current redistribution between wires, which is an advantage in DC operation. In fact, in case of a strand current saturation, the other wires can take on its current, as magnets are designed to operate at a certain margin from the critical surface. On the other hand, the contact among strands increases the coupling currents loss in transients. This effect is nevertheless reduced not only by the twist pitch but also by interleaving a steel foil between the two strand layers, thus increasing the so-called crossover resistance. In order to insulate the adjacent turns of a coil, the Rutherford cable is wrapped upon fabrication with a glass fibre sleeve, whose thickness is about 0.1-0.2 mm.

In fusion conductors, the cable-in-conduit conductor (CICC) configuration has been one of the most exploited since the 1990s. Proposed for the first time in 1975 [32], it consists in a multi-stage twisted strand bundle in a conduit called jacket, which is usually made up of steel. Forced-flow supercritical helium passes inside the conduit and provides direct cooling to the bundle. In particularly long windings, the hydraulic impedance is decreased by adding a parallel

pressure relief channel, as shown in Figure 2.3 [33]. The jacket has both the function of being He-tight and that of cable structural support, reacting against the hoop force of the magnet (axial to the conductor) and the accumulating transverse force coming from the innermost layers of the magnet. While the jacket manages these integrated forces, the highest stress contribution for the superconducting cable cross-section comes from the Lorentz force acting on it. Contrary to accelerator magnets, in which the mechanical structure is not part of the conductor because it would affect J_e, part of the mechanical structure of fusion magnets is thus distributed and consists in the jacket. Another difference between HEP and fusion Nb$_3$Sn conductors consists in the strand coating. In the latter, Nb$_3$Sn wires are often plated with a Cr layer (as in ITER CICCs [34]) to avoid sintering among strands during heat treatment but maintaining the electrical conductivity among strands to an acceptable level. Sintering would create stress concentrations, compromising the integrity of the strands. In HEP Nb$_3$Sn coils, the winding pack is instead a solid block because it is completely resin impregnated after heat treatment to limit micro-movements during operation. For this reason, strands sintering is here not perceived as a disadvantage.
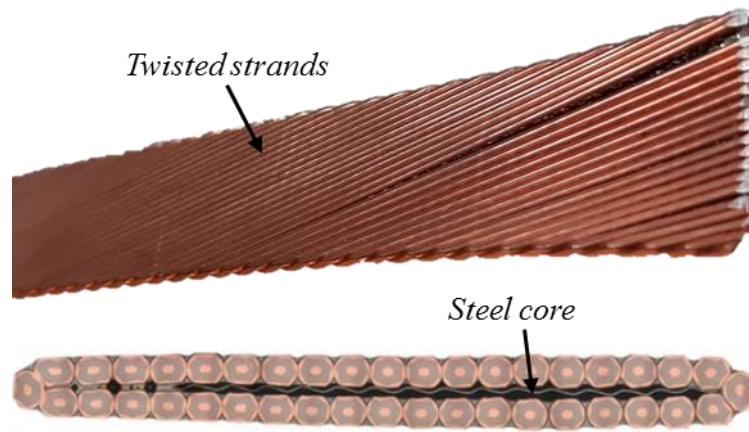
Figure 2.2 *Longitudinal view (top) and cross-section (bottom) of a Nb$_3$Sn Rutherford cable.*
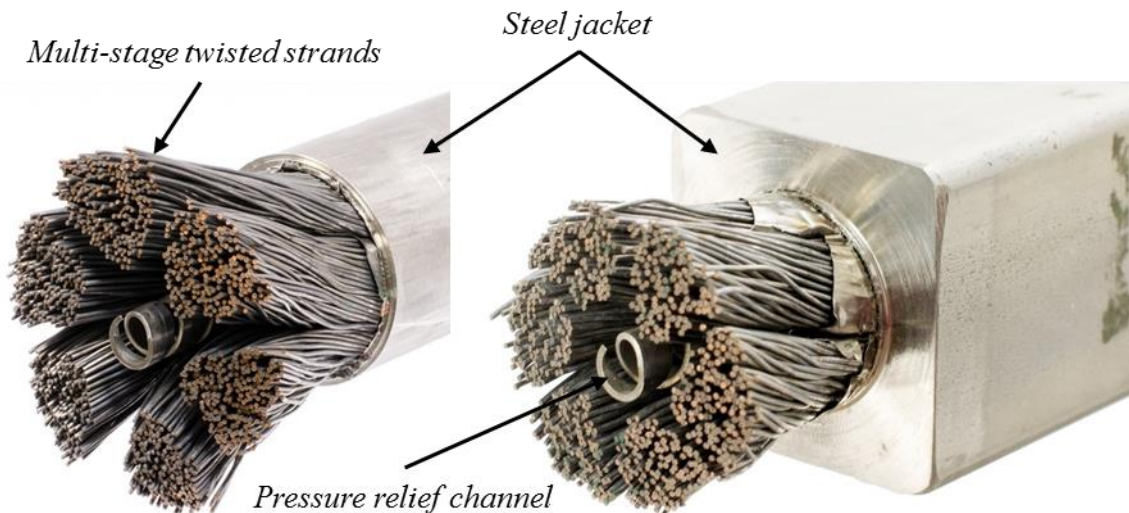
Figure 2.3. *ITER TF (left) and CS (right) conductor (adapted from* **[33]***).*

2.3. Magnet technology: Wind&React and React&Wind

While wires and cables are produced with Nb_3Sn precursors, the superconducting coils might be wound before or after the reaction heat treatment. We speak about the Wind&React technique (WR) in the former and React&Wind (RW) in the latter case.

Because of the brittleness of Nb_3Sn, the RW technique can be used only if the bending strain in the final winding is kept sufficiently low, that is $|\varepsilon_B| \leq 0.1$ % [35]. In the cable design phase, ε_B can be conservatively evaluated by approximating the cable to a solid body. Therefore, the maximum bending strain in the final winding depends on the thickness t of the cable, its bending radius during heat treatment R_{HT} and the one during the final winding R_{FIN}, according to the relation reported in equation (2. 1):

$$\varepsilon_B = \pm \frac{t}{2}\left(\frac{1}{R_{HT}} - \frac{1}{R_{FIN}}\right) \tag{2. 1}$$

In accelerator magnets, RW is prohibitive for most coil configurations except for the Common Coil one [36] because t is about 1-2 mm and the coil bending radius is ~10 mm as order of magnitude. This PhD thesis considers only accelerator magnets with WR technology.

In fusion magnets $t \sim 10\ mm$ and $R_{FIN} \sim 1\ m$, thus RW can be an option for a flat cable, such that the thickness and thus ε_B can be minimized.

When possible, the RW method is advantageous for a more efficient use of the superconductor and because it simplifies the assembly of the magnet. The more efficient use is linked to the different strain status of the Nb_3Sn microfilaments in a RW and WR fusion conductor. As already mentioned, the superconducting properties of Nb_3Sn are strain sensitive (Figure 2.4). It is possible to distinguish two types of strain contributions, namely the thermal one ε_{TH}, coming from the different thermal shrinkage between Nb_3Sn and the other CICC components when the magnet is cooled down to 4 K, and the operating strain ε_{OP}, which is due to the electromagnetic forces acting on a cable carrying current. In CS and TF magnets with steel conduits, ε_{TH} is usually compressive and ε_{OP} tensile. The net contribution of both is in general compressive. The main difference between WR and RW is in the lower value of $|\varepsilon_{TH}|$ of the latter, which allows using a lower amount of superconducting material in the coil. In WR fusion magnets, the steel conduit is assembled before heat treatment and compresses the microfilaments from their formation at ~923 K until the magnet operating temperature ~4 K, as steel has a coefficient of thermal expansion higher than the composite wire. In a RW magnet, ε_{TH} builds up between ~293 K and ~4 K because the jacket is assembled after heat treatment. In the SULTAN facility [37], tests can be performed to assess the cable effective strain ε_{eff}. This parameter is defined as the strain that the strands in the conductor should be subject to, in order to fit the I_c measured for the conductor with the parametrized $I_c(B,T,\varepsilon)$ obtained from single strand measurements. On round WR CICC samples of ITER, the effective strain ε_{eff} ranges between -0.97% and -0.63% [38], which is largely due to ε_{TH}, as discussed in [39] [40]. In rectangular WR CICCs produced by ENEA in the framework of the DEMO project, ε_{eff} ranges between -0.55% and -0.5% [41]. In the RW DEMO prototype designed by Swiss Plasma Centre (SPC) $\varepsilon_{eff} \sim$ -0.3% [42]. In this thesis, the focus is on fusion RW conductors and magnets.
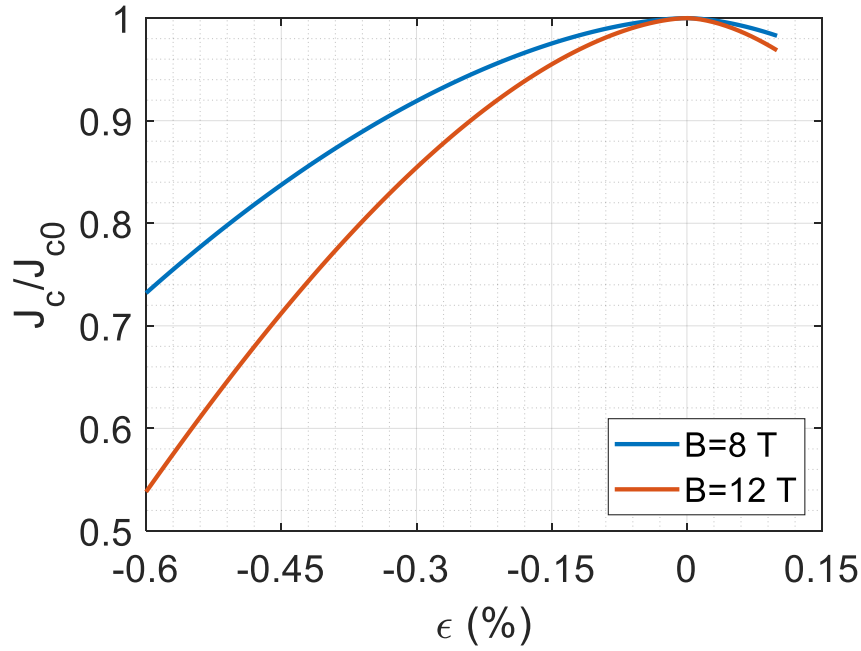
Figure 2.4 *Normalized critical current density as a function of strain.*

There are nevertheless other advantages in the adoption of the RW technique:

- The tolerances on the winding geometry are looser because they do not have to take into account the dimensional changes of the Nb_3Sn crystal structure occurring during heat treatment.
- Insulating the winding is more straightforward. There is no deterioration of the insulator upon heat treatment nor is a partial re-opening of the winding required to apply insulation, issues belonging to WR fusion coils.
- There is more cross-section available for the mechanical structure, as less superconducting material is needed.
- The heat treatment furnace can be smaller than the winding final dimensions.

2.4. Joints between superconducting cables and their classification

An *electrical connection* between two cables has the function of ensuring electrical continuity between them. In this thesis, the terms *joint* and *splice* generally refer to an *electrical connection* between two cables. The term splice recurs more often in the accelerator magnets literature than in the fusion. One exception is constituted by the ITER CS "splice joint" [43], which takes the name probably from its shape that recalls the one of nautical ropes being spliced, as shown in Section 2.5. Nevertheless, the accelerator magnet community is used to adopt this term also for cable joints that are not interwoven.

Every coil has at least two joints for the simple reason that the wound cable has a finite length with two extremities, named *conductor terminals*. In this case, the electrical connections are the *terminal joints* of the magnet. Through terminal joints, the coil is electrically connected either to other coils in series or to the power supply. In complex magnet systems such as in HEP or fusion, such a connection is not direct, but there are rather bus bars in between the different systems, i.e. intermediate cables having the role of routing current. In addition to this, between the bus bars and the room temperature power supply there are current feedthroughs,

often made up of High Temperature Superconductor (HTS) that manage the transition between cryogenic and room temperature in a more efficient way than LTS or copper conductors. Between one component and another, there is at least one electrical joint.

If embedded in the winding, the electrical connection is generally called either *internal joint/splice*, otherwise it is an *external joint/splice*. Joints could be located inside the winding pack either because of the limits in the cable production length, often the case for large fusion magnets, or because of a change of conductor inside the winding pack, introduced to optimize the quantity or type of superconducting material inside the magnet. This latter concept is called conductor *grading*. The electrical connection between two conductor grades might be called *intergrade joint*, which may be either external or internal. In a graded magnet, the use of the superconductor is optimized based on the fact that the superconducting properties are a function of the magnetic field, as shown in Figure 1.1, and that the field gradient in the winding of a magnet is generally non-null. By taking, as an example, an infinitely long solenoid radially wound with a superconducting wire or cable, the longitudinal magnetic field is the only component and decreases across the magnet thickness as in Equation (2. 2), derived by applying Ampere's law:

$$B(r) = \mu n I \frac{R_o - r}{R_o - R_i}, \qquad R_i < r < R_o \qquad \textbf{(2. 2)}$$

where μ [H/m] is the material magnetic permeability, n [m^{-1}] the number of turns per unit length of the solenoid, I [A] the conductor current and $R_{i/o}$ [m] the solenoid inner/outer radius. As B is lower when going from the innermost to the outermost turns of the magnet, the critical current density J_c increases for the same superconductor material when going from R_i to R_o. Therefore, a cable with lower superconductor cross-section but same current can be utilized along r. Examples of Nb$_3$Sn graded magnets in HEP are the HE-LHC/FCC dipoles currently under design: the Cos-θ [44], the Block [45], the Common [46] and Canted-Cos-θ [47] coils. In fusion magnets, the TF coils designed by SPC [48] and ENEA [49] for DEMO foresee grading. Research magnets are often graded to save cost, as for instance the 12 T EDIPO magnet [50]. The *hybrid* magnets constitute another grading concept. In the lower field magnet layers, they use a "less-performant" and thus less "noble" superconducting material, as for example in the DEMO CS proposed by SPC [51], which combines the use of HTS, Nb$_3$Sn and NbTi respectively from the innermost to the outermost layers.

The efficient use of the superconductor is not the only aspect of a graded magnet. There are other advantages, such as a smaller space required for the cable or a larger space at disposal for the structural support. In a fusion magnet, for example, the conductor grading allows also the jacket grading, i.e. the use of less structural material where it is not needed. A graded coil saves cost because of the lower amount of expensive superconductor and because of the potential space gain, which makes the entire fusion machine less cumbersome.

Joints are one of the most delicate components of a superconducting coil. With the function of ensuring electrical continuity between two conductors, they constitute a singularity in the magnet due to several reasons:

- The local heat power deposition, depending on the joint resistance and the current according to the equation $P = R I^2$.
- The local mechanical stress concentration, due to the geometrical discontinuity.

- It is a point of current redistribution among the strands of the cable, depending on the local contact resistance among strands.

Joints between cables can be classified based on their topology. We distinguish between the two macro-categories of overlap and butt joints (Figure 2.5). In the former, the lateral surface of the two cables are positioned one over the other, whilst in the latter the cut cross-sections touch each other. For each of these two joint types, there are some variations. For instance, among the overlap ones there are the praying hands and shaking hands joint. As opposed to shaking hands joints, in the praying hand ones the current is equal and in opposite direction in each of the two cables. As regards the butt ones, we count the bridge and interleaved joint.

Overlap joints offer a higher joining surface than pure butt splices, which is beneficial for the electrical resistance of the connection. On the other hand, they may present higher AC losses in certain varying magnetic field directions. From the mechanical point of view, the cable hoop load generated by the electromagnetic forces induces shear stresses in an overlap joint and tensile stresses in the butt one. The lower contact surface of butt joints is at times increased with the bridge or the interleaved variant. With respect to overlap joints, butt joints are "invisible" when embedded in the winding pack, in the sense that one cannot notice any change in the cross-section outer dimensions along the conductor. Therefore, the spacers and fillers needed for the integration of overlap joints into the winding pack are usually not foreseen for butt splices.
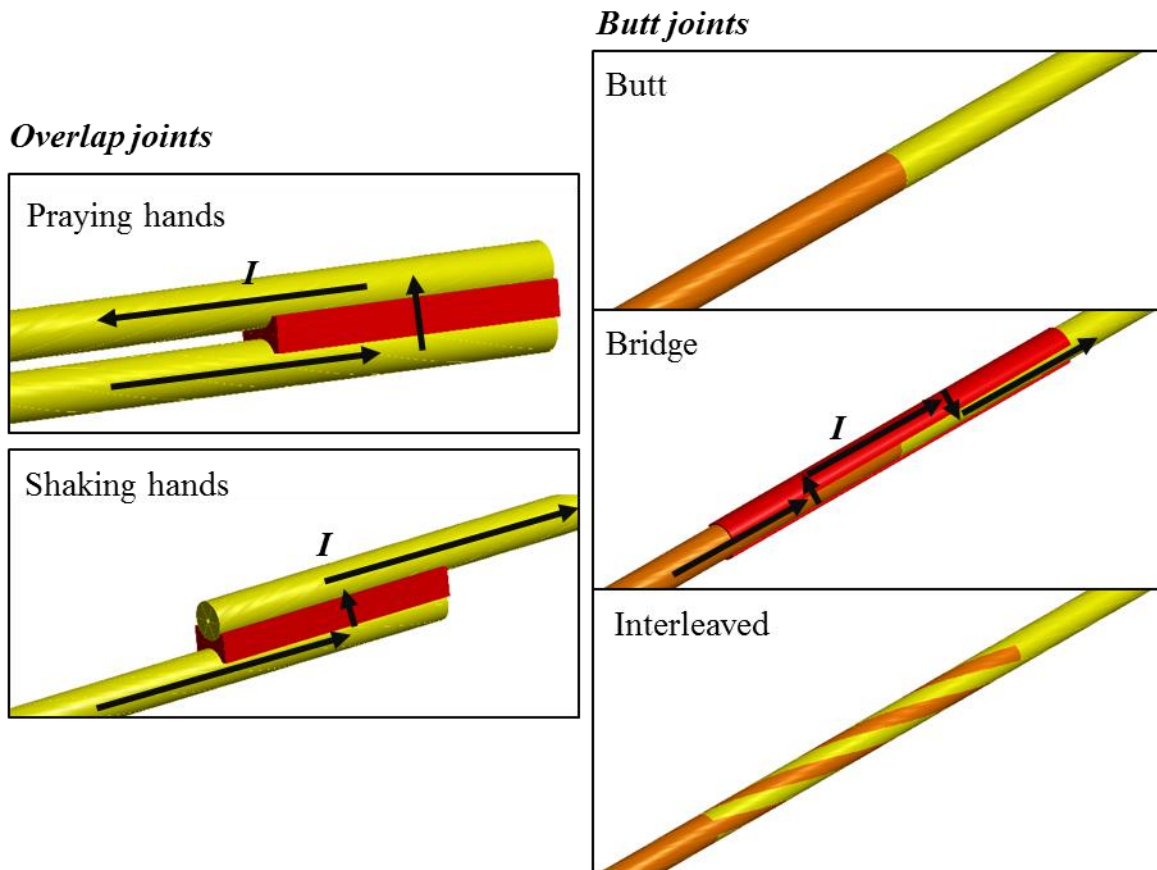
Figure 2.5 *Scheme of various joint configurations.*

2.5. Typical electrical joints between Nb₃Sn cables in fusion and HEP

The praying hand joint type is a configuration adopted in the Nb$_3$Sn "twin-box" joint of ITER TF coils [52], drafted in Figure 2.6 (the images are taken from [53], [54] and [55]). It consists in two clamped copper-steel bulky boxes, in which the cables are inserted and compacted before heat treatment, such that the contact resistance between strands and copper is minimized. After heat treatment, the copper part of the boxes are cleaned with fluxing agents, locally heated and tin-lead soldered. A variant is the one in which indium wires are squeezed between the copper surfaces instead of soldering [56]. With the drawback of a lower mechanical strength, the indium variant has the advantage of an easier disassemblability in case of repair, the avoidance of "dirty" fluxing agents and heating, which could damage the insulation, in case the last one must be put before splicing. The twin-box is a concept developed by CEA that is used also in other magnet systems, Tokamaks and between NbTi conductors as well, as in the TFs of JT-60SA [57]. The praying hand joint of ITER TF is external and unites two cable lengths of the same magnet through a protrusion of the winding that positions the joint in a low field region ($B \sim 2\,T$), thus increasing its operability because of the higher cable J_c, and makes it accessible for splicing and inspection after manufacture. Six joints like this are present in each ITER TF.

In the same magnet, two twin-box joints in shaking hands configuration are at the coil terminals, where the TF cable is mated with the NbTi bus bar. The shaking hands configuration allows routing the bus bar to the direction opposite to the TF. Each ITER TF praying hands joint has the electrical resistance requirement $R \leq 3\,n\Omega$ at operating conditions of current $I = 68\,kA$, background field $B = 2\,T$ and temperature $T = 4.5\,K$. The shaking hands joints must have $R \leq 4\,n\Omega$ each at the same conditions.
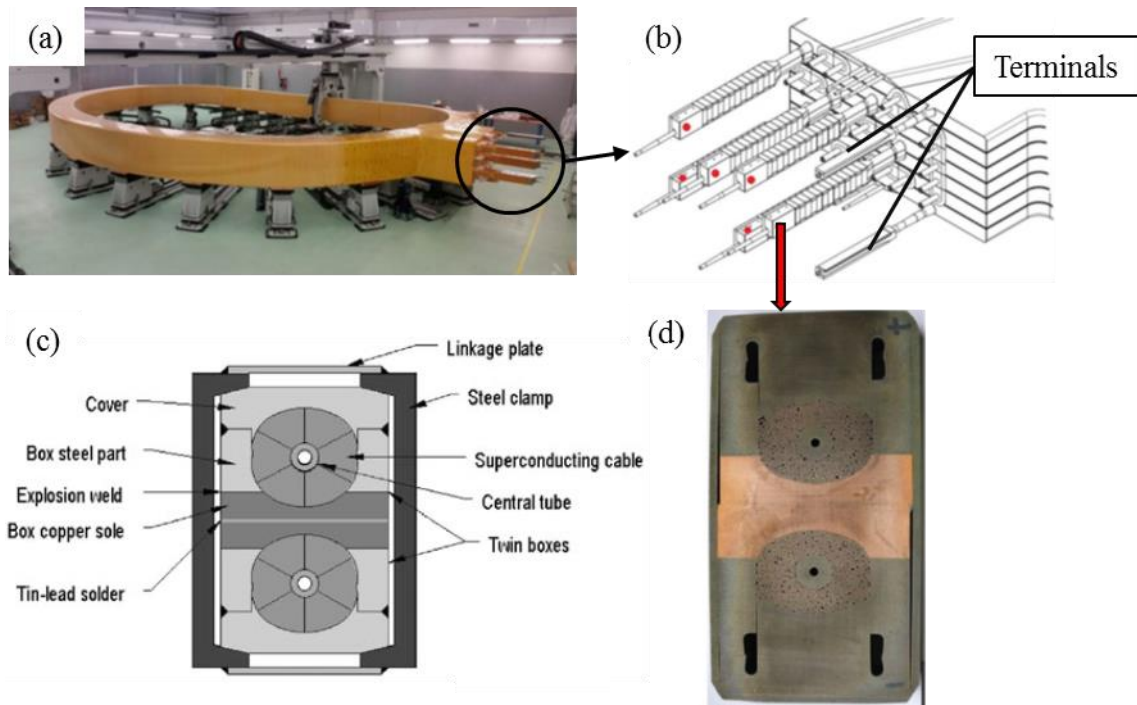
Figure 2.6 *One of the ITER TF (a) and sketch of the joints (b) (taken from* **[53]***); sketch (c) and cross-section (d) of the joint (taken from* **[54]** *and* **[55]***, respectively).*

An example of internal butt joint between Nb_3Sn cables can be found in the diffusion-bonded splice of the CS of JT-60SA (Figure 2.7). The butt-type configuration is chosen in order to continue the magnet turn in the outer CS radius and to fit in the winding pack. The two surfaces are put in butt position before heat treatment, after which a thin copper foil is put between the two mated conductor cross-sections for the copper diffusion-bonding. The procedure was developed during the joint R&D for the ITER CS Model Coil (CSMC) [58] and then optimized for the JT-60SA CS joint. The cables are pressed against each other at about 30 MPa, vacuum is provided around the joint region to limit the conductor oxidation, an induction heating system heats locally at 655 °C. These conditions are kept for about one hour. The joint resistance is 2 nΩ at 2 T, below the limit of 5 nΩ [59]. The choice to go for a diffusion-bonded joint, rather than for a soldered one, is mainly for mechanical reason. Copper has generally a higher mechanical strength than solders and the CS is a pulsed machine, due to which its materials suffer from fatigue. The CS of JT-60SA, in particular, is expected to undergo 36000 load cycles in the Tokamak lifetime. Nevertheless, a diffusion-bonded joint is not demountable, opposite to a pressed indium joint in which the pressure clamp can be released and unlike a soldered joint that can be in principle heated up again for melting the solder.
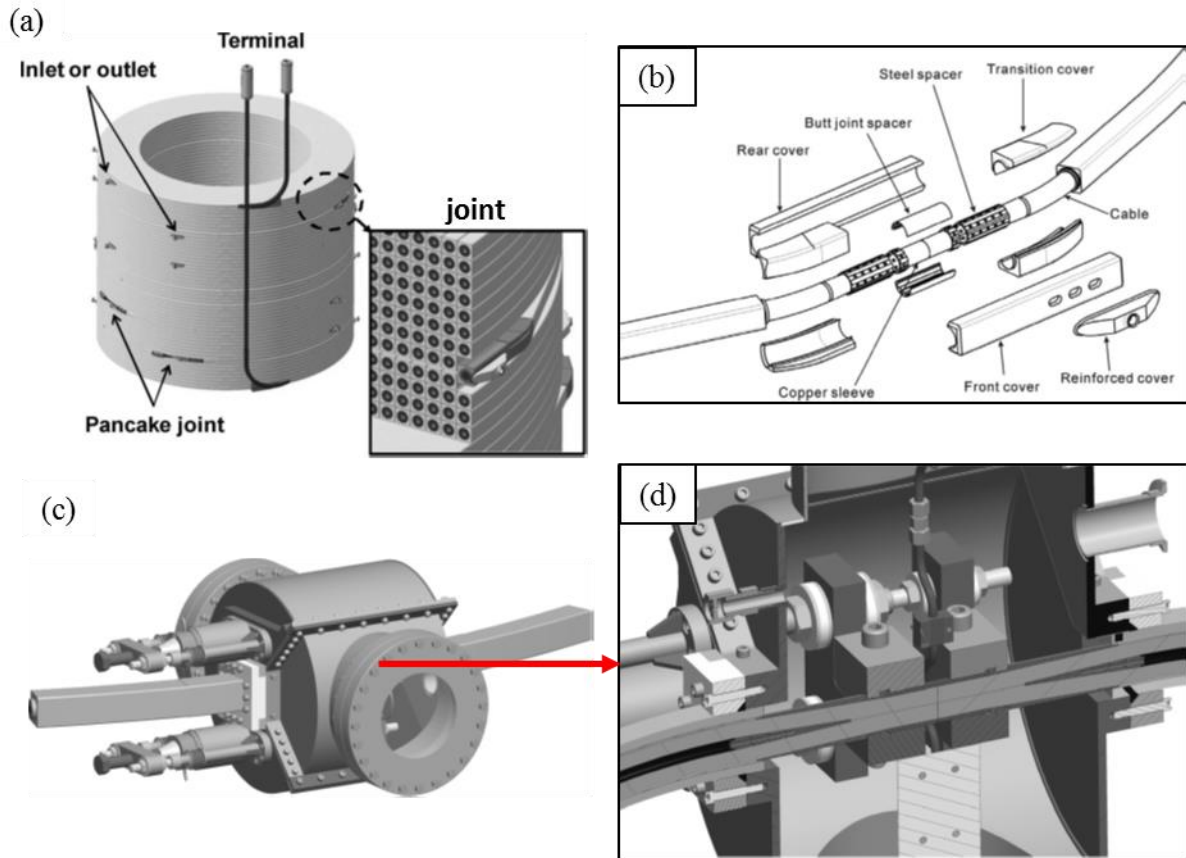
Figure 2.7 *Sketch of the CS of JT-60SA (a) with exploded view of the diffusion-bonded butt joint (b) (images taken from* **[59]***); system for applying pressure and heating by induction in vacuum in the joint region (c, d) (taken from* **[58]***).*

The "sintered joint", or "splice joint", is an example of interleaved butt joint connecting two conductor lengths of the ITER CS. The same one is used for the 12 T EDIPO magnet [60]. Like in the JT-60SA solenoid, it is located at the outer radius of the magnet. Before heat treatment, half of the strands of the two Nb_3Sn are cut, in order to fit each CICC into each other and

reconstruct the single cable geometry (Figure 2.8). The joint is then compacted and forms during the coil heat treatment per diffusion-bonding. With respect to the one of the JT-60SA CS, diffusion-bonding of the strand copper stabilizer takes place here longitudinally rather than transversely to the conductor. For its construction and position inside the winding pack, repair and maintenance are impossible. It is a joint able to operate only at low field. In fact, the conductor critical current I_c at high field would be heavily reduced, as half cable is cut. Nevertheless, the high contact surface between strands leads to a very low joint resistance, namely below 0.15 nΩ at 2 T, considerably below the 4 nΩ limit value of the ITER CS [61].

An external butt joint in bridge configuration is the terminal joint between the ITER CS module and the bus bar extension. This is called "coaxial joint", a solder based joint being spliced after heat treatment [62]. The bridges are constituted by two sets of soldered superconducting strands (Figure 2.8). With a second solder with lower melting point, these two sets are spliced to the sides of the two CICCs. The butt joint configuration ensures compatibility with the low space at disposal, while the soldering choice is conceived to be able to provide disassembly for repair, if necessary. The requirement is $R \leq 4\ n\Omega$ at $B = 2\ T$.

Steel Jacket
Cu crescent
Nb$_3$Sn laced union
Cu crimped cable
Nb$_3$Sn cable
He channel
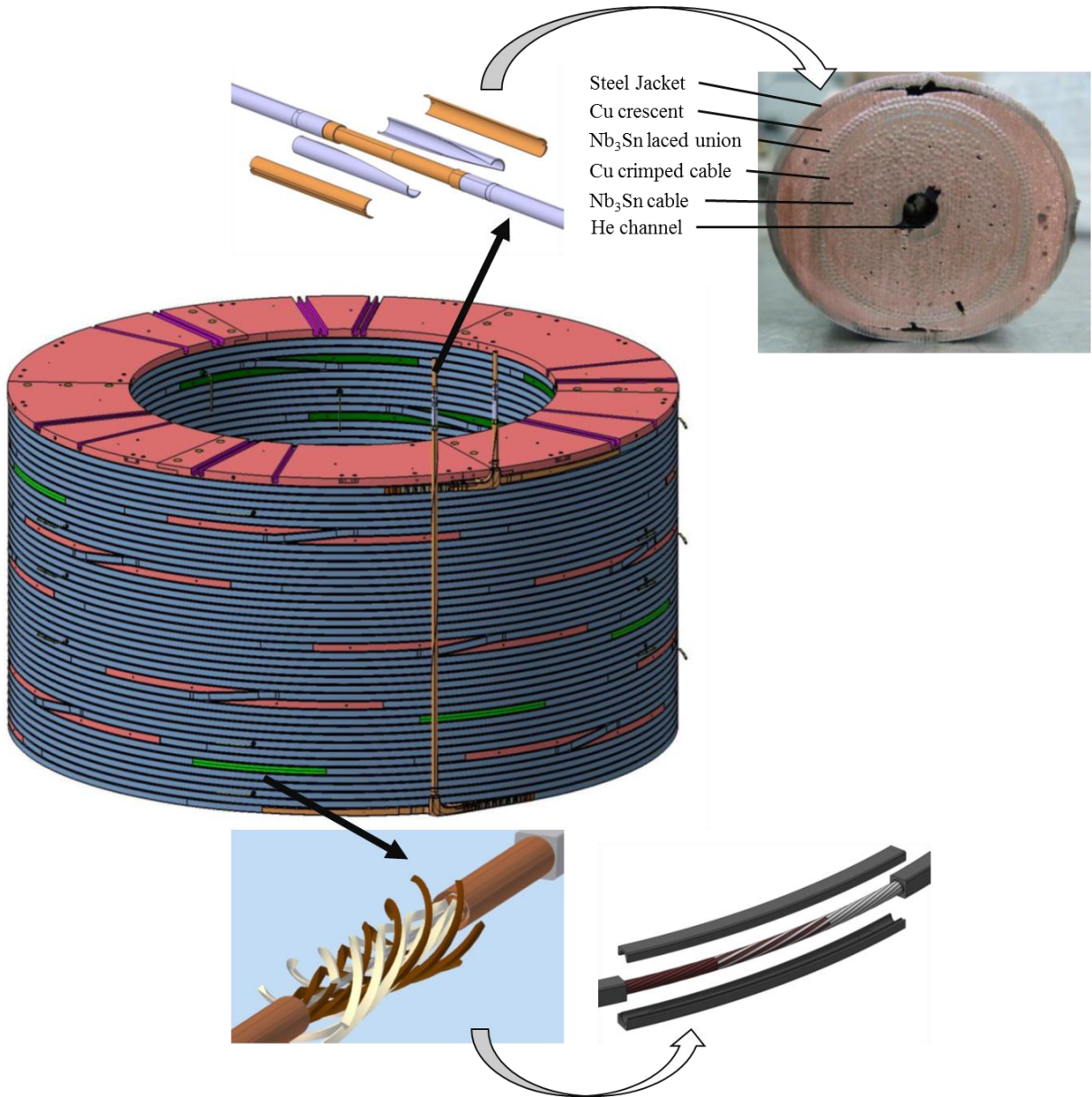
Figure 2.8 *ITER CS module (centre) with zoom on the coaxial joint (top) and sintered joint (bottom) (images readapted from* **[61]***)*

Most of the splices of existing Nb$_3$Sn WR accelerator magnets are external to connect the magnet terminals to the bus bars. For the low thickness in comparison to the cable width, they are often overlap splices. The brittle Nb$_3$Sn cable is soldered to the NbTi leads, as shown in Figure 2.9. Examples like these can be found in experimental magnets such as the UT-CERN Cos-theta LHC-Type Nb$_3$Sn Dipole Magnet, the LBNL Cos-theta Nb$_3$Sn Dipole Magnet D20, the Block-Type Nb$_3$Sn dipole at Texas A&M University, the HD Block-Coil dipole at LBNL, the CEA-CERN Block-Type dipole magnet FRESCA2, as well as in the 11 T dipoles for the HL-LHC [63].

Figure 2.9 *External splice between the Nb₃Sn cable of the Mirror-Geometry Dipole magnet TAMU2 and the NbTi lead (image taken from* **[63]***).*

2.6. Scope of the thesis

In Section 2.5 the typical joints between Nb₃Sn cables for high field and high current magnets of HEP and fusion were presented. In most of the cases, the joint is either an *external splice* that has the function of connecting the coil to bus bars (*terminal joints*) or a splice that connects two conductor lengths of the same winding pack. In the latter case, the joint can be either *external*, as the twin-box of ITER TFs and the soldered splices of research dipole magnets, or internal, as the diffusion-bonded joint of the CS of JT-60SA. All these joints have in common that they connect two sections of a high-grade cable, i.e. the one that is designed to operate in the most critical regions of the winding and is employed in the least critical turns as well. Hence, these magnets do not use conductor grading. Furthermore, all of the listed joints operate at relatively low field ($B \leq 2\ T$), far from the conductor critical conditions.

This thesis concentrates on the development of high-current Nb₃Sn joints able to operate at higher magnetic field ($B \geq 8\ T$), thus much closer to the limits of the superconductor. Such a development may find application in *intergrade joints* of the HEP and fusion magnets of the next generation. Indeed, conductor grading in superconducting magnets is the commonality of the current R&D in both fields. The *intergrade joint* is the component that, by connecting the different grades of the magnet, allows such a grade to take place. An intergrade joint might be either external or internal. In the former case, the joint operates in a low field region, thus with less risk of quench and higher accessibility in case of repair after winding, if applicable. The price to pay is the additional mechanical structure to support a joint that is outside the tight winding pack and the consequent additional space required. Even though an intergrade internal joint operates at high field and may not provide chance of reparability if the failure is detected after winding, it minimizes the quantity of space and structural support to withstand the electromagnetic forces because it is embedded in the winding pack.

The specific goal of this thesis is to demonstrate the feasibility of a high current and field joint for WR HEP dipole magnets and RW fusion magnets through the design, fabrication and test of 1:1 joint prototypes. As the requirements and the magnet technology are different for the two applications, the two developments are threated independently.

Chapter 3 is dedicated to the development of a high field Nb₃Sn internal joint for WR accelerator magnets. The splice requirements and the boundary conditions are first introduced. The potential joint techniques are investigated, the design of the prototypes are illustrated and

the experimental campaigns are reported. In the end, the Chapter focuses on the discussion about the integration of the developed prototypes into a WR accelerator magnet.

In Chapter 4, the development of a high field Nb_3Sn inter-layer joint for RW fusion magnets is discussed. The structure is very similar to the one of Chapter 3.

Chapter 5 ends the manuscript with the main achievements and implications that the work done has on the development of graded HEP and fusion magnets, and the identification of further investigations.

3. Internal splice for a Wind&React accelerator magnet

3.1 Splice location and requirements

The design of the joint is linked with that of the magnet and with the geometry of the coil. This thesis considers the WR dipole magnets of interest for HE-LHC/FCC, namely the cos-θ, the block-type, the common-coil and the canted-cos-θ (CCT) dipole. In these magnets, it is convenient for internal splices to be located at the dipole heads, i.e. at its extremities, where they minimally affect the field quality in the bore. These magnets might be produced using different winding technology, i.e. either *layer winding* or *pancake winding* (Figure 3.1), but share the fact that the head geometry is curved. Therefore, a first requirement is the joint integration in the magnet in bent geometry. Figure 3.2 shows the sketch of a *racetrack coil*, i.e. a coil consisting of only straight parts, while Figure 3.3 shows an example of two splices embedded in such a coil geometry at the magnet heads.

This Chapter defines common guidelines for WR accelerator magnets with curved head in general, without stressing the geometrical peculiarities of each of the dipole concepts of HE-LHC/FCC.

A second requirement is the minimization of the space occupied by the splice, which, in turn, minimizes the volume, the quantity of cable and the cost of the magnet.
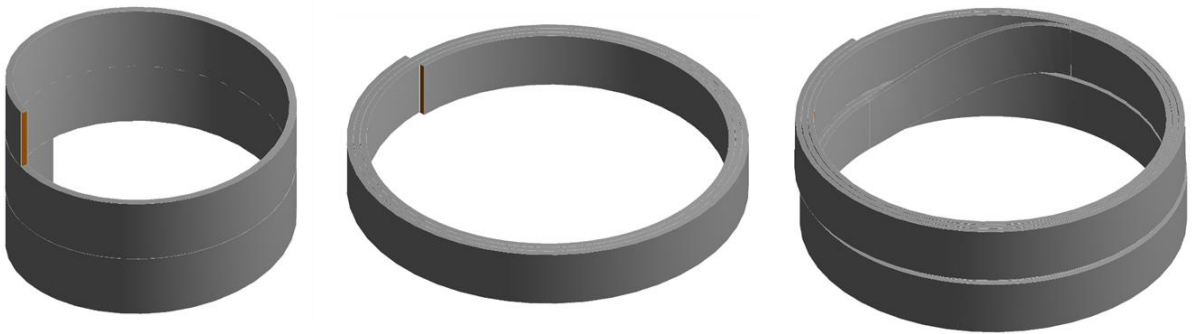
Figure 3.1 *Layer (left), single pancake (centre) and double pancake (right) winding of a coil.*
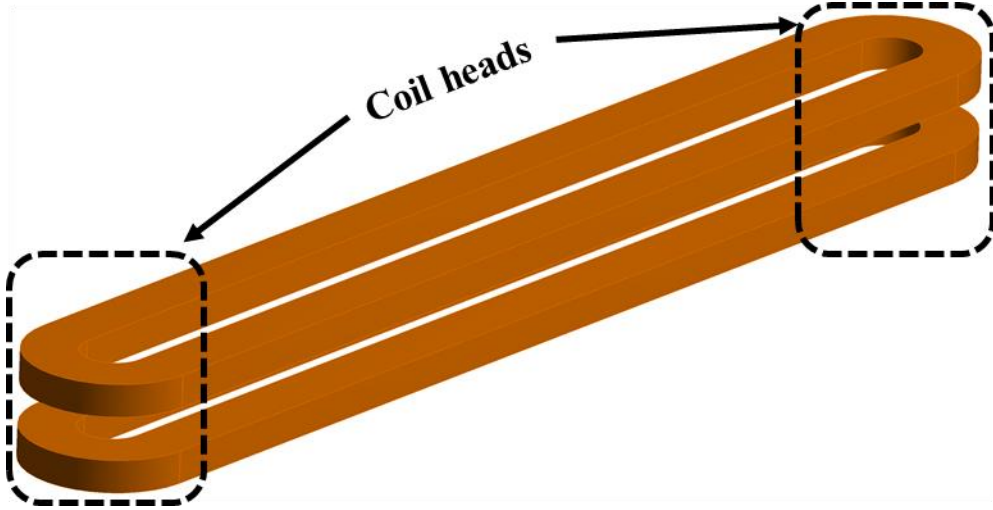
Figure 3.2 *Sketch of a racetrack dipole.*
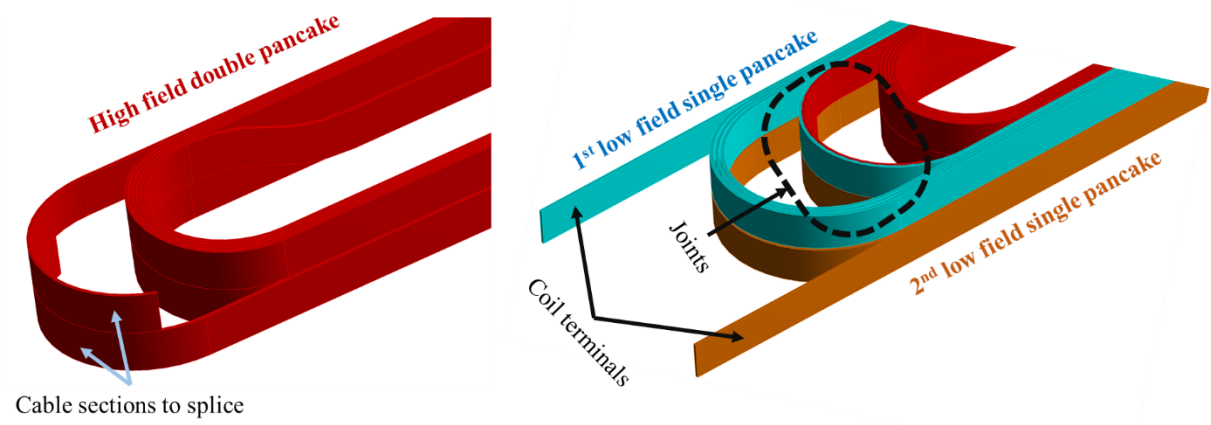
Figure 3.3 *Racetrack double pancake with highlight on the cable sections to splice (left) and racetrack coil with two internal overlap joints.*

Other commonalities among these WR dipole concepts are the operating temperature T=1.9 K, the similar operating current $I_{op}\approx$10 kA and the glass-resin impregnation after heat treatment, whose thermal conductivity is k_{ins}(1.9 K)=3.3·10^{-2} W/(m·K) [64]. These parameters define the local heat removal of the splice at operating conditions and lead to the definition of the third and most important joint requirement, i.e. the electrical resistance R_J. Assuming an allowable thermal gradient ΔT=0.3 K between helium and splice, a joint insulation area A_{ins}=10^4 mm^2 and an insulation thickness t_{ins}=1 mm, the maximum allowable R_J can be as in (3. 1).

$$R_J\left(B_{J,op}, I_{op}, T_{J,op}\right) = \frac{P_J}{I_{op}^2} = \frac{k_{ins} \cdot A_{ins} \cdot \Delta T}{t_{ins} \cdot I_{op}^2} = 1\ n\Omega \qquad \textbf{(3. 1)}$$

where $B_{J,op}$ [T] and $T_{J,op}$ [K] are, respectively, the magnetic field and temperature of the joint when the magnet is at operating conditions. The corresponding dissipated power by one splice is $P_J = R_J \cdot I_{op}^2 = 0.1\ W$. The total power dissipated by all the splices must be compatible with the cryogenic cooling power.

The operating magnetic field $B_{J,op}$ in the internal joint region is expected to be around 10 T in the magnet concepts considered by HE-LHC/FCC. However, the particular cable for such dipole magnets does not exist, yet. In the SULTAN test facility, which is used in this thesis to

characterize the developed splice prototypes, the minimum reachable temperature is 4.5 K. Therefore, one needs to define equivalent conditions at which the electrical resistance can be assessed. The proposed equivalent conditions are based on the ratio between the test current and the cable critical current, $I_{test}(B_{J,op}, T_{test})/I_c(B_{J,op}, T_{test}) \approx 1/3$. This value corresponds to a 14% safety margin [65] on the dipole load-line, value foreseen for the dipoles of HE-LHC/FCC by the European strategy for HEP (Figure 3.4). In particular, the load-line is the characteristic curve (*I*, *B*) of a magnet: each value of the cable current *I* corresponds to a value of the *B*-field in the bore. The safety margin at a certain temperature on the load-line is defined as the ratio between the length of the load-line segment comprised between the magnet operating field B_{op} and the critical line, and the length of the load-line segment comprised between *B*=0 and the critical line.

The joint must withstand the mechanical load. In a butt joint, the tensile stresses might dominate the other components. In the case of an overlap joint, the splice might experience mostly shear stress.

As in the dipoles for HE-LHC/FCC the cable to splice for the magnet grading have same width but different thickness, the more convenient splice layout option is the overlap. The overlap length should be in the order of one twist pitch length, to assure that each strand of the two cables in contact has similar contact length and thus a more homogeneous current distribution.
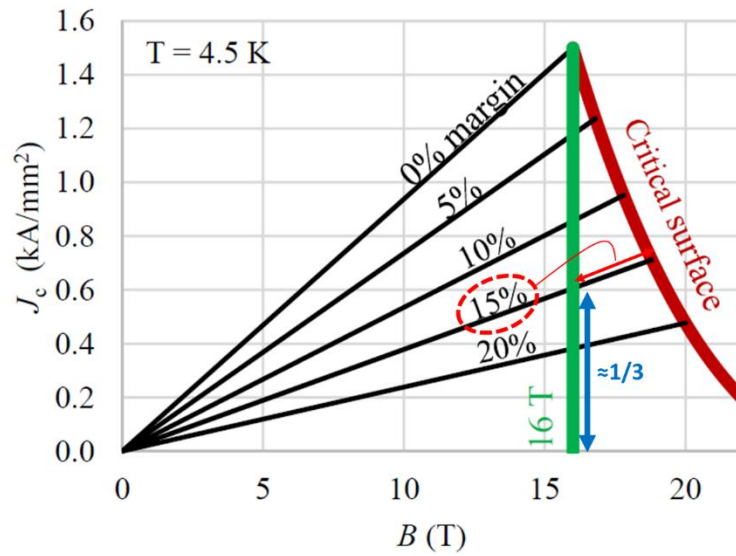
Figure 3.4 *Safety margin values for a dipole operating at B=16 T (adapted from* **[65]***).*

The requirements and characteristics for an internal joint between Rutherford cables in a WR dipole for HE-LHC/FCC are summarized as follows:

- The maximum splice resistance is $R_{J,max} = 1\ n\Omega$ at *T*=1.9 K, *B*≈10 T, I_{op}≈10 kA. In a test in SULTAN, the proposed equivalent conditions are $R_{J,max} = 1\ n\Omega$ at *T*=4.5 K, *B*≈10 T, I_{test}/I_c=1/3.
- The joint must be integrated in the bent geometry of the dipole head.
- The volume occupied by the splice must be minimized.
- The splice must withstand the mechanical load. The shear or tensile stresses are be the dominant components, depending on the joint layout.
- The splice is in overlap geometry.

- The splice length is about one twist pitch length.
- The joint must be inspectable for the quality assurance.

3.2 Splicing techniques for Wind&React magnets

In a WR magnet, the internal joint can form before, during or after the coil heat treatment depending on the splicing technique. Based on the joint requirements listed in this Chapter, three splicing techniques were identified as potential candidates:

- *Ultrasonic welding* (UW), suitable before the heat treatment of the magnet.
- *Diffusion bonding* (DB), for the formation of the splice during heat treatment
- *Soldering*, after heat treatment.

3.2.1 Ultrasonic welding

Ultrasonic welding (UW) is a friction bonding process, i.e., it does not require melting of filling metals. This makes it a clean technique. Another advantage is that the joint can be built before the magnet heat treatment. The main issue is that only materials with maximum 1-2 mm thickness can be welded. Rutherford cables are at the limit of the potential of this application.

In this process, the two pieces to weld are in overlap position between a stationary terminal (*anvil*) and a moving one (*sonotrode*). Vibration with frequencies in the range of 15-25 kHz and hundredths of millimetre of amplitude induce friction between the two pieces, breaking apart the oxide layer at the mating surfaces and allowing atomic inter-diffusion between the two clean surfaces. This method is also suitable for bonding dissimilar materials and is very popular in industrial manufacturing [66]. It has been used from large to thin pieces (as in field of microelectronics). References of its use for REBCO coated conductor tapes (copper to copper) are available in literature [67]. Thousands of interconnections between the corrector magnets in the LHC (NbTi wires) have been made with ultrasonic welding (Figure 3.5 [68]).

This process can be applied before the heat treatment of the cable with several advantages:

- Cable handling is allowed because Nb_3Sn has not reacted yet and thus the cable is ductile.
- A broad space at disposal for the dedicated tooling and splice operations. For instance, with reference to Figure 3.3, the high field double pancake is wound first. The two extremities of the winding are then spliced to the cables of the first and second low field single pancakes. Since these ones have not been wound yet, the joint assembly can enjoy minimum space constraints.
- Minimization of the splice volume. In fact, the tooling is removed soon after splicing and the winding of the coil can continue.

A feasibility study of this technique for Nb_3Sn strands and Rutherford cables is reported in this thesis, where it is attempted to splice the copper surface of the components.
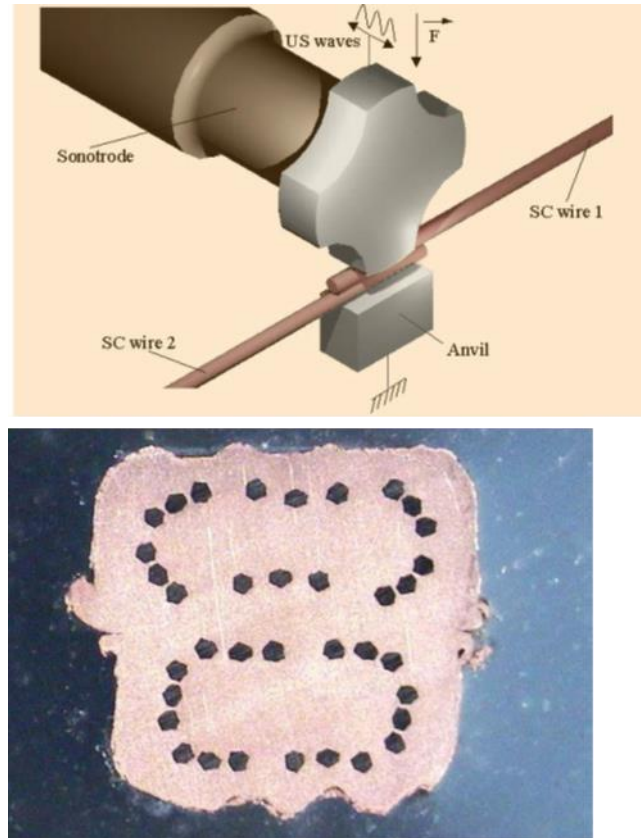
Figure 3.5 *Ultrasonic welding main components (top) and application to two NbTi wires of LHC (bottom). Pictures taken from* **[68]***.*

3.2.2 Diffusion-bonding

Diffusion-bonding (DB) is a solid-state process for making a joint through the formation of bonds at atomic level between similar or dissimilar metals [69]. A significant pressure is required to bring the mating surfaces close enough and allow a local plastic deformation at elevated temperature to break the thin brittle oxide layer between the clean metal surfaces. The inter-diffusion at the surface layers of the materials results in diffusion bonding. DB can be microscopically described as the succession of two stages (Figure 3.6):

- The two surfaces form a contact. A plastic deformation of the microasperities present on the contact surfaces due to the applied pressure occurs, thus increasing the contact between the two objects. The higher the temperature, the lower the yield stress of the material.
- Bulk, grain-boundary and surface diffusion of the metal take place. The principal parameters that activate the mechanism are pressure and temperature. The higher the pressure and temperature, the longer the diffusion distance and the lower the diffusion time.

As it is a splicing method based on contact, surface conditions such as roughness and level of impurities determine the required level of pressure and temperature [70]. In particular, low roughness and surface impurity concentration are favourable for the process.

In the DB splice between two Nb_3Sn Rutherford cables, the copper stabilizer of the two cables diffuses into each other. The optimum temperature for Cu is in the range 600-700 °C [71] [59],

which makes this technique suitable for its application during the magnet heat treatment, where the peak temperature 650 °C is kept for about 50 hours. Because of the high temperature, vacuum or an inert atmosphere have to be provided. The main challenge is the integration inside the magnet of the tooling system that applies the required pressure. Moreover, such a tooling shall be able to hold together the two cable sections to splice, such that the low field cable can be wound with the required mechanical tension when there is still no mechanical bonding between the two cables. Once the coil is heat-treated and the splice is formed, the cable is brittle and it is then preferable to minimize its handling. For this reason, the possibility of removing the splicing components after heat treatment is much limited.

A system that applies pressure and suits the joint and magnet requirements for HE-LHC/FCC was developed as part of this thesis work.
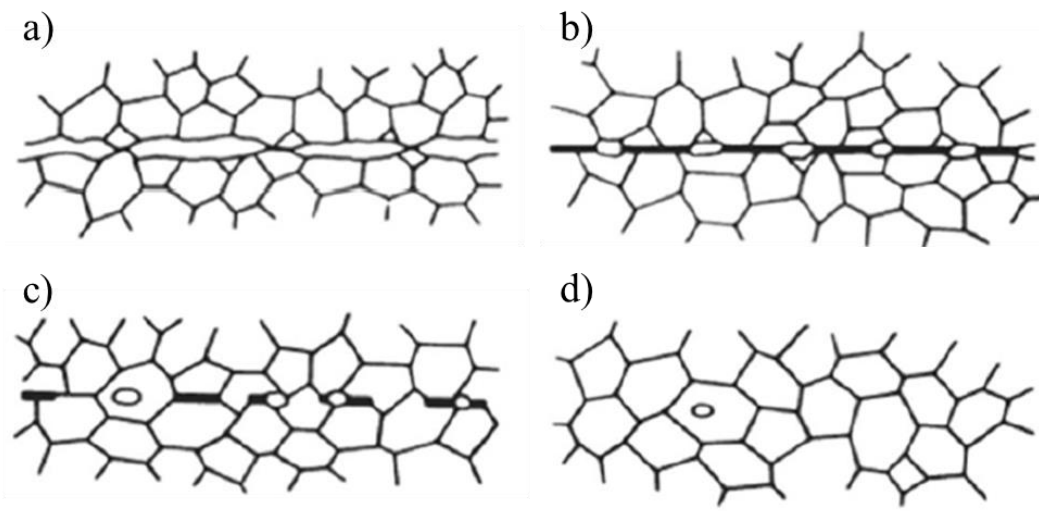
Figure 3.6 *Schematic of the diffusion-bonding mechanism: initial contact (a), deformation of the interfacial asperities (b), grain boundary diffusion (c), volume diffusion (d). Picture taken from* **[72]**.

3.2.3 Soldering

Low melting point filler material, for example SnAg or SnPb, melts in the contact area. The metallic bond between the solidified solder and the cable surfaces forms the joint.

The surfaces to splice usually need to be first activated. This is done through the employment of chemical fluxes, which are poured onto these surfaces to clean them from impurities and to increase their wettability, i.e. the adhesion between the molten metal and the surface. Moreover, such fluxes also reduce the surface tension of the molten solder in favour of the capillarity through the pieces to splice.

This method requires heating up the Nb_3Sn Rutherford cables after the heat treatment. Soldering is traditionally the most popular and widely used method in accelerators and fusion industry. Just to cite one among several example, it was used for soldering the NbTi bus bars of the LHC magnet system (Figure 3.7). However, this method still needed optimization for being used in HE-LHC/FCC.

As this technique is applicable after heat treatment, it shares with the diffusion-bonding technique the issue of the winding mechanical tension, which must be kept between two cables that are not splice, yet. Moreover, spacers shall be accommodated into the magnet before heat treatment to reserve space for heaters needed to splice. The handling of the section of the cables to splice might be not possible.
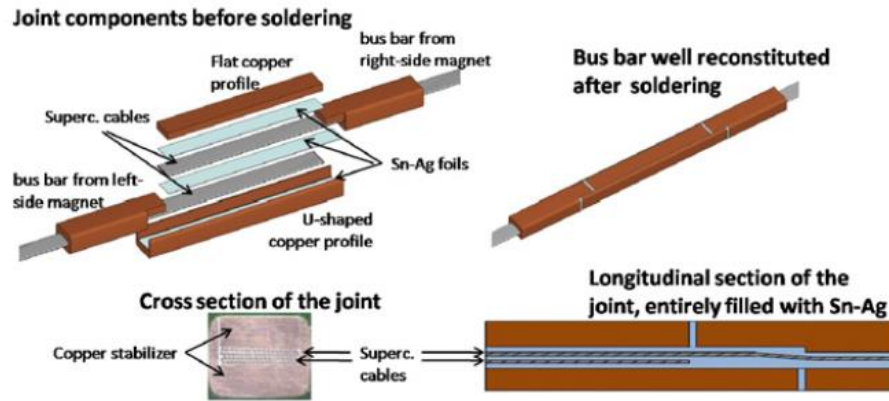
Figure 3.7 *Scheme and cross section of a soldered joint between two overlapped NbTi Rutherford cables for the LHC magnets. Picture taken from* **[73]**.

3.3 Ultrasonically welded splice development

The R&D was carried out using the Nb$_3$Sn cable MQXF 105, whose name is taken from the quadrupole coil prototype for HL-LHC. The wire is produced with the Rod Restack Process, i.e. a variation of the internal tin process. Its main characteristics are summarized in Table 3-1.

Table 3-1 *Characteristics of the cable MQXF 105* **[74]**.

Parameter	Value	Unit
Strand type	RRP 132/169	**-**
Cu to non-Cu ratio	1.2	-
Strand diameter	0.85	mm
Number of strands	40	-
Cable twist pitch	109	mm
Unreacted cable mid-thickness	1.525	mm
Unreacted cable width	18.15	mm
Width growth after reaction [75]	1	%
Thickness growth after reaction [75]	3	%
Cable keystone angle	0.55	°
Stainless steel core width	12	mm
Stainless steel core thickness	0.025	mm

The feasibility study of UW between of non-reacted Nb_3Sn consisted in overlapping two cables between the anvil and the sonotrode (Figure 3.8a-b). The overlap is arranged such that the keystone angle is compensated, i.e. the cross-section of the overlap is a rectangle and not a trapezoid. The trials were done in collaboration with the company Mecasonic [76]. Unlike NbTi, the two Nb_3Sn cables showed no bonding. The same happened when it was tried to weld two strands. In both cases, the copper stabilizer peeled apart from the wire core, as shown in Figure 3.8c-d. The cause is the weak metallic bonding between the copper stabilizer and the diffusion barrier of the wire. For this reason, new samples were prepared, in which the cables were coated with 0.5 mm copper via copper thermal spray. Such a Cu skin has the aim of reinforcing structurally the cable. The samples showed bonding neither in this case. Unlike the previous case, no peeling was observed. It rather seems that the samples are too thick for this application, implying that the vibration energy cannot concentrate on the mating surfaces.

It can be concluded that the realization of an ultrasonically welded splice between unreacted Nb_3Sn Rutherford cables made by the internal tin method revealed to be unfeasible.
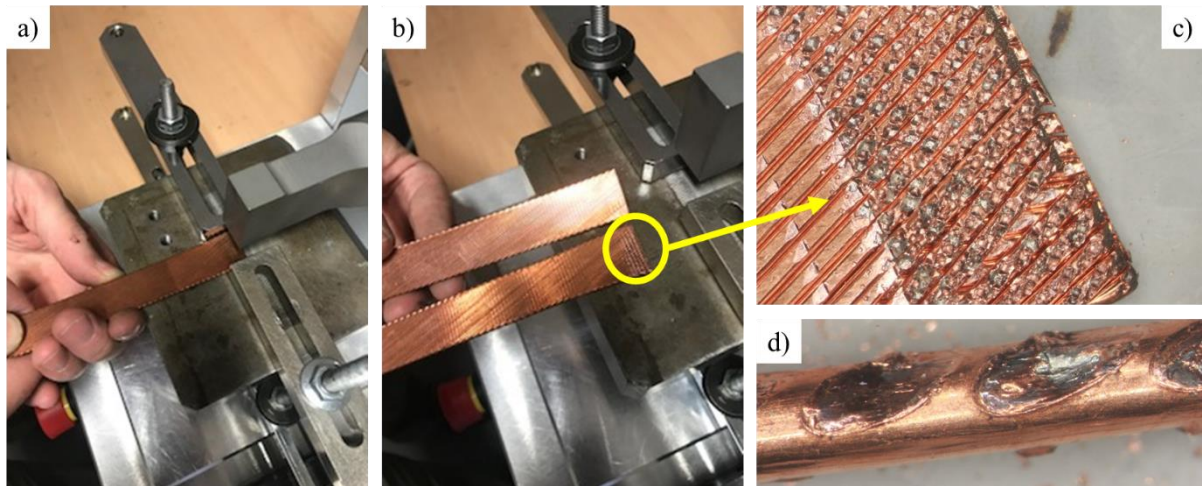
Figure 3.8 *Unreacted Nb_3Sn cables before (a) and after (b) an ultrasonic welding trial. Zoom of the cable (c) and strand (d) after a trial of cable-cable and strand-strand welding.*

3.4 Development of a bent diffusion-bonded splice

3.4.1 Preliminary studies on straight joints

The optimal value of the pressure to apply on copper surfaces, at a given temperature value and surface roughness, can be found in literature [71]. Nevertheless, for the application to a WR accelerator magnet, it is just possible to set the pressure at room temperature, as the coil is inaccessible during the heat treatment in the furnace. The pressure at the peak temperature of the heat treatment (640-650 °C), where copper DB mainly occurs, cannot be controlled but can rather be estimated. In particularly, this parameter depends on the thermal expansion coefficient of the cable and the clamping system, on the plastic deformation of materials and on the Nb_3Sn changing dimensions due to the heat treatment reaction. For this reason, the first part of the R&D on diffusion-bonded splices was dedicated to the experimental investigation of an optimal pressure value to set at room temperature, such that the electrical resistance is within the target value. Another goal of this experimental study was to verify if the increase of the contact area between the two cables could decrease the electrical resistance of the sample.

Such a contact area increase was obtained both by interleaving a 50 µm thick copper foil between the cables and by plating the cable surfaces with copper (Figure 3.9).
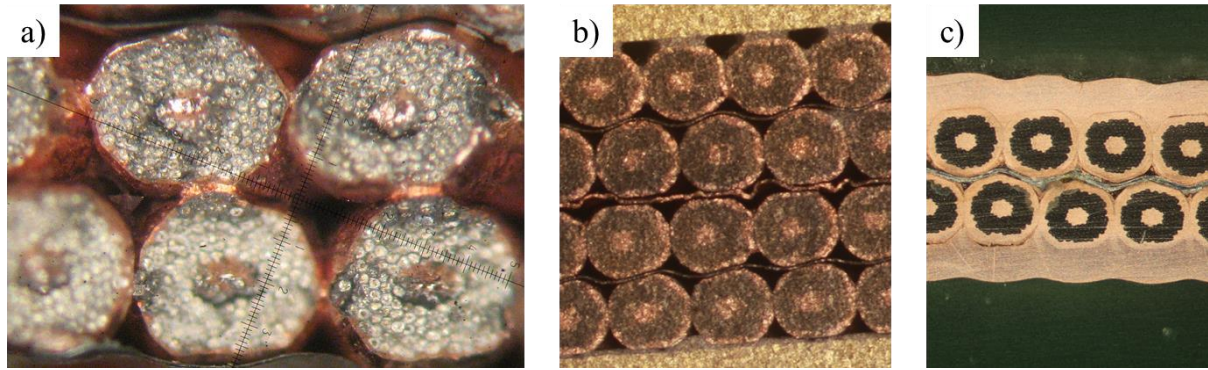
Figure 3.9 *Diffusion-bonded spots between two Nb₃Sn Rutherford cables (a); overlapped cables with a Cu foil in-between (b); Cu-plated cable (c).*

The clamping system consists in stainless steel plates and screws, as shown in Figure 3.10. Since steel has a higher thermal expansion coefficient α than the cable, conical spring washers made up of carbon steel are employed to dampen the loss of pressure from 20 °C to 640 °C. In particular, spring washers can be stacked in parallel to increase their stiffness or in series to increase their range of deflection (Figure 3.11). A high stiffness is useful to balance high forces, while a high range of motion counteracts relatively large displacements.

To estimate the relation between the pressure applied on the mating surfaces at T_1=20 °C and the one at T_2=640 °C, a set of equations (3. 2) based on the thermo-mechanics of the system is used as design instrument. These relate the displacement Δl of the materials, function of pressure p and temperature T, with the force F applied by screws and conical spring washers. In (3. 2), the thermo-mechanical problem is assumed 1D (perpendicular to the joint surface), the cable is modelled as a full homogenized object, the plasticization of materials is neglected because unknown and the volumetric growth of the strand due to the heat treatment reaction is not taken into account. While the neglect of the 3% growth of the cable thickness is conservative, the plasticization of the material causes a pressure relaxation. In particular, the copper stabilizer is the first to reach the yield strength, about 15 MPa at 640 °C [77]. The yield strength of the bronze of the matrix with 8 wt. % of tin is instead about 39 MPa. Therefore, in the worst case, 15 MPa is the saturated diffusion-bonding pressure value on the contact surface between strands. Nevertheless, the extension of this contact surface at 640 °C depends on the initial pressure at 20 °C. The broader the contact surface, the lower the electrical resistance.

$$
\begin{cases}
\Delta l_i = l_{i,T1} \cdot \left(\dfrac{p_{i,T2}}{E(T_2)_i} + \displaystyle\int_{T_1}^{T_j} \alpha_i(T) \cdot dT \right), \quad i = SC, SS, screw \\[2ex]
l_{spr,Tj} = \left(l_{screw,T1} + \Delta l_{screw} \right) - \left(l_{SS,T1} + \Delta l_{SS} \right) - \left(l_{SC,T1} + \Delta l_{SC} \right) \\[2ex]
l_{spr,Tj} = l_0 \left(1 + \displaystyle\int_{T_1}^{T_j} \alpha_{spr}(T) \cdot dT \right) - N_{ser} \cdot s \\[2ex]
F_{i,Tj} = \dfrac{p_{i,Tj}}{A_{SC}}, \quad i = SC, SS, screw \\[2ex]
F_{spr,Tj} = f\left(N_{spr}, D_{spr}, t_{spr}, l_{spr,Tj} \right) \\[1ex]
F_{SC,Tj} = F_{SS,Tj} = N_{screw} \cdot F_{spr,Tj} = N_{screw} \cdot F_{screw,Tj}
\end{cases}
\qquad \textbf{(3. 2)}
$$

In (3. 2), E [GPa] is the Young's modulus, SC stands for the cable, SS for the stainless steel plate, spr for spring washer, A [m^2] for the surface or cross-section of the material, N_{spr} for the number of spring washers, D_{spr} [m] for the diameter of the spring washer, t_{spr} [m] for its thickness, s [m] for the spring washer deflection, l_0 [m] for the height of one unloaded washer, Nser for the number of washers in series, and N_{screw} for the number of screws. The model parameters are shown in Figure 3.12.

The relation between the force exerted by a spring and its deformation s is non-linear. It is reported in equation (3. 3) and taken from reference [78], but can be found in several manuals.

$$F_{spr} = N_{par} \frac{4 E_{spr}}{1 - \mu^2} \frac{t_{spr}^4}{K_1 \cdot D_{spr}^2} \frac{s}{t_{spr}} \left[\left(\frac{l_0}{t_{spr}} - \frac{s}{t_{spr}} \right) \left(\frac{l_0}{t_{spr}} - \frac{s}{2 t_{spr}} \right) + 1 \right] \qquad \textbf{(3. 3)}$$

where μ is the Poisson coefficient, K_1 a coefficient, N_{par} the number of parallel spring washers.

By applying relations (3. 2) and (3. 3) at temperature T_1 and T_2, it is possible to find the ratio between the pressure on the mating surfaces at the two temperature values. This ratio depends, in particular, on the clamp materials and geometry, and on the spring washer number and configuration.
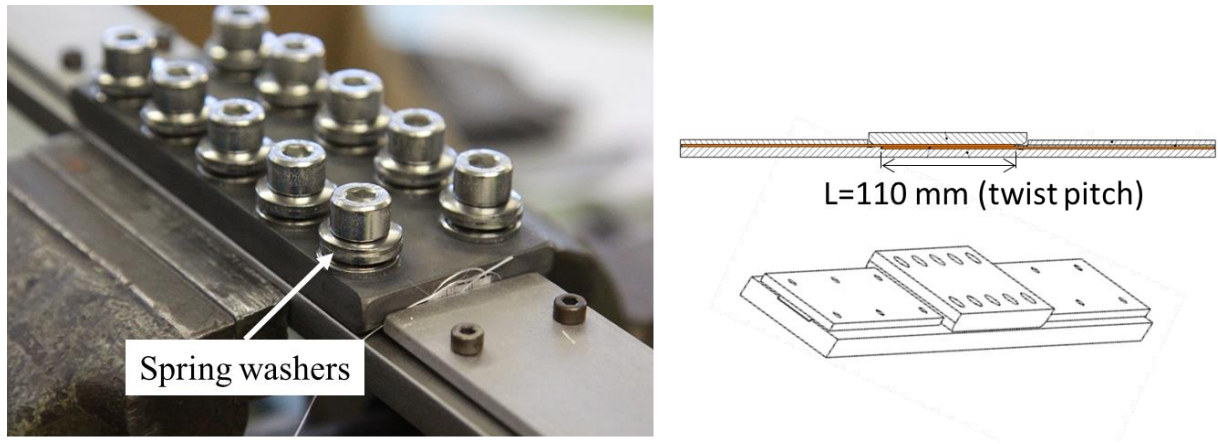
Figure 3.10 *Steel fixture for the diffusion-bonded straight splices.*
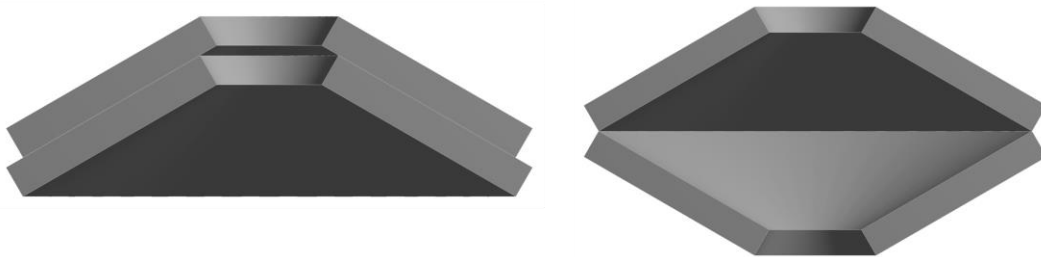
Figure 3.11 *Conical spring washers in parallel (left) and series (right).*
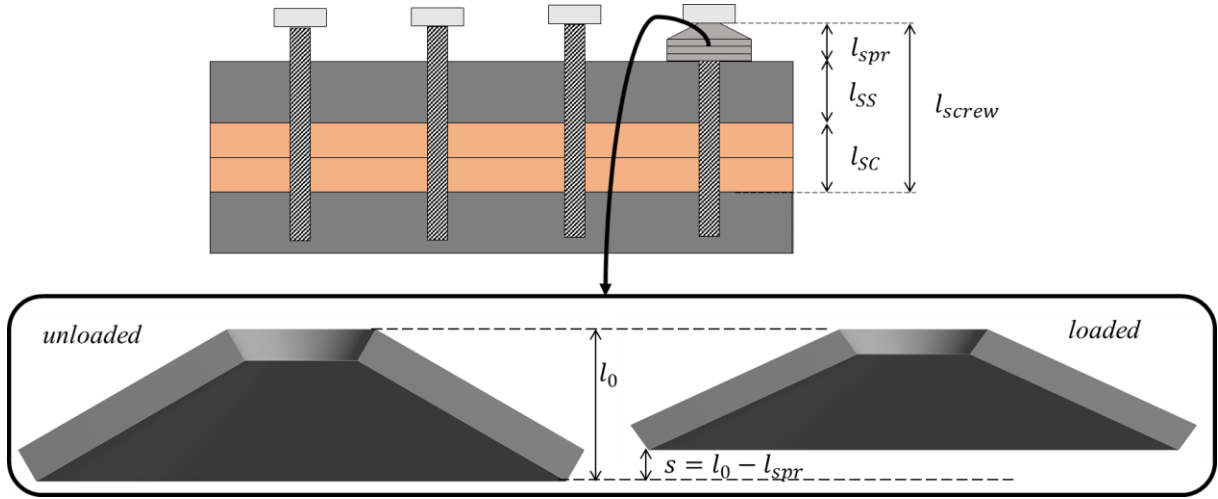
Figure 3.12 *Parameters involved in the simplified mechanical model in* (**3. 2**).

The system of equations in (3. 2) is then used to design the samples dedicated to the sensitivity study of the joint electrical resistance with respect to the pressure applied at room temperature. The cable used for R&D is the MQXF 105 (see Table 3-1), removing the steel core to promote diffusion-bonding also between the strands of the same cable. The heat treatment is divided into three steps: 48h at 210 °C, 48h at 400 °C, 50h at 640 °C [74]. Six samples were prepared for the experimental campaign in SULTAN. They are listed in Table 3-2, indicating the measured average pressure set at room temperature and the estimated one at 640 °C. Mainly three values of pressure are investigated: 4 MPa, 14 MPa and 35 MPa. Each of these values corresponds to the average pressure on the rectangle formed by the overlapped cables. As the contact area consists of contact spots between strands, the peak pressure can be four times higher than the average one. The contact surface of sample P56Pl, whose cables are electroplated, is instead the entire rectangle. For this sample, the average pressure is a good approximation of the contact pressure. For this reason, the pressure set on P56Pl was 56 MPa, in order to compare it with the 14 MPa samples, namely P14, P14Cu_a and P14Cu_b.

Table 3-2 *List of samples for the preliminary study on straight joints.*

	Name	$\bar{p}$ @ T=20 °C (MPa)	**Estimated** $\bar{p}$ @ T=640 °C (MPa)	**Parallel washers**	**Series washers**	**Total washers**	**Cu foil**	**Plating**
1	P04Cu	4	2.5	1	3	3	Yes	No
2	P14Cu_a	14	10	1	3	3	Yes	No
3	P14Cu_b	14	10	1	3	3	Yes	No
4	P56Pl	56	40	3	3	9	No	Yes
5	P14	14	10	1	3	3	No	No
6	P35	35	25	3	3	9	No	No

In the clamp, glass-fiber is put between the cable and the steel parts to avoid unwished bonding. The samples are heat treated in the furnace providing an inert atmosphere with argon (Figure 3.13). To mimic the same heat treatment conditions as in a magnet, additional glass-fiber and mica foils are added. Despite the inert atmosphere, a black soot is produced from the insulating materials during the heat treatment. This soot deposited on the cables (Figure 3.14). Such soot does not influence the splice quality, as the joint surface is pressed.

After the thermal cycle in the furnace, the samples are prepared for the electrical test in SULTAN. The samples are arranged in a single stack. The main advantage is that all the samples can be tested at once, while the disadvantage is that the worst sample might limit the maximum reachable current in the test.

All joints are electrically connected in series. The extremities of the samples are soldered to copper terminations. The copper terminations of two samples connected in series are spliced through indium joints, i.e. indium wires squeezed against the terminations (Figure 3.15). Two voltage taps per sample are soldered 100 mm away from the splices. With them, it is possible to assess the resistance of the sample joints and of each termination. For the mechanical stability of the stack, the samples are held by two steel plates and impregnated with stycast at ambient atmosphere (Figure 3.15c). A scheme of how the current circulates through the samples is reported in Figure 3.16.

The stack must be located at the peak field of the bore of the SULTAN facility, must be supplied with high current (~10 kA as order of magnitude) and its temperature has to be controlled. These requirements are fulfilled through a set of subsystems (Figure 3.17):

- The stack is connected through indium joints to two Nb_3Sn lead extensions soldered in a copper slot. The lead extensions hold the sample splices in the background peak field and provides electrical connection to the stack.
- Stack and lead extensions are inserted into a chamber, through which helium at 10 bar and tunable temperature (minimum T=4.5 K) flows. Outside this chamber, vacuum is kept. In this thesis, we refer to this chamber with the name *cryostat*. What is inside the cryostat is considered as sample holder.
- The lead extensions are electrically connected to a superconducting transformer, able to supply the stack with maximum 100 kA, through an HTS adapter. The adapter has the role of minimizing the heat conduction from the lead extensions in the cryostat, where an independent temperature regulation is wished, to the transformer, whose temperature must be 4.5 K constantly. Moreover, part of the adapter is in the cryostat at 10 bar, while its length connected to the transformer protrudes from the cryostat and is in vacuum.
- The superconducting transformer is connected to the room temperature power supply through current leads.
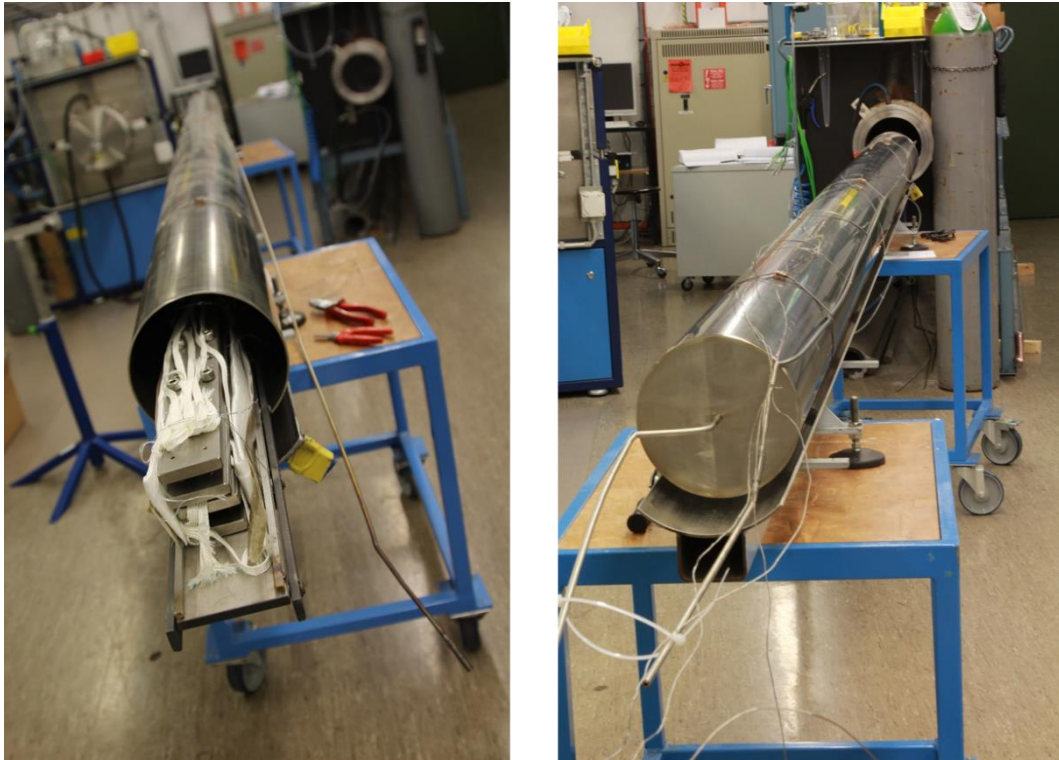
Figure 3.13 *Preparation of the straight joint samples for heat treatment and insertion in the oven.*
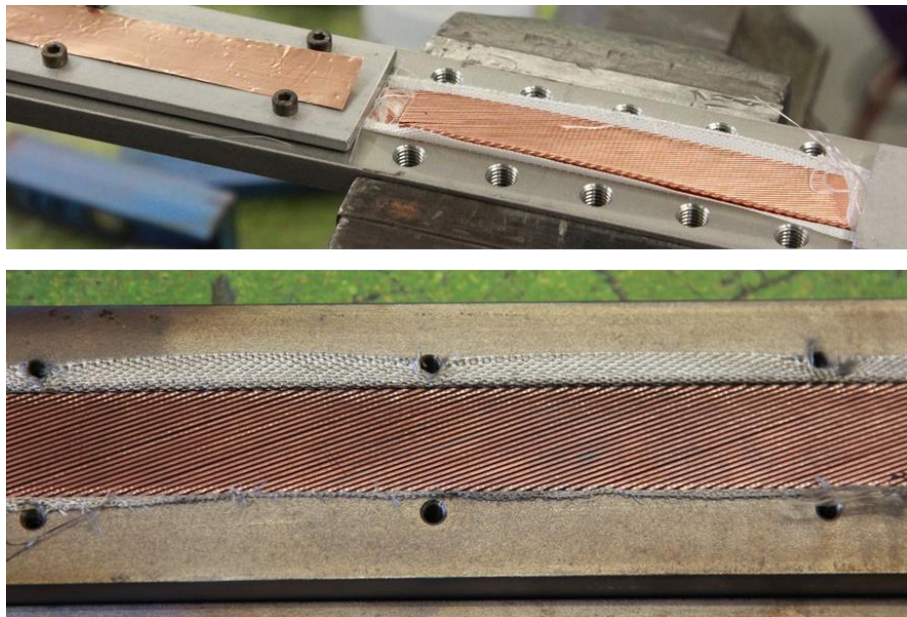
Figure 3.14 *Status of the surface of the cable before (top) and after (bottom) heat treatment.*
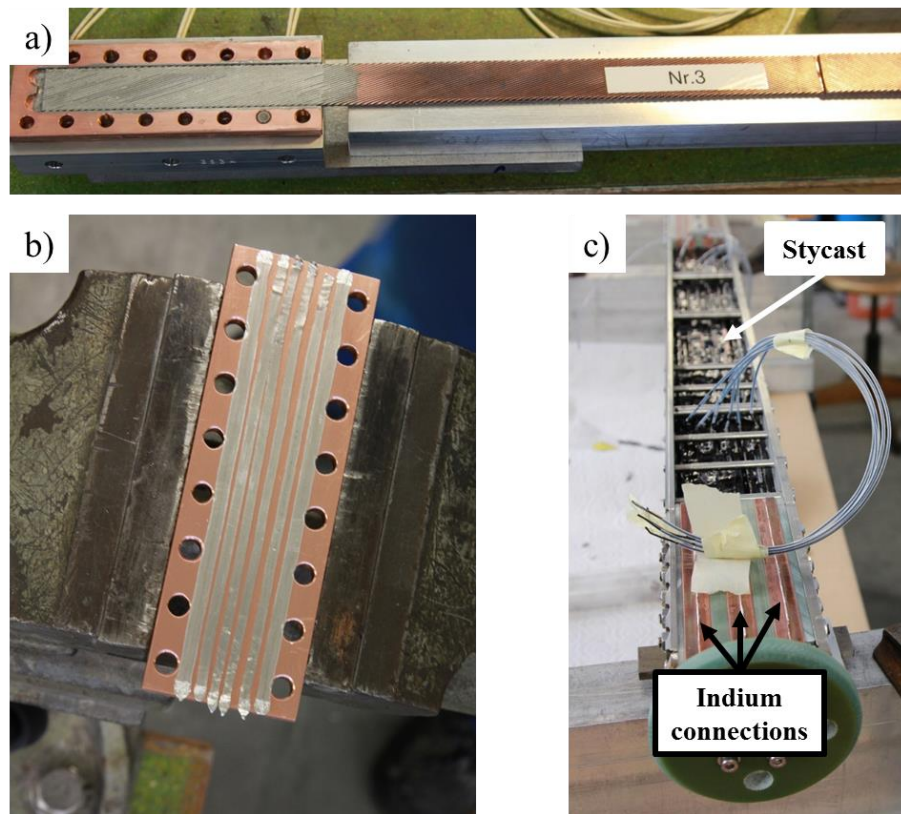
Figure 3.15 *Soldering of the sample termination (a); squeezing of indium wires (b) to connect the samples electrically in series (c).*
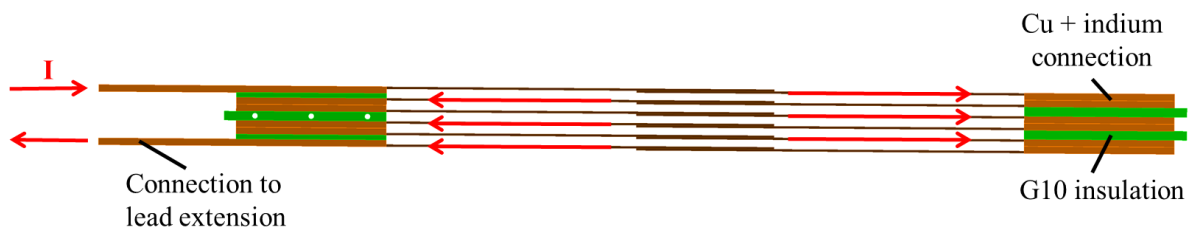
Figure 3.16 *Current circulation scheme in the stack.*
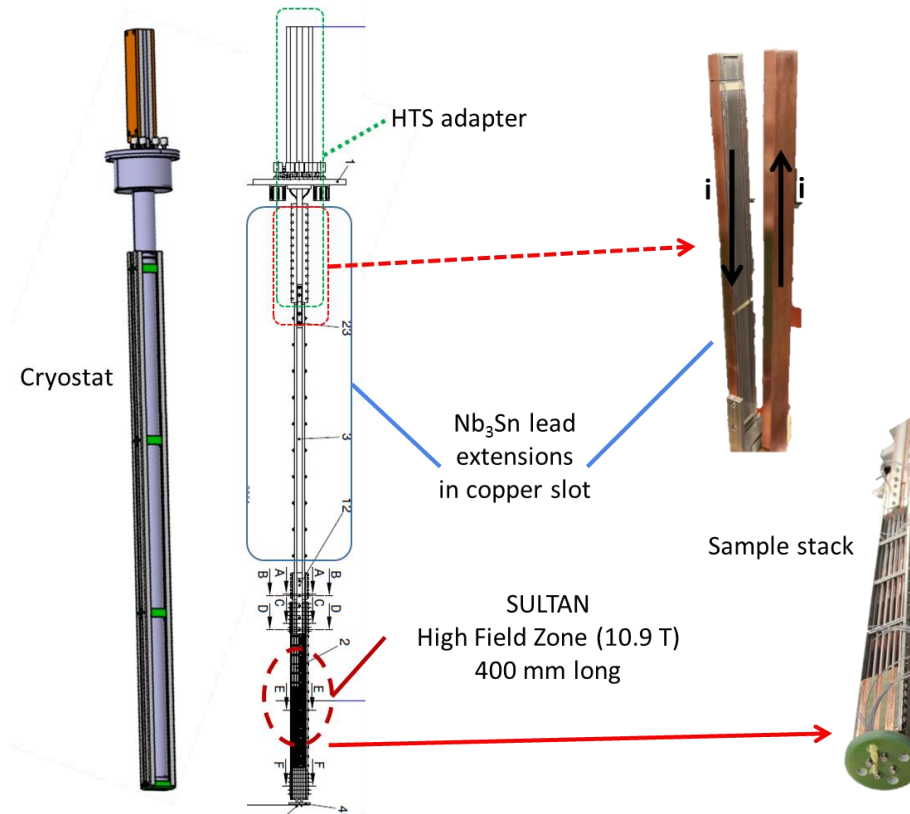
Figure 3.17 *Component of the test sample holder for diffusion-bonded straight splices.*

The sample holder is instrumented with voltage taps and Cernox temperature sensors, as reported in Figure 3.18. The goals of the tests are:

- To determine the resistance of each sample as a function of current and background field.
- To explore the maximum reachable current at B=10.9 T, i.e. the maximum background field provided by the SULTAN facility.

For each background field in the range B=0-10.9 T, the current is ramped-up to different values at which the current is kept constant for three minutes. The resistance is assessed through the ratio of the measured voltage drop and current. The results are reported in Figure 3.19-Figure 3.22.

The graphs can be commented as follows:

- **Maximum test current**. The maximum reachable current at B=10.9 T was I=5 kA, corresponding to 0.18% I_c at T=5 K. Above this value, a voltage runaway occurs during the current ramp-up. This limitation comes from the worst sample, namely P04Cu, whose resistance kept degrading during the experiment, exceeding 50 nΩ. Moreover, the impregnation with stycast, which is considerably viscous, showed voids and bubbles after tests. These left the samples uncovered in some regions. Several strands were found deformed.
- **Joint resistance vs current**. In non-degraded samples, at constant field, the resistance does not change with the applied current, suggesting no strand saturation and thus no change in the current path up to 5 kA, at 10.9 T and 5 K.

- **Joint resistance vs applied pressure** (Figure 3.19). Diffusion bonded joint with low pressure, 4 MPa, shows weak bonding, leading to an already high resistance at zero field and degradation with increased field. Joints with 14 MPa and 35 MPa show resistance values below 1 nΩ. However, one sample at 14 MPa (with Cu foil) showed higher resistance from the beginning of the experiment and degraded during the other ones (Figure 3.21). The minimum applied pressure which guarantees a resistance lower than 1 nΩ and shows reliability is then above 14 MPa.
- **Joint resistance vs enhanced contact area** (Figure 3.20). The 50 μm thick Cu foil subject to a 14 MPa applied pressure did not show any improvement compared to the sample without foil. The sample with copper deposition in the joint area did not give the expected improvements, thus not justifying the complication of the procedure.
- **Joint resistance vs magnetic field** (Figure 3.22). In general, the resistance of the samples increases with the magnetic field. The slope of the R vs B line, for the non-degraded samples, is comparable to the one of the copper magneto-resistivity. This is proved by comparing the *joint resistance ratio* $\frac{R(B)-R(2\,T)}{R(2\,T)}$ with the copper *resistivity ratio* $\frac{\rho(B)-\rho(2\,T)}{\rho(2\,T)}$, where the copper resistivity values are taken for a Residual Resistivity Ratio (RRR) equal to 170 and 250 [74], defined as $RRR = \rho(293\,K)/\rho(4.2\,K)$. The *joint resistance* and *resistivity ratio* coincide if the resistance is dominated by the copper bulk resistivity. Figure 3.22 shows that the samples results fall within the range given by the *resistivity ratio* lines given by RRR=170 and RRR=250.
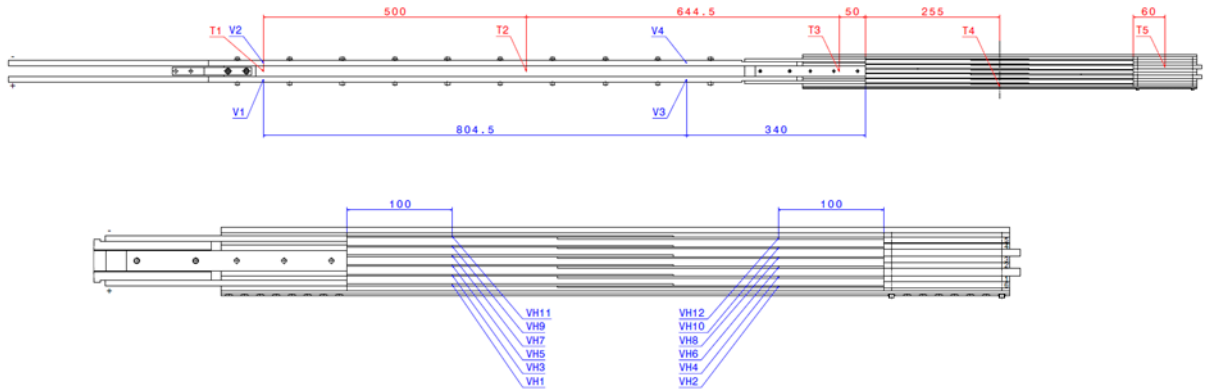
Figure 3.18 *Instrumentation scheme for the electrical test of the diffusion-bonded straight splices. Temperature sensors are in red, while voltage taps in blue.*
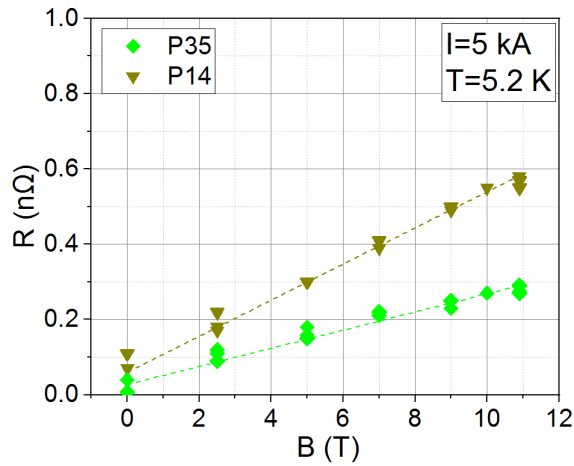
Figure 3.19 *Dependence of the resistance on pressure. P04 is not shown since* $R > 50\,n\Omega$.
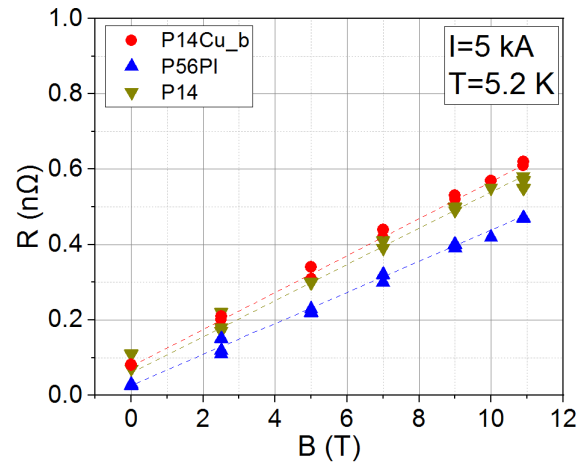
Figure 3.20 *Joint resistance with and without enhanced contact area.*
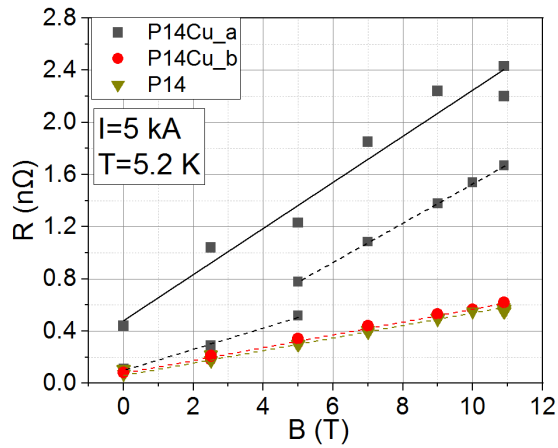
Figure 3.21 *Sample reproducibility for the 14 MPa pressure.*
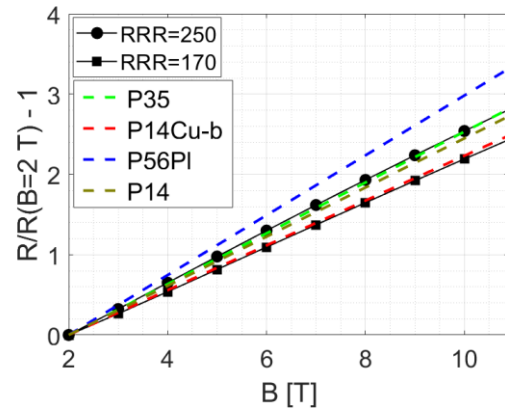
Figure 3.22 *Normalized results (dashed lines) compared to the normalized copper resistivity (solid lines).*

From the preliminary study on diffusion-bonded straight splices, the following conclusions can be drawn:

- The diffusion-bonding technique potentially satisfies the requirement of $R \leq 1\,n\Omega$, but a demonstration in a more relevant geometry at higher current is needed.
- Although the pressure at 640 °C on the contact surface between strands might be limited to 15 MPa, the pressure set at room temperature has still a key influence on the joint resistance.
- An average pressure at room temperature in the order of 30 MPa is needed for this type of cable and clamp design.
- Bare cables without steel core, removed to join also strands of the same cable, are sufficient to achieve an acceptable resistance value.

35

3.4.2 Bent joint design

The results presented in Section 3.4.1 on straight diffusion-bonded joints for WR accelerator magnets motivated the study of a splice design more relevant to accelerator magnets, namely in bent geometry. In this layout, the main challenges in the clamp design are to reach a uniform pressure distribution on the mating surfaces during diffusion-bonding and the integration of the clamp into the magnet, as the joint formation takes place during the magnet heat treatment. For these reasons, with respect to the preliminary study on straight splices, bulky components such as stacks of spring washers are eliminated. Moreover, the choice of the clamp materials is revised, in order to avoid the pressure relaxation from ambient to heat treatment temperature.

The cable used for R&D is the SMC-11T cable. It is thinner than the MQXF 105, thus allowing lower bending radii, which is favourable to the space limitations in the SULTAN sample bore. The characteristics of the cable are reported in Table 3-3. The steel core is removed. The heat treatment parameters are: 48h at 210 °C, 48h at 395 °C, 50h at 650 °C.

Table 3-3 *Characteristics of the cable SMC-11T.*

Parameter	Value	Unit
Strand type	PIT 192	**-**
Cu to non-Cu ratio	1.2	-
Strand diameter	0.7	mm
Number of strands	40	-
Cable twist pitch	100	mm
Unreacted cable mid-thickness	1.26	mm
Unreacted cable width	14.7	mm
Width growth after reaction [75]	1	%
Thickness growth after reaction [75]	3	%
Cable keystone angle	0	°
Stainless steel core width	12	mm
Stainless steel core thickness	0.025	mm

Two clamp options were designed, manufactured and their joint was electrically tested as two standalone samples in SULTAN.

The clamp design criteria are resumed as follows:

- Joint length next to one cable twist pitch, to guarantee contact between all the strands of one cable with the ones of the other cable, thus reducing current unbalance among strands.
- Joint pressure distribution as uniform as possible, to promote uniform contact distribution.

- Materials choice such that the pressure raises with increasing temperature due to the combination of different thermal expansion coefficients. Inconel 617 and stainless steel AISI 316 were combined for this purpose.
- Clamp volume minimization.
- Assembly in situ and partial disassembly after heat treatment of the parts protruding out of the joint plane, because not compatible with the space at disposal of a dipole for HE-LHC/FCC during operation.

Furthermore, the design of the clamp for the experiment is influenced by the space limitations inside the cryostat. The inner radius of the cryostat is 41.8 mm. Considering the space required for tooling (bolts, plates, supports), the joint radius can be maximum 31.9 mm. Moreover, to be relevant for an accelerator magnet, the joint overlap angle is limited to about 140 °, to avoid interfering with more external turns of the magnet (Figure 3.23). This sets the overlap length to 75 mm, thus 75 % of the twist pitch of the SMC-11T cable used in this test campaign. This overlap length limitation is not present in a magnet for HE-LHC/FCC.
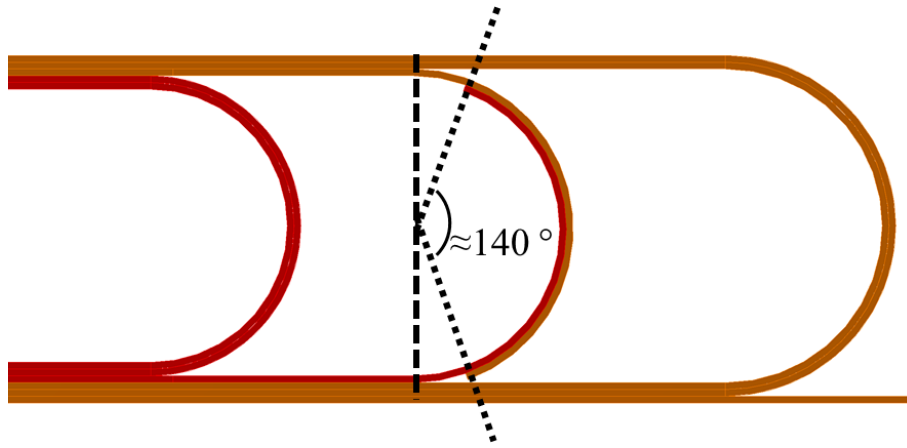
Figure 3.23 *Limitation in the overlap angle of a bent internal splice.*

The clamps design is performed through Finite Element Analysis. The main limiting assumptions are:

- The cable is modelled as a continuous body (but a low Young's modulus is kept to take into account the influence of the void fraction) with uniform thermo-mechanical properties, weighted with respect to the volume of Nb_3Sn, copper, bronze and void fraction after reaction [79].
- Plasticity of the cable at high temperature is not known and thus neglected.
- The change of cable dimensions during the reaction heat treatment are neglected.

The physical properties implemented in ANSYS are reported inTable 3-4. The two designed clamps are shown in Figure 3.24 as they appear during heat treatment, i.e. when diffusion bonding occurs. The same figure shows also the parts of the clamps that will remain after the heat treatment, i.e. during the lifetime of the magnet. The exploded view of the clamps shown in Figure 3.25-Figure 3.26 highlights the details of the components and defines their nomenclature.

Table 3-4 *Thermomechanical properties for the clamp design.*

	$\bar{\alpha}$ [K^{-1}] between 20-650 °C	E [GPa] @ 20 °C	E [GPa] @ 650 °C
SMC-11T cable	$14.7 \cdot 10^{-6}$	40	40
Steel AISI 316	$18.4 \cdot 10^{-6}$	195	150
Inconel 617	$14.4 \cdot 10^{-6}$	211	170

In these clamps, four M8 screws, gradually tightened with a torque wrench, apply the pressure. The screws are located in the convex side of the splice for "clamp#1", while on the concave side for "clamp#2". This sets a difference in terms of place requirements for the application of these two clamps in a magnet. In particular, "clamp#1" requires additional place to be able to access the screws during tightening. They will have to be substituted by spacers after heat treatment. The screws of "clamp#2" are "invisible" because inserted into the threaded plate. This is meant to be able to continue winding the turns of a magnet around the clamp. Therefore, these screws are meant to remain in the magnet during its lifetime and fillers need to be employed in the voids of the clamp during the magnet winding. As the screws of "clamp#2" cannot be released after heat treatment for the disassembly of the protruding parts, this clamping system needs more modularity and then increased complexity than "clamp#1". Indeed, its connecting plates are split in more pieces.
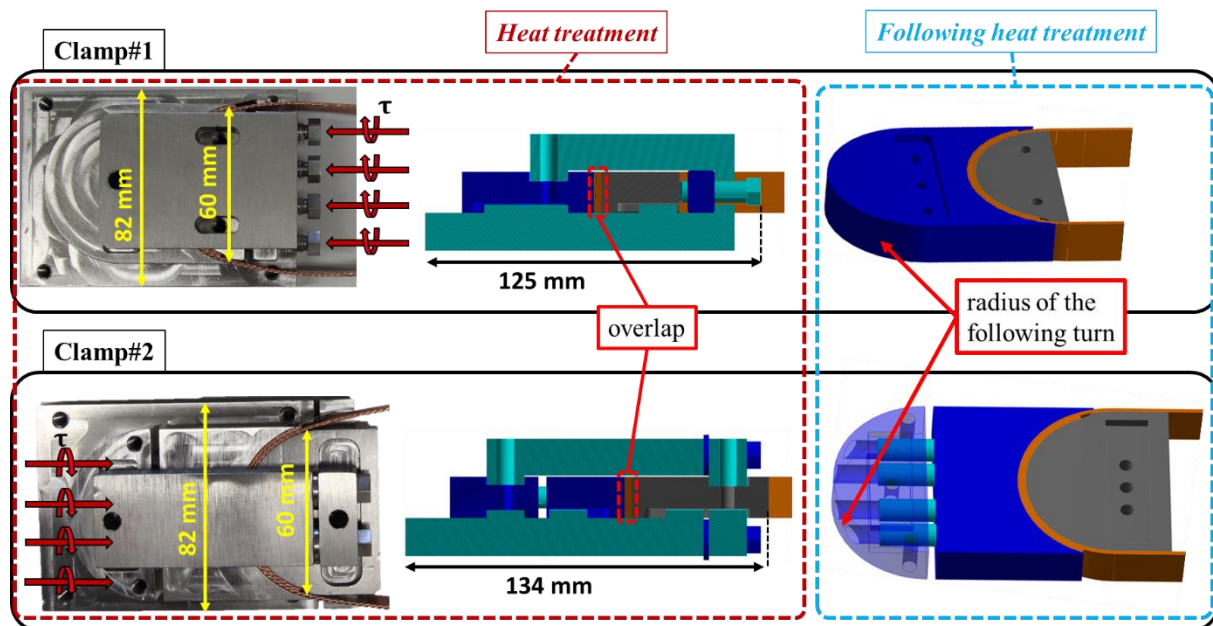
Figure 3.24 *Clamps for diffusion-bonded bent splices, highlighting the parts present during the heat treatment (left and centre) and the one remaining during the magnet operation (right). In blue and light blue the Inconel parts, while in grey the steel ones. Image readapted from* **[80]**.
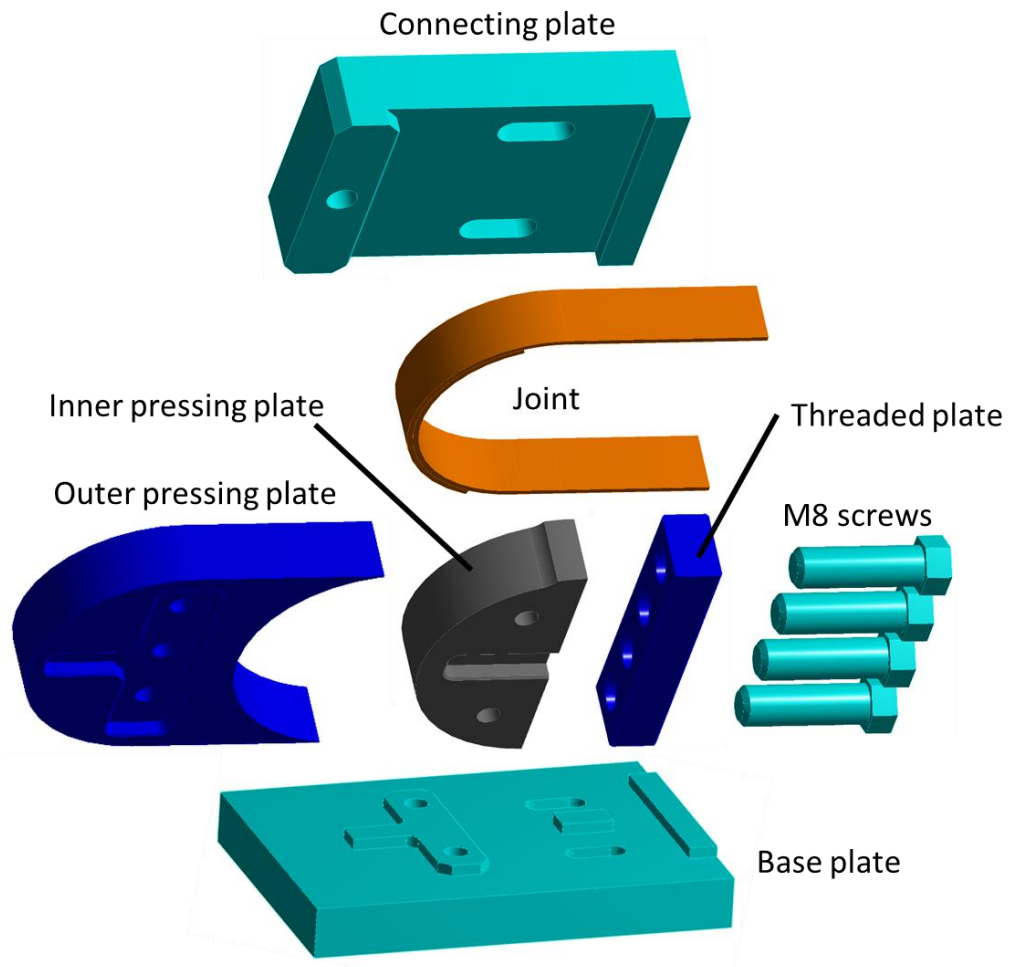
Figure 3.25 *Exploded view of the diffusion-bonding clamp#1. In blue and light blue the Inconel parts, while in grey the steel ones.*
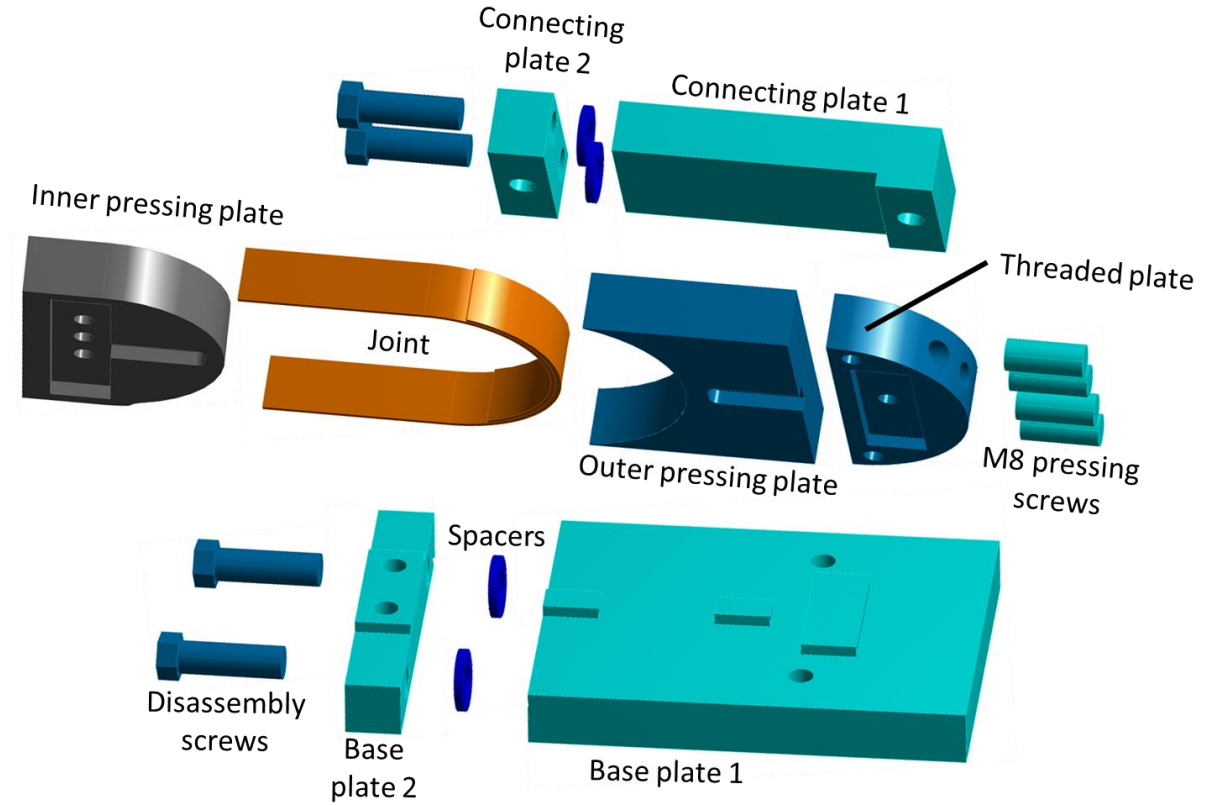
Figure 3.26 *Exploded view of the diffusion-bonding clamp#2. In blue and light blue the Inconel parts, while in grey the steel ones.*

The average pressure applied at room temperature on the joints is 26 MPa, thus in between the values of the straight samples in Figure 3.19. Such a pressure is computed applying formula $P = \frac{N \cdot \tau}{c \cdot D \cdot A}$, being N the number of bolts, τ [Nm] the torque equal to 12 Nm, c the friction factor coefficient assumed equal to 0.2, D [m] bolt diameter and A [m^2] the joint area. Figure 3.27 shows how the pressure distributes on the joint surface at 20 °C and its evolution to 650 °C. In comparison to the straight joint, the bent joint length is less than one twist pitch and the pressure is not uniform initially (see Figure 3.28), since the force is not applied radially. Even if the different radial thermal expansion of the materials improves its homogenization at 650 °C, the pressure goes gradually to zero at the joint edges because the radial thickness of the outer pressing plate goes to zero at the edges. Such a thickness cannot be increased because incompatible with the geometry of a dipole for HE-LHC/FCC. Moreover, the computed pressure at 650 °C is higher in clamp#1 (51 MPa) than in clamp#2 (36 MPa). A better electrical performance of the former can thus be expected.
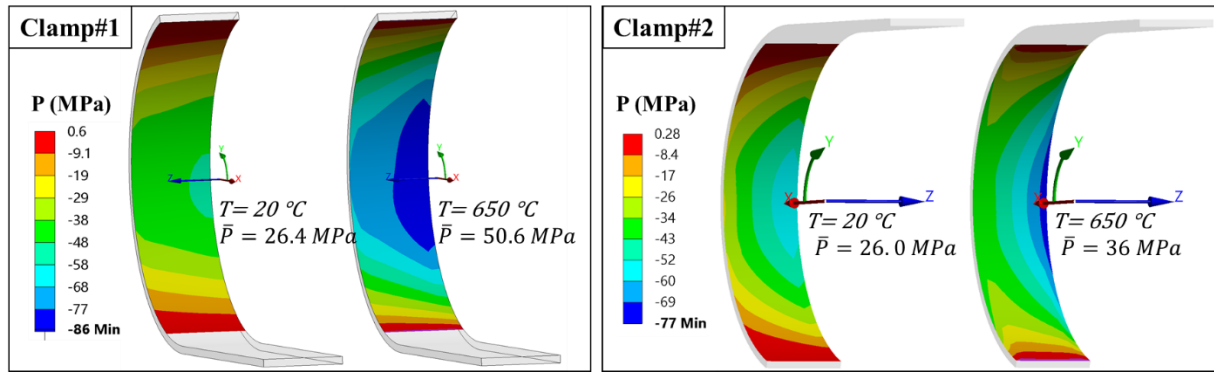
Figure 3.27 *Computation of the pressure distribution on the joint surface at room and DB temperature.*
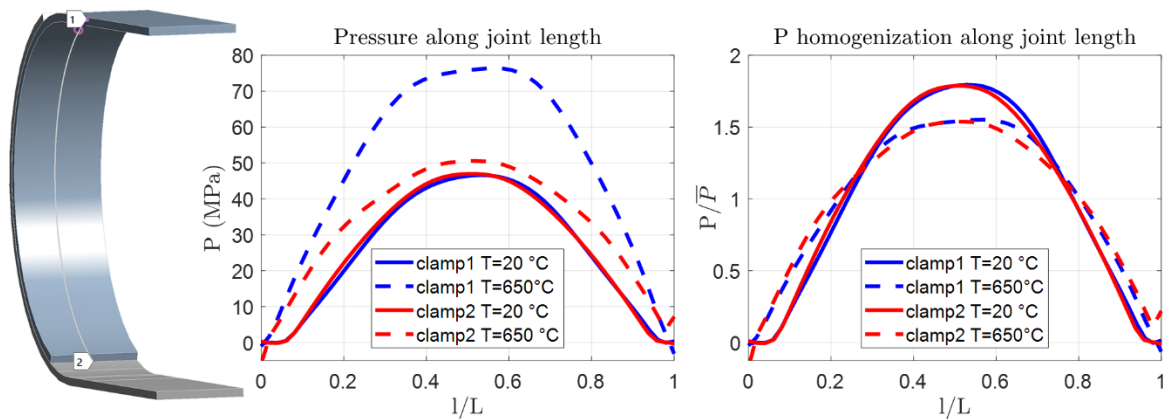
Figure 3.28 *Computation of the pressure profile and level of pressure homogenization ($P/\bar{P}$) along the joint central line l of length L.*

In conclusion to this section, two different DB bent joint concepts were designed taking into account the assembly and disassembly limitations that would be present in a magnet application. The two clamps have differences in terms of space requirements, level of complexity and assembly/disassembly procedure. With respect to the straight joints presented in 3.4.1, the joint length is limited by the space in the test facility and the pressure distribution is not uniform. From the electrical point of view, this leads to an inhomogeneous contact distribution. The worst contacts can limit the joint performance in terms of resistance and maximum current.

3.4.3 Bent joint prototype assembly

Each of the two samples is assembled for the heat treatment in argon atmosphere. The sample holder consists of a series of stainless steel parts. Glass-fibre is put between cable and sample holder, except in the joint. The base plates of the clamp would be part of the winding table of a magnet, while the pressing plates part of the winding pole. The pressing plates are temporarily linked to them with screws (Figure 3.29), which will be released when pressure starts to be applied on the joint. The overlap is arranged by hand, but a more effective way would be to crimp with a thin strip the cables to overlap and then bend them together. A picture of the sample ready for heat treatment is shown in Figure 3.30. The same heat treatment equipment as in Section 3.4.1 is used.

Figure 3.29 *Assembly of clamp#1 (left) and clamp#2 (right) for heat treatment.*
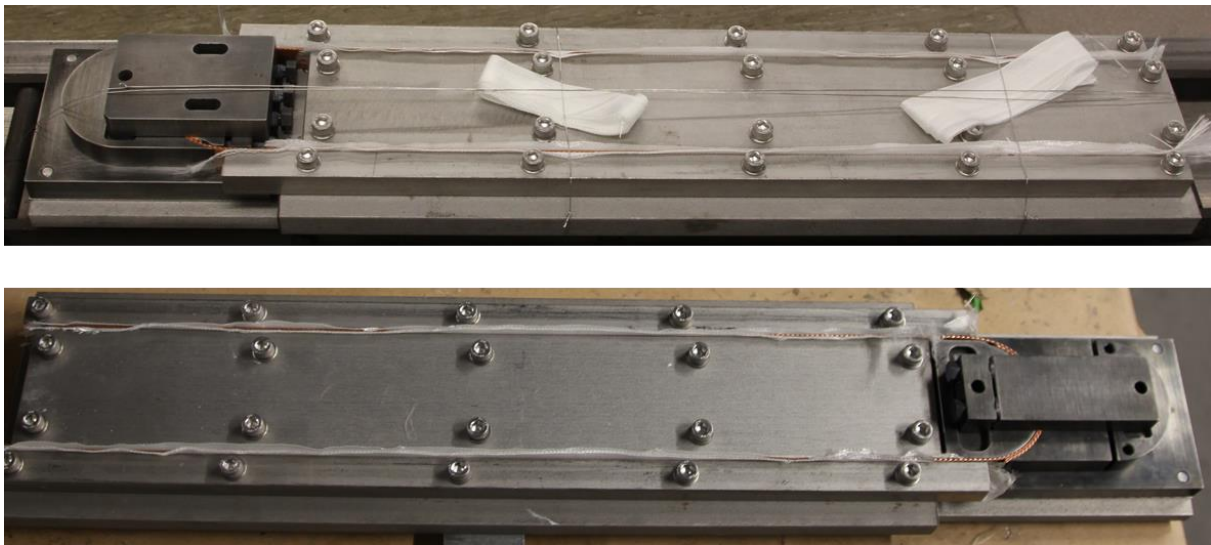
Figure 3.30 *Sample#1 (top) and sample#2 (bottom) ready for the heat treatment.*

After the thermal cycle, the partial disassembly of the clamp follows, removing the parts protruding out of the joint plane. In a real magnet, the protruding base and connecting plates would be substituted by the magnet mechanical structure. For the SULTAN test, "test connecting plates" mimic this mechanical structure. The guiding principle of this disassembly is the avoidance of the manipulation of those pressing plates in contact with the cable. The avoidance of their manipulation is realized by a disassembly in steps (Figure 3.31):

- The base plates are connected again to the pressing plates through screws.
- The connecting plates are removed from one side and substituted with the "mechanical structure".
- The same procedure is applied from the other side for substituting the base plates.
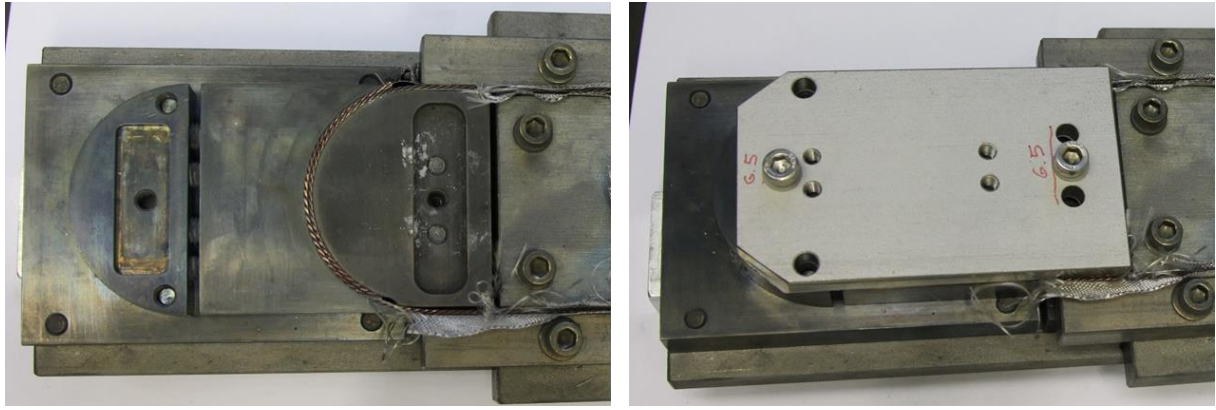
Figure 3.31 *Disassembly in steps of the clamps parts (only clamp#2 is shown in this picture) incompatible with the geometry of a magnet during operation without manipulation of the parts in contact with the cable (left), and their replacement with "mechanical structure" belonging to the test sample holder (right).*

For the sample holder for the electrical test, the same Nb_3Sn lead extensions, HTS adapter and cryostat as in Section 3.4.1 are used. First, the two cable sections belonging to the sample are soldered in a copper slot. However, the first 100 mm next to the joint are covered with Kapton tape and not soldered (Figure 3.32). This limits the influence of the solder on the measurement of the resistance of the diffusion-bonded splice. The sample is connected with the Nb_3Sn lead extensions through indium joints and the sample holder is inserted into the cryostat (Figure 3.33).

The reported assembly for the test in SULTAN did not foresee insulation between the joint and the clamp components. Therefore, the inner and outer pressing plates have the same potential as the splice of clamp#1, whilst the threaded, inner and outer pressing plates have the same potential as the splice of clamp#2. The lack of insulation does not influence the purpose of the experiment, i.e. the assessment of the splice resistance, as the clamp parts do not represent a short circuit for the test assembly and are much more resistive than the splice. On the other hand, insulation between clamp and joint might be necessary for the application to a coil, for instance by employing ceramic coatings on the surface of the clamp before heat treatment.
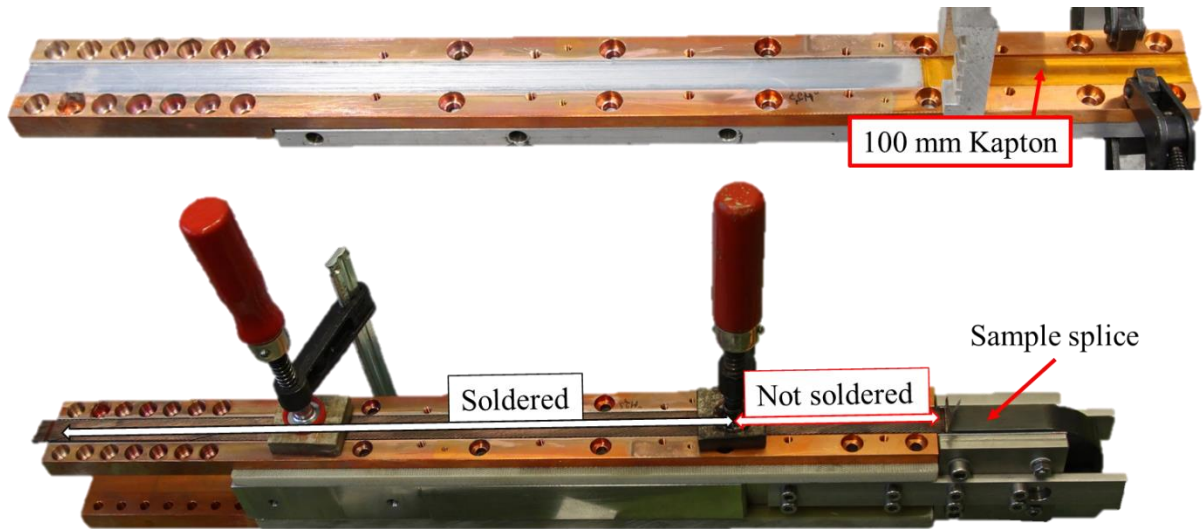
Figure 3.32 *Copper slot before soldering to the sample (top) and sample before the connection with the Nb₃Sn lead extensions (bottom).*

Figure 3.33 *Test sample holder before insertion into the cryostat.*

3.4.4 Bent joint DC electrical test in SULTAN

A scheme of the sample instrumentation is reported in Figure 3.34 for sample#1. The same scheme applies for sample#2. The temperature sensor T5 is installed on the Inconel outer plate, while T3 and T4 on the copper of the sample holder termination. The resistance is assessed not only by measuring the voltage drop between arrays VH1 and VH2, but also between VH3 and VH4 for comparison. Each array consists of two voltage taps. For instance, the array VH1 is made of the voltage taps VH1-1 and VH1-3, applied on two different point of the same cable cross-sections. The two signals are then averaged. The resistance of the connection to the leads is checked through voltage drops (VH4-4)-(V4) and (VH3-3)-(V3).

44
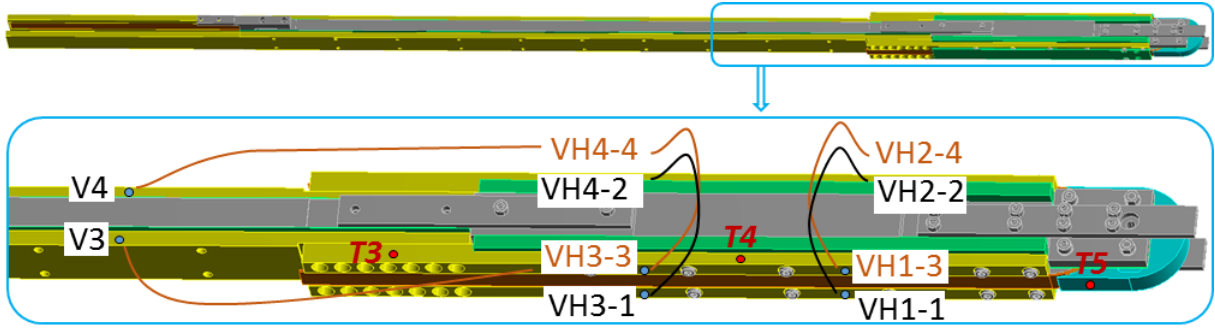
Figure 3.34 *Instrumentation scheme of the diffusion-bonded bent joint for sample#1 and sample#2.*

The main goal of the experimental campaign is the characterization of the splice resistance under different current flat-top I and magnetic field values B. The maximum target current to be tested is 15 kA at 10.9 T background field. The ratio between current and cable critical current I/I_c is in the range 0.67-0.77, thus higher than the 1/3 target. The strand critical current is evaluated from three parametrized curved (see A.1 in the Appendix) provided by CERN together with the cable. The curve is scaled with the number of strands of the cable. Since the strands of the cable come from unknown billets, all three critical lines and surfaces are reported in Figure 3.35.
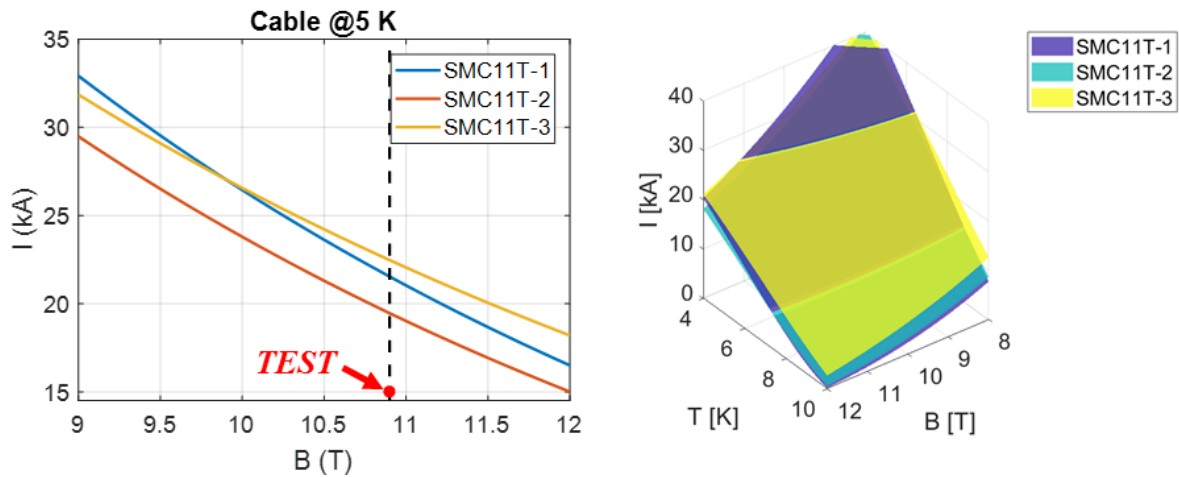
Figure 3.35 *SMC-11T cable critical line (left) and surface (right) scaled to the number of strands of the cable. Three different strand billets are represented.*

The results of the measurements are shown in Figure 3.36-Figure 3.37, in which the resistance is reported as a function of current for different values of SULTAN background field. The temperature of the sensor T5 ranged between 4.5 K and 5 K for the different runs. In particular, it was 4.5 K at 0 T and 5 K at 10.9 T, where the resistance of the diffusion-bonded joint was higher. However, in this temperature range, the resistance of the splice is not influenced by the temperature, as shown in later plots.

Figure 3.38 shows the dependence of the resistance with respect to the background field for the maximum current reached by the splice samples at B=10.9 T.

For the diffusion-bonded splice of sample#1, the dependence of R on I is negligible (Figure 3.36), except at 10 and 10.9 T, in which R increases with current. Such a non-linear behaviour

is present also in the *R* vs *B* plot of Figure 3.38, for values of *B* above 8 T. This non-linear behaviour may be interpreted as a change of the current path due to saturation of the best diffusion bonded spots. The maximum steady-state current achieved at maximum field was 14 kA (I/I_c=0.63-0.72). A voltage runaway during the current ramp-up occurred at 14.3 kA in the joint region (VH1-VH2 had the fastest reaction), while the conductor critical current is estimated to be within the range 19.5-22.5 kA (Fig. 21). Other two trials were performed in order to try to reach 15 kA, but the voltage runaway occurred always at 14.3 kA, thus bringing to exclude training as cause.

For the diffusion-bonded splice of sample#2, the dependence of *R* on *I* is negligible (Figure 3.37), but the highest reached current at 10.9 T was 8 kA (I/I_c=0.36-0.41), due to voltage runaways in the joint. Whereas *R(B)* of sample#1 is non-linear (Figure 3.38), linearity is observed for sample#2. However, the resistance of the diffusion-bonded joint of sample#2 behaves like the one of sample#1. To demonstrate this statement, current and background field were once kept constant, while the helium temperature was slowly constantly increased (Figure 3.39-Figure 3.40). While approaching saturation conditions, it was observed that the resistance was increasing non-linearly with the temperature until the voltage runaway occurred.

The different performance between the two diffusion-bonded splices is in line with the level of pressure during diffusion-bonding estimated by the FEA model (Figure 3.28). Even though the applied pressure at room temperature is the same, a higher pressure is estimated to be reached by clamp#1 during the heat treatment.

The resistance of the connections to the leads for sample#1-2 is reported in Table 3-5. These termination joints showed a resistance significantly higher than the diffusion-bonded splices. Their resistance depends on the SnPb solder, the copper of the termination and the indium between two terminations. The increase of the resistance with respect to the background field is due to the magneto-resistivity of copper. The different resistance between VH3-V3 and VH4-V4 can be attributable to the low reproducibility of joints based on squeezed indium wires. In particular the termination VH3-V3 of sample#1 had a resistance higher than 10 nΩ. The visual inspection after the test highlighted that not all the strands of the termination were in contact with solder. The terminations did not have any influence on the performance of the diffusion bonded joint but their resistance can rather limit the duration of each run. Indeed, the higher the total resistance of the sample holder, the higher the ramp rate of the primary circuit of the superconducting transformer to keep constant the current of the secondary circuit, of which the sample holder is part [81].
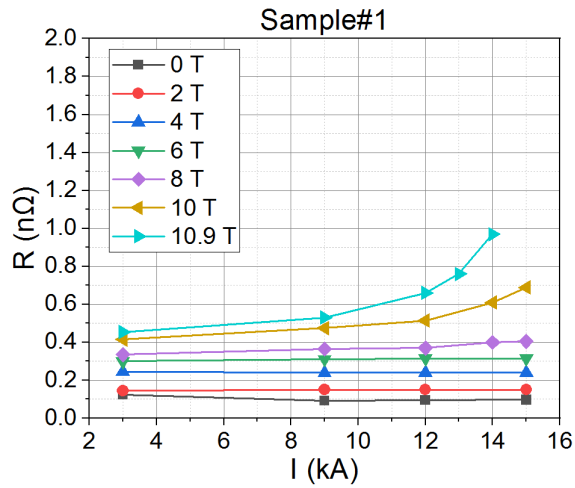
Figure 3.36 *Resistance of the bent diffusion-bonded sample#1 as a function of current. The temperature range is 4.5-5 K.*
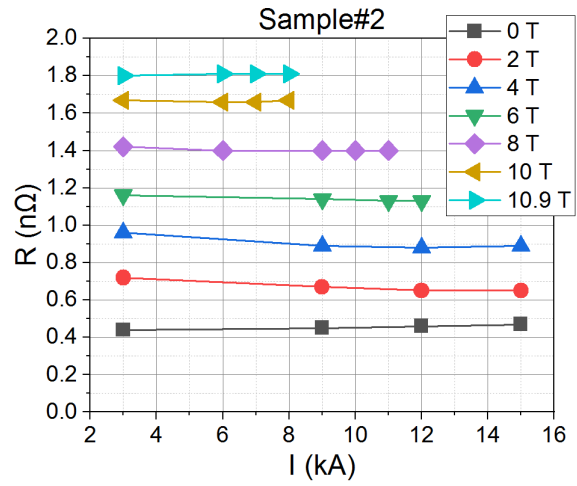
Figure 3.37 *Resistance of the bent diffusion-bonded sample#2 as a function of current. The temperature range is 4.5-5 K.*
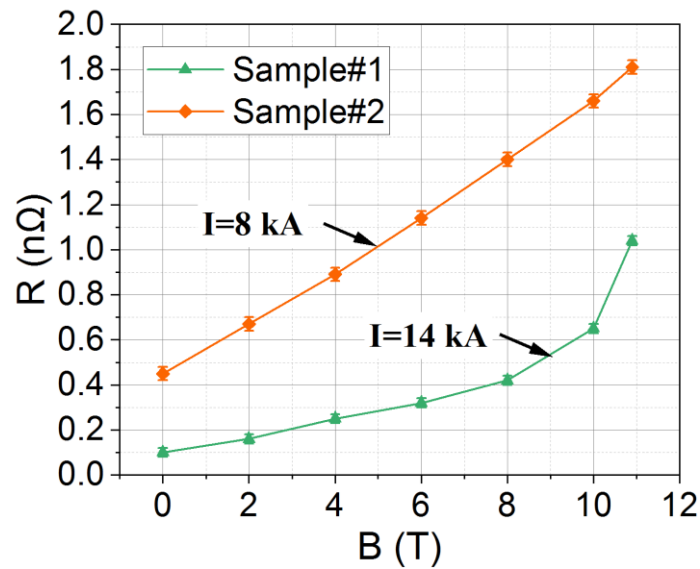
Figure 3.38 *Resistance of the bent diffusion-bonded samples as a function of the background field. The current is the maximum reachable one by each sample at B=10.9 T. The temperature range is 4.5-5 K.*
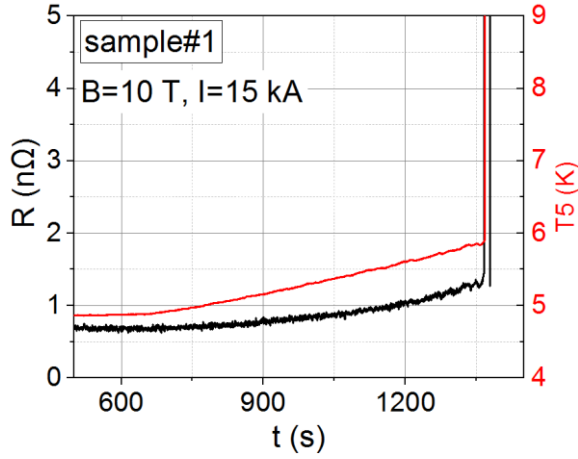
Figure 3.39 *Resistance of the diffusion-bonded joint of sample#1 as function of temperature.*
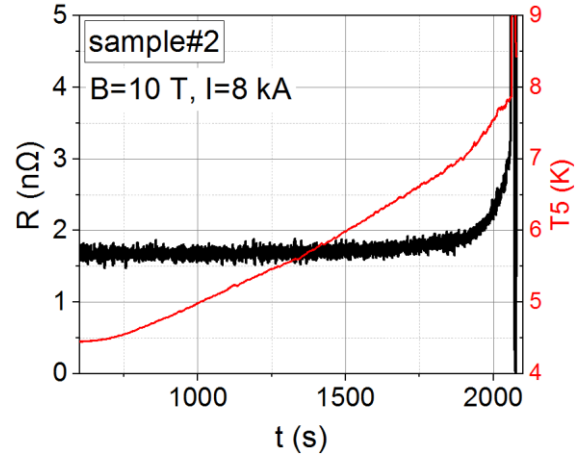
Figure 3.40 *Resistance of the diffusion-bonded joint of sample#2 as function of temperature.*

Table 3-5 *Resistance of the connections to the leads in the bent diffusion-bonded splice experiment.*

	Indium joint VH3-V3		Indium joint VH4-V4	
	R @ *B*=0 T	*R* @ *B* =9 T (*B*_{max} bore 10.9 T)	*R* @ *B* =0 T	*R* @ *B* =9 T (*B*_{max} bore 10.9 T)
Sample#1	14 nΩ	24 nΩ	6 nΩ	15 nΩ
Sample#2	3 nΩ	8.5 nΩ	2.5	8.2

The visual inspection after disassembly of the sample holder of sample#1 and sample#2 highlighted the incomplete bond between the two cables at the extremity of the splices, where the pressure was particularly low during the diffusion bonding of both joints (Figure 3.41). In particular, upon removal of the outer pressing plate, a spring back of the strands was observed at the extremity of the diffusion-bonded splice.

Due to the different performance of the two splices in terms of resistance and highest reached current, a different extent and quality of the diffusion bonded spots between the two splices is to be assumed. However, the resistance of both splices is in the range of nΩ, still too low in order to identify a bond difference through a visual inspection.
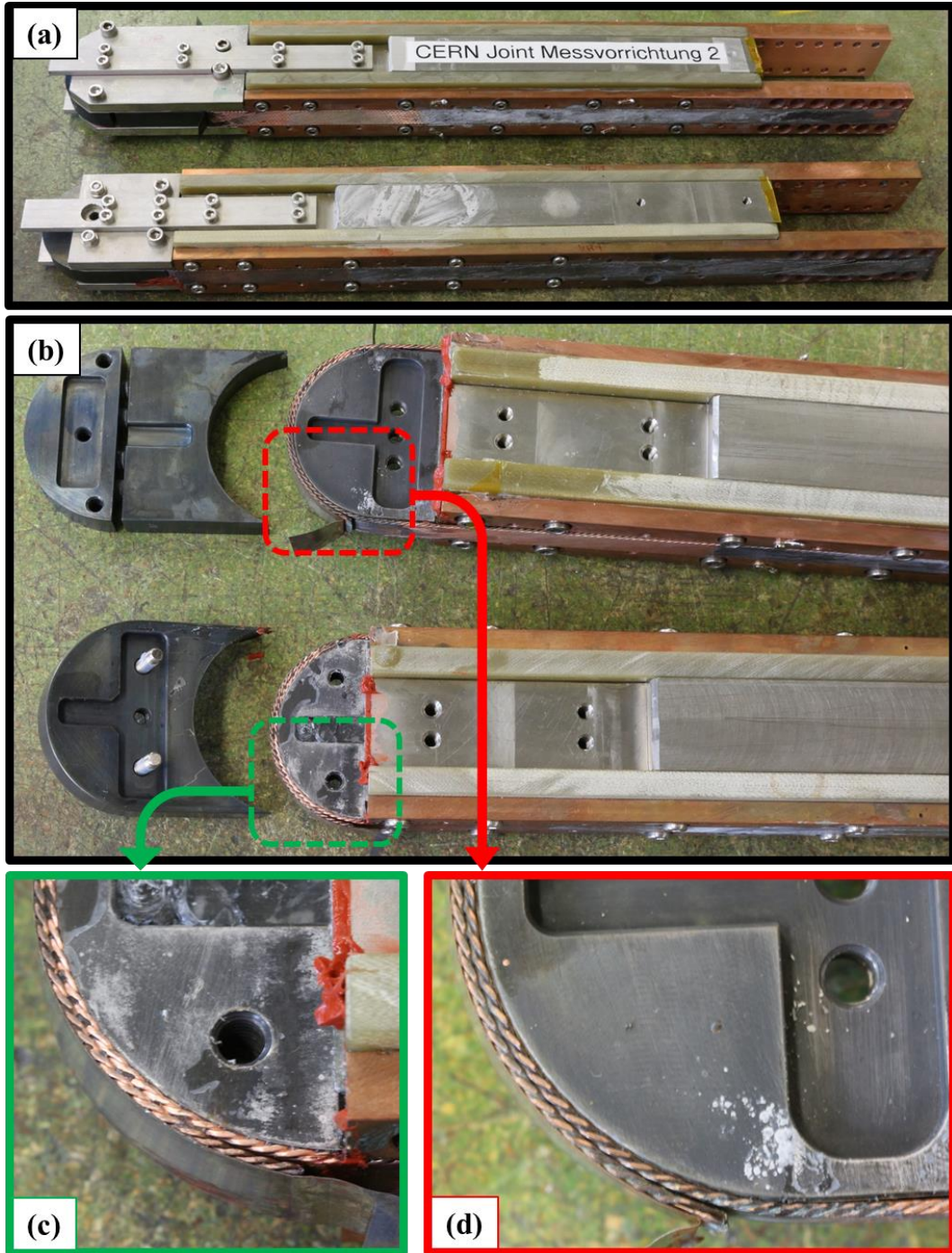
Figure 3.41 *Sample holder after test (a) and sample holder disassembly (b) of sample#1 (c) and sample#2 (d).*

3.4.5 Diffusion-bonding between strands

In joints between Rutherford cables, diffusion-bonding occurs in spots between strands. The global resistance is the combination of hundreds of parallel strand-to-strand contacts (Figure 3.42). The number of contacts N_c between the two cables is based on geometrical parameters and can be evaluated through equation (3. 4).

$$N_c = (N_s - 1) \cdot \frac{L}{L_p/N_s} \cong 1170 \tag{3.4}$$

where N_s is the number of strands, L_p =100 mm the twist pitch and L=75 mm the splice length. Knowing N_c and the total splice resistance R_{tot} measured in Section 3.4.4, it is possible to define the average diffusion-bonded contact resistance between two strands by applying the formula of the resistances in parallel (3.5).

$$\frac{1}{R_{tot}} = \sum_{i=1}^{N_c} \frac{1}{R_{c,i}} = \frac{N_c}{\bar{R}_c} \tag{3.5}$$

$\bar{R}_c$ is in the μΩ range and is reported as a function of field in Figure 3.43 for the two bent diffusion-bonded splices. In particular, the values reported at B=10 T and B=10.9 T for sample#1 were extrapolated from the values between B=0 T and B=8 T because the formula (3.5) applies only where $R_{tot}(B)$ is linear. Indeed, formula (3.5) takes into account only the resistance of the diffusion-bonded spots and not the resistance of saturated strands, whose effect is instead present in Figure 3.38.
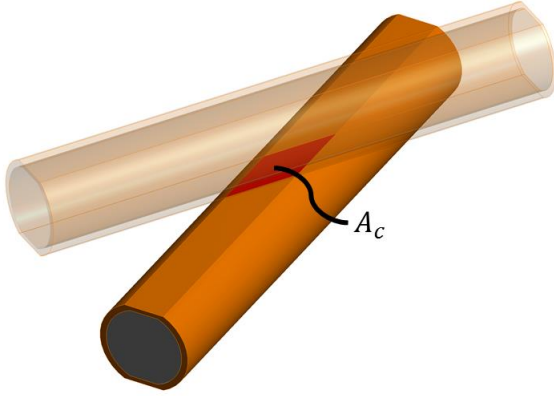
Figure 3.42 *Overlap area between two strands in a splice between Rutherford cables.*
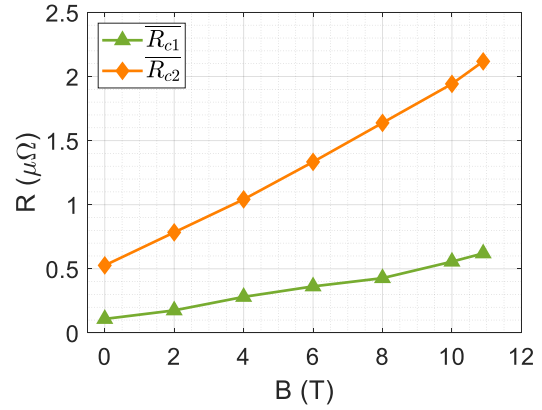
Figure 3.43 *Estimated average resistance of the diffusion-bonded spots of the two bent splices between cables tested in Section 3.4.4.*

It was tried to confirm the values of Figure 3.43 experimentally by preparing samples consisting in of the diffusion-bonding between two strands. The experimental campaign on a series of sample was unsuccessful due to lack of reproducibility of the samples. The followed procedure is reported in this section.

The strands are extracted unreacted from the SMC-11T cable. Such strands are deformed due to the compaction and shaping occurring during cabling and present a flat surface on the visible side of the cable. The two wires are overlapped in the heat treatment sample holder shown in Figure 3.44, such that the flat side of the strands match each other. The same sample holder made up of steel will be used in the electrical test. For this reason, the sample holder is oxidized before the sample is assembled, to avoid short circuits. The two strands are inserted into two slots that are less deep than the strand diameter, such that they can be pressed with a weight during the heat treatment. The overlap angle reproduces that of the cable. The choice of the

weight is made such that the pressure on the strands is comparable to the one estimated at T=650 °C in the bent splice between cables. For this purpose, the pressure acting on the contact between two strands needs to be estimated, as well as the contact area between two wires. By geometrical considerations based on the twist pitch and the strand compaction, i.e. the ratio between the strand diameter and the half-thickness of the cable, one can estimate the contact area between two strands as being a rhombus of area $A_c \cong 0.18 \ mm^2$ (Figure 3.42). The total contact surface between the two cables was then $A_{tot} = N_c \cdot A_c = 211 \ mm^2$. In the bent splice prototypes tested in SULTAN, the surface of the splice is given by the product of cable width and splice length, $A = w \cdot L = 14.7 \cdot 75 = 1100 \ mm^2$. The average pressure on A was about 26 MPa at room temperature. It is estimated to become $P_1 = 50 \ MPa$ and $P_2 = 36 \ MPa$ for clamp#1 and clamp#2, respectively, during heat treatment (Figure 3.27). The average contact pressure on strands of the bent splices during heat treatment is then $P_{1c} = P_1 \cdot A/A_{tot} = 260 \ MPa$ and $P_{2c} = P_2 \cdot A/A_{tot} = 190 \ MPa$. On a single spot of area A_c, P_{1c} and P_{2c} can be exerted by a mass of 4.7 kg and 3.4 kg, respectively. It may be observed that, while in the bent splice the pressure at high temperature can only be estimated by calculations based on simplifying assumptions, in the diffusion-bonding between two strands the pressures at room and high temperature coincide because the pressure is applied by a free standing weight.

Five identical samples with a 3.4 kg weight were prepared (Figure 3.44c) and heat treated following the same program as for the SMC-11T cable. The details of the sample holder for the electrical test are shown in Figure 3.45. The sample is inserted into the bore of a 15 T solenoid, a test facility at SPC-Villigen suitable for small samples. The sample is at 4.2 K, temperature of the helium bath in which it is immersed, and the power supply can provide up to 1 kA. As the expected resistance is in the range of μΩ, a current of 5 A is sufficient for good accuracy.
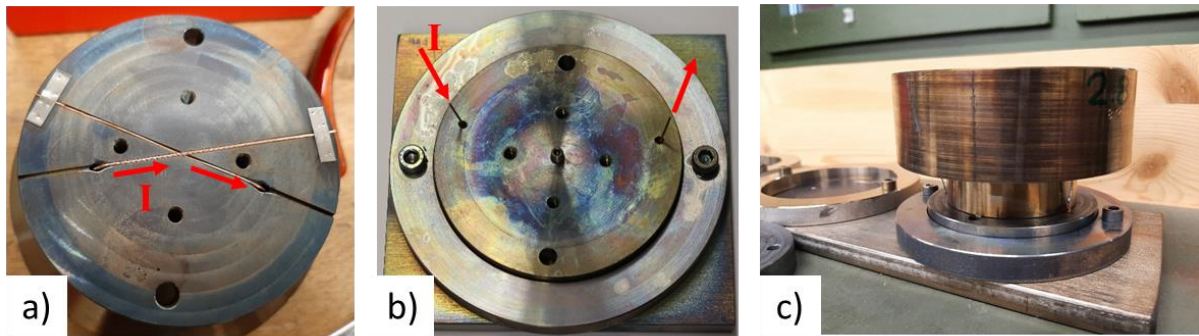
Figure 3.44 *Top view (a) of the sample holder with overlapped strands; bottom view (b) of the sample, where the weight is laid (c) in view of the heat treatment.*
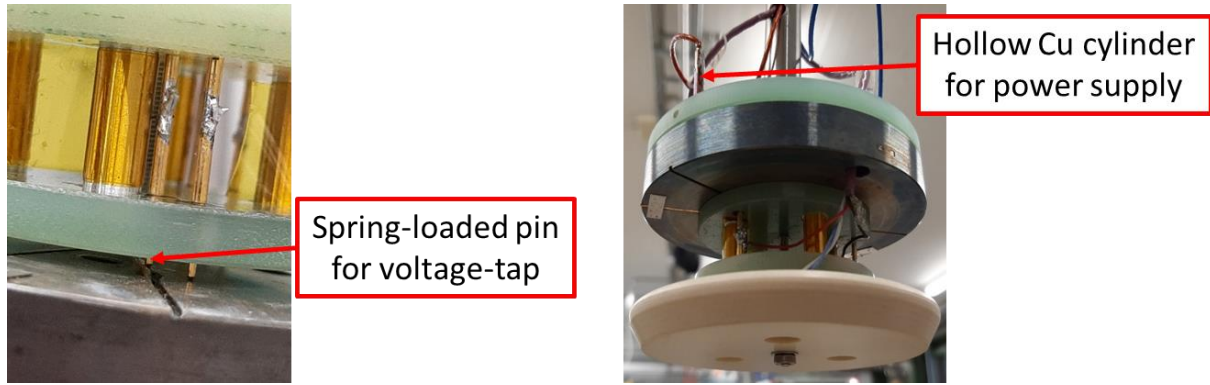
Figure 3.45 *Detail of one of the two voltage taps for the resistance assessment (left) and the sample before the electrical test (right).*
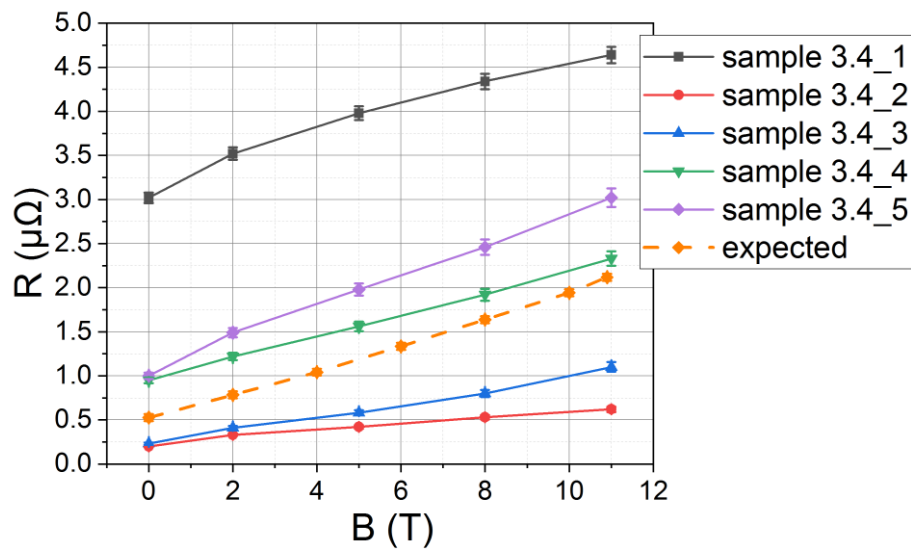
Figure 3.46 *Assessed resistance of strand-to-strand diffusion-bonded samples (solid lined) in comparison to the expected values (dashed line).*

The resistance of the five samples is reported in Figure 3.46, in which the measured values are compared with the expected ones taken from Figure 3.43. The five identically prepared samples show different resistance values and dependence on magnetic field. After the tests, the samples were destroyed for analyses at the optical microscope, in particular to inspect the imprint left by the diffusion-bonded contact (Figure 3.47). The pictures highlight that the samples have different contact area. The one with the smallest imprint area (sample 3.4_1), for instance, exhibited the highest resistance. Two main causes for the different strand-to-strand contact area are:

- The samples were prepared using wires extracted from the cable. Such wires may end up with a different geometry during cabling.
- The poor control of the matching of the flat surfaces of the two strands.

Therefore, there was no precise correlation between the pressure impressed on two strands to join via diffusion-bonding and the electrical resistance due to the large standard deviation among samples prepared with identical weight during diffusion-bonding. Nevertheless, it was confirmed that such a resistance between diffusion-bonded strands lays in the μΩ range.

52
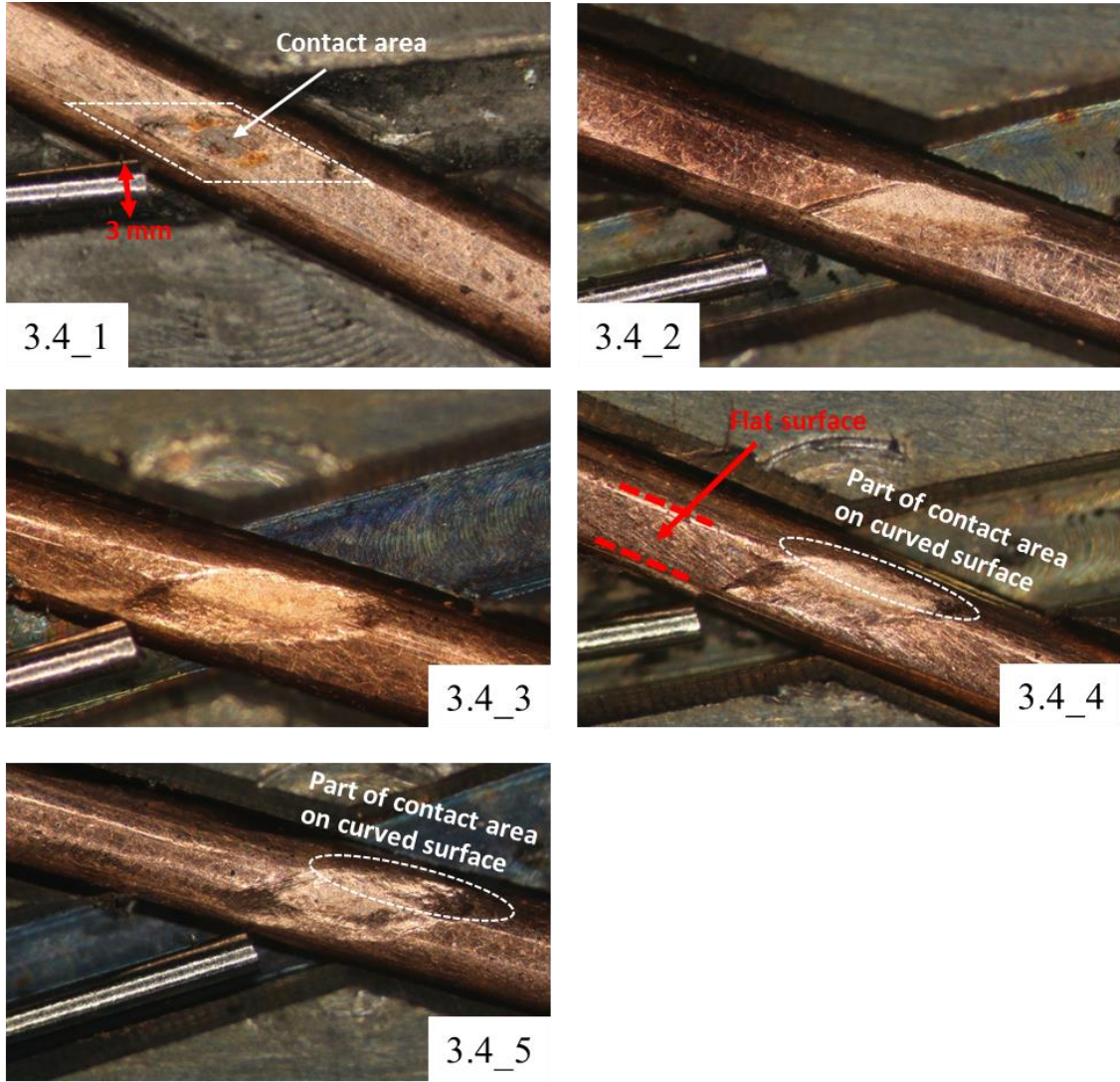
Figure 3.47 *Microscope pictures with magnification x30 of the strand-to-strand diffusion-bonding spot after heat treatment and test. A 3 mm thick wire is put as reference dimension.*

3.4.6 Analyses of bent splices through modelling

In Section 3.4.4, the joint prototype "sample#1" constructed with "clamp#1", met the resistance requirement. At the highest test-fields, namely B=10 T and B=10.9 T, the resistance $R(B)$ departed from the typical linear behaviour of joints based on copper. The interpretation that it was given was the saturation of the less resistive current paths, i.e. of strands hitting the critical surface. In this section, this assumption is checked with a modelling approach.

A Rutherford cable might be modelled as an electrical network of nodes interconnected by strand segments, adjacent and crossover contacts among these segments [82]. Each contact can be associated with a resistance. In particular, the adjacent contacts define the adjacent resistance R_a, while the crossover contacts are described through the crossover resistance R_{cr}. Such an electrical description and model of the Rutherford cable can be found in several references in literature [83] [84] [85] [86]. These models have often been used for the analysis of stability and AC losses in Rutherford cables. In this section, an electrical network model is developed to describe a diffusion-bonded splice between Rutherford cables. In addition to R_a and R_{cr}, the resistance between diffusion-bonded strands R_c is introduced in the model (Figure

3.48). An example of computational domain is shown in Figure 3.49. The parameters R_a and R_{cr} depend on many factors, but are generally equal to several tens of μΩ [87], thus significantly higher than R_c, whose estimate is given in Section 3.4.5. In the bent splices designed and tested in this Chapter, the resistance R_c is not uniform along the joint length because of the non-uniform pressure distribution in the clamp during diffusion-bonding. The detached edges shown in Figure 3.41 are a proof of this fact. In the model, a distribution of R_c based on the computed pressure distribution of Figure 3.28 is assumed. In more details, it is assumed the proportionality $R_c \propto 1/P$ along the splice length, thus obtaining the distribution in Figure 3.50. The average value $\bar{R}_c$ is taken from Figure 3.43. In particular, R_c has a minimum at the centre, where the pressure has a maximum, and $R_c \to \infty$ when $P \to 0$. Next to the edges of the splice and the centre, R_c approaches the values of R_a and R_{cr}, i.e. there is no diffusion-bonding between two strands of the joint but rather contact. Other possible causes for inhomogeneous R_c distribution, such as the non-uniform shape of strands (Figure 2.2), are neglected.
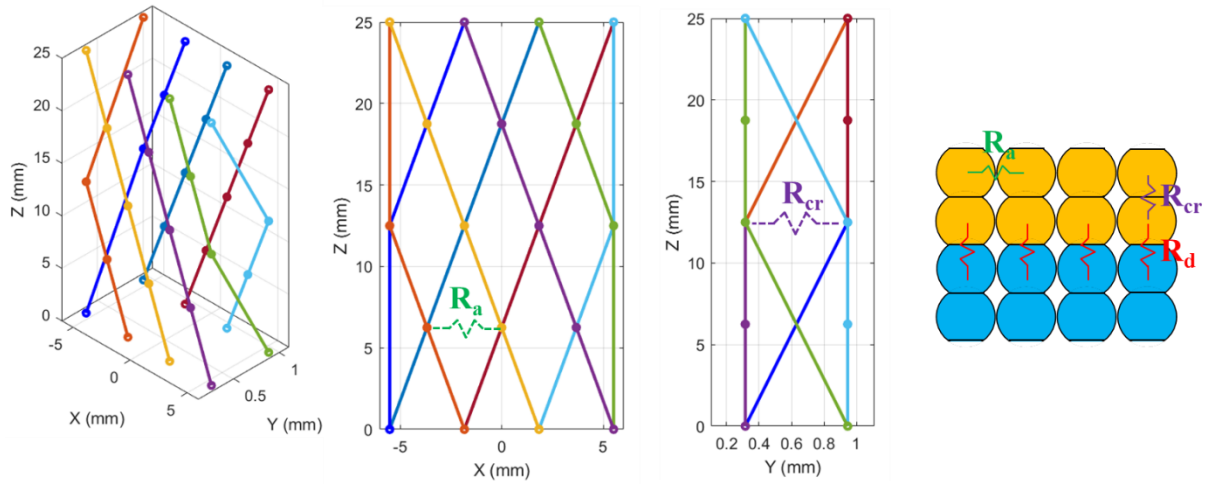
Figure 3.48 *Nodes description and parameters of an 8-strands Rutherford cable and of a joint.*
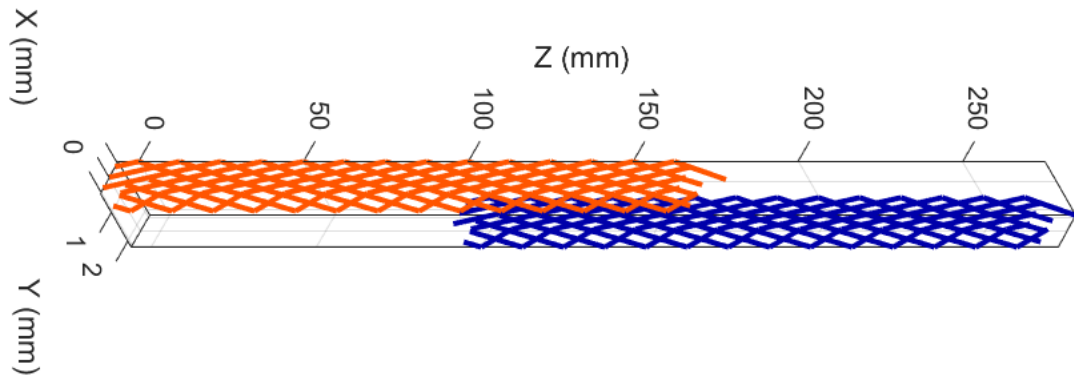
Figure 3.49 *Computational domain for the analysis of a splice between two Rutherford cables with 8 strands.*
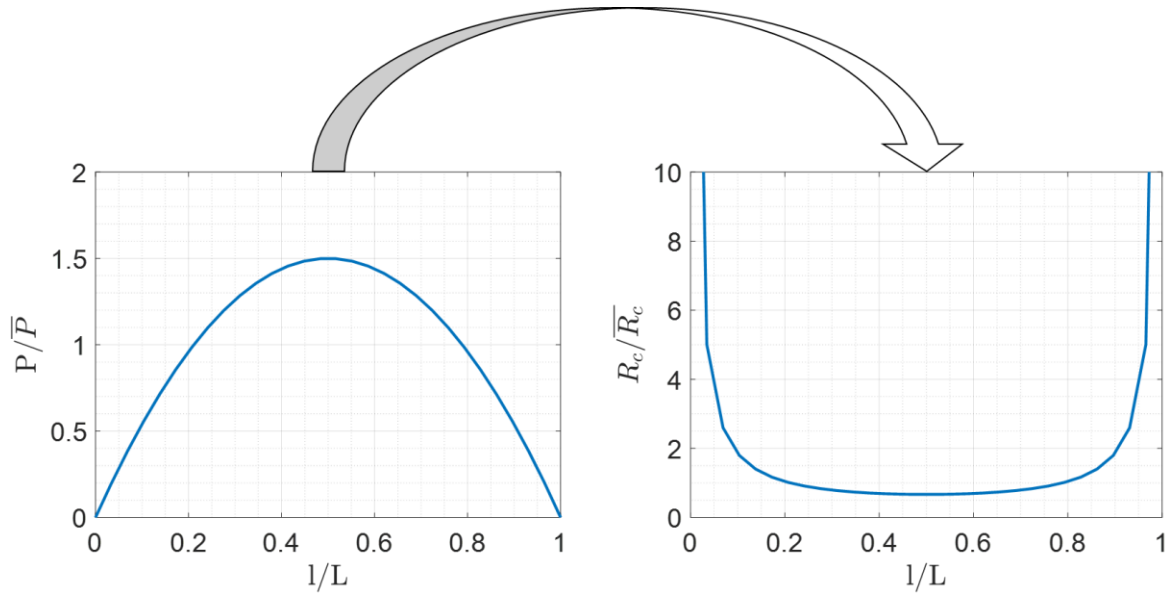
Figure 3.50 *Normalized distribution of R_c on the joint length (right) assumed according to the computed normalized pressure distribution during diffusion-bonding (left).*

In this network model, four types of currents are the unknowns:

- I_s, the strand current, passing through the strand segment.
- I_a, the adjacent current, passing through R_a.
- I_{cr}, the cross-over current, passing through R_{cr}.
- I_d, the joint current, passing through the diffusion-bonded spot R_c.

These currents are related to each other in the nodes according to Kirchhoff's first law (3. 6). For each identified circuit, the Kirchhoff's second law is applied (3. 7).

$$\sum I_s + \sum I_a + \sum I_{cr} + \sum I_d = 0 \tag{3. 6}$$

$$\sum U_s + \sum R_a I_a + \sum R_{cr} I_{cr} + \sum R_c I_d = 0 \tag{3. 7}$$

The strand segment voltage U_s is different from zero only if the critical current I_c is overcome in the segment. If this happens, it is assumed that the current splits between superconductor and copper matrix and stabilizer. In particular, U_s is expressed according to formula (3. 8), where it is assumed a sharp transition from the superconducting to the normal state, i.e. $n \to \infty$ in the power law $E = E_c(I/I_c)^n$ [87], where E is the electric field and E_c the critical electric field, conventionally equal to 0.1 µV/cm in LTS strands.

$$U_s(I_s) = \begin{cases} 0, & I_s < I_c \\ R_{Cu}(B)(I_s - I_c(B)), & I_s \geq I_c \end{cases} \tag{3. 8}$$

The resistance of copper depends on the magneto resistivity ρ, on the length of the strand segment l_s, on the wire diameter d_s and on the fraction of copper in the strand α, as expressed in equation (3. 9).

$$R_{Cu}(B) = \rho_{Cu}(B) \frac{l_s}{\alpha \cdot \pi d_s^2/4} \tag{3. 9}$$

For each cross-section of the cable along the z direction, it is imposed that the sum of the z-component of the currents is equal to the transport current, as in (3. 10).

$$\sum \vec{I}_s \cdot \hat{e}_z + \sum \vec{I}_a \cdot \hat{e}_z + \sum \vec{I}_{cr} \cdot \hat{e}_z + \sum \vec{I}_d \cdot \hat{e}_z = I_{tr} \tag{3. 10}$$

To solve the system of equations, boundary conditions are needed in the first and last cross-section of the computational domain on the xy plane, i.e. for $z(0)$ and $z(L_{end})$. It is assumed that the nodes laying on the plane $z(0)$ have the same potential, as well the nodes in $z(L_{end})$. This implies that the current of each strand j changes neither between $z(0)$ and $z(\Delta z)$ nor between $z(L_{end}\text{-}\Delta z)$ and $z(L_{end})$, as stated in equation (3. 11) and (3. 12).

$$I_{s,j}(0) = I_{s,j}(\Delta z), \qquad j = 1,2,\dots, N_{strands} \tag{3. 11}$$

$$I_{s,j}(L_{end}) = I_{s,j}(L_{end} - \Delta z), \qquad j = 1,2,\dots, N_{strands} \tag{3. 12}$$

Once the system of equations is solved, the total resistance is computed as in equation (3. 13).

$$R_{tot} = \frac{\left(U(z = 0) - U(z = L_{end})\right)}{I_{tr}} \tag{3. 13}$$

R_{tot} is computed for each field and compared to the experimental results of sample#1 in Figure 3.51. Two cases are taken into account. "Computation 1" assumes that, in the overlap region, diffusion-bonding occurs also among the strands of the same cable, i.e. $R_{cr}=R_c$ in the joint. This can be the case if the steel core is removed, as in the built prototypes. "Computation 2" assumes instead the presence of the steel core. In the range B=0-8 T, experimental and computational results coincide by construction: there is no strand saturation and the computed R_{tot} just depends on $\bar{R}_c$, which is extracted from the experiments themselves. For B=10 T, some strands reach the criticality condition in the computation, but they are too few for impacting R_{tot}. For B >10 T, several strands saturate and R_{tot} is not linear anymore in the computed results. The difference between the two computational cases highlights that the removal of the steel core starts playing a role next to saturation conditions. Both computational cases underestimate the results coming from the measurements. It is then possible that the R_c distribution proposed in Figure 3.50 is too optimistic and that the real one is sharper.

Figure 3.52 compares the current distribution calculated by the model at B=2 T and at B=10.9 T, to compare a case without and with strand saturation, occurring at $I_c(5\ K,\ 10.9\ T)$=490 A. The broad current distribution at B=2 T is the results of two effects:

- The joint length is 75% of one twist pitch. This leads to strands with a lower and higher number of contacts in the joint. The ones with more contacts tend to carry more current.
- The diffusion-bonded resistance R_c between two strands has a non-uniform distribution along the joint length. The strands with less resistive contacts can carry more current.

At B=10.9 T in Figure 3.52, the current distribution narrows because several strands saturate and current redistribute to strands with higher R_c and lower contact points in the joint. This causes the resistance increase observed in Figure 3.51.

Figure 3.53 shows a 3D view of the current distribution in the computational domain at B=10.9 T.
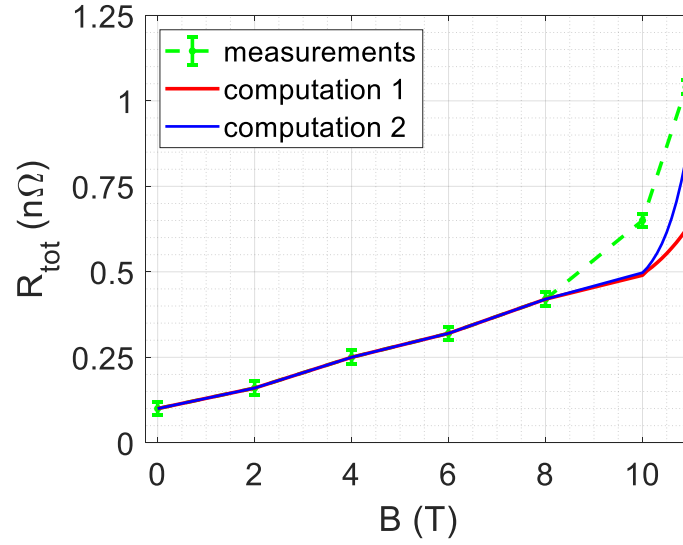
Figure 3.51 *Comparison between the measured and the computed total joint resistance of sample#1 at $I_{tr}=14$ kA.*
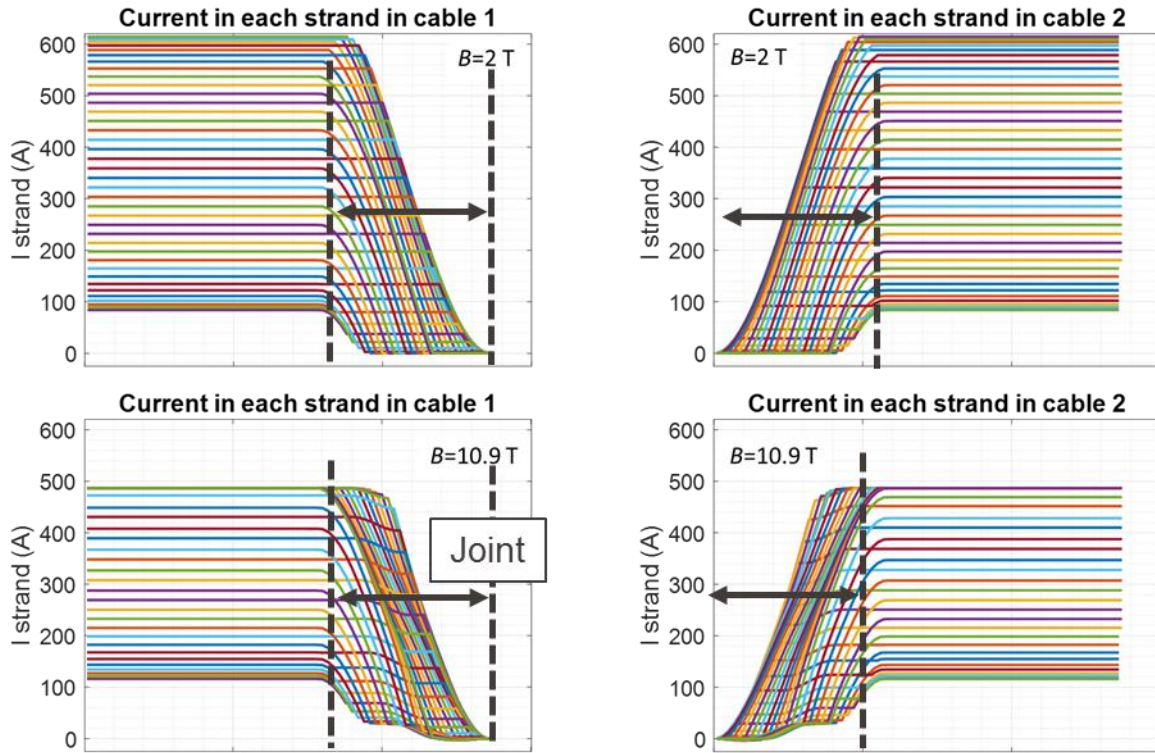
Figure 3.52 *Computed current distribution in the strands along the computational domain at B=2 T and B=10.9 T. The transport current is $I_{tr}=14$ kA.*
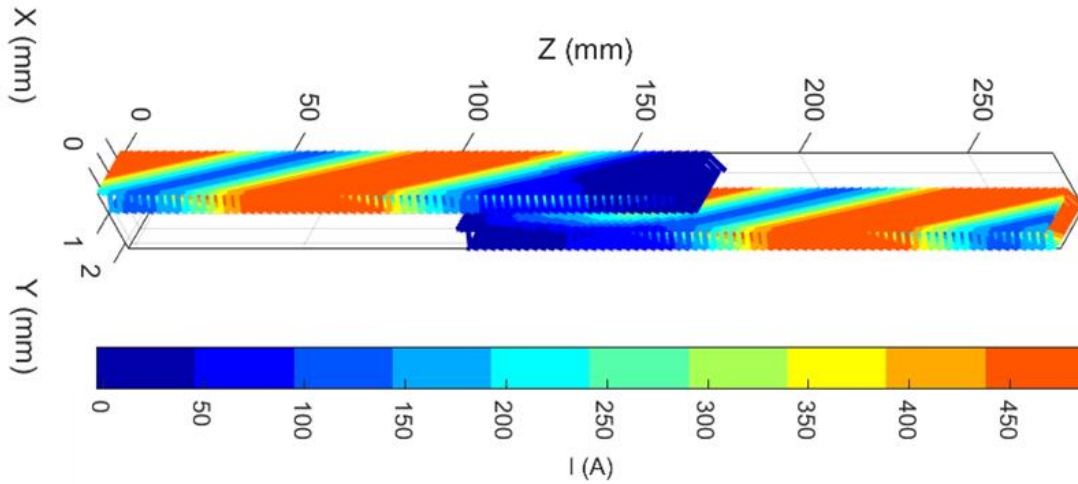
Figure 3.53 *Current distribution in the computational domain at B=10.9 T.*

3.4.7 Integration into a dipole: racetrack coil study

The sequence of figures in this section shows schematically the assembly and partial disassembly steps for the integration of the designed diffusion-bonded clamps into the head of a pancake-wound Racetrack magnet. It is assumed that clamp and cable are separated by electrical insulation.

The procedure for clamp#1 can be summarized as follows:

- The high field (HF) pancake is first wound (Figure 3.54).
- The cable sections of the high and low field (LF) cables are put in overlap position in straight geometry (Figure 3.55) and crimped with a thin point-welded foil (Figure 3.56) to keep the winding tension.
- The crimped cables are turned around the inner pressing plate (Figure 3.57).
- The outer pressing plate, threaded plate and pressing screws are inserted (Figure 3.58). The outer pressing plate is linked to the base plate through temporary screws.
- The connecting plate is put in position and connected to the outer and inner pressing plates through temporary screws (Figure 3.59).
- The threaded plate, initially in contact with the inner pressing plate (Figure 3.60), is pushed by screws against the edge of the connecting plate (Figure 3.61). The temporary screws are removed while applying full pressure by tightening the pressing screws (Figure 3.62), which push the inner pressing plate against the future joint.
- The LF pancake is wound (Figure 3.63).
- After heat treatment, the partial disassembly of the clamp begins. Screws block inner and outer pressing plate (Figure 3.64) such that the pressing screws can be untightened without manipulation of the joint and the threaded and connecting plates are disassembled (Figure 3.65).
- A filler between the head of the HF pancake and the clamp is put in place (Figure 3.66).
- The coil mechanical support can start to be assembled where the connecting plate was removed. Afterwards, the base plate can be disassembled with the same procedure described above.

A view of the coil with the remaining parts of the clamp is shown in Figure 3.67.
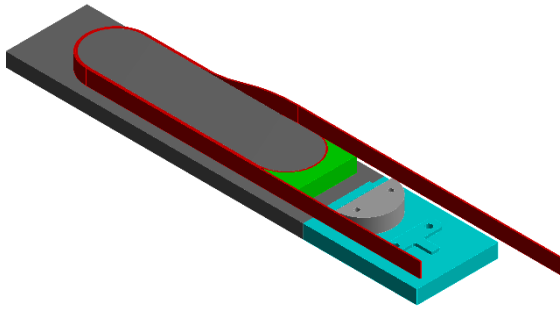
Figure 3.54 *HF pancake of the racetrack coil, winding table and pole of the coil.*
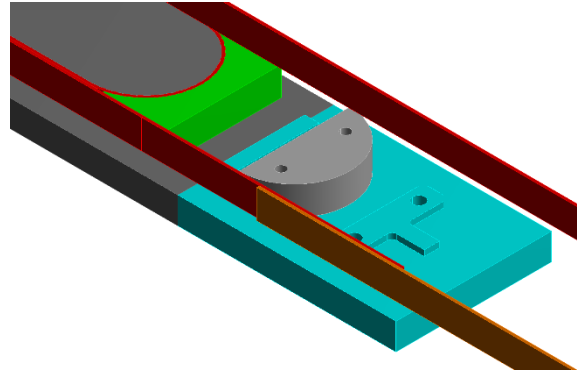
Figure 3.55 *HF and LF cable sections to join.*
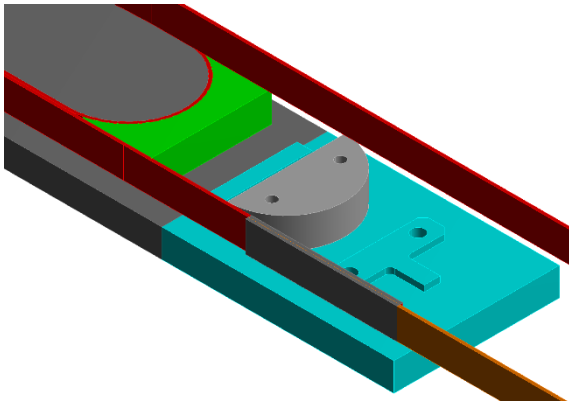
Figure 3.56 *HF and LF cable sections are crimped with a thin point-welded foil.*
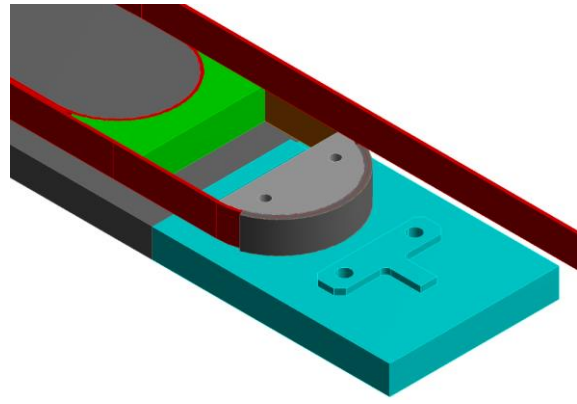
Figure 3.57 *Turning of the crimped cables around the outer pressing plate.*
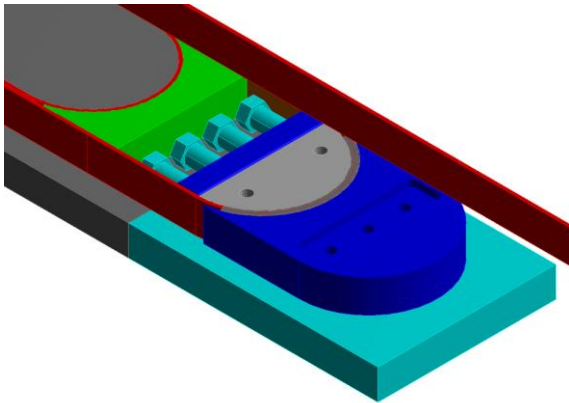
Figure 3.58 *Assembly of threaded, outer pressing plates and pressing screws.*
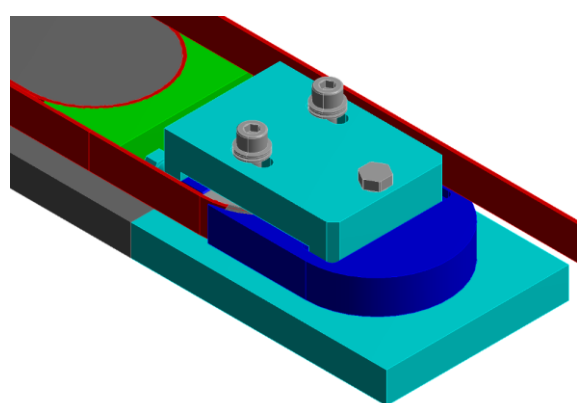
Figure 3.59 *The connecting plate is put in place.*
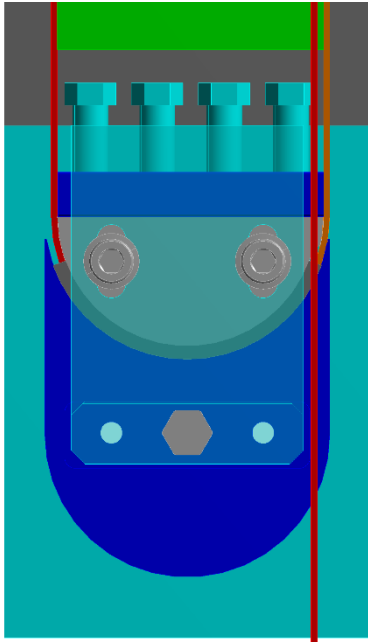
Figure 3.60 *Clamp#1 before the pressing bolts are tightened.*
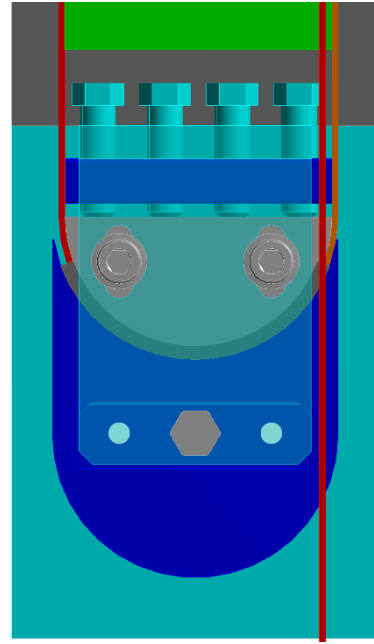
Figure 3.61 *Tightening of the pressing bolts.*
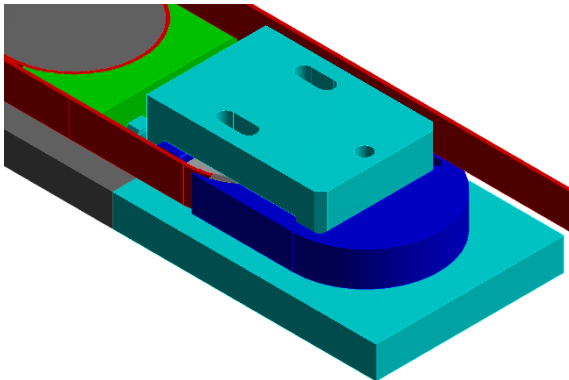
Figure 3.62 *The screws between connecting and pressing plates are removed and full pressure can be applied.*
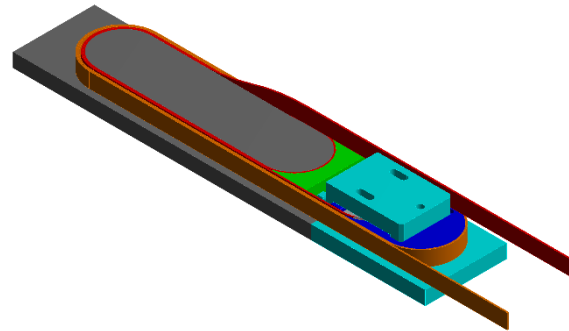
Figure 3.63 *The LF pancake is wound.*
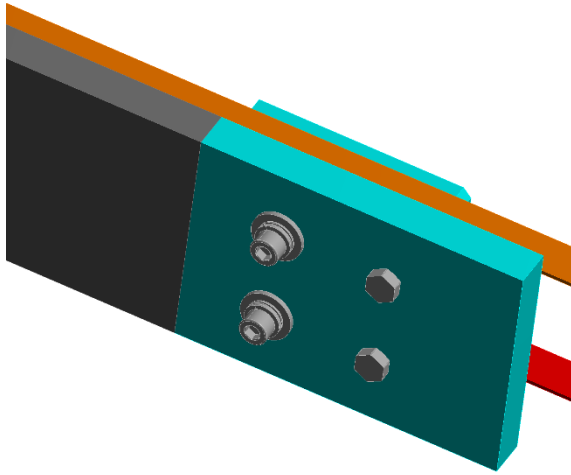
Figure 3.64 *Screws between base and pressing plates tightened after heat treatment.*
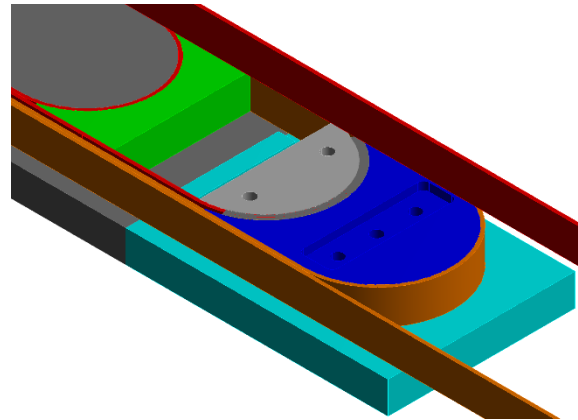
Figure 3.65 *Connecting and threaded plates are disassembled after that the pressing screws are untightened.*
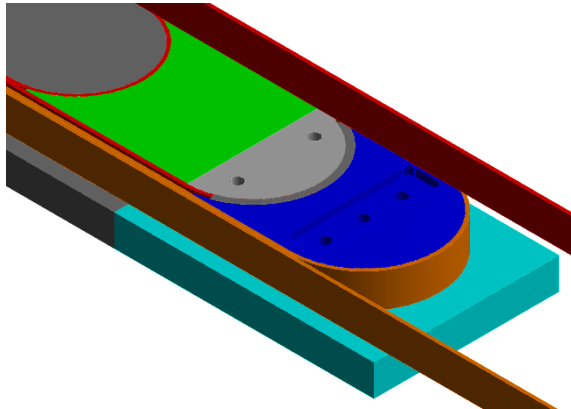
Figure 3.66 *Filler between HF pancake and clamp.*
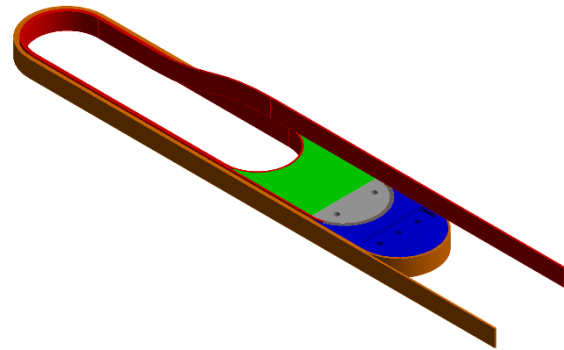
Figure 3.67 *Components of clamp#1 remaining in the coil during the magnet operation.*

The assembly and partial disassembly procedure for clamp#2 can be summarized as follows:

- The high field (HF) pancake is first wound (Figure 3.68).
- The cable sections of the high and low field (LF) cables are put in overlap position in straight geometry (Figure 3.69) and crimped with a thin point-welded foil (Figure 3.70) to keep the winding tension.
- The crimped cables are turned around the inner pressing plate (Figure 3.71).
- The threaded and outer pressing plates are put in place (Figure 3.72).
- The connecting plates are linked with threaded and inner pressing plates through temporary screws (Figure 3.73), before the pressing bolts are tightened (Figure 3.74).
- The pressing bolts are tightened (Figure 3.75) and the temporary screws of the connecting bolts are removed for applying full pressure.
- The voids of the threaded plate are covered with fillers (Figure 3.76) and the LF pancake is wound (Figure 3.77)

- After the heat treatment, the threaded and inner pressing plates are connected to the base plates through temporary screws (Figure 3.78) for the disassembly of the connecting plates without manipulation of the joint. The disassembly is carried out by untightening the disassembly screws (Figure 3.79-Figure 3.80).
- The connecting plates are removed (Figure 3.81).
- The coil mechanical support can start to be assembled where the connecting plate was removed. Afterwards, the base plates can be disassembled with the same procedure described above.

A view of the coil with the remaining parts of the clamp is shown in Figure 3.82.
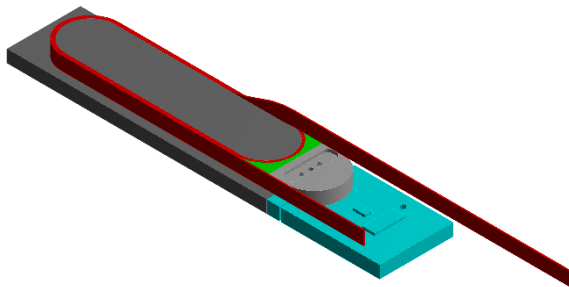
Figure 3.68 *The HF cable is wound.*
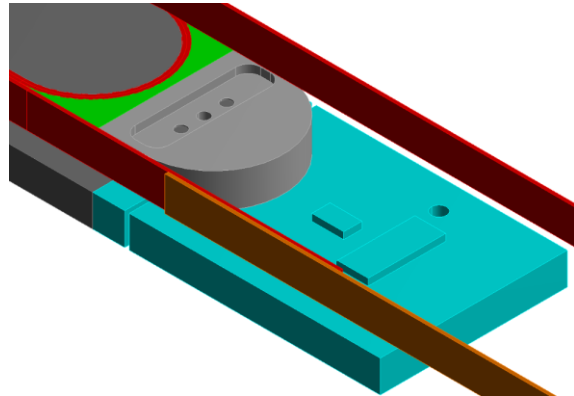
Figure 3.69 *The cable sections to join are overlapped straight.*
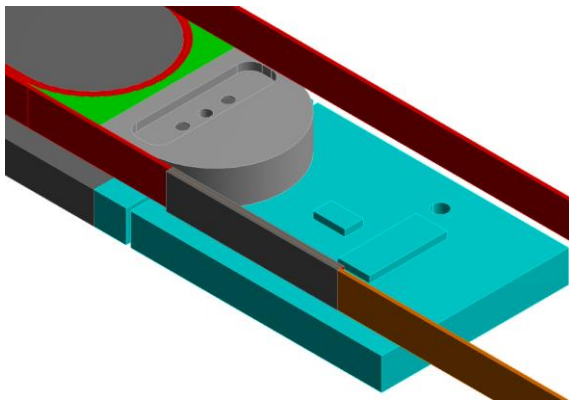
Figure 3.70 *The mating cables are crimped with a point-welded foil.*
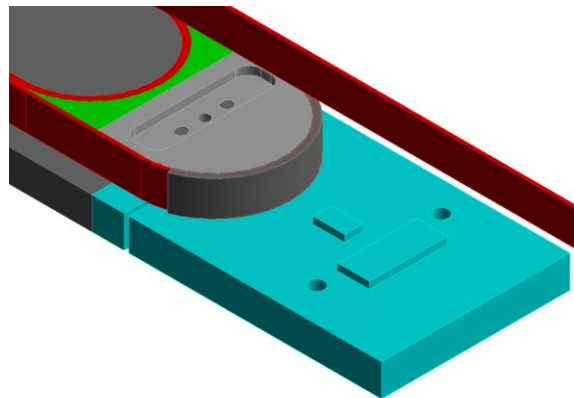
Figure 3.71 *The future joint is turned around the inner pressing plate.*
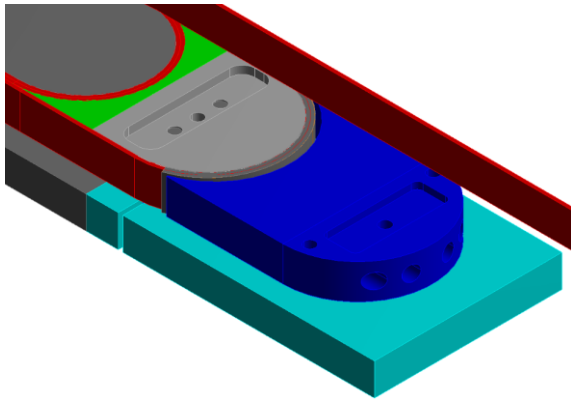
Figure 3.72 *Threaded and outer pressing plate are put in place.*
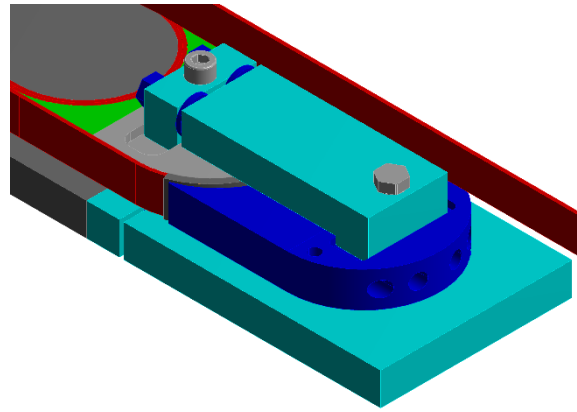
Figure 3.73 *The connecting plates are put in place.*
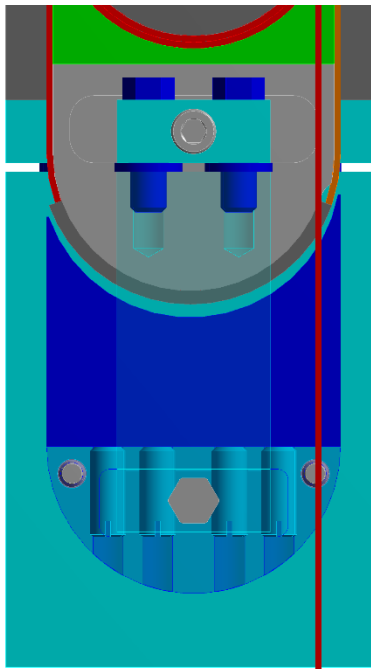
Figure 3.74 *Clamp#2 before the pressing bolts are tightened.*
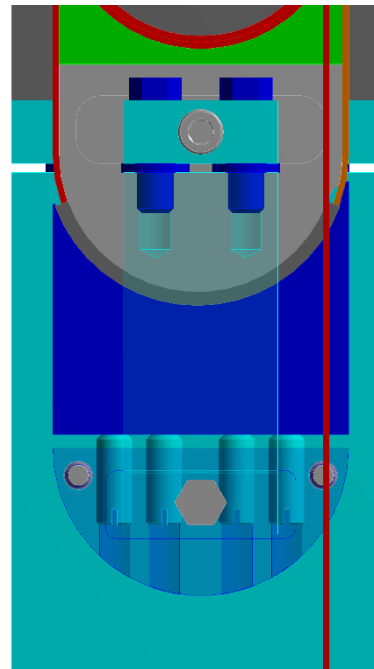
Figure 3.75 *The pressing bolts are tightened and push the inner pressing plate.*
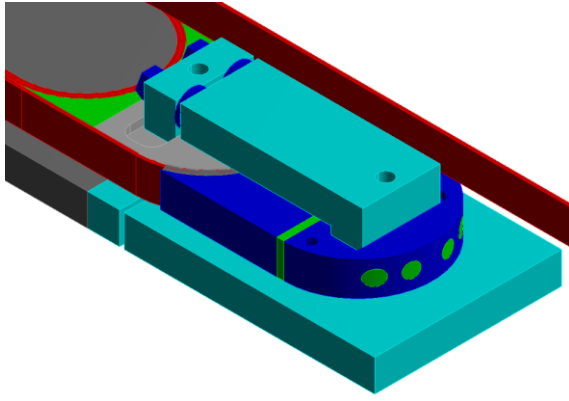
Figure 3.76 *Fillers are put into the voids of the clamp.*
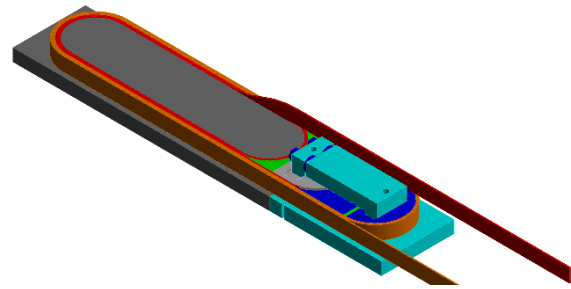
Figure 3.77 *The LF pancake is wound.*
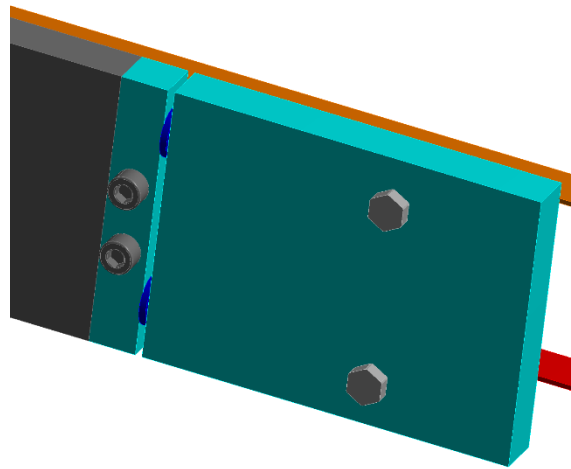
Figure 3.78 *After heat treatment, temporary screws link the threaded and inner pressing plate to the base plates.*
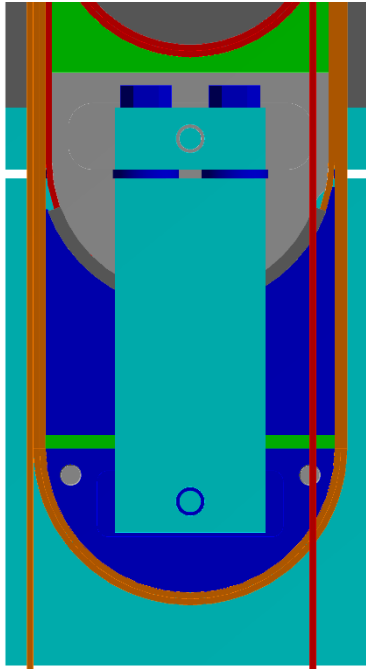
Figure 3.79 *Clamp#2 before partial disassembly after heat treatment.*
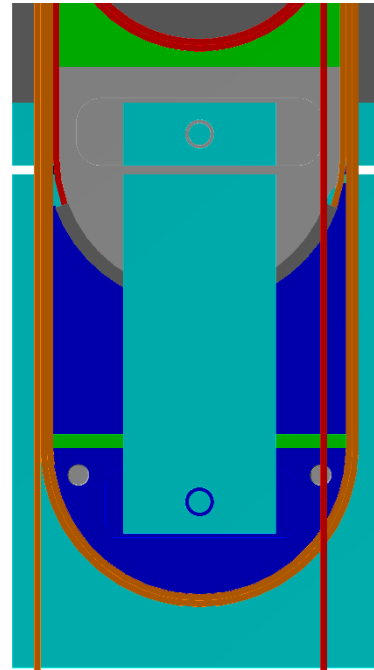
Figure 3.80 *The disassembly screws are untightened.*
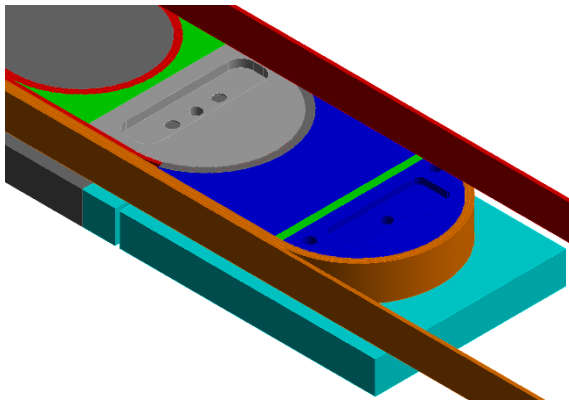
Figure 3.81 *The connecting plates are removed.*
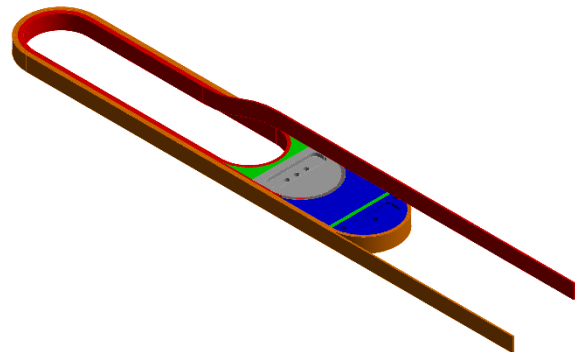
Figure 3.82 *Components of clamp#2 remaining in the coil during the magnet operation.*

3.4.8 Summary and conclusions

A diffusion-bonded internal splice is attractive for WR magnets because the joining material is the copper of the cable itself, and the thermal energy of the heat treatment is exploited to form the joint.

The pressure needed on Rutherford cables for manufacturing a splice that satisfies the resistance requirement was investigated through straight joints. As this layout is not fully representative of the geometry of a dipole head, where the splice is located, two bent splice prototypes were then designed with the criterion of the integration into a coil head. The parts of the clamps are meant to be part of the winding table and pole of a magnet.

The two bent prototypes have similar size but differ in terms of pressure distribution and assembly/disassembly steps in a magnet. In bent geometry, in comparison to the straight joint samples, the overlapped length is 75% of the twist pitch due to size limitations in the test bore. Moreover, the pressure distribution is not as uniform as in the straight case. Despite this, the experimental campaigns in SULTAN demonstrated that the better designed joint meets the requirements. In particular, the resistance is R=1.04 nΩ at B=10.9 T, T=5 K and I/I_c=0.63.

In the model it was shown that the limited joint length and the uneven contact distribution, generated by the non-uniform pressure distribution during diffusion-bonded, cause an uneven current distribution inside the strands. It was also shown that the strands with more contact points in the joint and with the less resistive ones can saturate if the cable transport current or the background magnetic field increase, leading to an increase of the splice resistance because the current redistributes among the strands with less and more resistive contact points. If the number of saturated strands is high enough, a voltage runaway may occur.

The mechanical strength of the joint was not part of the experimental characterization. This is recommended for future work.

3.5   Development of a soldered splice

3.5.1 Choice of flux and solder

The basic phenomenon occurring when two metallic components are spliced through soldering is the formation of an alloy between the parent materials, i.e. the ones being spliced, and the filler one, i.e. the solder [88]. In order for such an alloy to form on the surface of the parent, there must be chemical compatibility between parent and filler. In this case, the copper stabilizer of the two Nb_3Sn Rutherford cables constitutes the parent material. If parent and filler have comparable atomic size, they are generally miscible. Once the filler is molten, it can diffuse through the surface of the parent to form a metallic bond while solidifying. The higher the size difference of the atoms between parent and filler material, the lower the solubility.

In addition to the chemical compatibility, another important parameter for the choice of the solder is its melting temperature. This must be low enough such that it does not compromise the integrity of the parent. In reacted Nb_3Sn Rutherford cables, soldering temperature and time should be as low as possible to limit the diffusion of the tin of the cable into the copper, process that turns part of the stabilizer into resistive bronze.

For the purposes of this thesis, the solder must also have a relatively low electrical resistivity, such that the splice resistance is within the target.

A further requirement is the environmental and health compatibility of the solder. For this reasons, lead and cadmium based fillers have been discarded.

In this thesis, the filler alloy selected for the R&D on soldered splices between Nb_3Sn Rutherford cables was Sn95Ag5 because of its good compatibility with Cu, the relatively low melting temperature of 240 °C and for its low resistivity at cryogenic temperature (4.3 nΩ·m at 10.9 T).

When the filler is molten, it is fundamental for it to have a good wettability with the parent material, i.e. a sufficient attraction between the solid phase (parent) and the liquid one (filler). A precondition for a good wettability is the absence of oxides from the metallic surface of the

parent, such that the metallic bond between solder and parent can take place. In order to free the metallic surface of the parents from oxides, fluxes are used prior to soldering to activate the surface of the parent, i.e. they clean the surface from impurities and prevent further oxide formations. Common activators are acids or compounds releasing acids when thermal energy is added. For instance, a hydrous flux based on zinc chloride leads to the reduction of the copper oxide according to the reactions reported in (3. 14), when sufficient thermal energy is given. The resulting copper chloride is a flux residue that can be removed by rinsing water, in which $CuCl_2$ is soluble.

$$ZnCl_2 + H_2O \rightarrow Zn(OH)Cl + HCl$$
$$CuO + 2HCl \rightarrow CuCl_2 + H_2O$$

(3. 14)
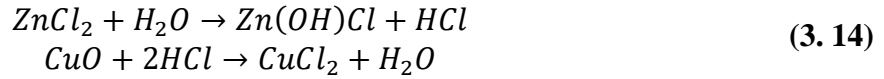
The activity of fluxes depends on temperature. It generally increases up to a maximum value after which they are not active anymore or become volatile. Fluxes are divided into organic (e.g. resin based) and inorganic (e.g. salts and acids) types. The former ones have lower activation temperature and maximum temperature of activity than the latter ones. The most suitable flux type for a certain solder, in terms of activation, depends on the melting temperature of the filler. Moreover, inorganic fluxes leave behind residues that might corrode the parent, i.e. the copper stabilizer in this case.

In the R&D on soldered splices, it is assumed that the two mating surfaces of the joint are paired before heat treatment and cannot be separated afterwards, when they have to be soldered. This assumption makes the splicing procedure employed for the NbTi LHC magnets, and shown in Figure 3.7, not applicable. In fact, there the mated cables are separated and a solder foil is inserted in between. Therefore, a new soldering layout has to be conceived.

From the geometry of the head of the dipole magnets for HE-LHC/FCC, it is also assumed that the width of the cables is in vertical direction, i.e. parallel to the gravity force, as shown in Figure 3.83. This implies that the access for flux and solder is just from the top of the overlap. Therefore, the capillarity attraction must be high enough such that flux and solder can penetrate through the narrow gaps between the mating surfaces of the cables. Moreover, after the heat treatment, the surfaces of the cable are covered by the soot coming from the mica and glass-fibre insulation. This requires the flux to be able to remove such impurities.

Based on these requirements and on the melting temperature of Sn95Ag5, Soldaflux K was selected as flux. It is an inorganic flux based on zinc chloride and ammonium chloride. Therefore, it leaves behind corrosive flux residues. Nevertheless, studies in [89] reported that corrosion stops once the splice and the magnet are impregnated because of the lack of oxygen, one of the reagents of the corrosion reaction. Therefore, the integrity of the copper stabilizer should not be affected by this type of flux.

3.5.2 Manufacture of a stack of straight joints

The R&D on soldered splices was carried out on straight prototypes, allowing the test in SULTAN of more than one samples at once, by adopting the same stack layout introduced in Section 3.4.1.

The cable used for building the samples is MQXF 105 (Table 3-1).

Before the heat treatment, the cable overlapping region was placed in a u-shaped copper (Cu) foil envelop (Figure 3.83-Figure 3.84). This region was then wrapped with thin steel strips.

These strips were then spot welded. The function of Cu foil is to prevent flowing out of solder and solder flux during the soldering procedure, while the steel strips withstand the winding tension.

The heat treatment is carried out with plenty of mica and glass-fibre insulation. The samples come out of the furnace covered with soot (Figure 3.85).

After the heat treatment, the following procedure was used (Figure 3.86):

- Two aluminium heaters are put in vertical position.
- Pouring Soldaflux K at room temperature with a syringe from the top.
- Warming up to 250 °C and melt Sn95Ag5 solder wire from the top by contact with the hot cable. Flux is added meanwhile.

The use of an aggressive flux was the unique case in which a deep penetration of the solder was achieved (Figure 3.87).
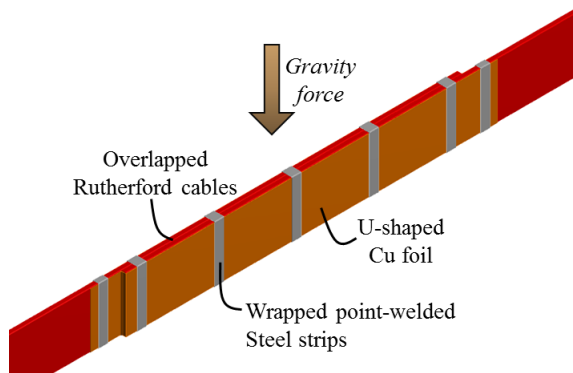
Figure 3.83 *Layout of the soldered splice.*

Figure 3.84 *Crimped sample before the heat treatment.*

Figure 3.85 *Samples after heat treatment.*
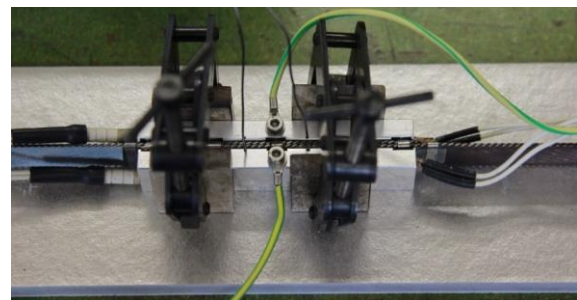
Figure 3.86 *Soldering layout: vertical position, aluminium heaters and temperature sensors*

.
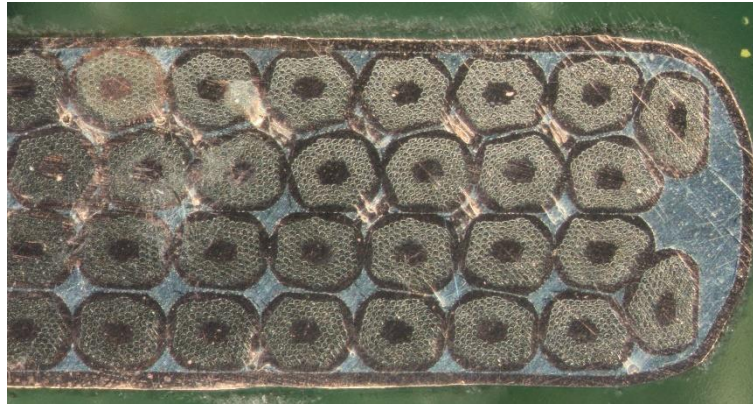
Figure 3.87 *Cross-section of a crimped soldered splice. The bottom of the u-foil is visible on the right.*

For the samples stack assembly, the same procedure as the previous test was used, except that the samples were impregnated with Araldite instead of Stycast, as the former is more fluid. The sample holder assembly is also unchanged.

Two stacks of six samples were produced for two experimental campaigns. The first one aimed at investigating the influence on the resistance of parameters such as the joint length and the presence of the steel core. The second experimental campaign aimed at investigating the reproducibility of the samples, thus all the samples are identical. The samples of the two stacks are reported in Table 3-6 and Table 3-7.

Table 3-6 *List of samples of the first experimental campaign on crimped soldered splices.*

	Name	Splice length [mm]	Steel core
1	L110S_a	110	Yes
2	L110S_b	110	Yes
3	L80S_a	80	Yes
4	L80S_b	80	Yes
5	L110_a	110	Removed
6	L110_b	110	Removed

Table 3-7 *List of samples of the second experimental campaign on crimped soldered splices.*

	Name	Splice length [mm]	Steel core
1	L110_1	110	Removed
2	L110_2	110	Removed
3	L110_3	110	Removed
4	L110_4	110	Removed
5	L110_5	110	Removed
6	L110_6	110	Removed

3.5.3 DC electrical tests in SULTAN

For the test layout, it is used the same system based on the Nb_3Sn lead extensions, HTS adapter and cryostat as in Section 3.4.1. The assessed resistance is reported in Figure 3.88-Figure 3.90.
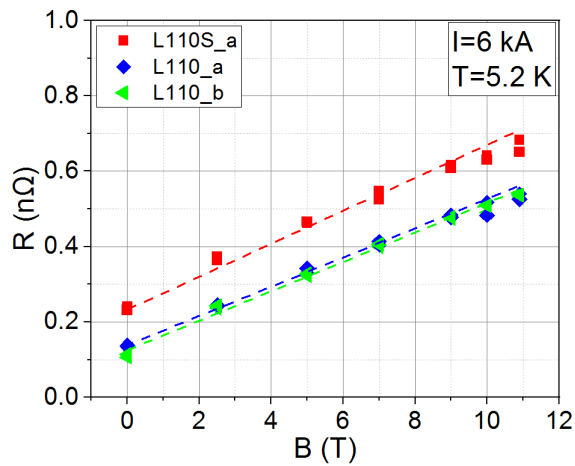
Figure 3.88 *First experimental campaign. Splice resistance with and without steel core.*
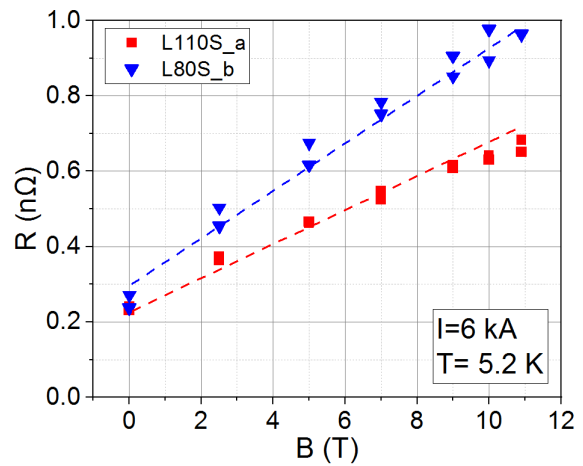
Figure 3.89 *First experimental campaign. Splice resistance as a function of the length.*
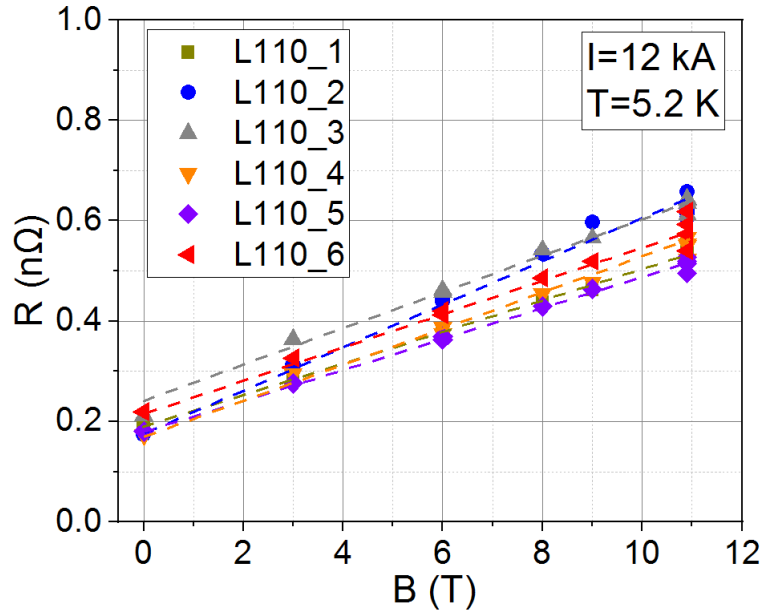
Figure 3.90 *Second experimental campaign. Resistance reproducibility of six samples without steel core.*

The results for the first stack are reported for I=6 kA (I/I_c=0.22 with self-field), the maximum current reached at B=10.9 T background field. The limiting factor was a damage of samples L110S_b and L80S_a because the resin did not cover the samples entirely. This caused the deformation of the strands, as it was identified in the disassembly after the test campaign (Figure 3.91). In the second stack of sample, the maximum current at maximum field was I=12 kA (I/I_c=0.54 with self-field), thus satisfying the 1/3 the requirement.

The main conclusions of these experiments are:

- **The steel core influence**. With reference to Figure 3.88, the ratio of resistance at 10.9 T between samples without and with steel core is 0.77. The latter showed resistance below 0.75 nΩ.

- **Joint length.** With reference to Figure 3.89, the ratio of resistance at 10.9 T between long and short samples is 0.70, while the ratio of length between short and long sample is 0.72. Therefore, the resistance and joint length are inversely proportional in the range studied.

- **Resistance as a function of current and magnetic field**. As Sn95Ag5 resistivity has a lower dependence on magnetic field than copper, the sensitivity of the splice resistance with respect to B is lower than in diffusion bonded joints. The dependence on B is as linear as the solder and copper magneto-resistivity. Moreover, the resistance does not change with the applied current. These two considerations suggest a balanced current distribution in the joint in the range of I and B studied.

- **Reproducibility**. It is studied in the second stack, for the samples showing the lowest resistance in the previous test campaign, i.e. the splice length is one twist pitch long and the steel core is removed. The samples show reproducibility in the range 0.5-0.6 nΩ at B=10.9 T, in agreement with the results obtained in the first stack for the same kind of samples.
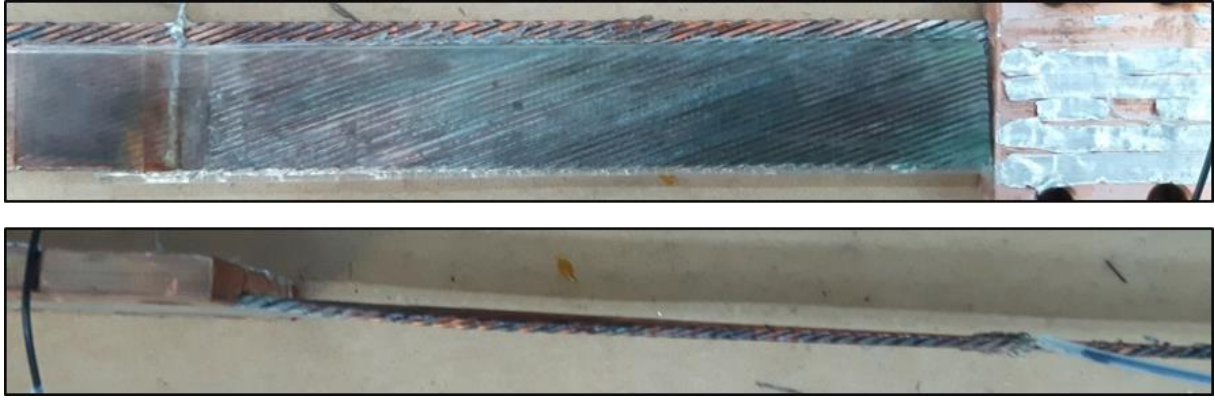
Figure 3.91 *Insufficient quantity of impregnating resin in sample L110S_b (top) and consequent deformation of its strands (bottom).*

3.5.4 Analysis and discussion

In the previous Section, it was demonstrated that the crimped soldered splices meet the resistance requirement. In the second test campaign on crimped soldered splices, it was highlighted $I/I_c< 0.54$ as operational limit. Nevertheless, it cannot be stated that this coincides with the operational limit of such a splice concept. This is rather a limitation given by the stack layout concept with araldite impregnation at ambient atmosphere. The first limitation of the stack layout concept consists in the praying hand joints connecting the samples in series (Figure 3.15). In such a configuration, the possible current paths have different length and thus inductance. During a current ramp-up, it happens that the current flows through the shortest paths, then several strands can saturate, leading to a voltage runaway. In the second experimental campaign on soldered splices, a voltage runaway started in sample L110_5 already at B=6 T and I=14.5 kA, during the current ramp-up at 200 A/s. The test was repeated with the minimum current ramp-up possible in SULTAN, i.e. 50 A/s. In this case it was possible to reach the target current I=16.5 kA without voltage runaways.

The second limitation of this test layout concept is in the impregnation. Araldite was used because of its low viscosity, which allowed to impregnate completely the samples of the second test campaign without inserting the samples into a vacuum chamber, but simply pouring the resin through a syringe. On the other hand, araldite has low mechanical strength and cracks easily at cryogenic temperature. A crack can occur due to the mechanical stresses and it suddenly releases enough energy to bring to a thermal and voltage runaway of the superconductor. If the run is performed again at higher current and thus higher mechanical solicitation, a new point of the resin may release energy through a crack. This phenomenon is familiar to accelerator magnets and is deemed to be one of the causes of the *training* of a magnet [3]. In the training, the current is ramped-up until the quench. The process is repeated several times. During this procedure, the magnet progressively experiences an improvement of its performance. Initially, the quench current can be far below the operating one. Through successive quenches, the quench current tends to the operating one. Tens of repetitive quenches may be needed to reach the magnet performance.

In the second experimental campaign in SULTAN on crimped soldered splices, this process was followed. The Table 3-8 reports successive runs at B=10.9 T and the progressive increase of the current at which a voltage runaway was observed. The same table shows also that the

72

runaway started at a different location for each run. The series of run was stopped due to lack of time, as thirty minutes of cool-down are needed after each thermal runaway.

To conclude, it can be stated that the ratio $I/I_c= 0.54$ is the operating limit for the developed crimped soldered splices with the limiting conditions of the experimental layout. In a crimped soldered splice between Nb$_3$Sn Rutherford cables in a dipole, such ratio is potentially higher.

Table 3-8 *Current value at the time of the voltage runaway in successive runs of the second experimental campaign.*

Run	B (T)	dI/dt (A/s)	I (kA) at voltage runaway	Location
1	10.9	50	12.4	L110_6
2	10.9	50	14.6	L110_5
3	10.9	50	13.9	L110_3
4	10.9	50	14.5	L110_6

A simplified electrical model was developed to estimate the joint resistance measured in Figure 3.90 and compare it to the measured one. The model assumptions (Figure 3.92):

- Steady-state.
- Uniform solder distribution, as observed in Figure 3.87.
- No steel core.
- Even current distribution, as suggested from results in Figure 3.90. This allows to reduce the computational domain to 4 strands.
- The strands are completely surrounded by the solder, i.e. there is no contact between strand and strand.
- The strand-to-strand resistance R_c is assumed uniform since on average there is contact for half twist pitch between strands 1-3, 1-4, 2-3 and 2-4.
- This resistance R_c is assumed to depend only on the solder resistivity. In particular, $R_c = \rho_s \cdot \frac{1}{L_j/2}$, being ρs the solder resistivity of Sn95Ag5 [90], Lj the joint length (set to one twist pitch). The parameter L_j is divided by two because the strands are next to each other two by two for half twist pitch and thus half joint length.

The voltage drop depends on the total resistance and cable current, $\Delta V = R_{tot} \cdot I_{tot}$, but also $\Delta V = R_c(I_1 + I_2 + I_3)$, i.e. the voltage drop between "strand 1" and "strand 4" in Figure 3.92. In this figure, the current circuits are represented in red. The model implements the first and second Kirchhoff's laws to compute the currents and so R_{tot}. The model inputs and outputs are summarized in Table 3-9. Estimated and measured results are in good agreement for B=0 T, while the model predicts $R(B$=10.9 T)=0.94 nΩ instead of the 0.5-0.6 nΩ, measured valued. It is reasonable to get overestimated values from this simplified model, as this one considers only the resistive contribution of the solder, thus neglecting the parallel resistance given by the direct contact between strands. In this sense, this model provides the maximum resistance of a soldered joint based on Sn95Ag5, for a certain overlap length, and constitutes a conservative approach for the joint design.
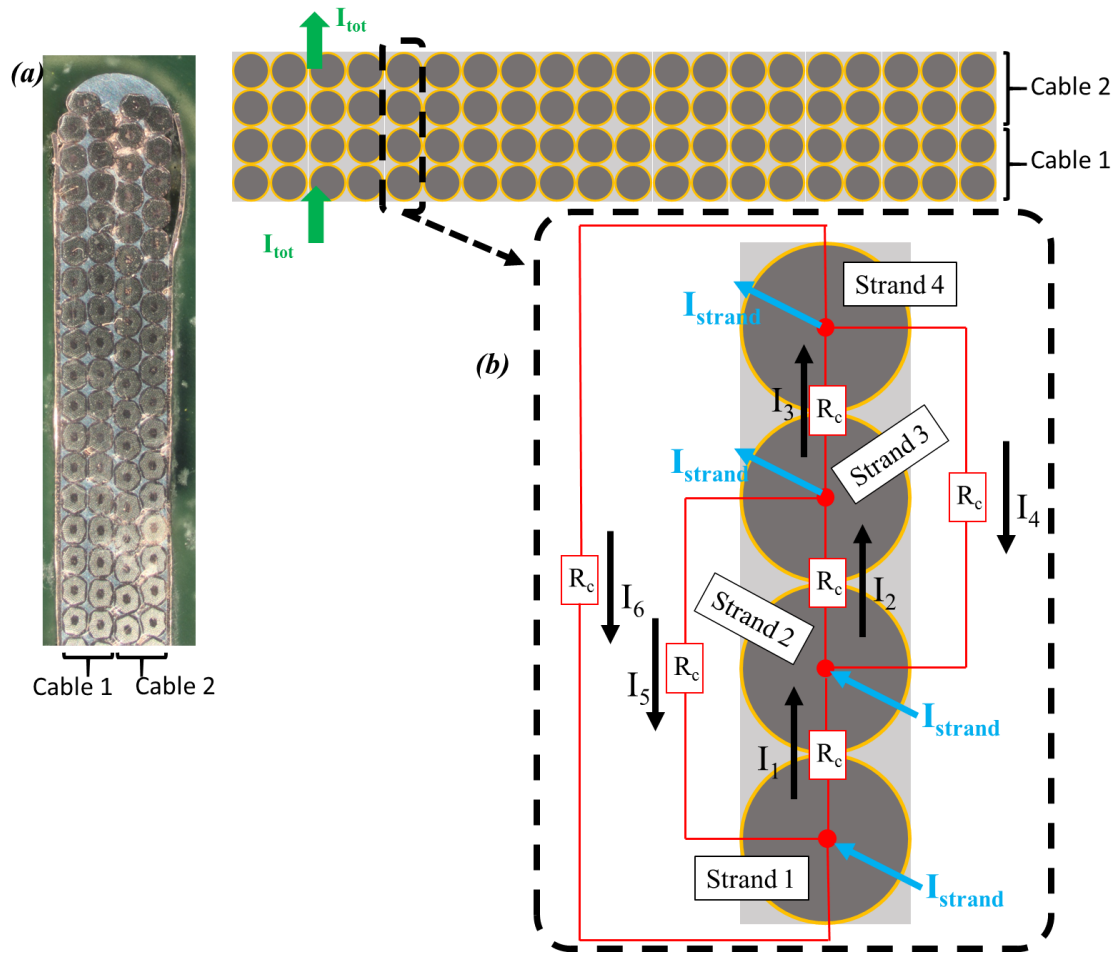
Figure 3.92 *(a) soldered splice cross-section; (b) simplified electrical model for estimating the joint resistance of a soldered joint without steel core. The circuit is in red and R_s is the strand-to-strand resistance.*

Table 3-9 *Soldered joint electrical model parameters & results.*

	Parameters	*B*=0 T	*B*=10.9 T
INPUT	ρ_s [nΩ·m]	1.05 [90]	4.3 [90]
	I_{tot} [A]	12000	
	$I_{strand1}$ [A]	300	
	$I_{strand2}$ [A]	300	
	$I_{strand3}$ [A]	-300	
	$I_{strand4}$ [A]	-300	
OUTPUT	I_1 [A]	0	
	I_2 [A]	150	
	I_3 [A]	0	
	I_4 [A]	-150	
	I_5 [A]	-150	
	I_6 [A]	-150	
	R_{tot} [nΩ]	0.24	0.98

3.5.5 Integration into a dipole: racetrack coil study

The sequence of figures in this section shows schematically the assembly of a crimped soldered splice into the head of a pancake-wound Racetrack magnet. The winding table and other structural elements are not shown in figure.

- The high field (HF) pancake is first wound (Figure 3.93).
- An inner spacer made out of ceramic, for instance Macor, is put in place (Figure 3.94). The crimped cables are going to be wound around it. The ceramic material will limit the heat propagation during soldering.
- The cable sections of the high and low field (LF) cables are put in overlap position in straight geometry (Figure 3.95).
- The thin Cu foil is wrapped around the cables (Figure 3.96) and steel strips are point-welded (Figure 3.97).
- The crimped cables are pulled around the inner spacer (Figure 3.98).
- Two outer ceramic spacers are put on the concave side of the crimped cables (Figure 3.99) and the LF pancake is wound (Figure 3.100).
- The coil undergoes the heat treatment.
- One of the outer spacers is removed (Figure 3.101) and substituted by an aluminium plate to heat up the joint area during soldering (Figure 3.102).
- The soldering procedure is followed. After that, the aluminium plate can be substituted with a filler.
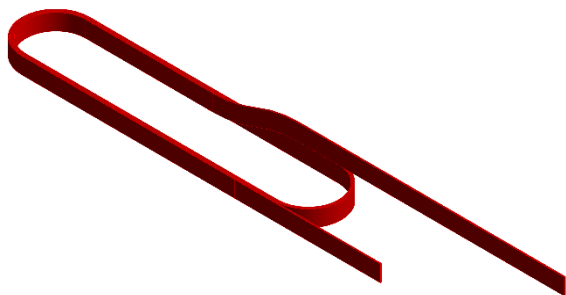
Figure 3.93 *HF cable of the racetrack coil.*
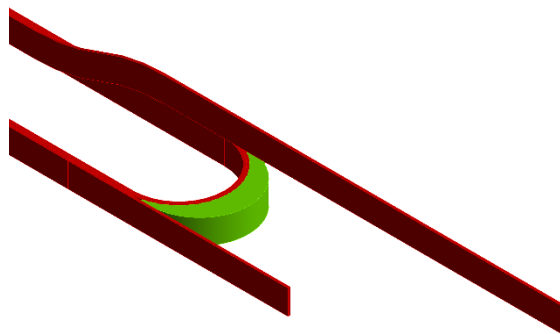
Figure 3.94 *Spacer between the HF cable and the future joint.*
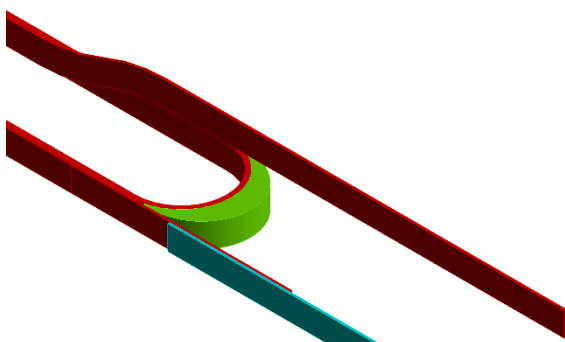
Figure 3.95 *Overlap between HF and LF cable.*
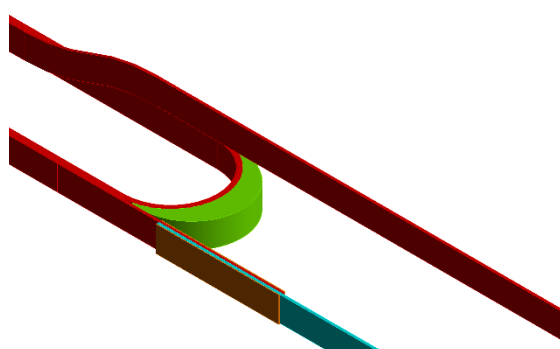
Figure 3.96 *Wrapping of the copper foil.*
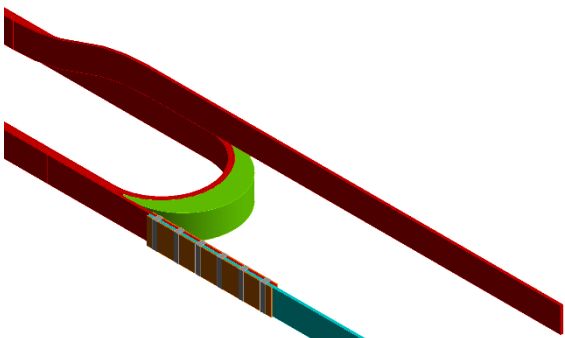
Figure 3.97 *Point welded steel strips.*
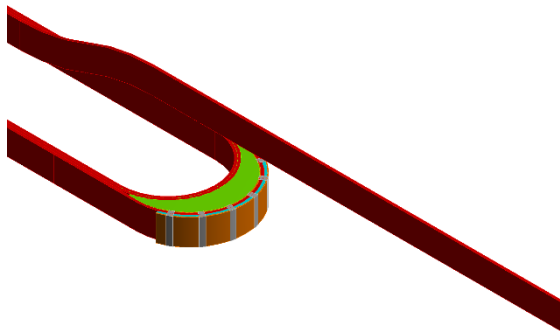
Figure 3.98 *Winding of the crimped cables.*
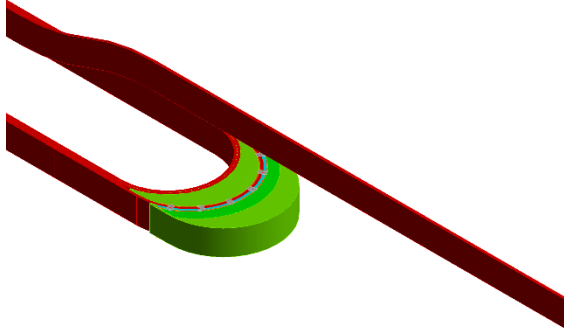
Figure 3.99 *Spacers between the future joint and the LF cable.*
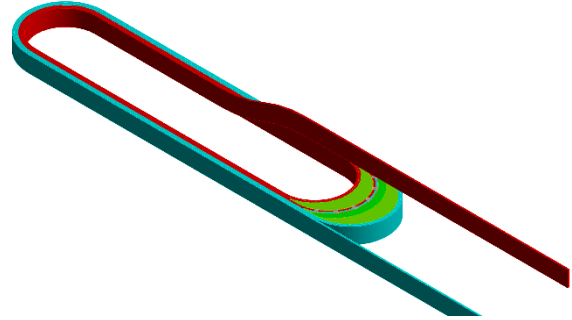
Figure 3.100 *Winding of the LF pancake.*
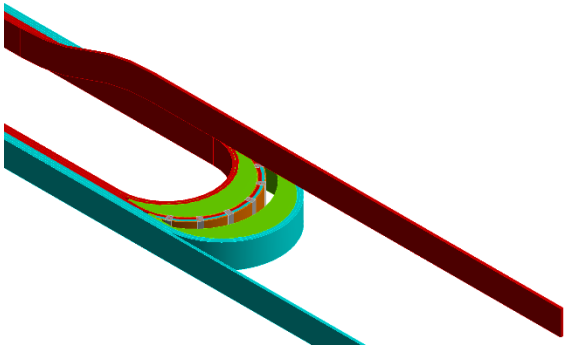
Figure 3.101 *Removal of one external spacer after heat treatment.*
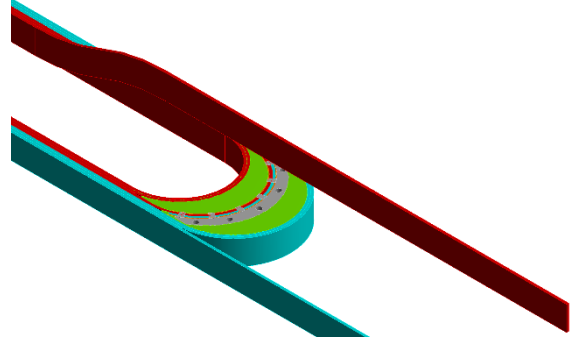
Figure 3.102 *Insertion of the aluminium plate for heating the joint region.*

3.5.6 Summary and conclusions

A splicing procedure was proposed. This takes into account the limited handling possibility of the cable after heat treatment. It was demonstrated that the soldered splice is a solution that meets the resistance requirement. The preparation of the splice starts before heat treatment, by embedding the joint with a copper u-foil that prevents the solder from spreading out and by crimping the two cables to join with thin steel strips that withstand the winding tension. After the cable reaction, the soldering procedure is applied. The best result was R=0.58 nΩ at B=10.9 T, T=5 K and I/I_c=0.54.

The arranged experimental campaigns studied the influence of the splice length and the steel core on the splice resistance. The reproducibility of the proposed splicing technique was also experimentally illustrated and demonstrated.

The R&D was carried out on straight samples, although the bent geometry is more interesting for an internal splice in a dipole. Nevertheless, for a soldered splice, the bent geometry just influences the shape of fillers, spacers and heaters. There is no particular parameter of this technique depending on a straight rather than a bent geometry, as opposed to diffusion-bonded splices, in which the geometry influences the pressure distribution of the clamp.

As for the diffusion-bonded joints, the mechanical strength of the joint was not part of the experimental characterization. This is recommended for the future.

4.   Inter-layer joint for a React&Wind fusion magnet

4.1   Joint requirements and location

In the pre-Conceptual Design Phase of the magnet system of the European DEMO Tokamak, which lasted from 2014 to 2020, four different TF design concepts based on Nb_3Sn and one on HTS conductors were realised [49]. This Chapter focuses on the Nb_3Sn TF design variant proposed by SPC, the only one based on the RW technology and one of the two concepts selected for the Conceptual Design Phase [91], which is foreseen to last until 2027.

During the pre-Conceptual Design Phase, each design variant had to satisfy the requirements given by a common baseline updated every 2-3 years. This Chapter takes as reference the 2015 DEMO baseline [92], as the R&D was carried out with the conductor prototype designed and manufactured by SPC according to that one. Nevertheless, the joint design principles are applicable to every RW conductor developed by SPC, including the latest 2018 DEMO baseline [93].

The DEMO Tokamak of the 2015 baseline has 18 TF coils. The TF coil designed by SPC [48] is wound in 12 layers consisting of CICC conductor type. Each layer has a different conductor grade for cable and jacket. The superconducting cables have rectangular shape with relatively low radial build thickness, such that they can be bent after heat treatment fulfilling the requirement $|\varepsilon_B| \leq 0.1$ %, introduced in Section 2.3. The innermost layer is exposed to the highest magnetic field intensity and has the largest superconductor cross-section, while the outermost layer experiences the lowest field intensity and can thus have the minimum superconductor quantity. For the jacket, the steel quantity increases from the innermost to the outermost layer, as the forces push the TF towards the outermost layer. The operating current is I_{op}=63.3 kA and the peak field is B_{peak}=12.23 T, on which the design of the superconducting cable of the innermost layer is based.

The layers are electrically connected in series through inter-layer joints. Therefore, there exist 11 inter-layer joints and two terminal joints (Figure 4.1). The layers are cooled in parallel by liquid helium as in Figure 4.2, in which the helium inlets and outlets are located at the joints. The joint exposed to the highest field is located at the helium inlet, where the mass flow rate splits between the first and second layer at 4.5 K.
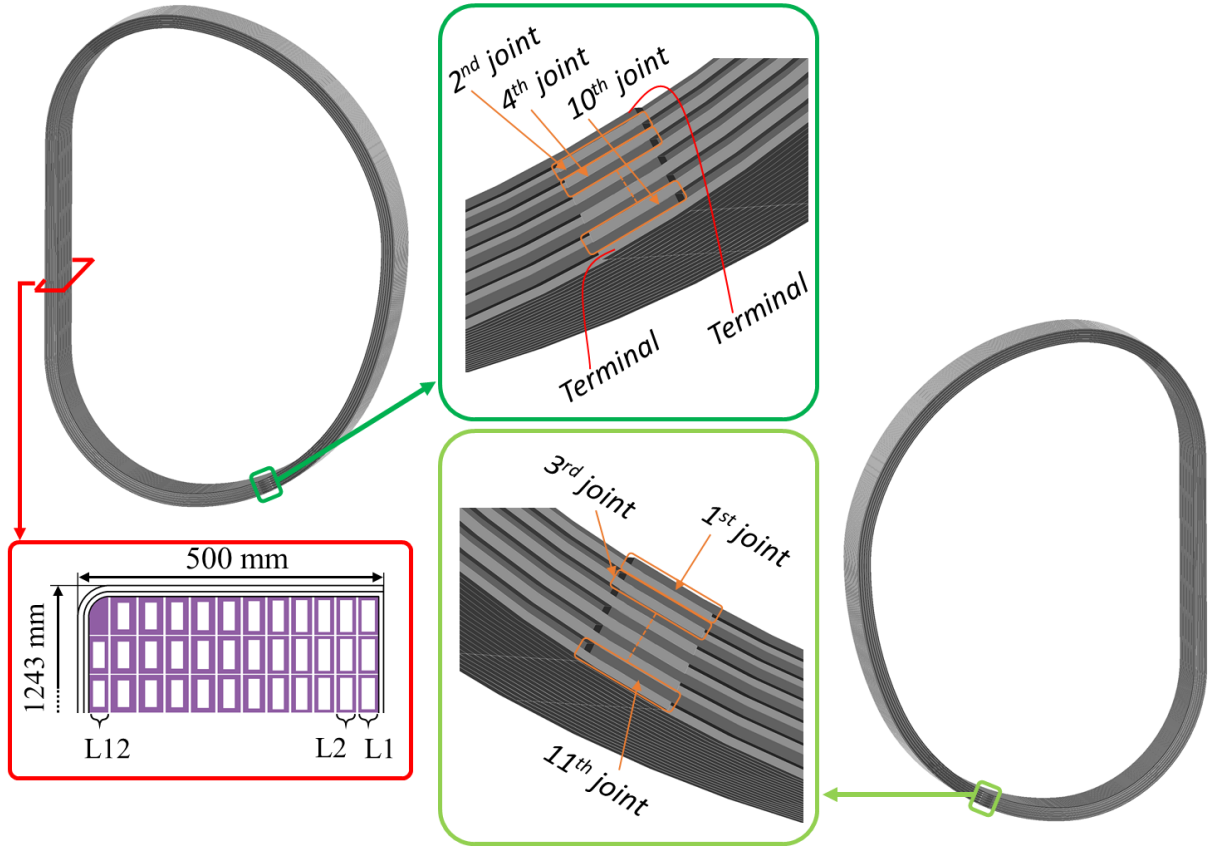
Figure 4.1 *Joint location in the RW layer wound TF for DEMO proposed by SPC.*
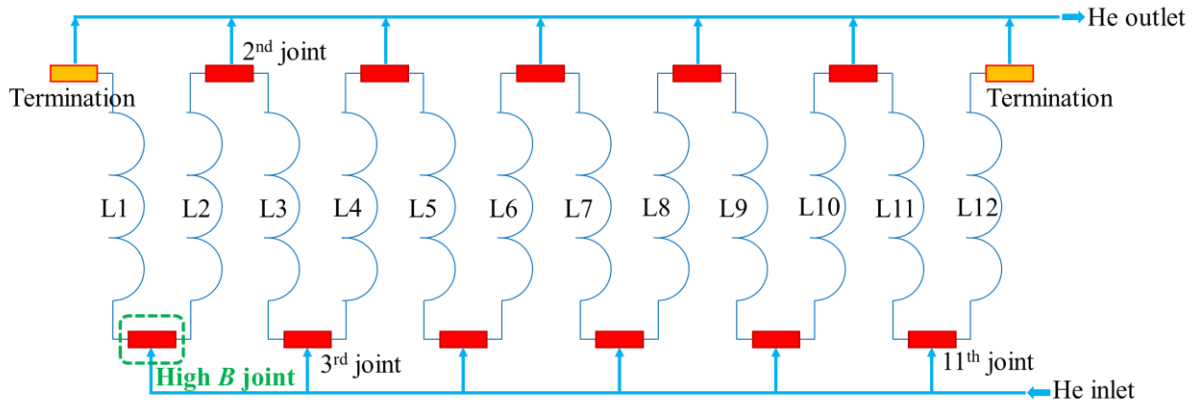
Figure 4.2 *Cooling scheme for the layer-wound TF proposed by SPC. The layers are numbered from the innermost to the outermost layer.*

Among the 11 inter-layer joints, this Chapter considers the one between the highest and the second highest cable grade, i.e. between the innermost and second layer, for the following reasons:

- This electrical connection is exposed to the highest magnetic field among all the joints, namely $B \approx 8\,T$. Therefore, it is the one with the highest copper magneto-resistivity, which influences non-negligibly the overall joint resistance, as already shown in Chapter 3.
- The joint experiences the highest Lorentz force among the other joints in the TF.

The computation of the maximum allowable electrical resistance is based on the *temperature margin*. This is defined in equation (4. 1) as the difference between the *current sharing temperature*, T_{cs}, and the temperature of the conductor at a given location. The current sharing temperature is the one at which the local critical current of the conductor is equal to the operating current, i.e. $I_c=I_{op}$, at the local magnetic field and temperature.

$$\Delta T_{margin} = T_{cs} - T \qquad (4. 1)$$

The minimum ΔT_{margin} for the TF is set in the requirements to $\Delta T_{margin,min}$=1.5 K [94]. This must be fulfilled in each location of the magnet. The innermost layer of a TF is the most exposed to the nuclear heat load coming from the neutrons of the nuclear fusion reactions taking place in the plasma. For the first layer of the TF, it amounts in total to 36.1 W, according to the 2015 DEMO baseline. To fulfill the $\Delta T_{margin,min}$ requirement in the first layer of the TF, the maximum Ohmic power that can be produced by the joint is 2 W, corresponding to a helium temperature increase of 0.03 K at 6 bar, for the given helium mass-flow-rate and cooling channel. Assuming that the power of the joint is equally transferred to the first and second layer because the helium mass flow rate equally splits at the inlet (Figure 4.2), the maximum allowable joint power is 4 W, corresponding to a joint resistance $R_{J,max}$ =1 nΩ at the joint operating field and current.

The target joint resistance is equal to the one stated for the splices of WR dipoles in Section 3.1, even though there is a factor 40 of difference in the power dissipated by the two joint types because of the different operating current. Despite the higher operating current of the TF joint, its $R_{J,max}$ is not required to be lower than the one of the WR dipoles because of the active and direct helium cooling of the CICC, more effective than the bath and indirect cooling of the resin-impregnated dipole magnets of HE-LHC/FCC.

With respect to the D-perimeter of the TF, the inter-layer joints are located where the displacements are foreseen to be the minimum ones, so that the stresses of these delicate components can be minimized. Such displacements come from the interaction of the TF current with the magnetic field generated by the TFs, CS, PFs and plasma current. In particular, the inter-layer joints are located on the two side surfaces of the TF, i.e. at the beginning and ending of each layer, as shown in Figure 4.1.

In the Wind&React dipole magnets illustrated in Chapter 3, it was possible to identify splicing techniques taking place before, during or after the heat treatment. In React&Wind magnets, the joint formation takes always place after the heat treatment of the cable. In this thesis, the inter-layer joints are considered to be assembled during the winding of the coil. In particular, the innermost layer is wound, the joint is fabricated between this layer and the cable that will constitute the second layer, the second layer is successively wound, and so on with the successive joints and layers. The shaking hands joint layout (introduced in Figure 2.5) may be considered the most convenient choice, as the layers are wound on each other. With respect to a praying hands joint, the required space of the former is much lower (see Figure 4.3). Moreover, in a layer-wound coil, the praying hands configuration is more convenient if all the layers have already been wound, as the praying hands joint protrudes out of the coil. In this thesis, instead, the assembly of each joint is considered to take place after the winding of the corresponding layer.
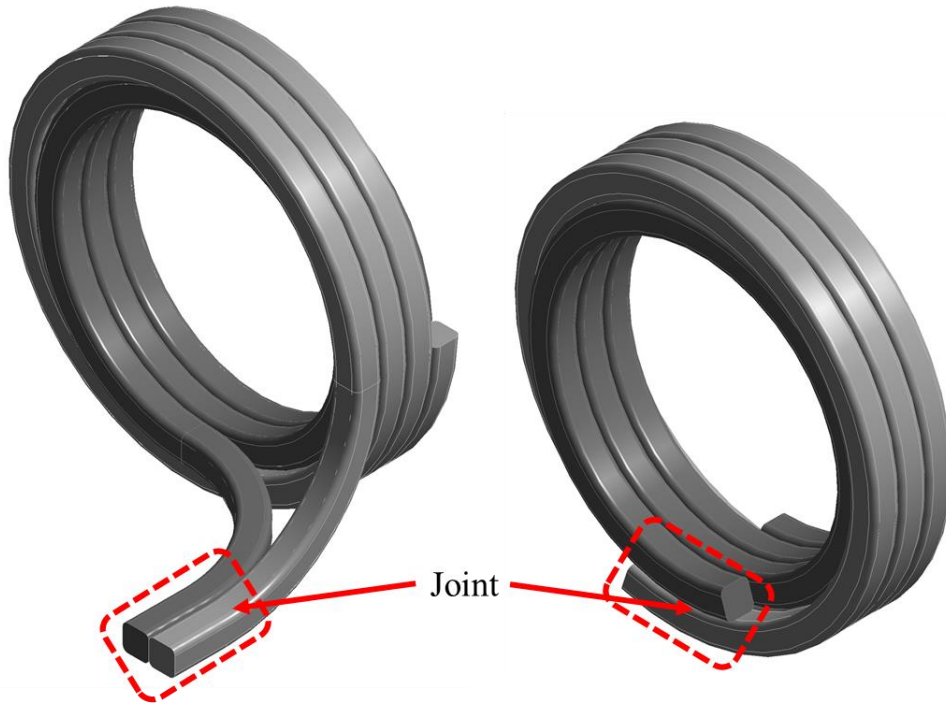
Figure 4.3 *Sketch of a praying hands (left) and shaking hands (right) joint in a layer-wound coil.*

The requirements and characteristics of an internal joint between CICC cables in a RW Nb$_3$Sn magnet for the European DEMO Tokamak are summarized as follows:

- The maximum allowed splice resistance is $R_{J,max} = 1\ n\Omega$ at *T*=4.5-5 K, *B*≈8 T, I_{op}=63.3 kA.
- The joint manufacture procedure must be compatible with the in-line winding procedure and must thus be applicable in situ.
- The volume occupied by the splice must be minimized.
- The joint must withstand the mechanical load.
- The joint is in overlap geometry.
- The joint length is about one twist pitch length.
- The joint must be inspectable for the quality assurance.

4.2 The React&Wind conductor designed by SPC

The conductor prototype designed by SPC for the 2015 DEMO baseline is meant for the first layer of the TF magnet. It comprises the Nb$_3$Sn superconducting cable, the *segregated stabilizer* and the stainless steel jacket. The conductor is shown in Figure 4.4 and is called RW2 because it is the second React&Wind prototype designed by SPC for the TF of DEMO.

The superconducting cable has a rectangular shape with a 3.2 aspect ratio to make winding possible perpendicular to the wide side of the cable. It is cabled in two stages. In the first one, 18 Nb$_3$Sn precursor strands and 1 copper wire are twisted together (twist pitch 105 mm) to form the sub-cable. The strands are chromium plated to reduce AC losses and avoid sintering during the cable heat treatment reaction. In the second stage, 13 sub-cables are twisted to form the cable (pitch 390 mm), whose characteristics are summarized in Table 4-1.
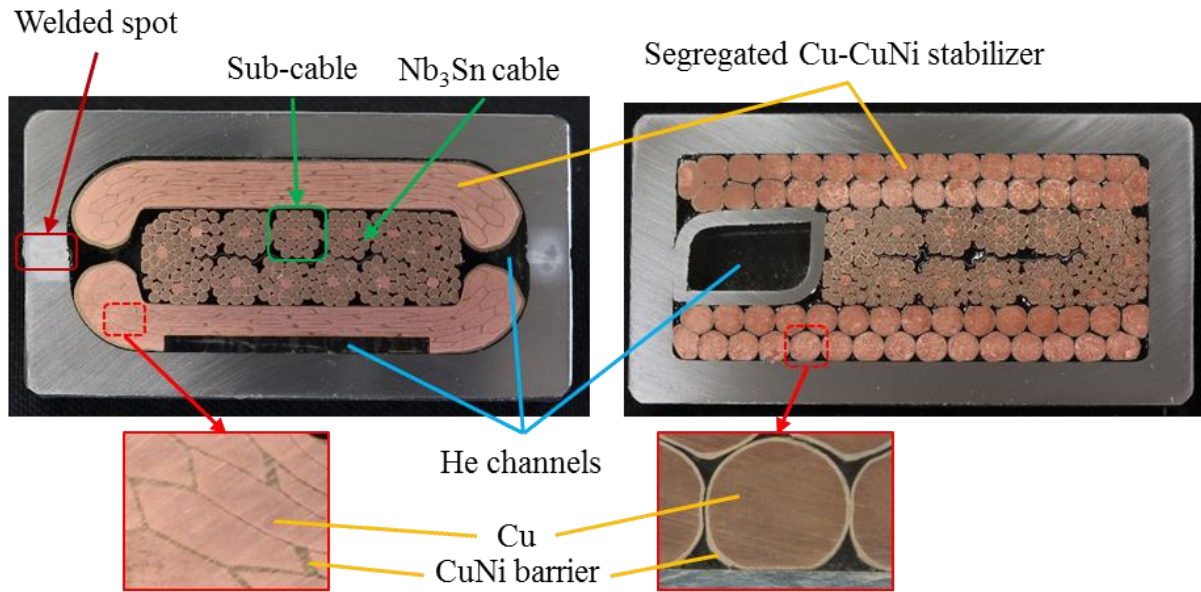
Figure 4.4 *RW2 conductor prototype with segregated stabilizer in monolithic shape (left) and Rutherford cable form (right).*

Table 4-1 *Characteristics of the Nb_3Sn cable of the RW2 conductor prototype.*

Parameter	Value
Operating current	63.3 kA
Peak operating field	12.23 T
Strand diameter	1.2 mm
Cu to non-Cu ratio	1
Sub-cable scheme	1 Cu + 6 Nb_3Sn + 12 Nb_3Sn
Number of sub-cables	13
1st stage twist pitch (strand)	105 mm
2nd stage twist pitch (sub-cable)	390 mm
Cable thickness	10.9 mm
Cable width	35.2 mm
Void fraction	23 %
Central steel strip	25 mm x 0.2 mm

The segregated stabilizer consists of 90% of Cu and 10% of Cu-Ni and is meant for the quench protection of the superconducting cable. If a thermal runaway accidentally occurred in the superconducting magnet, the current would flow through the copper part of the segregated stabilizer, less resistive than Nb_3Sn in normal conducting state. In this way, the heat dissipation during the quench is reduced and the hot spot temperature, i.e. the maximum temperature reached by the magnet during the quench transient, is kept under the safety limits. The Cu-Ni

distributed barrier of the segregated stabilizer is meant to reduce its AC losses. In fact, while the segregated stabilizer must have a high electrical conductivity in the longitudinal direction, i.e. parallel to the cable, it must be electrically resistive in the perpendicular direction to minimize eddy currents generated during field transients.

A first version of the segregated stabilizer had a monolithic shape, which was used in the conductor of the joint prototype described in the following sections. The final version of the segregated stabilizer has the shape of a Rutherford cable, which adds an additional resistive barrier to the formation of eddy currents, namely the contact resistance between the wires of the Rutherford cable. This allows to dramatically decrease the AC losses with respect to the monolithic segregated stabilizer, as reported in [95].

The steel jacket is formed by two steel shells, which are laser welded longitudinally during the assembly of the conductor. In RW CICC conductors, it is possible to apply a pre-compression on the superconductor because the jacket is assembled after the heat treatment reaction. This operation compacts the Nb$_3$Sn strands, thus minimizing unwished movements of the wires during operation due to the electromechanical forces. In fact, the cyclic Lorentz force acting in a Tokamak due to its pulsed operation principle can cause strand micro-bending in Nb$_3$Sn conductors based on CICC with void fraction. This was recognized to be the cause of filament breakages in WR CICC conductors and the subsequent drop of their performance [96]. The pre-compression of a RW CICC conductor allows to eliminate this degradation, as it was demonstrated in [42]. The pre-compression is instead not effective in a WR CICC conductor, as the superconducting cable is in the jacket already before the cable heat treatment. In fact, the pre-compression would be lost at heat treatment temperature through the annealing of copper.

In an industrial production process, the pre-compression can be reached by producing a jacket with higher thickness, while keeping constant the overall height of the jacket itself. In the RW2 conductor prototype, the pre-compression is applied by interleaving a steel foil between the superconducting cable and the segregated stabilizer. Without this foil, the superconducting cable would geometrically fit in the conductor, i.e. the pressure would be null. The thickness of this foil is chosen such that it is equal to the displacement of the superconducting cable induced by the Lorentz force on the uncompressed superconductor. In this way, the movements of the strands in operation are prevented. The Lorentz force per cable length is $\lambda = B_{peak} \cdot I_{op} = 774 \, kN/m$ at the peak field, mostly directed normal to the wide side of the superconducting cable. The relation between this force per unit length and the displacement can be assessed by modelling the superconducting cable as a full body. In particular, one considers:

- The balance of forces per unit length of cable f along the thickness direction y (Figure 4.5), in which the terms appearing are the distributed linear body force λ [N/m] and geometrical parameters. The boundary condition is that the force is null at the upper

surface of the cable, i.e. $f(s){=}0$, as no force acts on it. By integration, the expression of the force per unit length is $f(y) = \lambda(y/s - 1)$, where s [m] is the cable thickness.

- The relation between force per unit length and pressure. It is a function of y, in particular $\sigma_y(y) = f(y)/w$, where w is the cable width.
- The relation between pressure and displacement in 1D. This one is $\sigma_y = E_y(u_y) \cdot du_y/dy$, where E_y [Pa] is the Young's Modulus and u_y [m] the displacement in the thickness direction.

In particular, E_y as a function of the displacement has the physical meaning that, if the cable is compacted, its void fraction decreases and the cable becomes stiffer, i.e. E_y increases. Vice versa, if the cable relaxes along y, it softens and E_y decreases.
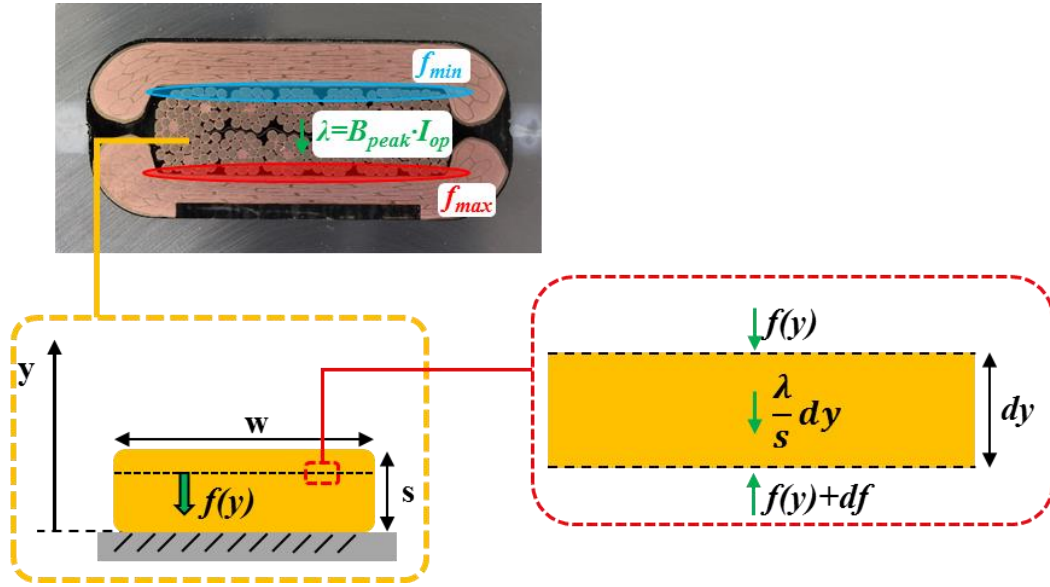
Figure 4.5 *Equilibrium of the superconducting cable of the RW2 conductor.*

Combining the relations expressing $f(y)$ and $\sigma_y(y)$, one obtains the differential relation $E_y(u_y) \cdot du_y = \frac{\lambda}{w}\left(\frac{y}{s} - 1\right) dy$. This expression can be integrated with the boundary condition $u_y(0) = 0$, whose physical meaning is that the segregated stabilizer is much stiffer than the superconducting cable, thus neglecting the movement of the lower surface of the cable with respect to the re-compaction of the superconducting cable. This is reasonable, as the RW2 cable has a void fraction, whereas the segregated stabilizer is monolithic. The expression obtained by integration is reported in Equation (4. 2).

$$u_y(y) = \frac{\lambda}{\overline{E}_y \cdot w}\left(\frac{y^2}{2s} - y\right) \qquad (4.2)$$

The displacement is always negative across the thickness because the cable is compressed by the body Lorentz force. The minimum displacement is $u_y(s) = -\frac{1}{2}\frac{\lambda \cdot s}{\overline{E}_y \cdot w}$, equal, in absolute value, to the thickness of the steel foil to design. As $\overline{E}_y$ is not known, an experiment was carried out, in which the reacted Nb$_3$Sn cable is pressed by an external force. When the force is applied on the upper surface of the cable, the relation between the applied external load and the displacement is like in Equation (4. 3).

$$u_{y,E}(y) = -\frac{\lambda_E}{\bar{E}_y \cdot w}y \qquad\qquad \textbf{(4. 3)}$$

where λ_E [N/m] is the force per unit length applied on the upper surface of the superconducting cable. The minimum displacement is then $u_{y,E}(s) = -\frac{\lambda_E \cdot s}{\bar{E}_y \cdot w}$. By setting $u_y(s) = u_{y,E}(s)$, one obtains the value λ_E to apply in the experiment to have the same displacement that would be induced by the Lorentz force in an uncompressed cable, as reported in Equation (4. 4). Once λ_E is applied in the experiment, $u_{y,E}(s)$ is measured and so the thickness of the steel foil for the pre-compression is known.

$$\lambda_E = \frac{\lambda}{2} = 387 \; kN/m \qquad\qquad \textbf{(4. 4)}$$

The experimental set-up is shown in Figure 4.6. In this test, the load is applied along 400 mm of the superconductor length through a series of steel screws pushing an intermediate plate put between screws and superconducting cable. The micrometer measures the displacement of this intermediate steel plate in several points and at several load steps, up to 387 kN/m. The cable thickness at null load is 10.9 mm, while at 387 kN/m is 10.4 mm, by averaging the several points of measurement. To obtain the 10.4 mm pre-compressed thickness value, two 0.25 mm thick steel foils, one for each side, were interleaved between the jacket and the segregated stabilizer (Figure 4.7) during the assembly of RW2.
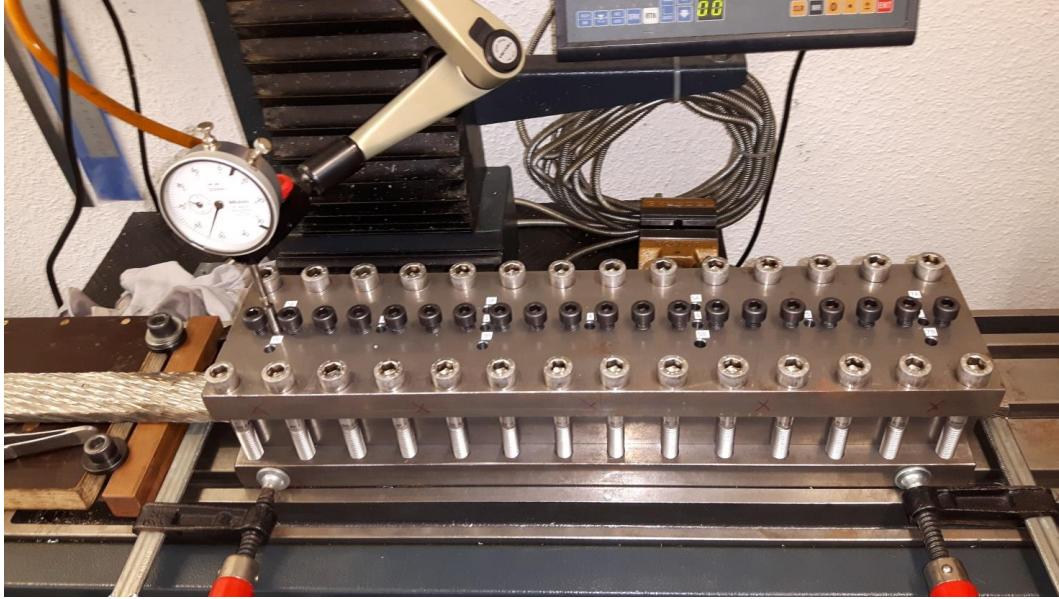
Figure 4.6 *Experimental set-up to determine the load displacement curve of the superconductor of RW2.*

Figure 4.7 *Position of the pre-compression foil in the RW2 conductor.*

4.3 Splicing techniques for React&Wind magnets

In Section 3.2, the splicing techniques identified to build an internal joint in WR dipole magnets were classified based on their applicability before, during or after the heat treatment of the superconducting cable. In a RW magnet, the joint forms after the reaction of Nb_3Sn. In particular, the technique and procedure must be compatible with the in-line winding of the coil, as stated in Section 4.1.

In Section 2.5, several joint types for Nb_3Sn cables were mentioned:

- The twin-box joint (Figure 2.6), employed in several magnets of ITER.
- The diffusion-bonded butt joint of the CS of JT60-SA (Figure 2.7).
- The coaxial joint, installed at the terminal of the CS modules of ITER (Figure 2.8).
- The sintered joint, employed in the inter pancake connections of CS of ITER (Figure 2.8).

The twin-box is a concept which would not be suitable for RW magnets, if one applied the same assembly procedure as for WR magnets. In fact, this concept is based on the considerable compaction and consequent deformation of the conductor cross-section, as shown in Figure 2.6. This would not be withstood by an already reacted cable. However, Nb_3Sn cables with rectangular cross-section like the one presented in Section 4.2 are much more compact than the round CICC of ITER. For this reason, they might not need such a huge compaction. Moreover, the twin-box layout is very bulky, which makes this concept more convenient for joints protruding out of the winding pack. In addition to that, the electrical requirement stated in Section 4.1 would not be fulfilled, as the measured resistance of the twin-box joint exceeds 1 nΩ with non-null background field [52].

The diffusion-bonded butt joint could be implemented in a RW magnet. As a matter of fact, for the joint of the CS of JT60-SA, the diffusion-bonding procedure is applied to already reacted cables. Nevertheless, the butt-type layout is characterized by a relatively small contact area between the two conductor sections. This resulted in a measured resistance of joint prototypes of about 2 nΩ at 2 T [59], thus higher than the requirements mentioned in Section 4.1.

The ITER-like coaxial joint, which has the topology of a bridge joint, could be implemented in a RW magnet. Nevertheless, the tests in SULTAN of ITER prototypes proved an electrical resistance higher than the requirement stated in Section 4.1.

The sintered joint cannot be implemented in a RW magnet. It requires the trimming of half of the petals or sub-cables and the handling of the two cables to bond for reconstructing the geometry. This is possible only if the cable is not reacted, yet. Moreover, by halving the number of strand of each cable section, the I_c of the cable is also halved, thus making this concept not applicable either to WR graded magnets with joints operating at high field.

A pressed joint with squeezed indium that electrically connects the surfaces to mate just requires the physical contact of involved parts. Neither heating nor chemical agents are needed for its manufacture. Before the work for this thesis started, SPC assembled a prototype based on this concept (Figure 4.8). This joint is of the bridge type. Each of the two bridges is constituted by Nb_3Sn soldered on a Cu plate. The bridges have the function of transferring current between the superconducting cables to link. The interface of connection between cable and bridge is constituted by indium wires. As indium is very ductile, it increases the contact surface of bridge and cable when it is squeezed because it fills the asperities of the mated surfaces. Moreover, it has a low electrical resistivity, about 0.1 nΩ·m at 4.2 K [97]. Despite its simple assembly, the electrical test of such joint resulted not only in a high resistance, namely 6 nΩ at 0 T and 13 nΩ at 8 T, but also in a noticeable degradation of the electrical resistance after mechanical load cycles [98], thus proving that this concept does not satisfy the requirements. The wavy surfaces of the superconducting cable and superconducting bridges given by the round geometry of the strands prevent a good contact between the superconductor and the indium wire, despite the pressure applied to squeeze the indium wires. Joints of comparable size and based on indium are employed in almost every termination of the SULTAN sample, in order to ensure its disassembly non-destructively. In these joints, the indium is squeezed between two flat copper surfaces, thus the contact is better than in the prototype with superconducting bridges. In such termination joints, the resistance at null magnetic field is on average around 0.5 and 1 nΩ.
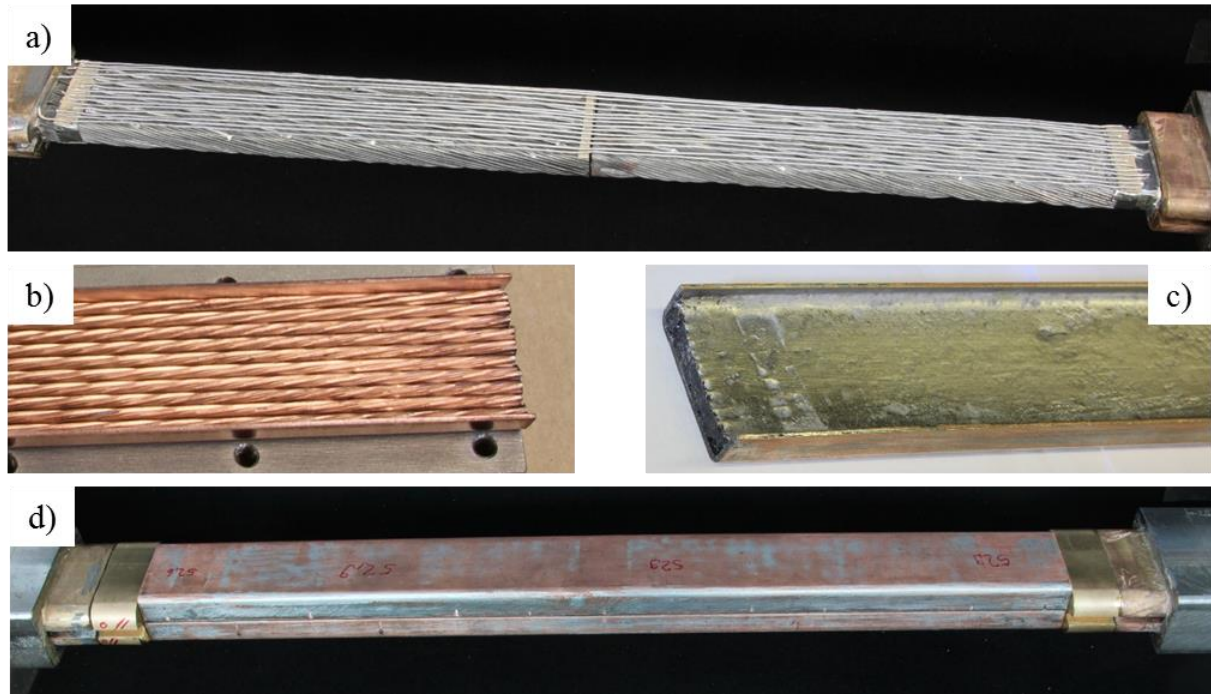
Figure 4.8 *Indium wires on the superconducting cables before squeezing (a); Nb₃Sn on the copper plate of the bridge before (b) and after (c) soldering; superconducting bridges forming the joint with the superconducting cables (d).*

Soldering is a well-known option in joints for superconducting magnets. The low accessibility to the mated surfaces of WR dipole magnets described in Section 3.5 is not an issue in this case, as the joint is formed during the winding of the RW coil. Therefore, it is possible to interleave solder foils between the surfaces to join and heat locally. There is the risk that the molten solder is dispersed per capillarity through the interstices among the strands, thus causing insufficient bonding between the surfaces of the two cables. This potential issue can be solved by first copper-coating the surfaces of the cables by thermal spraying and machining them flat, thus creating a monolithic layer. The soldering procedure could then take place between the two flat layers of the cables. A similar concept can be seen in the ITER lap twin-box joint introduced in Section 2.5. There, the superconducting cable is round and not flat. Therefore, there is the additional issue of joining round surfaces. With reference to Figure 2.6c-d, this is managed by shaping curved a monolithic copper termination pressed against the non-reacted Nb₃Sn cable. The joint between the two conductors takes place at the flat side of the copper termination, by soldering. Possible corrosion issues of copper due to the residues of the solder flux are in common with the soldered splices for WR dipole magnets described in Section 3.5.1. However, during the operation of the magnet, there is no oxygen, fundamental for the corrosion-reaction to take place.

The diffusion-bonding technique was introduced as a technique suitable for building a splice during the heat treatment of a WR dipole magnet. In a RW coil, this technique is applicable after the cable heat treatment by applying pressure and heating locally the surfaces to joint. The requirement for the pressure is that it is as uniform as possible on the mated surfaces. The clamp applying pressure must be completely removable after the joint formation. The integration of the clamp in the winding pack is not a requirement, contrary to the diffusion-bonding clamp illustrated in Section 3.4. In fact, in WR dipole magnets, some components of

the clamp constitute the winding pole because the joint formation takes place after winding and, as the clamp is embedded in the winding pack, it cannot be removed after the Nb$_3$Sn reaction.

This Chapter focuses on the development of a diffusion-bonded joint for Nb$_3$Sn RW conductors of fusion magnets. With respect to the soldering option, diffusion-bonding was selected because Cu to Cu diffusion-bonding has in general better mechanical properties than the bond between solder and cable. Moreover, it does not involve materials different from the ones that already constitute the cable, thus constituting a clean solution.

According to the TF design, the bending radius of the conductor is 6.7 m in the joint region (Figure 4.1). Considering 390 mm overlap (cable twist pitch), the joint could be manufactured and positioned either in bent or straight geometry (Figure 4.9). In the latter case, the cables next to the joint should be bent with a lower bending radius, i.e. 5.5 m, so that the straight joint can be accommodated respecting the requirement on ε_B. In the R&D, the straight geometry was considered, as it allows to electrically test the joint prototype in SULTAN.
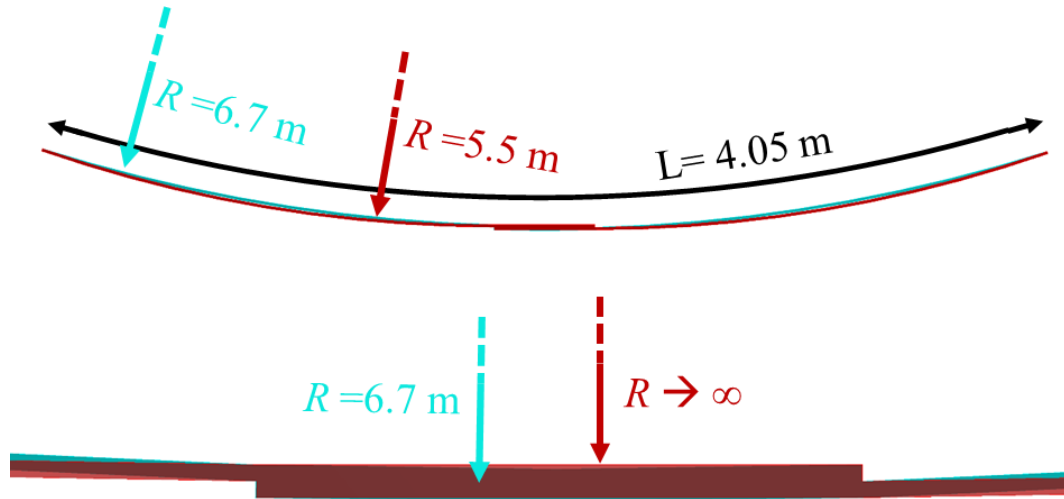
Figure 4.9 *Sketch of a 400 mm long RW joint for the DEMO TF in bent and straight geometry.*

4.4 Development of a diffusion-bonded joint prototype

4.4.1 Joint design

Cable preparation

The extension of the diffusion-bonded area depends on the contact between the cables to join. However, the surface of the RW2 cable is wavy because it is made of round strands. A diffusion bonded joint between such cables would then occur on limited contact spots. This would lead to high electrical resistance and inhomogeneous current distribution in the joint, thus limiting its maximum current. To overcome this issue, it is proposed to deposit copper on the cable surfaces and subsequently machine them to flatten them. The thickness of the layer to deposit is in the order of the ~2-3 mm, so that the wavy surface can be machined flat. The deposition of copper can be generally performed either by electroplating or by thermal spray. Electroplating is suitable when the thickness of the layer to form is in the order of 1-10 µm because it's a slow process. Moreover, it might leave electrolyte residues due to its capillary penetration through the interstices among the strands. For these reasons, thermal spray was

preferred. Its instrumentation is portable and can thus be employed in situ. The thermal spray deposition of copper was carried out in collaboration with the company Bührer AG [99].

Thermal spray consists in propelling molten material at high speed onto a cleaned and prepared surface (Figure 4.10a). The preparation of the cable surfaces consists of sandblasting them, aiming both at removing the chromium layer and roughening the surface. The roughness increases the adhesion of the impinging particles to the surface. In fact, in the thermal spray process, the adhesion between spray particles and substrate consists of a mechanical bond: the particles hit the relatively cold surface of the cable (60 °C was measured during the process), the impact deforms the particles, which spread and get stuck among the ripples of the cable surface (Figure 4.10b). As the bond is not chemical, many possible combinations of parent and sprayed material are possible. In this thesis, both are made of copper. In typical industrial thermal spray applications, thermal spray is employed for covering the parent material with abrasion resistant materials, electrically/thermal insulating materials or with the same parent material for reparation purposes.
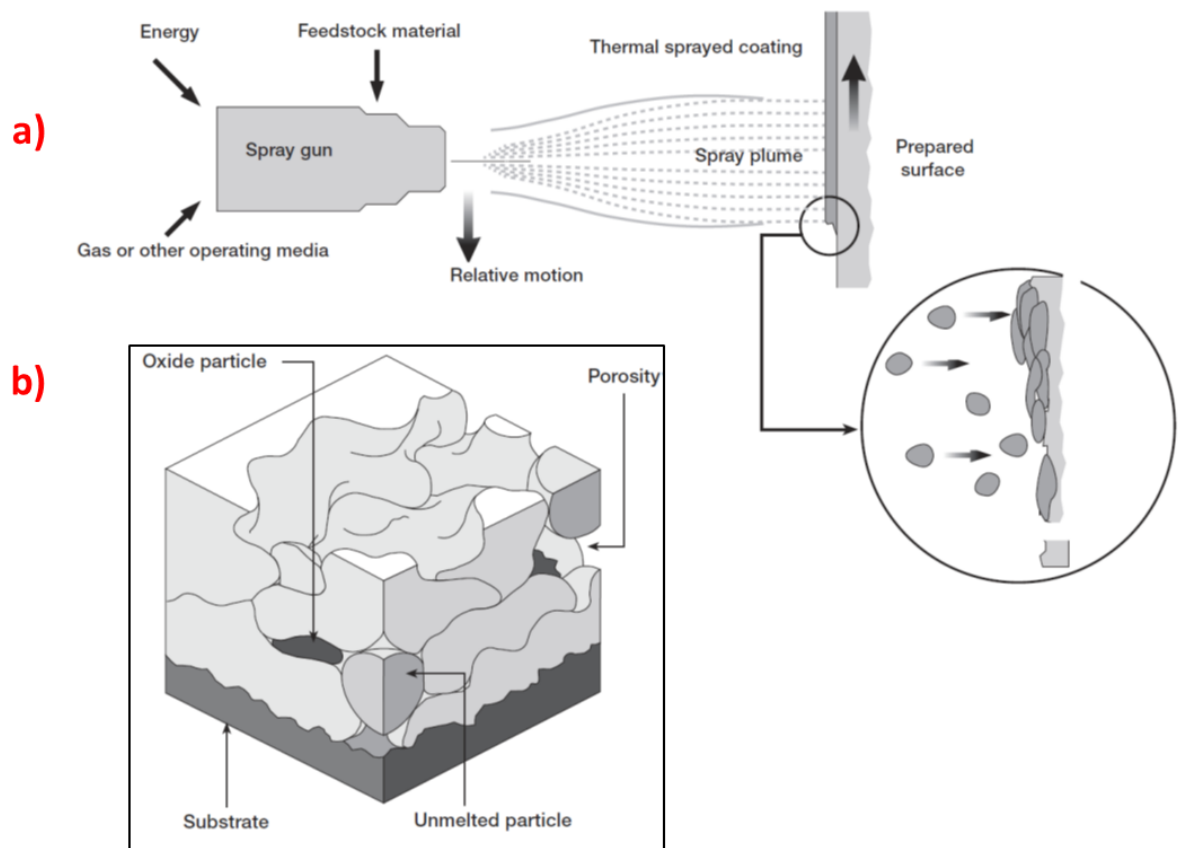
Figure 4.10 *Working principle of thermal spraying (a) and schematic diagram of the created substrate (b).*

Among the several thermal spray techniques (Table 4-2), we use Electric Arc Wire Spray (Figure 4.11), which is suitable for spraying metals and uses an electric arc between two consumable electrodes consisting of the material to be sprayed. This leads to melting at the tip of two wires. Dry compressed air atomizes the molten spray material and accelerates the particles onto the cable surface. The deposited layer can reach a few millimetre thickness with a deposition rate is higher that is higher than with the other techniques. The deposition of a 2-3 mm thick layer around the perimeter one superconducting cable section (400x35x11 mm^3)

takes a few minutes. Arc spraying is relatively cheap, as it just needs a DC power supply to create the arc, without the need of a combustion system like in the flame spraying and in the high-velocity oxygen fuel (HVOF) methods. Moreover, arc spraying has a better coating quality than flame spraying, in terms of porosity and pulling strength. The process is much less complex than in plasma spraying, whose much higher temperature (about 20'000 °C) is more suitable to melt ceramic materials. Therefore, arc spraying was selected as thermal spray method to employ in the development of this joint. The copper wire used for the arc spraying has a diameter of 1.58 mm. Its purity was measured in the SPC lab in terms of RRR before and after annealing the wire. RRR=43 and 200 in the former and latter case. The deposited material was extracted by a joint dummy sample by electro-erosion and its measured RRR was 70 (Figure 4.12), whose value is acceptable for a good joint resistance. For this reason, it was decided not to try other more complicated and costly spraying techniques, such as plasma spraying or HVOF.

Table 4-2 *Characteristics of different thermal spraying techniques* **[99]**.

Method	Particle velocity (m/s)	Oxide content (%)	Adhesive pull strength (MPa)	Porosity (vol.-%)
Arc spraying	100	10-20	10-30	5-10
Flame spraying	40	10-15	<8	10-15
HVOF	500-1000	1-2	>70	1-2
Plasma spraying	200-300	1-3	20-70	5-10
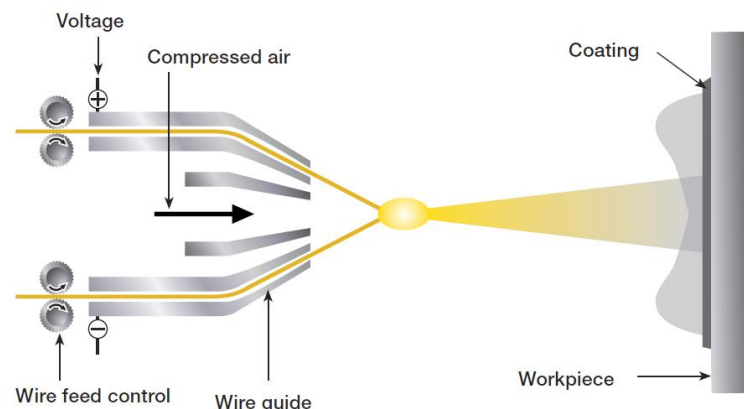
Figure 4.11 *Schematic diagram of the electric arc wire spray process.*

Figure 4.12 *RRR measurement of the wire melted for coating (left); dummy diffusion-bonded joint used to extract samples from the Cu coating (centre); samples extracted from the coated layer to measure the RRR value (right).*

Before carrying out the Cu thermal spray procedure, the reacted superconducting cables are prepared with an aluminium fixture having the function of providing support to the cables during the Cu deposition procedure. In particular, a set of Al clamps are set along the length to be sprayed with Cu, preventing the transversal movement of the strands. In fact, it was observed that, without any support, the strands would lose their original compaction due to the 60 °C temperature reached during the Cu spray deposition, as the thermal energy causes relaxation of the twisted strands (Figure 4.13). Since such an Al support interferes with the area to be covered with Cu, the procedure was carried out in two stages. In the first stage, Cu is sprayed between the clamps. The stiff layer that is formed can now prevent the movement of the strands. Therefore, the clamps are removed and copper is sprayed once again. After the copper thermal spray procedure, the surface of the copper layer is rough, compatible with the fact that the coating consists in a bunch of crushed particles hooked to each other (Figure 4.10b). Moreover, the wavy form of the original Nb$_3$Sn conductor is maintained, but the surfaces can be milled to remove the excessive Cu layer and flatten them, thus increasing the contact surfaces of the cables to be spliced. When machining, the surface becomes flat and smooth, when removing the first tenths of millimetre from the coated thickness. The quality of the surface decreases when approaching the cable surface, as if there was a transition in the sprayed layer. Therefore, on the side to join, 1 mm was left, thus milling 2 mm in total. The preparation of the cables is summarized in Figure 4.14.

92
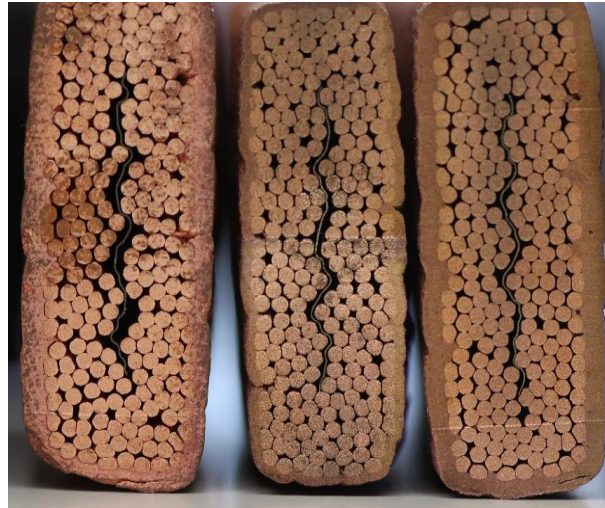
Figure 4.13 *Comparison between the dummy cable free-standing (left) and constrained by an Al fixture (centre and right) during the Cu thermal spray procedure.*

Figure 4.14 *Cable prepared with Al clamps and bars (a); cable after sandblasting (b); cable after clamps removal and second stage of sandblasting (c); cable after being sprayed with Cu (d); cable after milling all sides (e).*

Diffusion-bonding clamp

To obtain the required level of pressure, a clamping system for diffusion-bonding (Figure 4.15) was designed with the following design criteria:

- Assembly/disassembly in situ.
- Uniform pressure distribution along the joint width.
- Materials choice such that the pressure increases with increasing temperature due to the combination of different thermal expansion coefficients.

The disassembly requirement leads to a modular design of the clamp, which is made up of several components. The uniform pressure distribution influences the thickness of the various components, which also depends on the maximum allowable von Mises stress of the materials.

A 70 Nm torque is applied on M16 Inconel bolts at room temperature, corresponding to 24.6 MPa on the joint area. Using a 2D thermomechanical model that assumes uniform temperature distribution, this pressure is estimated to rise up to 30 MPa at 650 °C. The transversal screws, connecting the two u-shaped Inconel plates, are not in the calculation because their function is to act as spacers between these two plates during assembly. We note that the model has the following main limitations:

- Temperature is not uniform in reality, as the joint will be heated locally, while the rest of the cable is at room temperature.
- The cable is modelled as a continuous body with uniform thermomechanical properties, weighted with respect to the volume of Nb_3Sn, copper, bronze and void fraction.
- The plasticity of the cable at high temperature is not known and thus not taken into account.

The equations to solve consist in the displacement differential equations, derived from the linear theory of elasticity of isotropic bodies. These equations are written in variational form [100] and reported in the Appendix, namely in A.1. Once the displacement field is found, the strain field can be computed with the kinematic equations, linking the displacement with the strain. The stress components can be assessed through the material constitutive equations, linking the strain with the stress. The results of the calculation, performed with Freefem++, are reported in Figure 4.16. This, in particular, shows the deformation and the von Mises stresses of the parts as a consequence of the temperature increase and the torque applied on the bolts passing through the threaded plate. The pressure distribution along the width of the joint shows a peak in the edge and a minimum in the centre, as a consequence of the fact that the edges of the bearing plate lie on the u-plates while its centre does not have contact with any structure on its bottom.
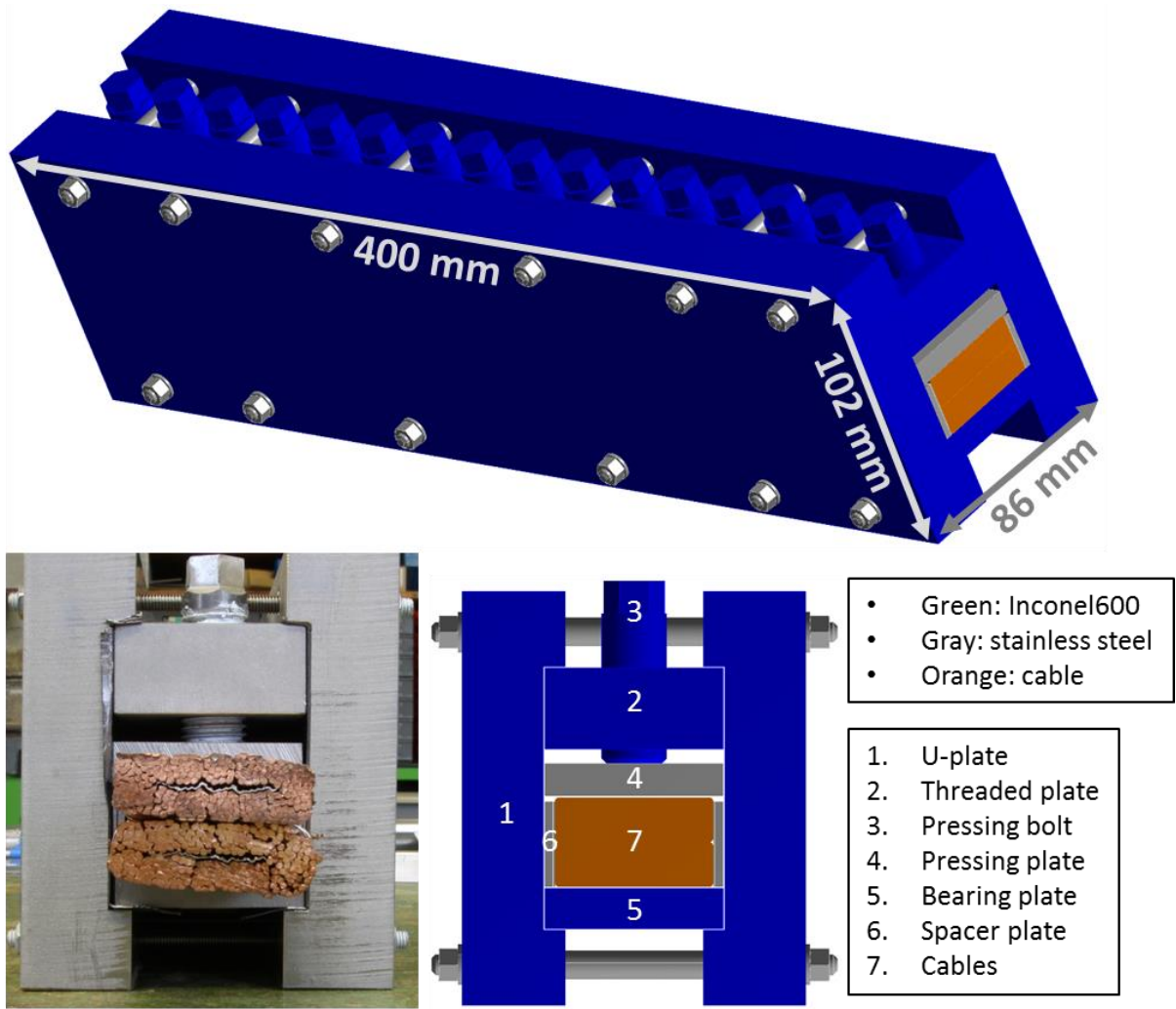
Figure 4.15 *Clamping fixture for the diffusion-bonding of RW2 cables.*

Displacement due to pressure,
amplification factor 50
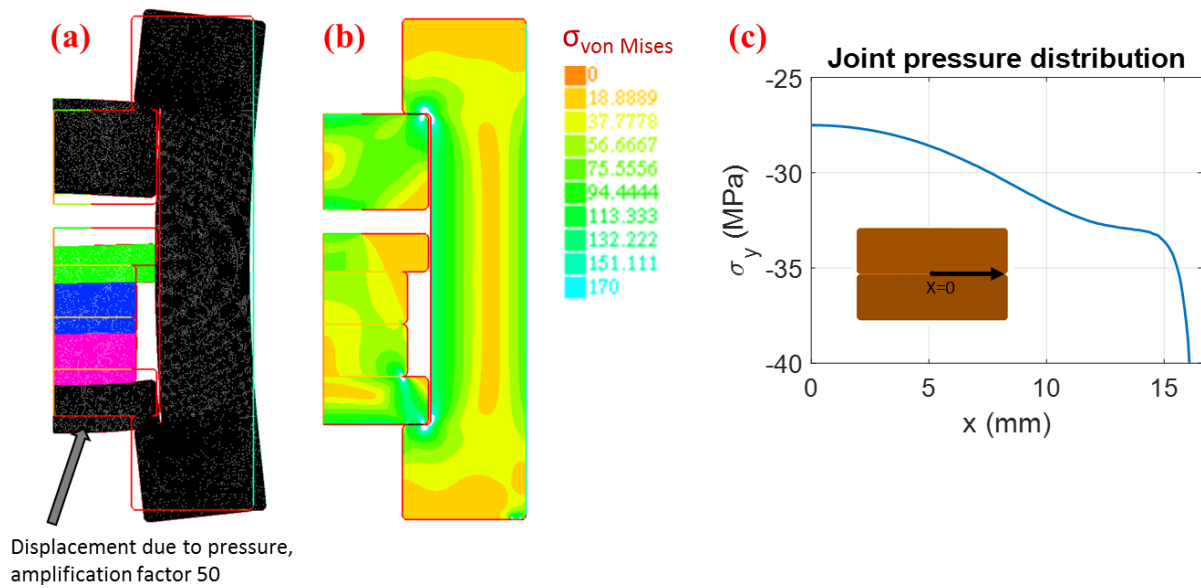
Figure 4.16 *Clamp displacement at 650 °C (a); von Mises stresses at 650 °C (b); pressure distribution on half joint width at 650 °C (c).*

Heating system for diffusion-bonding

The overlapped cables must be heated locally to reach the required 650 °C temperature. In collaboration with the company Plustherm Point AG [101], an induction heating system was designed to optimize the heat deposition into the region to splice (Figure 4.17). In comparison with a resistive heating system, the inductive one is more efficient because the heat is directly generated in the clamp. This system consists in a RLC circuit fed by a generator. The shape of the inductive coils is such that it allows their removal once the joint is formed. The cables are cooled outside the clamp to keep the temperature at 20 °C. This limits the region to which the heat propagates and speeds up the transient until the set-up temperature is reached. The low temperature outside of the clamp has the drawback of an uneven temperature distribution along the joint length: the temperature of the forming joint has a maximum in the centre and a minimum at the edges. To limit this effect, the inductive coils are equipped at the extremes with ferrite, a ferromagnetic material that concentrates the field lines and thus the induced power at the edges of the diffusion-bonded clamp. The Ohmic power distribution induced by the inductive coil in the joint region is computed with the ANSYS software and is shown in Figure 4.18 in a case with and without ferrite blocks. The computation is the input for a steady-state thermal analysis (Figure 4.19) having the aim of estimating the temperature distribution in the joint region as a result of the deposited power, convection with stagnant air and cooling of the cables 500 mm aside from the clamp extremes. In a real magnet application, this distance must come from a compromise between the length of the layer to unwind and the maximum acceptable temperature difference between the centre and the edge of the joint during diffusion-bonding. According to the analysis, this set-up causes a difference between the temperature of the cable at the centre and at the border of the diffusion-bonding clamp of just 32 °C, as shown in Figure 4.20.
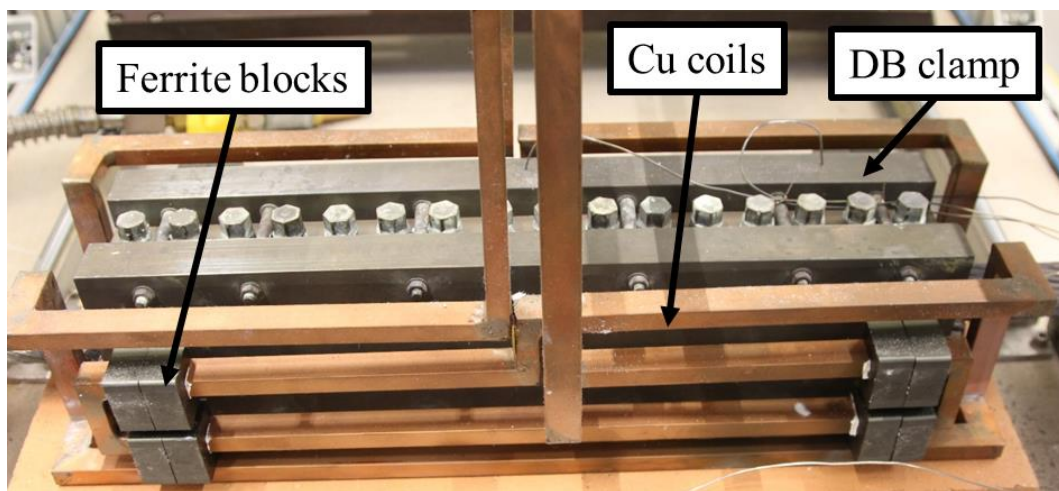
Figure 4.17 *Inductive coils for heating the joint region of the diffusion-bonding between RW2 cables.*
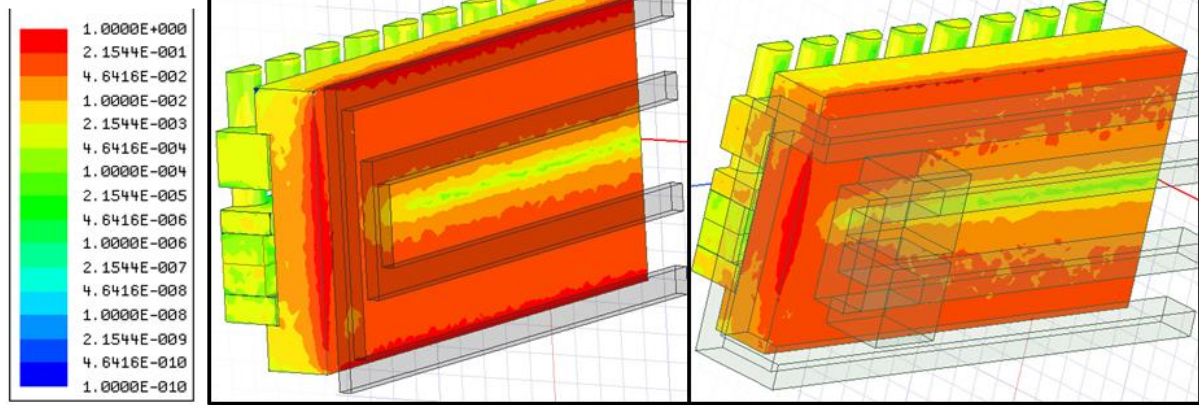
Figure 4.18 *Ohmic power generated by induction heating in the joint region when the current frequency is 52 kHz and the coil current amplitude 1 kA. The results are normalized to the maximum power in the case without (left) and with (right) ferrite blocks.*
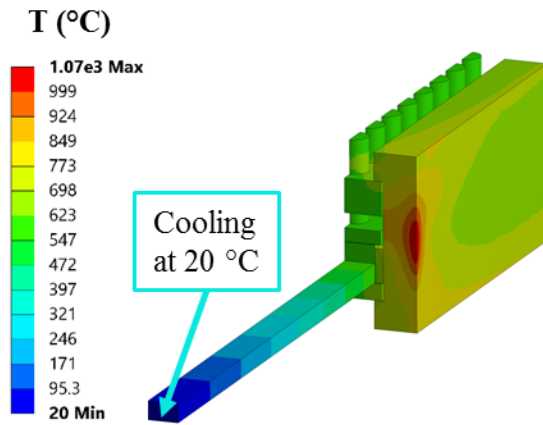
Figure 4.19 *Computed steady-state temperature distribution during diffusion-bonding in ¼ of the domain.*
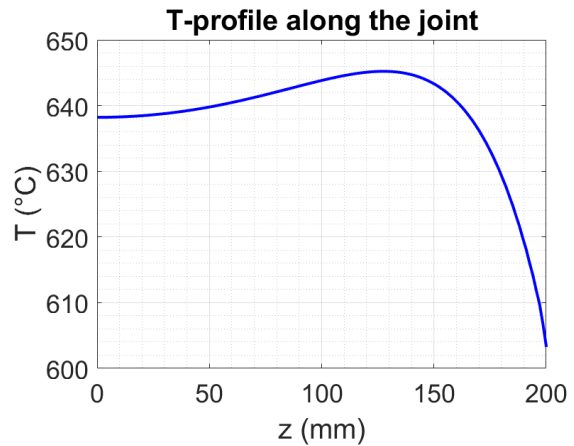
Figure 4.20 *Computed Steady-state temperature profile in the centre of the joint. Only 200 out of 400 mm are shown because of symmetry.*

4.4.2 Manufacture of a joint prototype

The surfaces of the cables are sprayed with copper and milled flat, leaving 1 mm thickness at the sides to splice. The setup for making diffusion-bonding is then prepared. Temperature sensors are installed in different locations of the diffusion-bonding clamp, according to the scheme reported in Figure 4.21. They allow to regulate the power of the generator feeding the inductors and check the temperature gradient inside the set-up. The sensor T4 is of particular interest, as it is next to the edge of the forming joint. No temperature sensors can be directly installed on the cables inside the clamp because they are inaccessible. For this reason, trials with copper dummy cables were performed, during which temperature sensors were installed at the centre and edges of the joint after removing the spacer plates introduced in Figure 4.15. The outcome of these trials is that the temperature of the cables at the edge and centre of the joint is 620 °C and 690 °C, respectively, when T4=630 °C. Therefore, the temperature gradient shown in Section 4.4.1 is underestimated, likely due to an overestimation of the thermal

conductivity of the superconducting cable. Thermal images of the heated region were also taken, but these do not allow to have an insight of the inner region and, in particular, of the cables, which are of major interest. Therefore, a finite number of temperature sensors was preferred for the control of the heating process.
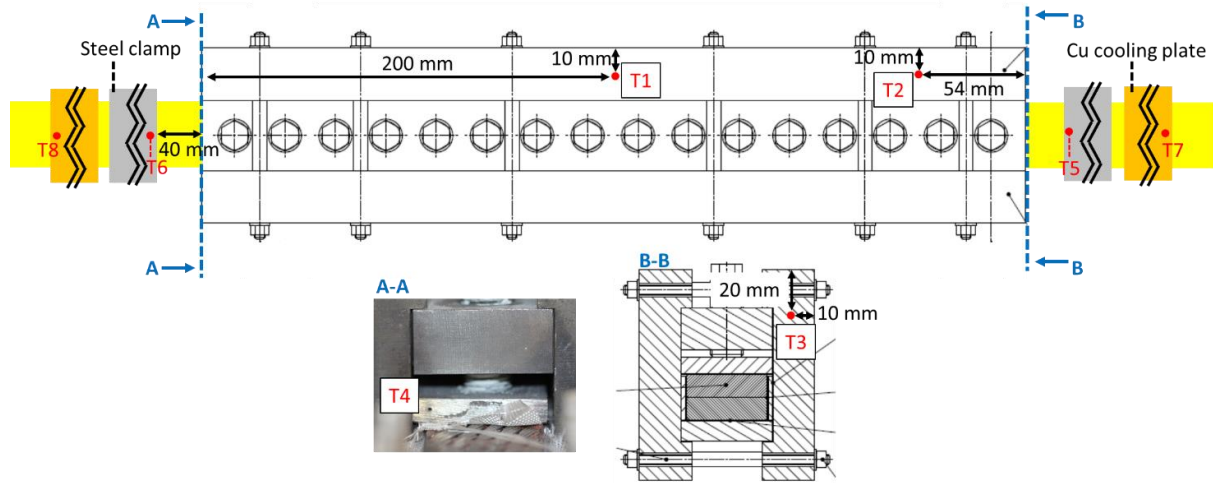
Figure 4.21 *Instrumentation scheme for the diffusion-bonding treatment.*

Mica foils are put to shield the inductors from radiation and ceramic wool is used as additional insulation (see Figure 4.22).

Additional 200 mm long steel clamps restrain the cables outside the diffusion-bonding clamp to avoid cable deformation in the high temperature gradient region between heated and cooled zone, where 200 mm long hollowed copper plates are bolted to the cables (Figure 4.23). A chiller provides water cooling to inductors and hollowed copper plates with a total 15 l/min mass-flow-rate equally splitting between inductors and copper plates, keeping the former below 30 °C and the latter at 20 °C.

The heated region is then closed using plastic blankets, as reported in Figure 4.24. Nitrogen gas is released from a liquid nitrogen dewar during heat-up and cool-down. This provides an inert atmosphere that limits the oxidation of copper.

The temperature evolution is reported in Figure 4.25. T7 and T8 registered always 20 °C. The inductors frequency was 52.3 kHz. The power was initially 5 kW. It was then decreased to 4.6 kW to keep T4=630 °C. The time to arrive to steady-state is 1.5 h, while the steady-state lasted 2 additional hours, after which the inductors were switched off and cool-down lasts 6.5 hours.
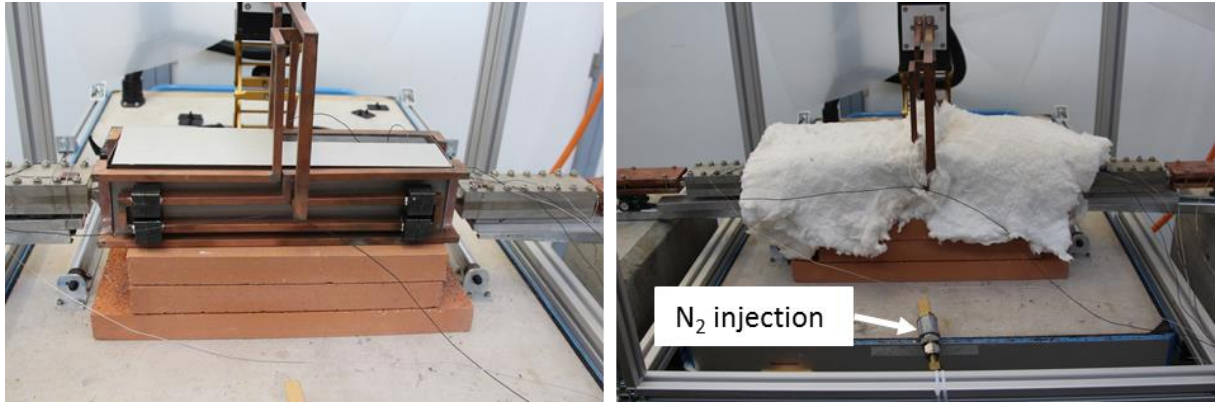
Figure 4.22 *Diffusion-bonding clamp with radiation-reflecting mica foils (left) and insulating ceramic wool (right).*
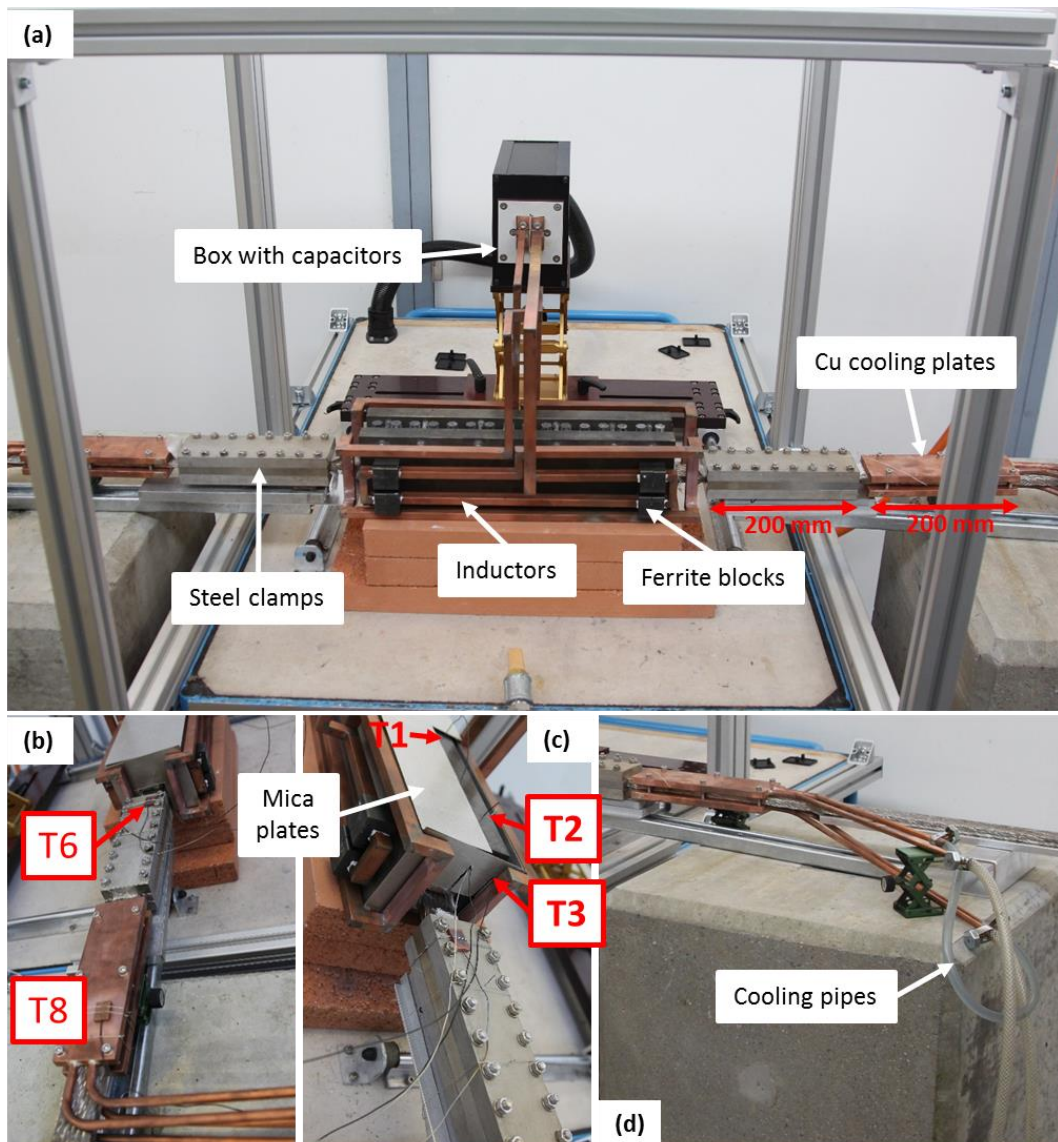
Figure 4.23 *Diffusion-bonding set-up and temperature sensors position. (a) View of the assembled Inconel-steel clamp on the mobile station; (b) left supporting steel clamp and cooling copper plates; (c) right supporting copper plates; (d) cooling pipes connected to the copper plates.*

99

Figure 4.24 *Plastic blanket embedding the joint to delimit the inert atmosphere region.*
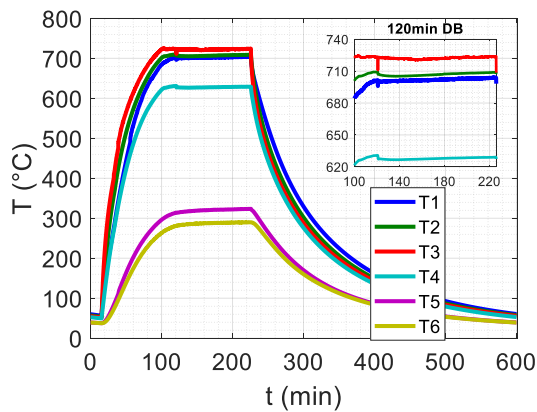
Figure 4.25 *Temperature evolution during diffusion-bonding.*
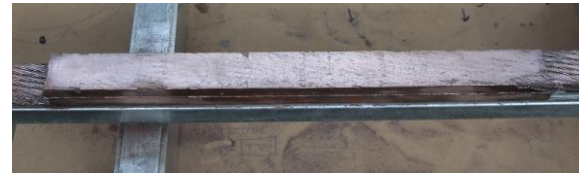
Figure 4.26 *The joint after diffusion-bonding treatment.*

The diffusion-bonding set-up is dismantled and the joint (Figure 4.26) is prepared for the assembly with the segregated stabilizer and the steel jacket. During it, a pre-load is applied on the cable with the procedure introduced in Section 4.2. Nevertheless, the tape is inserted only on one of the conductors of the joint, as shown in Figure 4.27, otherwise the preload would not be homogeneous, as the joint has a different stiffness than the conductor and because the joint was already compacted by the diffusion-bonding procedure. In particular, the segregated stabilizer of the two cables was connected through a copper bridge (Figure 4.28). Indium wires are squeezed between the surfaces of the connected pieces. This ensures the electrical continuity of the stabilizer, fundamental in case of quench in a real magnet application rather than in this experiment.

The one with the joint prototype, whose cross-section is shown in Figure 4.29, constitutes one of the two SULTAN legs of the electrical test. The other leg, necessary to close the electrical circuit, is constituted of the RW2 conductor. The two legs (Figure 4.30) are connected by a bottom joint made of copper surfaces electrically connected through squeezed indium. The conductor of each leg is soldered in these copper slots. Such an indium joint makes the prototype dismountable from the paired leg. The upper part of the overall sample is made up of terminations connected to the superconducting transformer, already introduced in Section 3.4.1, through the same joint concept as in the bottom joint.
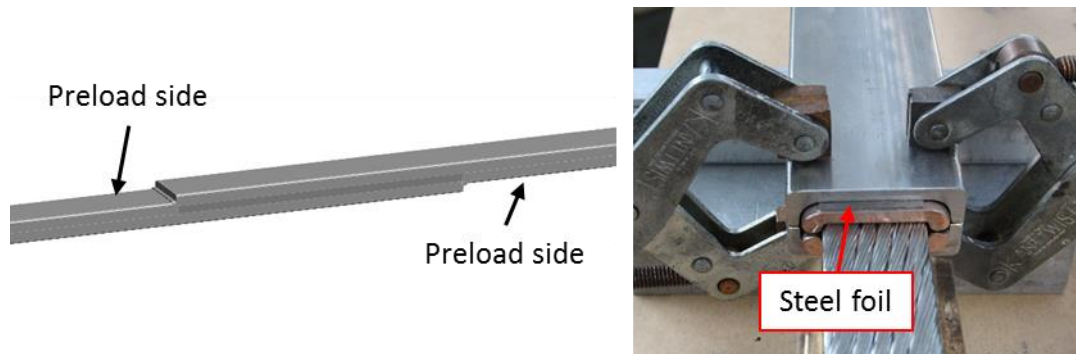
Figure 4.27 *Cable pre-compression with a steel foil.*
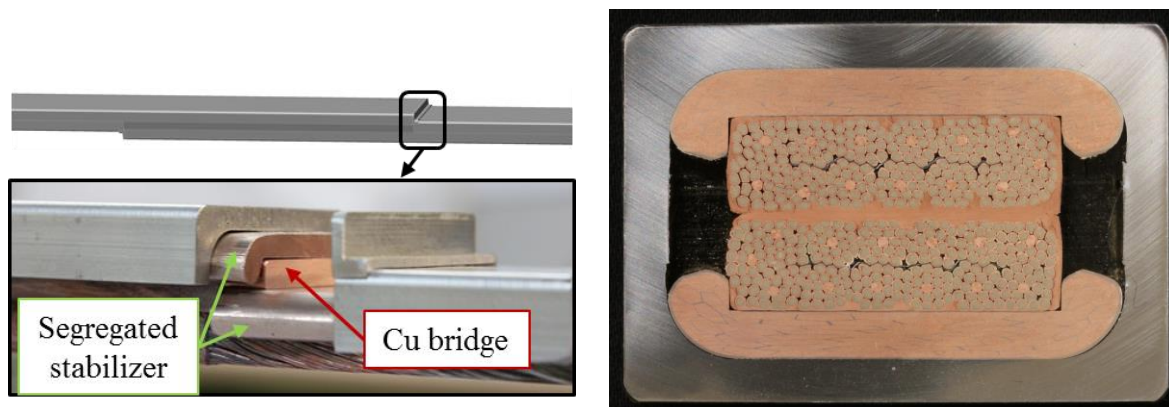
Figure 4.28 *View of the copper bridge connecting the segregated stabilizer of the two cables.*

Figure 4.29 *Cross-section of the diffusion-bonded joint prototype for a react-and-wind DEMO TF.*
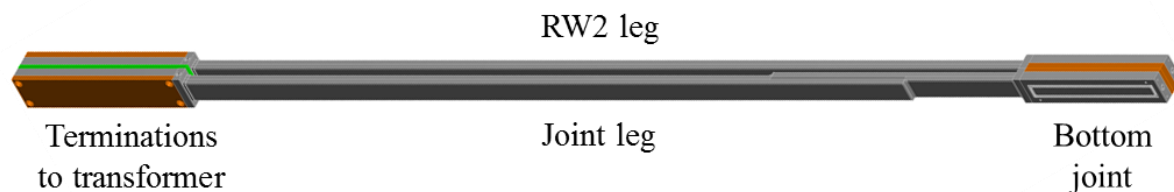
Figure 4.30 *SULTAN sample for the test of the diffusion-bonded joint prototype for RW fusion magnets.*

4.4.3 Electrical test in SULTAN

Test program

The SULTAN test instrumentation diagram is shown in Figure 4.31. It comprises temperature sensors (T) and voltage taps. These last ones may be single (V) or arrays of 6 taps (VH), for redundancy. The joint resistance is measured through the arrays of voltage taps VH3-VH5 and VH1-VH7, whose measured length is 450 mm and 600 mm, respectively. Temperature sensors T1 and T3 are used for AC loss assessments.

The voltage drop between arrays, say between VH3 and VH5, comes from the average of the voltage drop between the 6 single taps of the arrays, i.e. VH3_1 and VH5_1, VH3_3 and VH5_3, VH3_5 and VH5_5, VH3_7 and VH5_7, VH3_9 and VH5_9, VH3_11 and VH5_11.

Before performing this average, it is checked that the 6 signals are similar. In this way, it is possible to check if the cross-sections on which the voltage taps are installed are equipotential.
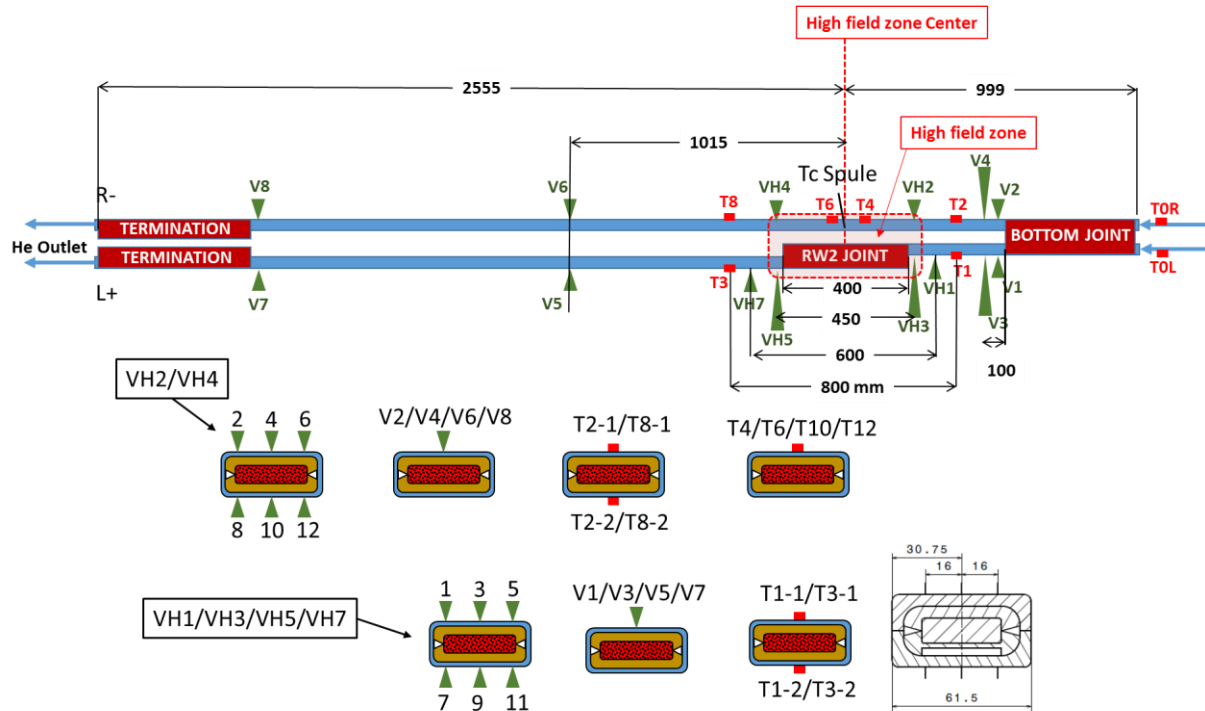
Figure 4.31 *Instrumentation diagram for the DC and AC SULTAN test of the diffusion-bonded prototype.*

The DC test aims primarily at characterizing the joint electrical resistance behaviour with respect to the background magnetic field and the injected current. In particular, the resistance at 8 T and operating current 63.3 kA is of interest, since these would be the operating conditions in the DEMO TF for the joint with high grade conductor, according to the SPC TF design following the baseline of 2015. Being able to reach 10.9 T (about 12 T with the self-field) at 63.3 kA is also another objective in order to demonstrate that the joint prototype, built with the highest grade conductor of the DEMO TF instead of one highest grade and second highest grade, can reach high magnetic field and current without quenching.

A quench test is carried out at operating field and current to measure the take-off temperature T_q, i.e. the maximum temperature at which the joint can operate at the operating field and current. The temperature is smoothly increased till voltage take-off. T_q is then compared with the conductor current sharing temperature T_{cs} at the same current and magnetic field.

AC losses and transient stability tests are also included in the program at both perpendicular and parallel AC field orientation (see Figure 4.32). The perpendicular AC field orientation is of interest for a joint in a TF coil because of the transient poloidal field generated by the PFs. In a CS coil, both perpendicular and parallel AC field components are present. AC losses are of interest for defining the heat generated in the joint region during field transients. This heat causes a temperature increase of both conductor and coolant. The magnet designer must cope with these losses, so that the magnet does not undergo a quench. The transient stability test aims at assessing the maximum fast field transient, measured in T/s, that the joint can withstand without a temperature or voltage take-off.

One thousand electromagnetic cycles at 8T x 63.3kA=506 kN/m are performed, after which DC and AC test are repeated to ascertain if the joint performance degrades due to fatigue. Moreover, a warm-up-cool-down (WUCD) is performed and the sample is tested again in DC and AC, in order to see if the thermal fatigue affects the joint performance.
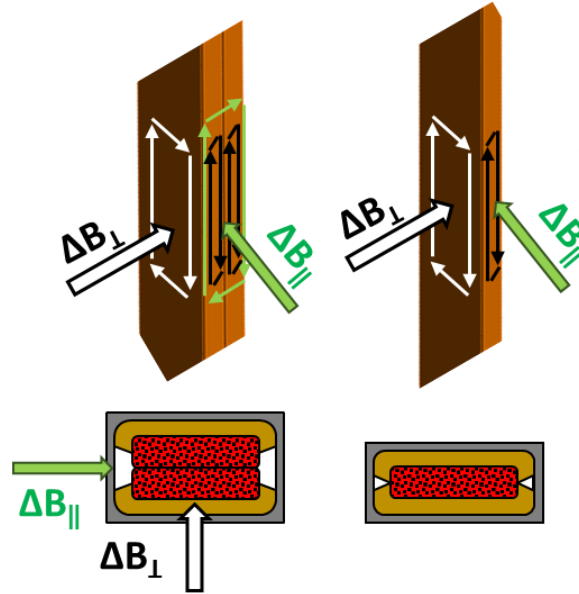
Figure 4.32 *Orientation of the AC field with respect to joint and conductor broad side.*

DC test

The electrical resistance of the sample is the combination of: copper coating bulk resistivity, strand stabilizer bulk resistivity, coating-strands contact resistance, inter- and intra-strand resistances (Figure 4.33). The contribution given by the copper coating can be estimated by considering the electrical resistivity of copper with RRR=70, the 2 mm thickness and the surface 36 x 400 mm^2. If the current is perpendicular to the joint surface, the resistance of the cooper coating is in the range 0.03-0.1 nΩ, for *B*=0-11 T at *T*=4.5 K. This corresponds to the minimum joint resistance that one can expect from the measurements.
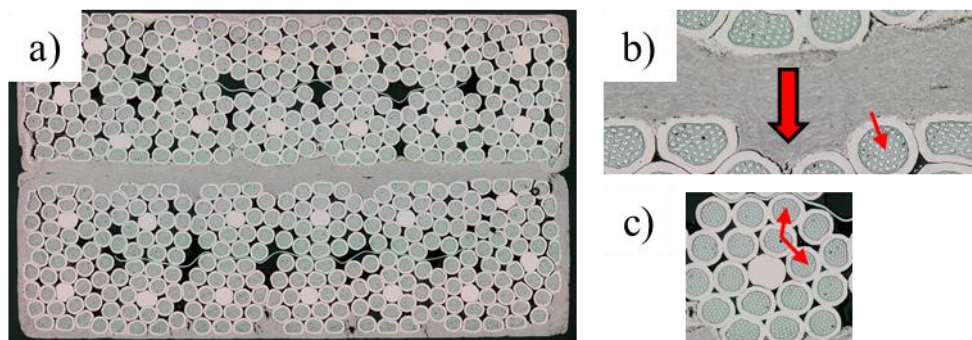
Figure 4.33 *Diffusion-bonded joint (a) and main resistive paths, including the bulk resistance of the coated layer, the contact resistance between layer and strand (b), the contact resistance between strands (c).*

The joint resistance was measured at different values of current flat-top. The average of the resistance measured at 450 mm and 600 mm is shown in Figure 4.34 and Figure 4.35, while their difference is highlighted in Figure 4.36. These three figures report the measured joint

103

resistance before cycling, after cycling and after WUCD. The different curves of Figure 4.34 show a different behaviour of the resistance as a function of current:

- For B=0 T, one can observe a slight increase of the resistance as a function of current. This could be attributed to the slight increase of the copper magneto-resistivity caused by the self-field of the sample, which amounts to about 1 T at 63.3 kA.
- As the background field becomes higher, the difference between the resistance at high and low current becomes more pronounced. A possible interpretation for this behaviour is that 1/3 of the strands of each sub-cable are not in contact with the diffusion-bonded surface (see Figure 4.33c). This might leads to saturation of some strands and an increase in resistance.

Figure 4.35 shows the behaviour of the joint resistance as a function of the background field. The slope of the "Initial" curve is linear up to 8 T, becoming non-linear for higher fields, symptom of saturation of the low resistive paths, which leads to a redistribution of the current among more resistive paths.

Figure 4.36 concentrates on the comparison of the resistance measured between the 450 mm and 600 mm distant voltage taps. The fact that their difference is non-null suggests the presence of an exchange of current between strands outside the joint region. Moreover, this difference increases after the electromagnetic cyclic load, which suggests that the region outside the joint is affected by fatigue. After a WUCD cycle, the resistance difference between the two pairs of voltage taps remains constant, suggesting that only the cyclic electromagnetic load is responsible for the conductor degradation at the extremities of the joint.

Figure 4.37 shows the comparison between the Relative Difference of Measured Resistance (RDMR), expressed as $\frac{R(B)-R(B=0)}{R(B=0)}$, and the Relative Difference of copper Magneto-resistivity (RDMr), expressed as $\frac{\rho(B)-\rho(B=0)}{\rho(B=0)}$. Each curve is traced at constant current I. RDMR coincides with RDMr if: the bulk resistance dominates over the contact resistance and the current path does not change with field at constant current. Such an agreement is observable before cycling up to B=8 T. After cycling, the steepness of RDMR curves is higher than for RDMr curves, which means that the joint resistance increases with magnetic field more than the copper bulk resistance. However, the estimated contribution of just the bulk resistance of the copper cladding is significantly lower than the measured joint resistance. Therefore, the two observations, i.e. the agreement between RDMR and RDMr in the "Initial" curves of Figure 4.37 and the difference in absolute value between measured and computed resistance suggest that the cladding bulk resistance gives the major contribution to the joint resistance, but the effective area through which current flows is about 5-6 times lower than the joint area.

After cycling, the measured resistance is higher than before cycling, for $B > 4$ T. Instead, for $B \leq 4$ T, the average resistance between 450 mm and 600 mm is lower than first measurements (Figure 4.34-Figure 4.35), but the difference between measurements at 450 mm and 600 mm gets higher (Figure 4.36). As already stated, this observation suggests that cycling damages the conductor at the joint extremities, mechanically weakly supported in the geometrical transition, rather than the joint itself.

The joint was tested for quench temperature at operating 8 T field with nominal 63.3 kA current. The quench temperature changes from initial value to cyclic loading and to thermal

cycle: 8.57 K, 8.47 K and 8.5 K correspondingly at practically identical helium mass flow rate 2.2 g/s. The change of the quench temperature is well in line with the change of resistance. The current sharing temperature of the conductor at 8 T background field and 63.3 kA is instead about 9.6 K, extrapolated from measurements with RW2 and segregated stabilizer, since the T_{cs} measurements were carried out between 9 T and 10.9 T [42]. It is reasonable to expect a $T_q \leq T_{cs}$, as a joint works per definition in current sharing mode. The difference between T_q of the joint and T_{cs} of the conductor depends on the current balance among the strands. The more uniform is the current in the strands of the joint, the less will be the difference between T_{cs} and T_q. As the development of this joint prototype is meant for its application next to saturation conditions, it is important that T_q is as close to T_{cs} as possible.
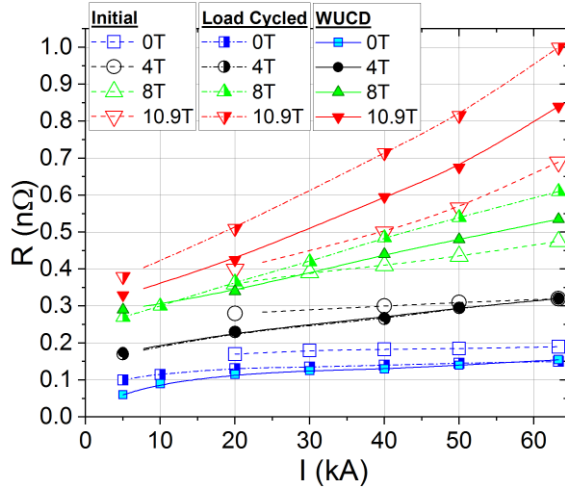
Figure 4.34 *Joint resistance vs current.*
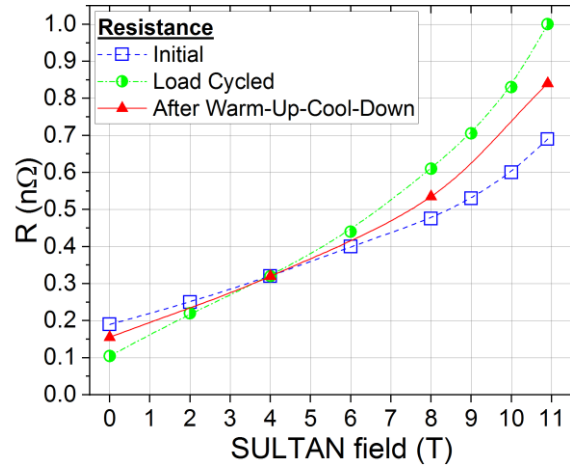
Figure 4.35 *Joint resistance vs background field at I=63.3 kA.*
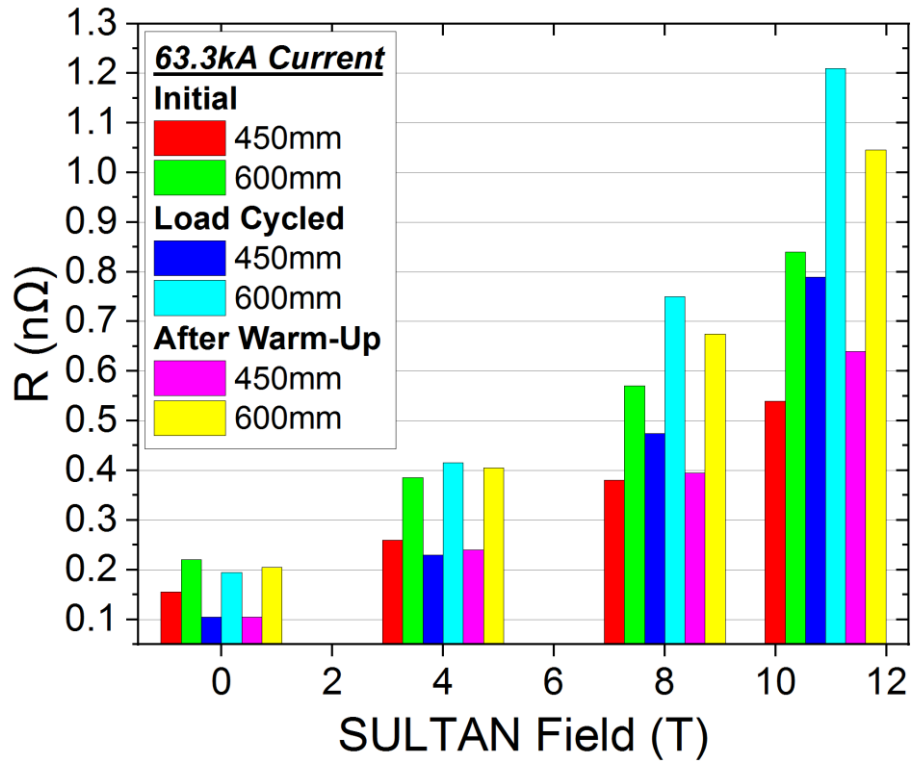
Figure 4.36 *Resistances at 450 mm and 600 mm at 0, 4, 8 and 10.9 T background field. I=63.3 kA.*
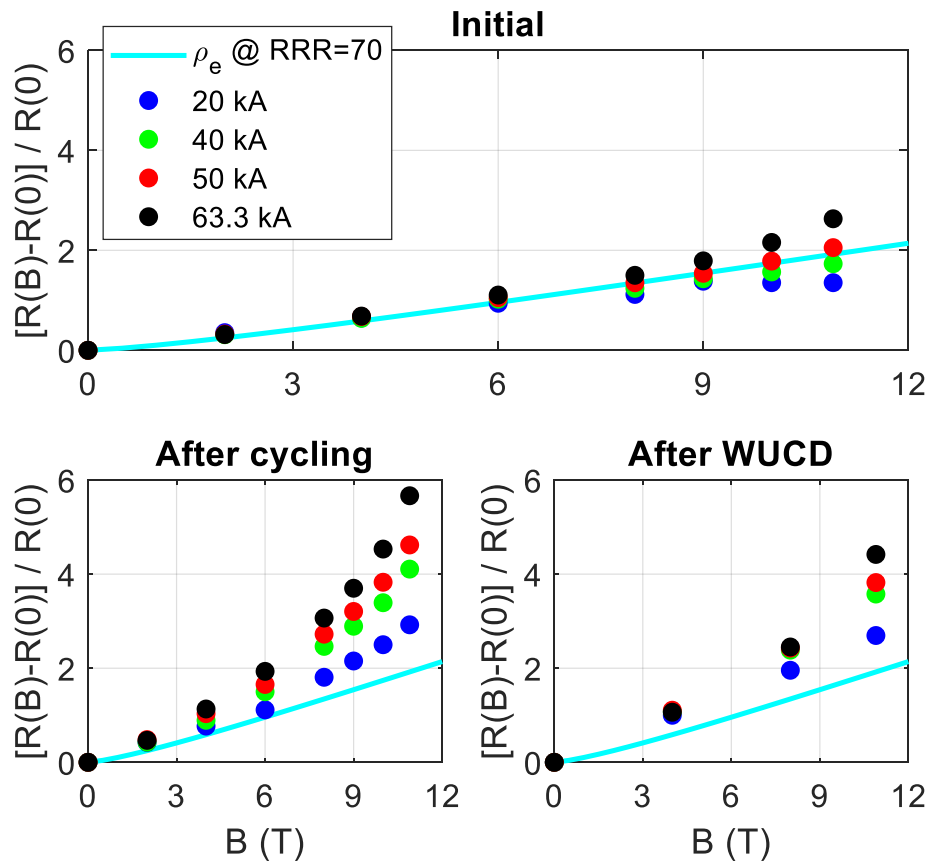
Figure 4.37 *Comparison between joint resistance and magneto-resistivity of copper cladding at different field and current values.*

AC losses

In CICC conductors, the AC losses give three major contributions: the magnetization losses occurring within the superconductor filaments, the coupling losses due to the coupling currents among filaments (intra-strand losses) and strands (inter-strand losses), and the eddy currents of copper. In measurements at 4.5 K, all these components give a contribution. At 20 K, above the critical current of Nb_3Sn, only eddy currents are present, as the resistance of copper is much lower than Nb_3Sn in the normal state [102]. The assessment of AC losses at 4.5 K with pulse field at low frequency allows us to assess the magnetization losses. Therefore, by combining these tests, it is possible to reconstruct each component of the AC losses.

The measurements of the joint AC losses are performed perpendicularly and parallel to the cable broad side. The transport current is null and does not influence the test results. Measurements are carried out for a sinusoidal field sweep at different frequencies [103].

During AC loss measurements, the background field of SULTAN is usually at least 2 T to avoid that the solder of the bottom joint is superconducting. Otherwise, coupling currents not belonging to the tested prototype but to the experimental set-up would arise and influence the measurements.

AC losses are assessed using the gas-flow calorimetry method, assuming that all the heat generated by the joint prototype is transferred to the helium, whose change of enthalpy is quantified through the temperature sensors T1 (upstream) and T3 (downstream) illustrated in Figure 4.31. For sinusoidal field sweeps at 4.5 K the assessment is performed at steady-state using Equation (4. 5). This states that the energy per cycle E generated by the joint and the segregated stabilizer is transferred to helium, causing an increase of its downstream enthalpy with respect to upstream, as in Equation (4. 6). Equation (4. 5) considers also that a part of the energy leaves the control volume per thermal conduction through the segregated stabilizer. This energy goes both upstream ($Q_{conduction,1}$) and downstream ($Q_{conduction,2}$), as shown in the sketch in Figure 4.38. The term $Q_{conduction,1}$ is computed using Equation (4. 7), which assumes that the energy transferred via thermal conduction increases the final upstream helium enthalpy with respect to the initial value, the one before the AC field is applied. An example is reported later in Figure 4.41. The term $Q_{conduction,2}$ is neglected because there is no temperature sensor installed downstream beyond T3.

$$E = \left(P_{He} + Q_{conduction,1}\right)/f \quad [J/cycle] \qquad \textbf{(4. 5)}$$

$$P_{He} = \dot{m}\left(h_{d,f}(T,p) - h_{u,f}(T,p)\right) \quad [W] \qquad \textbf{(4. 6)}$$

$$Q_{conduction,1} = \dot{m}\left(h_{u,f}(T,p) - h_{u,i}(T,p)\right) \quad [W] \qquad \textbf{(4. 7)}$$

Here $\dot{m}$ [g/s] is the helium mass-flow-rate; $h_{d/u,i/f}$ [J/g] the downstream/upstream, initial/final helium enthalpy; f [Hz] the AC field frequency.

It was not possible to reach steady-state conditions in measurements carried out at 20 K because of the influence of the heat-exchanger that links the helium entering and exiting the SULTAN sample. This heat exchanger is always installed for measurements needing temperatures above 10 K, as the helium going back to the cryoplant must be below this temperature value, so that the cryoplant can withstand the thermal load. In particular, the employment of a heater at the inlet of the SULTAN sample and of this heat exchanger allows having temperatures up to 50 K

in the sample environment respecting the requirements of the cryoplant. As it was not possible to reach a steady-state condition in measurements at 20 K, the time-integral of the helium enthalpy is performed using Equation (4. 8), i.e. considering a time interval for the integration, instead of applying Equation (4. 5).

$$E = \frac{\dot{m}}{f \cdot (t_{end} - t_i)} \left(\int_{t_i}^{t_{end}} h_d(T(t), p(t)) \cdot dt - \int_{t_i}^{t_{end}} h_u(T(t), p(t)) \cdot dt \right) \quad [J/cycle] \quad \textbf{(4. 8)}$$

being $t_{i/end}$ [s] the instant before/after the sinusoidal field sweep in which downstream and upstream helium temperature coincide. An example of experiment at 20 K is reported later in Figure 4.42.
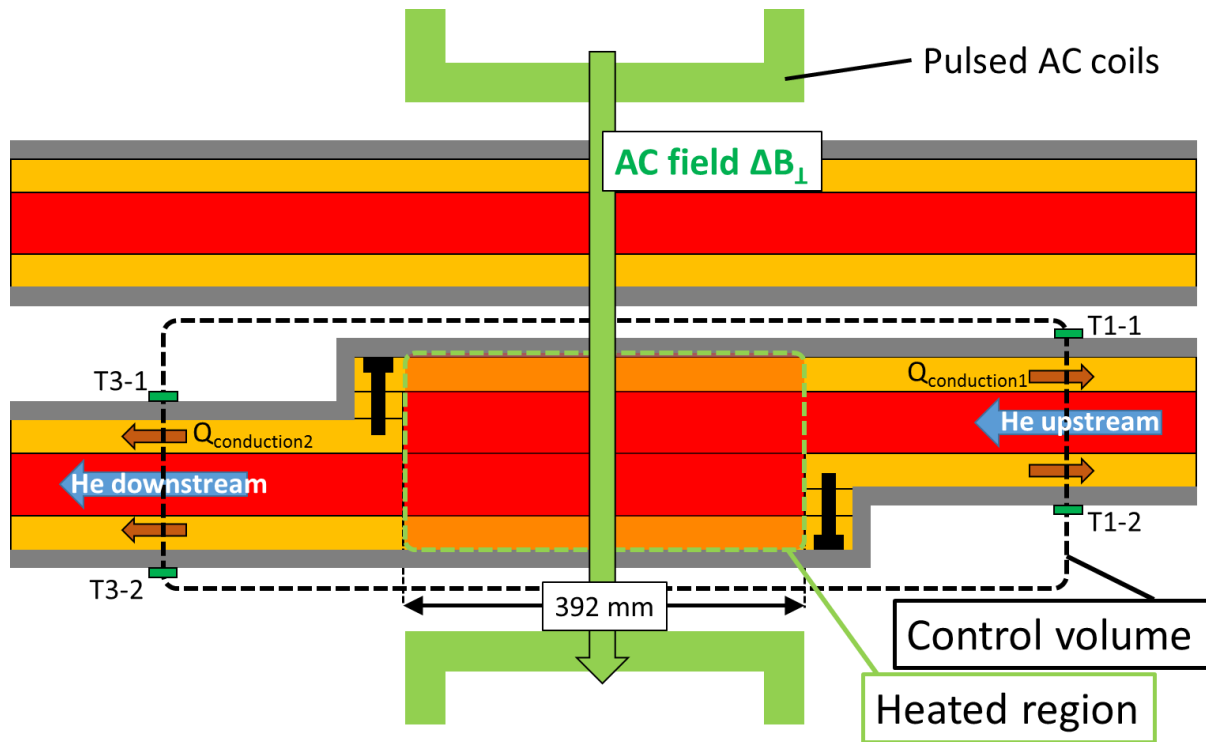
Figure 4.38 *Sketch of the control volume for AC losses assessment and of the main heat contribution to assess the deposited power: upstream and downstream helium enthalpy and copper heat conduction power (Q$_{conduction1}$ and Q$_{conduction2}$).*

The results are summarized in Figure 4.39, in which the comparison between conductor and joint AC losses at 4.5 K is highlighted for the perpendicular field orientation $\Delta B_\perp$. Measurements at B=2 T and B=8 T are reported. The former are meaningful for the powering of the magnet, while the latter for field transients induced by the pulsed operation of CS and PF coils occurring while the TF joint is working at operating conditions. AC losses occurring at B=8 T are lower than at B=2 T because of the higher copper resistivity at 8 T and the smaller supercurrents, as $I_c(8\,T) < I_c(2\,T)$. The comparison between conductor and joint in perpendicular orientation shows on one hand similar AC losses between joint and conductor at frequencies higher than 0.2 Hz, because of the screening exerted the stabilizer limiting the penetration of the magnetic field. This means that the eddy currents of the segregated stabilizer are dominating the AC losses and, since there is the same quantity of segregated stabilizer both in the joint and conductor prototypes, the AC losses are similar. On the other hand, at lower

frequency, the joint losses become almost a factor of two larger than those of the conductor, as the field penetrates both the segregated stabilizer and the two conductors constituting the joint.

When the sinusoidal AC field is in parallel orientation, $\Delta B_{||}$ (Figure 4.40), additional coupling current loops arise, i.e. the ones between the two cables constituting the joint. Due to these, AC losses in the joint are higher than the ones in the single conductor for each frequency explored. In this direction, in fact, the stabilizer does not play any role, and the surface perpendicular to the joint is twice as wide as the one of the single conductor.

Figure 4.40 reports also the comparison between results at 4.5 K and 20 K. These show that stabilizer and copper losses contribute up to 70% of the total losses at $f \geq 0.6$ Hz. At $f \leq 0.3$ Hz, joint measurements at T=20 K have higher uncertainty, due to lower signal-to-noise ratio and higher influence of the inlet helium temperature in the sample. As an example, Figure 4.41-Figure 4.44 compare runs at T=4.5 K and T=20 K, at high and low frequency.
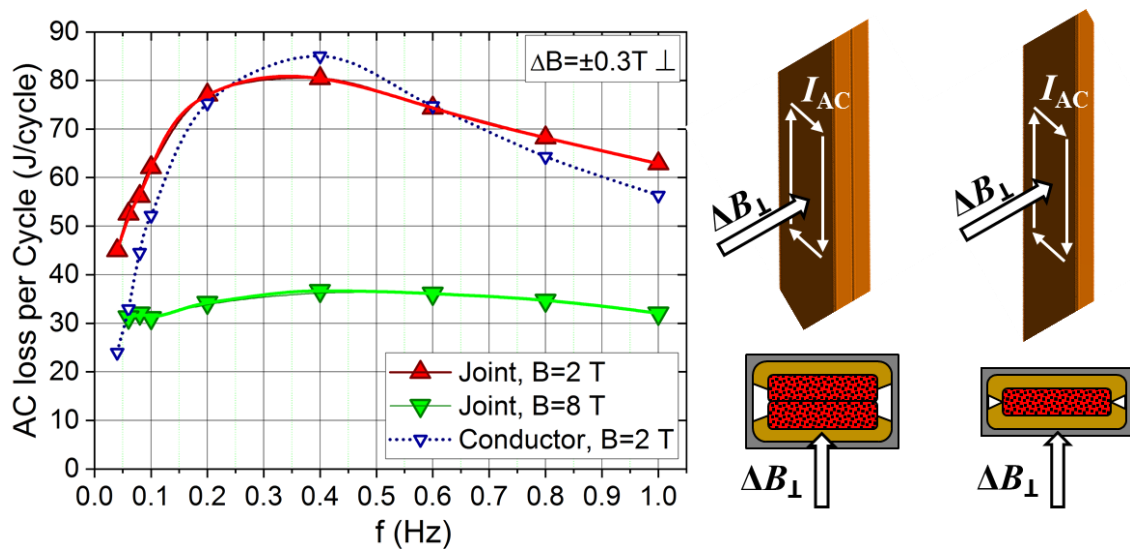
Figure 4.39 *Perpendicular joint and conductor AC losses at T=4.5 K with sinusoidal field sweep.*
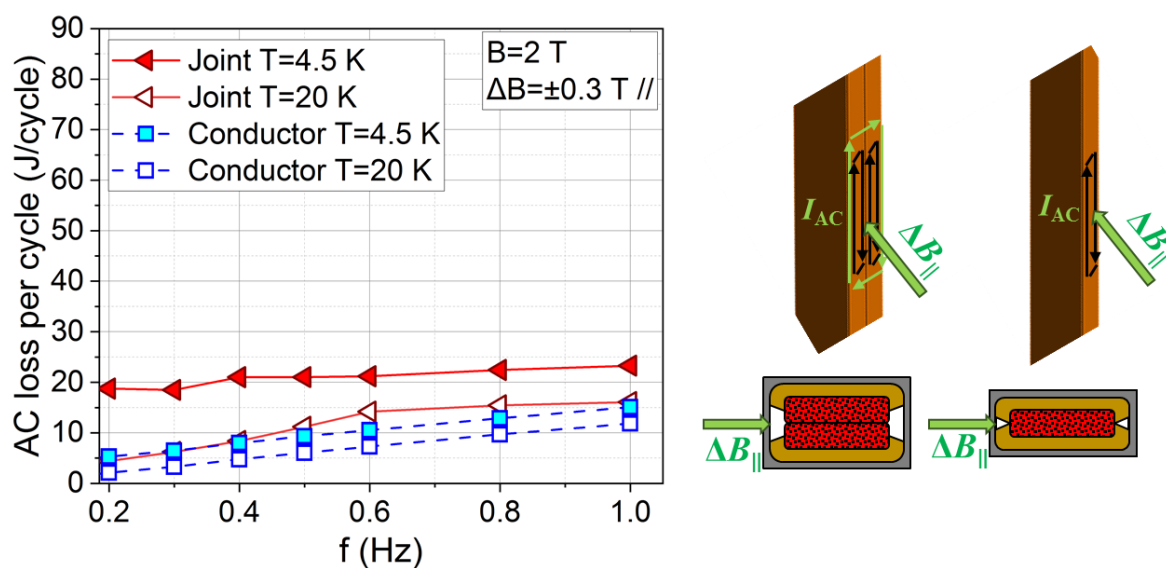
Figure 4.40 *Parallel joint and conductor AC losses at T=20 K with sinusoidal field sweep.*
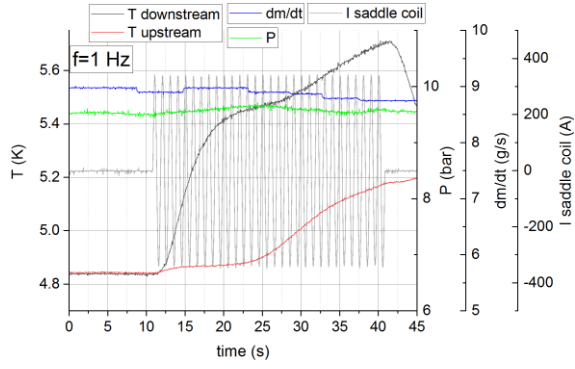
Figure 4.41 *Run of AC losses with parallel AC field at f=1 Hz, T=4.5 K, B=2 T.*
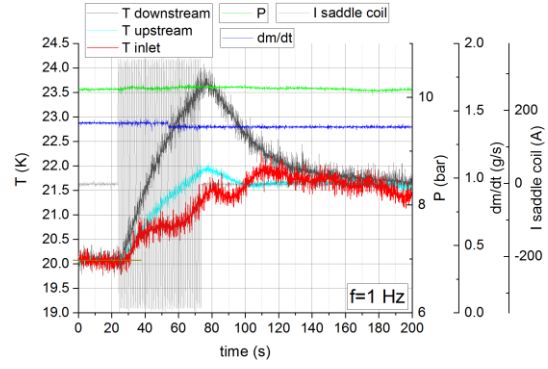
Figure 4.42 *Run of AC losses with parallel AC field at f=1 Hz, T=20 K, B=2 T.*
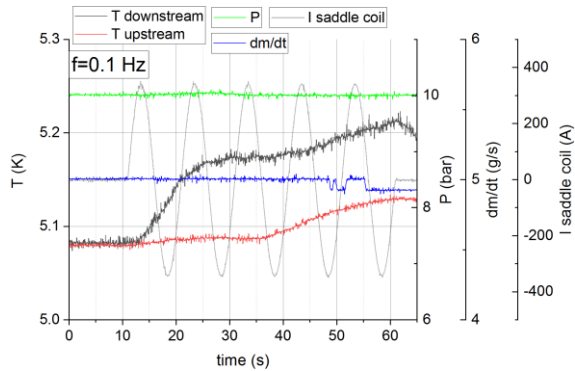
Figure 4.43 *Run of AC losses with parallel AC field at f=0.1 Hz, T=4.5 K, B=2 T.*
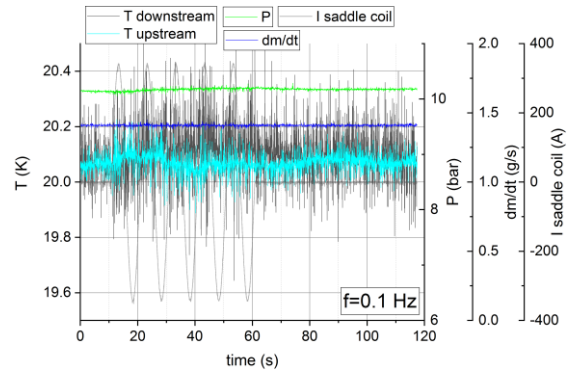
Figure 4.44 *Run of AC losses with parallel AC field at f=0.1 Hz, T=20 K, B=2 T.*

Transient stability

In the transient stability test, a bipolar pulse battery consisting of a set of capacitors is discharged in a short time period, namely 128 ms, in the pulsed coils (Figure 4.38). Depending on the initial voltage of the battery, a maximum field rate of 60 T/s can be reached in the sample. In this test, the discharge voltage is gradually increased in each run, aiming at the maximum field rate that the joint prototype can withstand without a quench.

The test is performed at perpendicular AC orientation, the only one in which it is possible to inject current, as the sample inserted in SULTAN in the parallel field orientation consists only of the joint leg, thus without the conductor leg that would allow to close the electrical circuit (Figure 4.30). In fact, because of the limited dimensions of the sample bore, the leg closing the current circuit cannot be inserted in parallel field orientation. The background field is 8 T, the current 63.3 kA and the mass-flow-rate 9 g/s. The capacitors were charged and discharged in steps from U=100 V, corresponding to dB/dt=4 T/s, up to U=460 V, corresponding to dB/dt=18.4 T/s, when a voltage take-off occurred in the leg of the conductor leg, thus not in the joint. The deposited energy in the joint sample is computed calorimetrically and the results are reported in Table 4-3. The parameters of the experiment are summarized in Figure 4.45, while Figure 4.46 reports an example of helium temperature and enthalpy evolution to integrate in order to get the deposited energy. Equation (4. 9) was used to determine it.

$$E = \dot{m}\left[\int_{t_0}^{t_{end}} h_d(T,p) \cdot dt - h_{d,0} \cdot (t_{end} - t_0)\right]$$
$$- \dot{m}\left[\int_{t_0 - \Delta t}^{t_{end} - \Delta t} h_u(T,p) \cdot dt - h_{u,0} \cdot (t_{end} - t_0)\right]$$

(4. 9)

Here E [J] is the joint sample absorbed energy; $\dot{m}$ [g/s] the mass-flow-rate; $h_{u/d}$ [J/g] the inlet/downstream enthalpy; $h_{u/d,0}$ the upstream/downstream enthalpy before the begin of the field sweep; t_{end} [s] is the time in which the temperature is equal to the one at t_0 before the field sweep started; Δt [s] is the time that helium takes to flow from the upstream to the downstream temperature sensor.

From Table 4-3, it can be concluded that the minimum quench energy of a joint with mixed matrix stabilizer made by two high grade RW2 is higher than 65.6 J at 8 T background field and operating current 63.3 kA, when the transient field is applied perpendicularly to the broad side of the conductor. The current sharing temperature of the conductor at 8 T background field and 63.3 kA is 9.6 K [42], higher than the temperature values reached in this experiment and reported in Figure 4.45. In fact, the temperature sensors installed on the jacket cannot pick up such rapidly changing temperature values in the strands. Moreover, the 65.6 J value is linked to the mass-flow-rate of the experiment, which is 9 g/s, the highest possible in this test. The mass-flow-rate influences the heat removal time scale. Until this is comparable to the heat production time scale, no thermal runaway occurs. The 9 g/s value is in any case conservative, as the first and second TF layers are designed with 18 g/s.

Table 4-3 *Transient stability test results in the joint sample for the test in perpendicular orientation.*

U [V]	B [T]	dB/dt [T/s]	I [kA]	E [J]
100	8	4	63.3	3.51
200	8	8	63.3	16.0
300	8	12	63.3	45.4
400	8	16	63.3	56.7
440	8	17.6	63.3	65.6
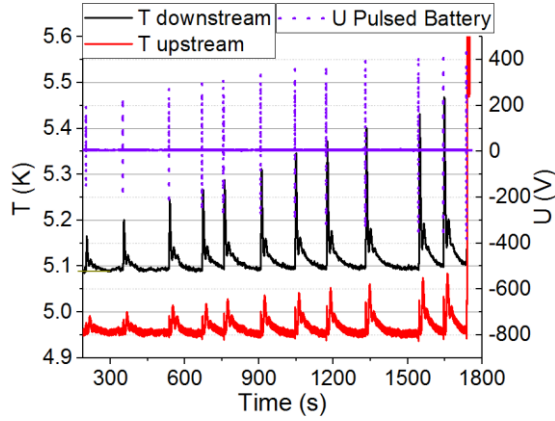
Figure 4.45 *Example of one run of stability test in perpendicular orientation, 8 T and 63.3 kA. The reported temperature refer to the joint leg.*
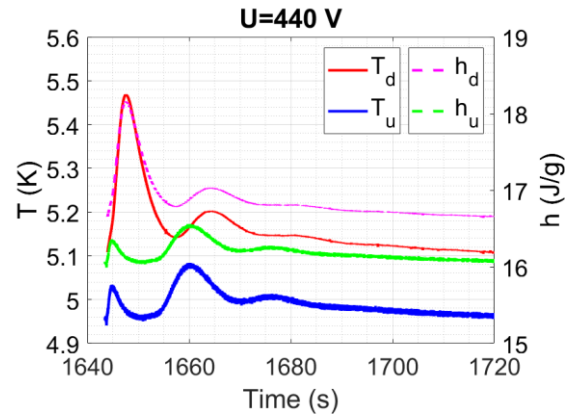
Figure 4.46. *Downstream and upstream enthalpy and temperature evolution in the joint leg when the battery is discharged at U=440 V.*

4.4.4 Metallographic analysis of the joint

The main characteristic of the joint prototype is the copper layer deposited through thermal spray. Such a layer changes its metallographic properties when it undergoes the diffusion-bonding heat-treatment. Its properties influence the electrical performance of the joint discussed in Section 4.4.3.

Four samples were prepared for metallographic analyses (Figure 4.47):

- A reacted cable section (sample #1).
- A reacted cable section after sandblasting, copper thermal spray and milling (sample #2).
- A section of a diffusion-bonded joint taken from the edge of the tested prototype (sample #3).
- A section of a diffusion-bonded joint taken from the centre of the tested prototype (sample #4).
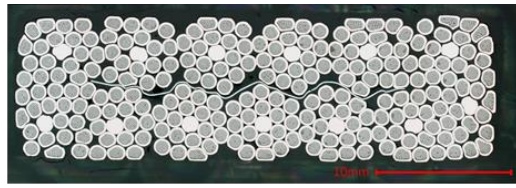
Sample #1 - reacted Nb$_3$Sn   Sample #2 - reacted Nb$_3$Sn with Cu spray
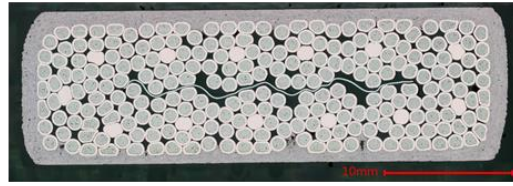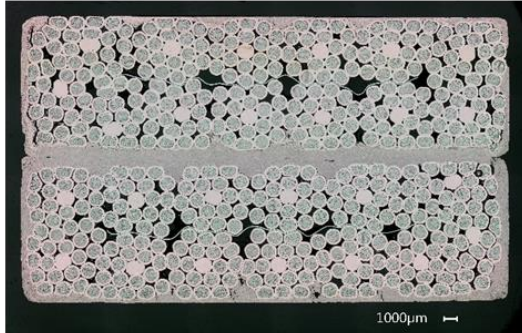
Sample #3 - tail of the Nb$_3$Sn joint   Sample #4 - center of the Nb$_3$Sn joint
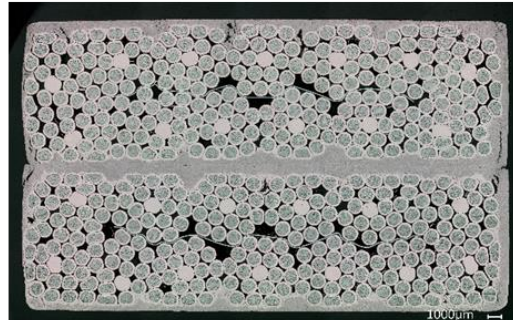
Figure 4.47 *Samples for the metallographic analysis.*

By comparing the samples, it is possible to reconstruct the metallographic evolution of the joint during the manufacture steps.

The analyses were carried out in collaboration with the Engineering Department of CERN [104] and in their laboratories.

Magnifications at the digital microscope of the interface between strands and coating of sample #2 highlighted that the sandblasting of the cable surface, performed by hand by the operator, did not remove completely the chromium from the surface (Figure 4.48). Chromium is more resistive than copper, but, given its limited size ($\sim\mu m$), it should not have an impact on the joint resistance.

The observations of the compositions of the coated layer highlight the difference in shape of the copper oxides distribution in the instants before (sample #2) and after diffusion-bonding (samples #3-4). The Energy-dispersive X-ray spectroscopy (EDX), which allows to identify the elemental compositions of objects, confirmed that the grey spots seen with the digital microscope correspond to copper oxide. As shown in Figure 4.49, such oxides are first present in an elongated form, before the diffusion-bonding heat treatment, and subsequently in globular form. Moreover, the automatic analysis system measures in samples #3-4 a concentration of 40 ± 5 % of the oxides, higher than the 10-20 % range given by the thermal spray company (Table 4-2), likely because the coating process was not carried out in an inert atmosphere. We exclude that the 20-30 % difference comes from the diffusion-bonding process, as it can be noticed that a comparable concentration of oxides is already present in the not diffusion-bonded sample #2. The porosity concentration is instead within the range declared in Table 4-2, i.e. 5-10 %. Despite the high concentration of oxides, their conversion into a globular form during the joint formation enhances the connectivity of copper, the reason why the electrical resistance assessed in Section 4.4.3 is low and within the target.

The contact between strands and coated layer is not homogeneous, as shown in Figure 4.50c. This is a consequence of the fact that the interstices between sub-cables are the deepest points and are therefore more difficult to access by the molten particles.

By collecting a series of zoomed images as the one in Figure 4.50b, it is possible to determine the extension of the contact line between the diffusion-bonded surfaces of the coating of the two cables. In particular, it was measured that the non-contact interface, namely pores, consists of 2255 out of 34942 μm (5.5 %) along the joint width of sample #3, whilst for sample #4 this corresponds to 1338 out of 36169 μm (3.7 %). This percentage difference between a cross-section taken at the tail and at the centre of the joint is a consequence of the inhomogeneous flatness of the milled surface, as visible in Figure 4.14e, as well as of the inhomogeneous temperature along the forming joint during-diffusion bonding, as already discussed during the joint design and manufacture in Sections 4.4.1 and 4.4.2.
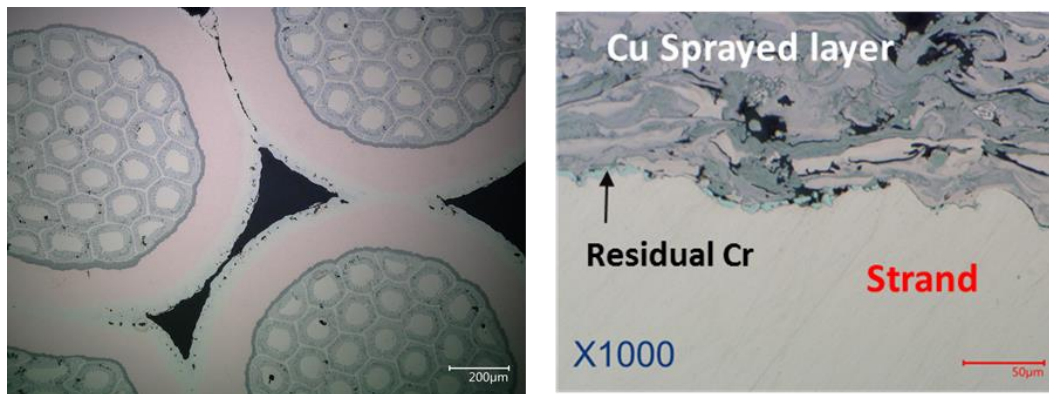
Figure 4.48 *Comparison between the chromium layer of the strands (left) and its residues after sandblasting of the surface of the cable (right).*
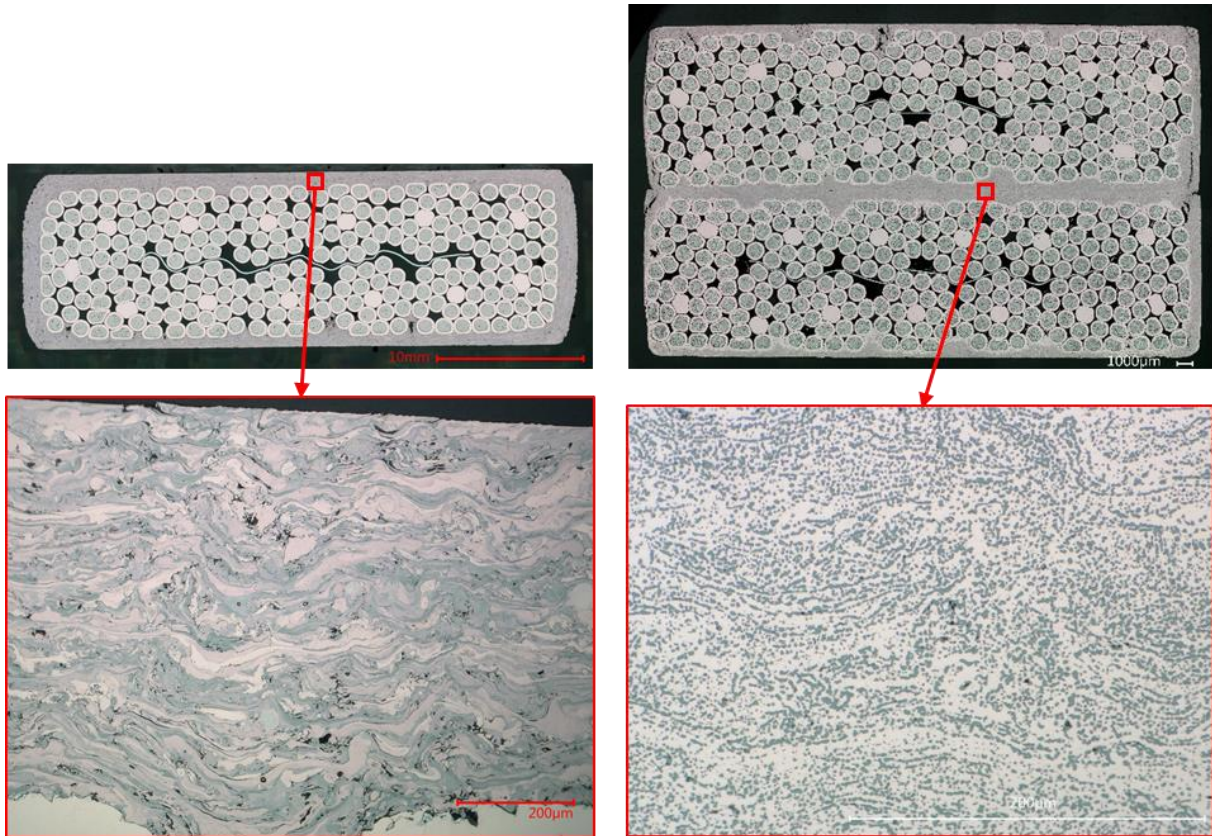
Figure 4.49 *Magnification at the digital microscope of the oxides (grey) and porosities (black) in the coating of the reacted Nb₃Sn cable after thermal spray (left) and diffusion-bonding (right).*
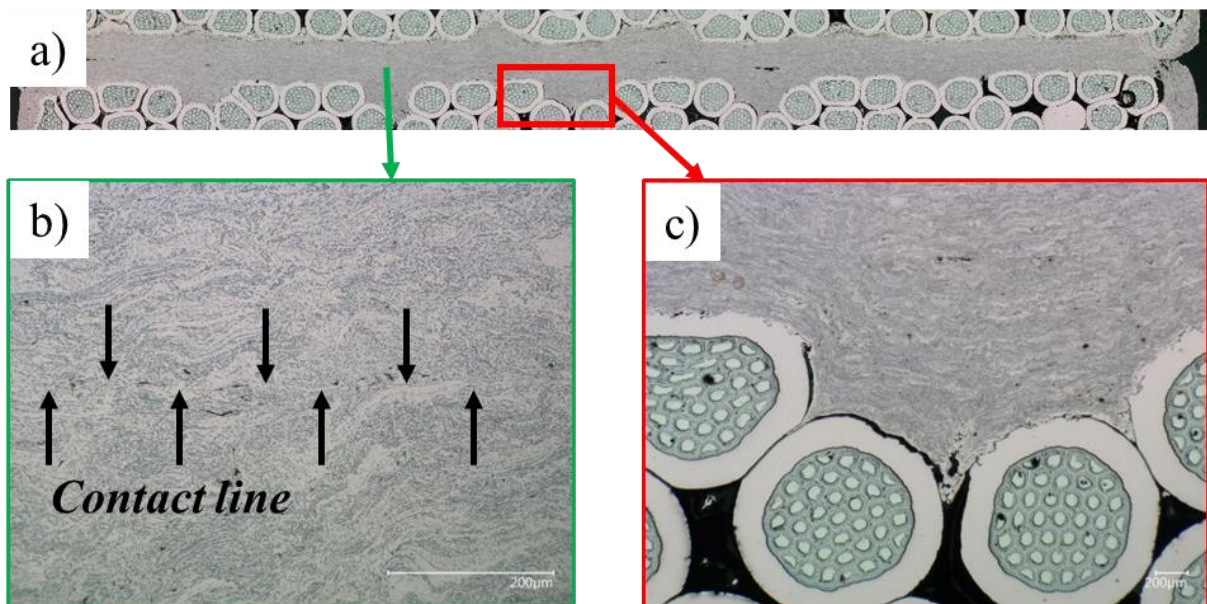
Figure 4.50 *Diffusion-bonded joint with magnification on the contact line between the two coatings (bottom left) and interface between strands and copper coating (bottom right).*

In conclusion to this section, the metallographic analyses of the sprayed layer after diffusion-bonding are in line with the measured degree of copper purity, i.e. RRR=70 (Section 4.4.1). In particular, the presence of the oxides catalyses the impurities that would contaminate copper.

The chromium residues at the strand-coating interface, the concentration of oxides and pores, and the inhomogeneous contact between strands and coating decrease the effective area for the passage of current through the coated layer, as already observed in the comparison between expected and measured results of Section 4.4.3. The chromium residues might be removed by a better control of the sand-blasting process. In the case of this thesis, the sand-blasting procedure was carried out manually by the operator, but its automation can be envisaged in view of an industrial application. Such an automation would favour a homogenized application of sand-blasting on the cable surfaces. The concentration of oxides could be diminished by providing an inert atmosphere during thermal spray, for instance as it was done during the diffusion-bonding procedure illustrated in Section 4.4.2. In alternative, a more complicated and expensive thermal spray technique like plasma spraying or high-velocity oxygen fuel might be chosen. A more homogeneous contact surface between the two cables might be achieved with another thermal spray technique as well, since the better coating quality should improve the machinability of the surfaces to flatten.

Despite the presence of these defects, the requirements on the electrical performance are fulfilled. Nevertheless, if in another joint application should require a lower resistance than the target of this thesis, these conclusions could provide helpful suggestions.

4.4.5 Mechanical analysis of the joint in the DEMO TF coil

The joint has to withstand the mechanical stresses that arise during operation. In this section, such stresses are computed for the joint between the first and second innermost layer of the DEMO TF through FEA modelling using the software ANSYS. The analysis starts with the assumption of a zero stress intensity at room temperature. Given this initial condition, the model takes into account the cool-down of the TF magnet from room temperature to 4.5 K and the electromagnetic forces due to the interaction of the current with the field generated by the TFs, CS and PFs in the plasma pre-magnetization phase, i.e. when the plasma discharge is about to begin and the CS provides the maximum field. The stresses in the joint are not expected to be sensitive to the particular plasma scenario.

Computational strategy

The objective is to determine the stresses in the joint, which require a level of detail in the order of the ~mm. The TF has a characteristic length of ~10 m. Nevertheless, the modelling of its components would require the same level of detail as the joint. The search for a solution to such a numerical model would require a considerable numerical effort. In order to make the computation affordable, components out of the goal of the analysis are merged together. Their actual thermomechanical properties are substituted with homogenized properties, also called smeared properties. In particular:

- The superconducting cable, the segregated stabilizer, the turn and layer insulation of the first layer (L1) are substituted with a unique object with homogenized mechanical properties.
- The same procedure is applied to the second layer (L2).
- The layers from 3 to 12 (L3-L12) are unified in a unique object, using the same procedure.

The smeared properties of the three macro objects (L1, L2 and L3-L12) are implemented in the mechanical model of the TF with a "coarse" mesh, i.e. still not fine enough for describing in

detail the stresses generated in the joint. The output of the model of the TF is a coarse distribution of displacement, strain and stress in the magnet. A sub-domain of the TF containing the joint is afterwards analysed in closer detail. As boundary conditions, the displacements derived from the coarse model are imposed on the cut surfaces of the sub-domain and a more precise solution is found far from the boundary conditions. This procedure is justified by the Saint-Venant's principle, which states that the effects at a sufficient distance from the boundaries are the same for two different boundary load distributions being statically equivalent. As a consequence, even if the coarse displacement field of the coarse global model is used to define the boundary conditions on a detailed sub-domain, here there will be an equivalent but more accurate representation of the local stresses.

The same sub-domain extraction procedure is implemented one more time to model the details of the joint. The described steps and the strategy approach are summarized in Figure 4.51.
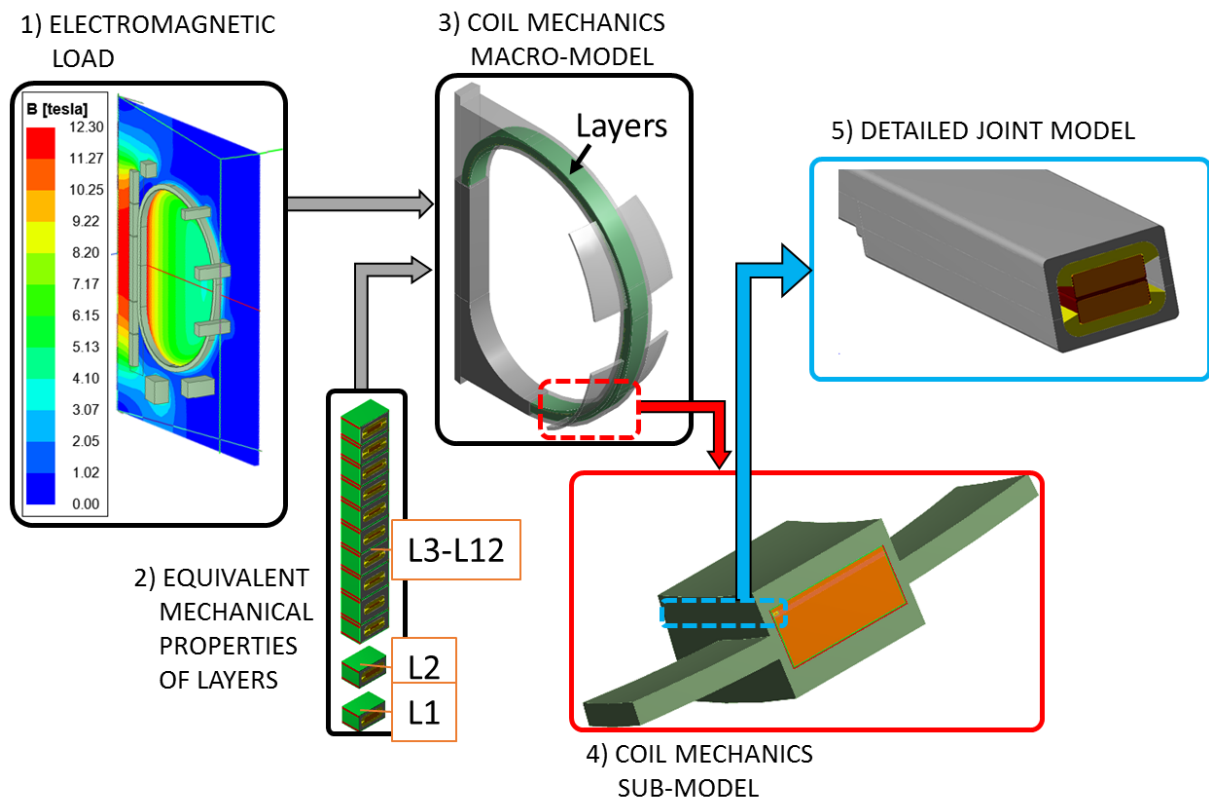
Figure 4.51 *Steps for the computation of the stresses in the joint between first and second innermost TF layer.*

Magnetic field computation

The magnetic field computation is performed taking into account the current of TFs, CS and PFs at the pre-magnetization phase, according to the 2015 DEMO baseline. The symmetry of the magnet system is exploited and the computational domain is 1/18 of the total one. The results are reported in Figure 4.52. The electromagnetic force distribution is computed and exported to the mechanical module.

117
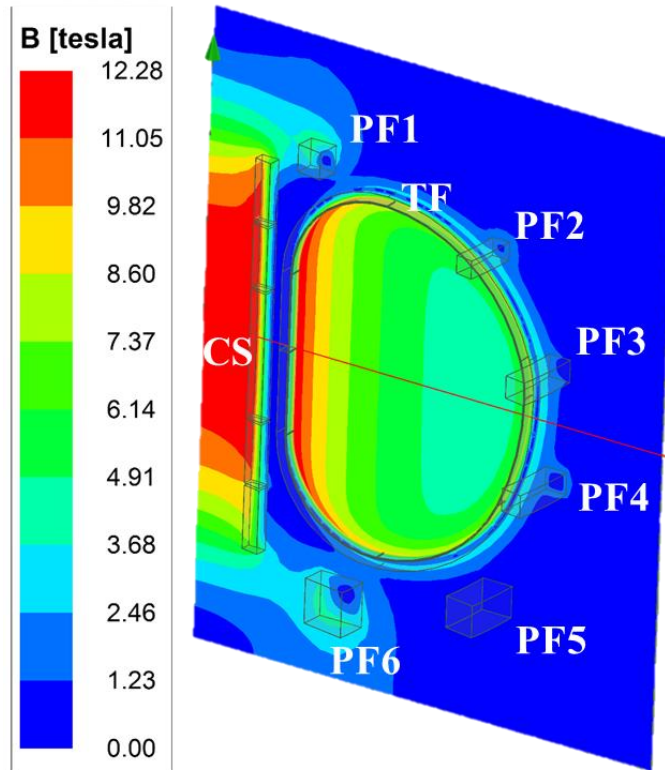
Figure 4.52 *Magnetic field intensity at the pre-magnetization phase.*

Smeared mechanical properties

The computation of the smeared mechanical properties of L1, L2 and L3-L12 consists in finding the equivalent mechanical properties of a homogenized object, whose components (cable, segregated stabilizer, jacket and insulation) are considered glued together. In particular, for each of these three objects, one has to find the following orthotropic thermomechanical properties:

- The Young's modulus in the three directions, namely E_x, E_y and E_z [GPa].
- The Poisson's ratios, namely v_{xy}, v_{yx}, v_{xz}, v_{zx}, v_{yz} and v_{zy}.
- The shear moduli, namely G_{xy}, G_{xz} and G_{yz} [GPa].
- The thermal expansion coefficient in the three directions, namely α_x, α_y and α_z [K^{-1}].

The relation between these parameters and the normal (σ) and shear (τ) components of the stress state, normal (ε) and parallel (γ) components of the strain state is given in the matrix system (4. 10), valid for bodies at constant temperature.

$$\begin{bmatrix} 1/E_x & -v_{yx}/E_y & -v_{zx}/E_z & 0 & 0 & 0 \\ -v_{xy}/E_x & 1/E_y & -v_{zy}/E_z & 0 & 0 & 0 \\ -v_{xz}/E_x & -v_{yz}/E_y & 1/E_z & 0 & 0 & 0 \\ 0 & 0 & 0 & 1/G_{xy} & 0 & 0 \\ 0 & 0 & 0 & 0 & 1/G_{xz} & 0 \\ 0 & 0 & 0 & 0 & 0 & 1/G_{yz} \end{bmatrix} \begin{pmatrix} \sigma_x \\ \sigma_y \\ \sigma_z \\ \tau_{xy} \\ \tau_{xz} \\ \tau_{yz} \end{pmatrix} = \begin{pmatrix} \varepsilon_x \\ \varepsilon_y \\ \varepsilon_z \\ \gamma_{xy} \\ \gamma_{xz} \\ \gamma_{yz} \end{pmatrix} \qquad \textbf{(4. 10)}$$

118

The procedure to find these equivalent mechanical properties is described in detail in [105] and has to be repeated for L1, L2 and L3-L12. In particular, to find the equivalent Young's moduli and the Poisson coefficients:

- On a unit cell (Figure 4.53), an elementary displacement u_j along the direction j is applied on one of the two faces perpendicular to j, while imposing $u_j = 0$ on the opposite surface.
- The stress and strain components are extracted from each element of the simulation and the average of each one is computed in the volume of the unit cell.
- As the stress component $\bar{\sigma}_j$ is the only one different from zero, it is possible to compute E_j, v_{ij} and v_{kj} by applying the System (4. 10), being i and k orthogonal to each other and to j.

To assess the equivalent shear moduli, the procedure is similar but the elementary displacements are parallel to the faces of the unit cell. In the example reported in Figure 4.54:

- The elementary displacement u_x is applied to one of the two faces parallel to the xz plane, while on the opposite one $u_x = 0$ is imposed.
- u_y is imposed on one of the two faces parallel to the yz plane, while on the opposite one $u_y = 0$ is imposed.
- The stress and strain components are extracted from each element of the simulation and the average of each one is computed in the volume of the unit cell.
- From the shear stress $\bar{\tau}_{xy}$ it is possible to compute G_{xy}.

The equivalent coefficients of thermal expansions are assessed by applying the temperature difference $\Delta T = (293-4.5)$ K to the unit cell. The correspondent coefficients are $\alpha_j = \bar{\varepsilon}_j / \Delta T$ for each direction j.

The actual material properties are given as input parameters and are summarized in Table 4-4, while the output smeared properties of the homogenized components L1, L2 and L3-L12 are summarized in Table 4-5. In particular, it can be noticed that the equivalent homogenized components have a higher Young's modulus along z, i.e. the winding direction, because the stainless steel jacket, the stiffest component, has the same dimension as the other materials in the extrusion orientation. Moreover, it can also be seen that the stiffness increases while going from the innermost to the outermost layer, as the quantity of steel increases in the same direction.
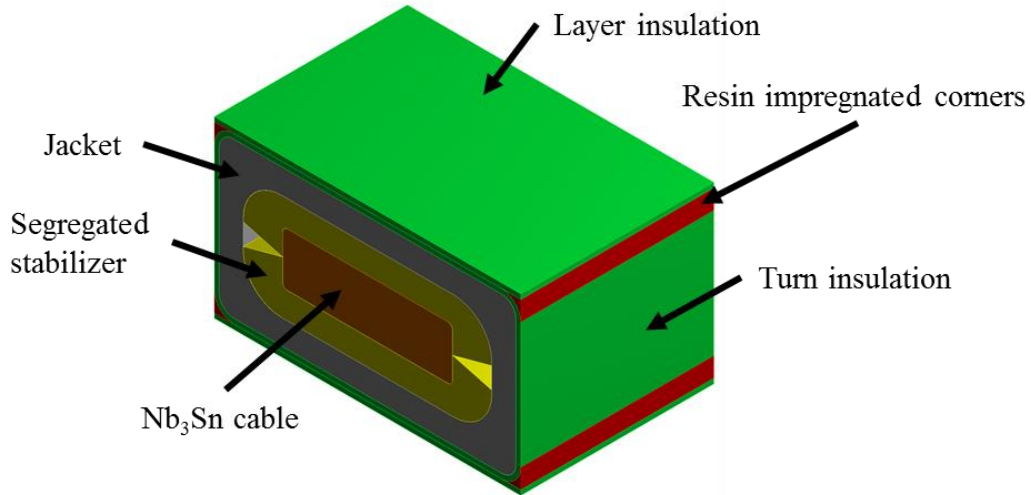
Figure 4.53 *Unit cell for the computation of the smeared thermomechanical properties of L1.*
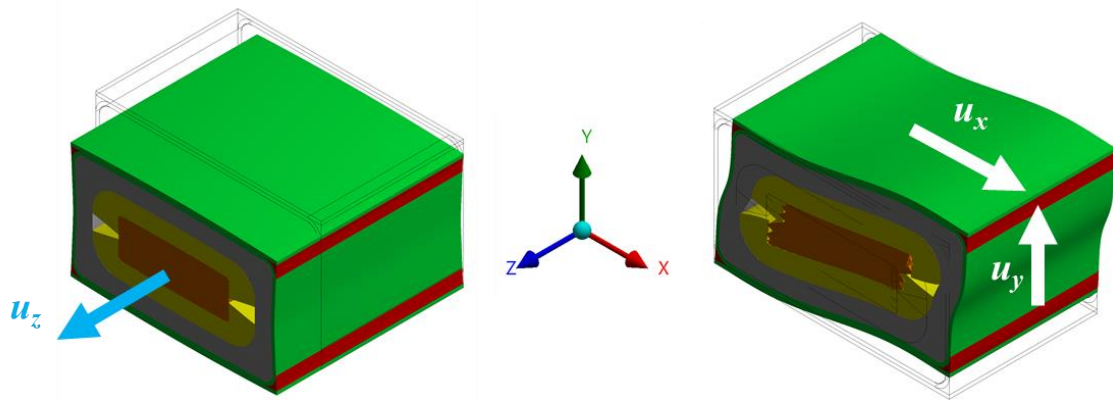
Figure 4.54 *Elementary displacements to extract the smeared properties of the unit cell.*

Table 4-4 *Material properties at T=4.5 K of the components of the unit cell.*

Component	Material	Properties			
		E	v	G	α
		(GPa)	(-)	(GPa)	(K^{-1})
Jacket [106]	AISI 316 LN	205.0	0.29	79.5	$10.7 \cdot 10^{-6}$
Superconducting cable	Non-Cu, Cu, void fraction	0.31	0.30	0.2	$10.4 \cdot 10^{-6}$
Segregated stabilizer	Cu, Cu-Ni	137	0.36	50.5	$11.3 \cdot 10^{-6}$
Corners [106]	Epoxy resin	7.0	0.30	2.7	$17.3 \cdot 10^{-6}$
Turn/layer insulation [106]	Vacuum pressure impregnated epoxy glass	20.0 (E_x)	0.17 (v_{xy})	6.0 (G_{xy})	$6.9 \cdot 10^{-6}$ (α_x)
		20.0 (E_y)	0.33 (v_{yz})	6.0 (G_{yz})	$6.9 \cdot 10^{-6}$ (α_y)
		12.0 (E_z)	0.33 (v_{xz})	6.0 (G_{xz})	$24.7 \cdot 10^{-6}$ (α_z)

Table 4-5 *Smeared mechanical properties of L1, L2 and L3-L12 at T=4.5 K.*

	L1	L2	L3-L12
E_x (GPa)	88.2	96.1	119
E_y (GPa)	29.8	29.7	44.7
E_z (GPa)	122	128.1	149
ν_{xy} (-)	0.68	0.65	0.32
ν_{yx} (-)	0.16	0.14	0.14
ν_{xz} (-)	0.20	0.22	0.25
ν_{zx} (-)	0.31	0.31	0.30
ν_{yz} (-)	0.12	0.11	0.11
ν_{zy} (-)	0.24	0.24	0.28
G_{xy} (GPa)	10.9	11.8	18.2
G_{xy} (GPa)	34.9	37.1	43.2
G_{yz} (GPa)	15.5	15.5	21.4
α_x (K^{-1})	$10.7 \cdot 10^{-6}$	$10.6 \cdot 10^{-6}$	$10.6 \cdot 10^{-6}$
α_y (K^{-1})	$10.1 \cdot 10^{-6}$	$9.27 \cdot 10^{-6}$	$10.2 \cdot 10^{-6}$
α_z (K^{-1})	$11.2 \cdot 10^{-6}$	$10.6 \cdot 10^{-6}$	$11.1 \cdot 10^{-6}$

TF and joint mechanics

The winding pack is inserted and resin-impregnated in the case of the TF for structural support. The TFs are linked each other through the outer intercoil structures (OIS), which react against the lateral deflections of the TF caused by the out-of-plane electromagnetic load (Figure 4.55).

The mechanical calculation involves the cool-down from room temperature to 4.5 K and the import of the electromagnetic forces from the electromagnetic module. The stresses in the winding pack are shown in Figure 4.56 at the pre-magnetisation phase. The largest stresses lie on the last layer, where the force of the other layers cumulate and push against the case towards the CS direction.
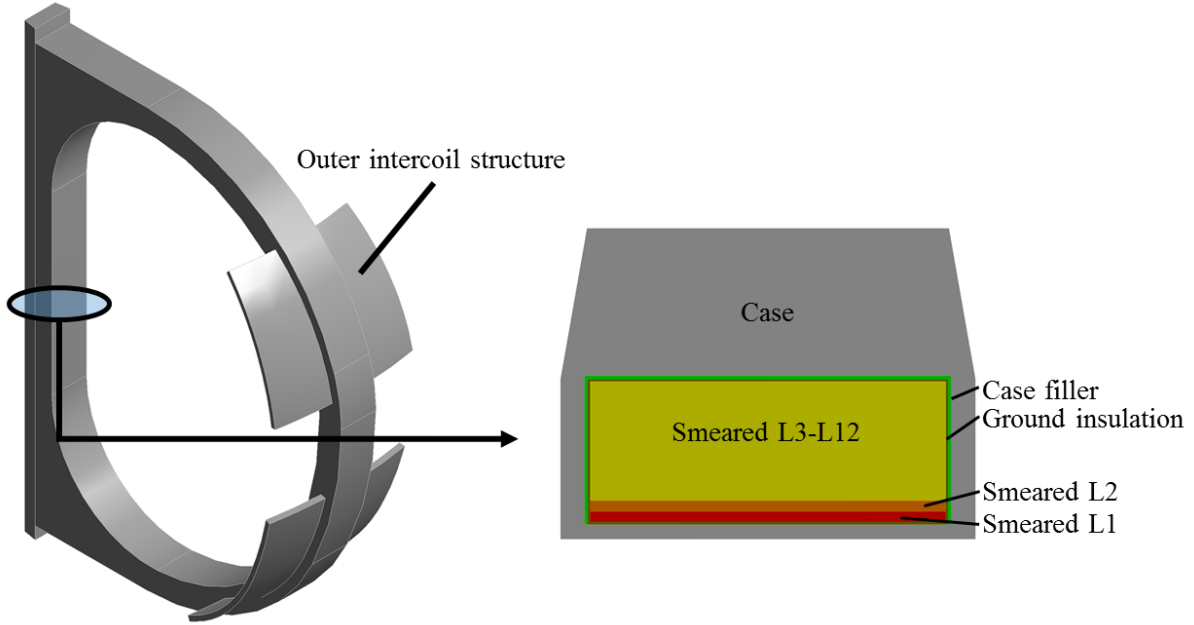
Figure 4.55 *Main components of the DEMO TF for the mechanical calculation.*
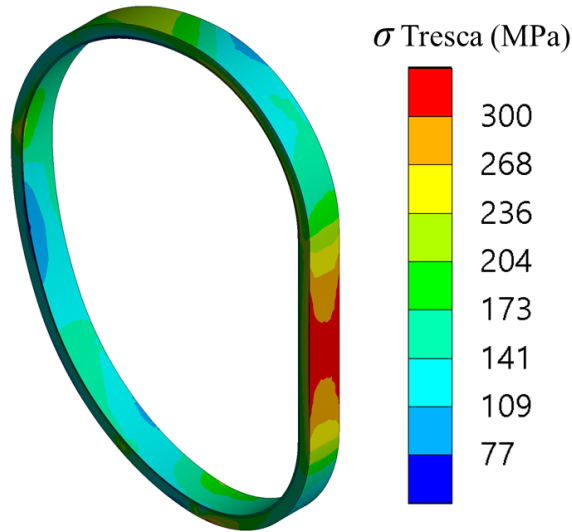
Figure 4.56 *Tresca stress distribution in the winding pack at the pre-magnetisation phase.*

The macro-model serves to impose the boundary conditions in the sub-model that includes the joint. In the latter, it is possible to compute the hoop force acting on the joint during operation, which is $F_{hoop} = 268\ kN$ (Figure 4.57). If there was no structural support, this force would be entirely transmitted to the joint surface, i.e. to the copper coating. In this case, the average shear stress would be $\bar{\tau} = F_{hoop}/(w*L) = 19\ MPa$, being w=35.2 mm the width of the superconducting cable and L=400 mm the overlap length of the joint. Nevertheless, most of this force reacts in the jacket, stiffer than the joint, resulting in a much lower average shear stress on the joint surface, as reported in Figure 4.58. Even in the pessimistic case of $\bar{\tau} = 19\ MPa$, the copper would withstand this stress intensity without yielding or breaking, as $\sigma_Y = 86\ MPa$ [107] and $\sigma_U = 310\ MPa$ [107] are the yield and the ultimate tensile strength, respectively. This pessimistic $\bar{\tau}$ value could be instead higher than the coating pull strength

range 10-30 MPa cited in Table 4-2, which would imply the detachment of the coating from the strands. However, this should not be a concern, as this $\bar{\tau}$ value is very pessimistic.

The average Tresca stress takes into account the combination of the principal stress components, among which the pressure created by the local Lorentz force. The average Tresca stress on the joint surface is about 100 MPa, according to the numerical computation. This could bring to the plasticization of copper with subsequent relaxation of the stresses, without leading to a joint failure.

In conclusion, it must be reminded that the joint is an object constituted by Nb_3Sn strands bonded with a heterogeneous copper coating being in turn bonded with the sprayed layer of the other cable, its mechanical properties are different than pure copper. It is not straightforward either to judge which the weakest point of the joint is, whether the strand-coating or the coating-coating contact, or which is the strength of such interfaces without a test designed on purpose.
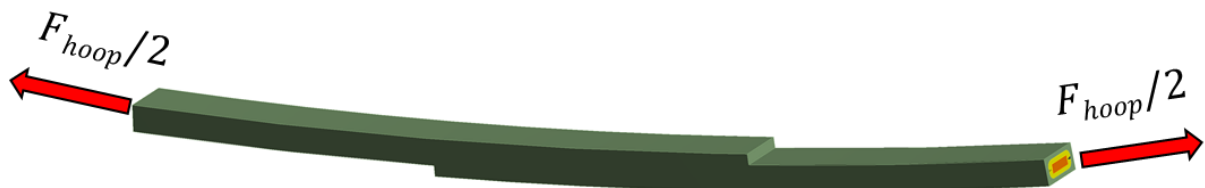
Figure 4.57 *Direction of the hoop force in the joint region.*
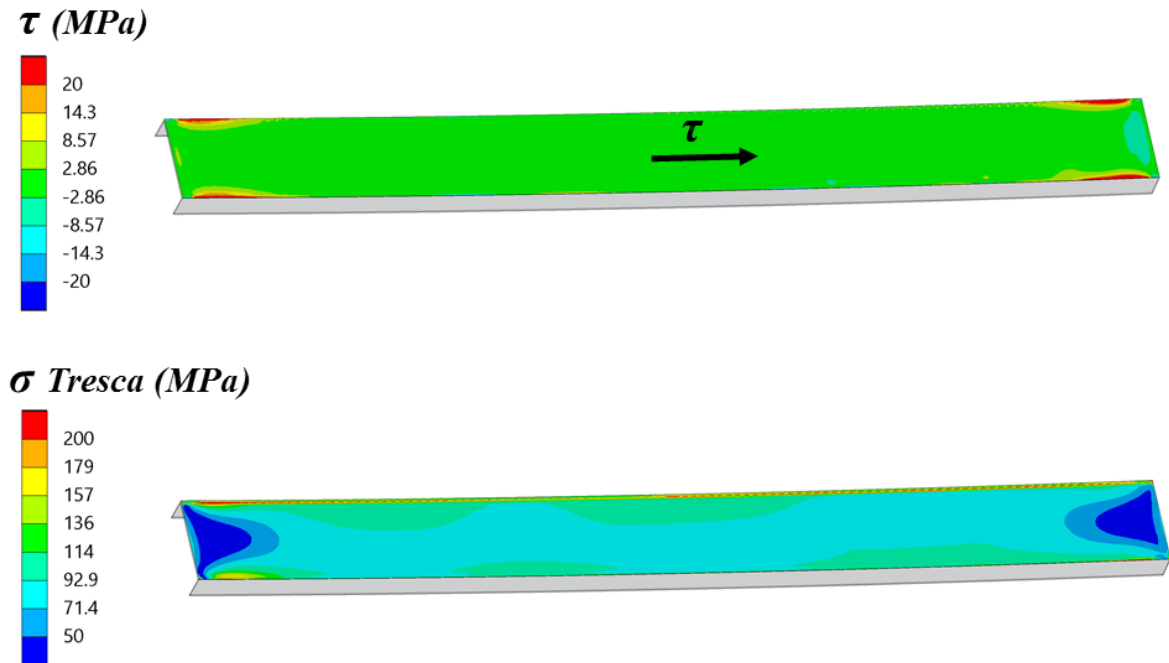
Figure 4.58 *Shear stresses along the cable length (top) and Tresca stress (bottom) distribution on the coating of the joint surface.*

4.4.6 Assembly procedure in a layer-wound RW Toroidal Field coil

The steps involved in the assembly sequence of the developed joint are summarized in this section through a series of sketches. The vertical winding set-up of the TF is taken as an example. These steps involve:

- The winding of the first layer.
- The removal of insulation, jacket and segregated stabilizer from the cable sections to splice (Figure 4.59).
- The copper-coating through a thermal spray technique of the section of first and second layer, the latter being still in the spool, to splice (Figure 4.60-Figure 4.61-Figure 4.62).
- The insertion of the cables into the diffusion-bonding clamp and its assembly (Figure 4.63).
- The assembly of the equipment for the inductive oven and the inert atmosphere (Figure 4.64).
- The diffusion-bonding procedure.
- The disassembly of the diffusion-bonding equipment.
- The reassembly of segregated stabilizer, steel jacket and turn insulation (Figure 4.65).
- The winding of the second TF layer.
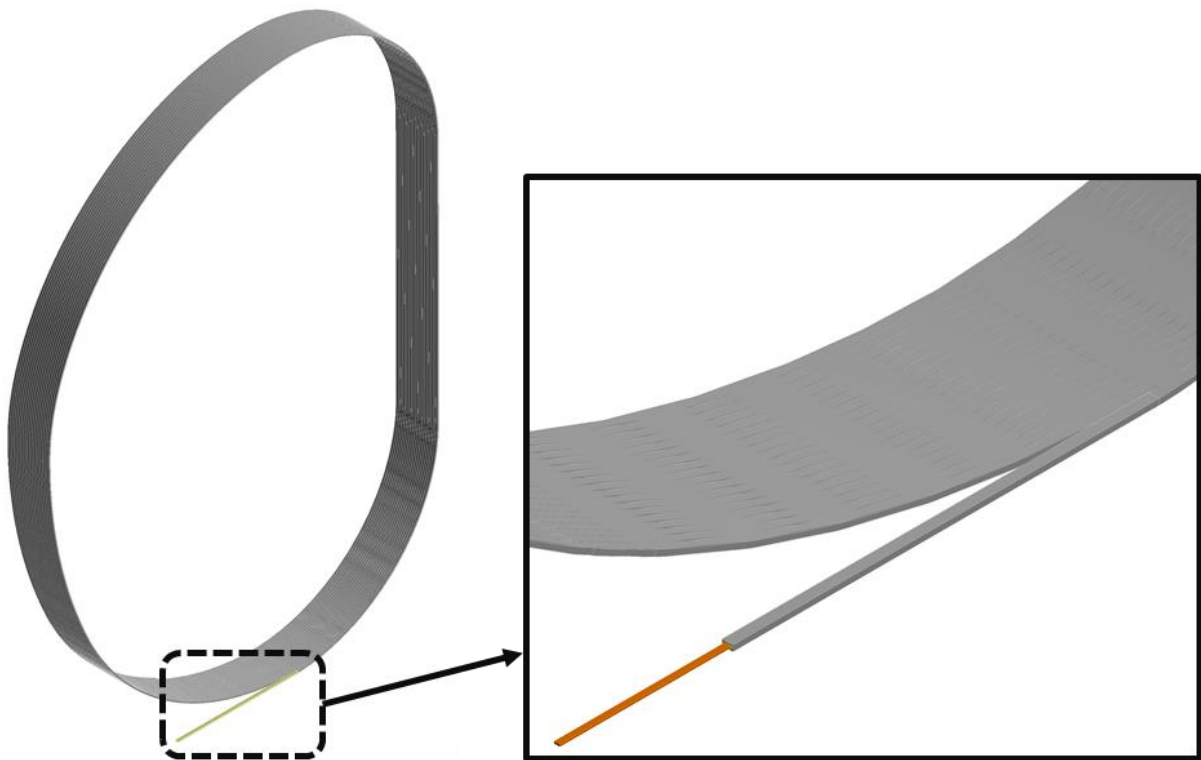
Figure 4.59 *Removal of the segregated stabilizer and jacket from the cable section of the first layer to splice.*
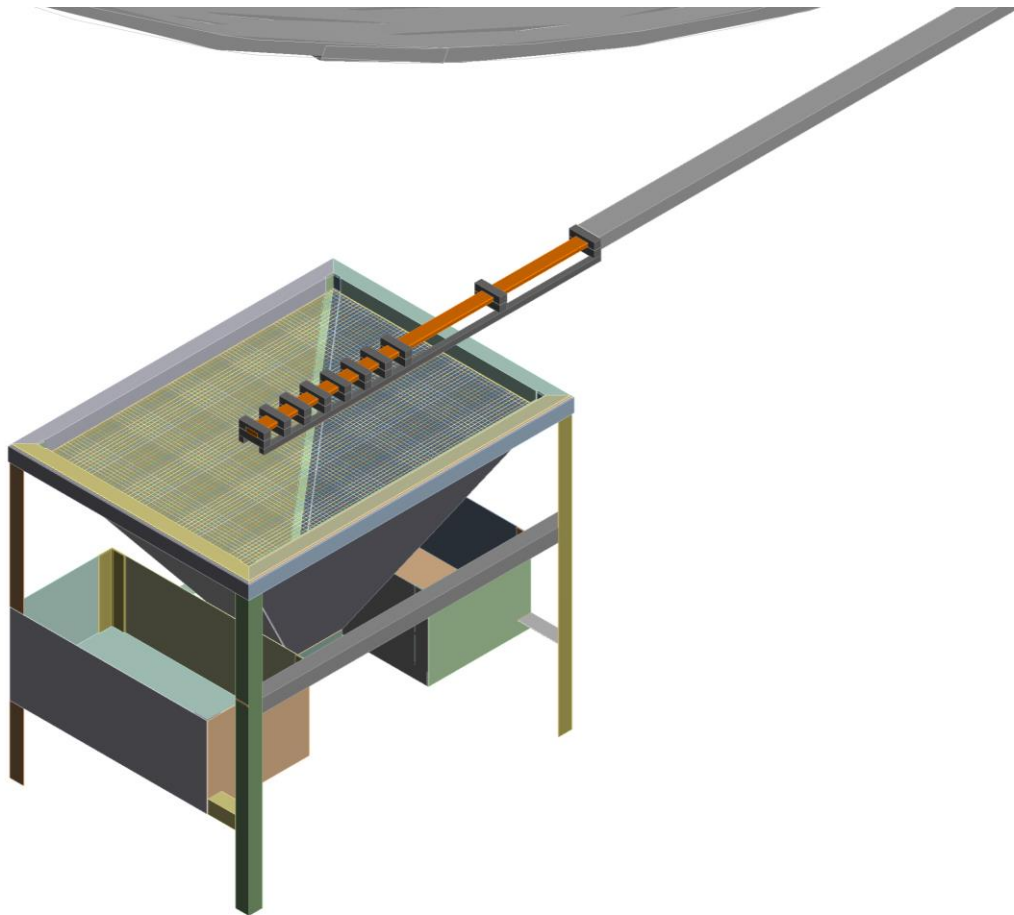
Figure 4.60 *Aluminium clamps assembly prior to sandblasting and copper thermal spray.*
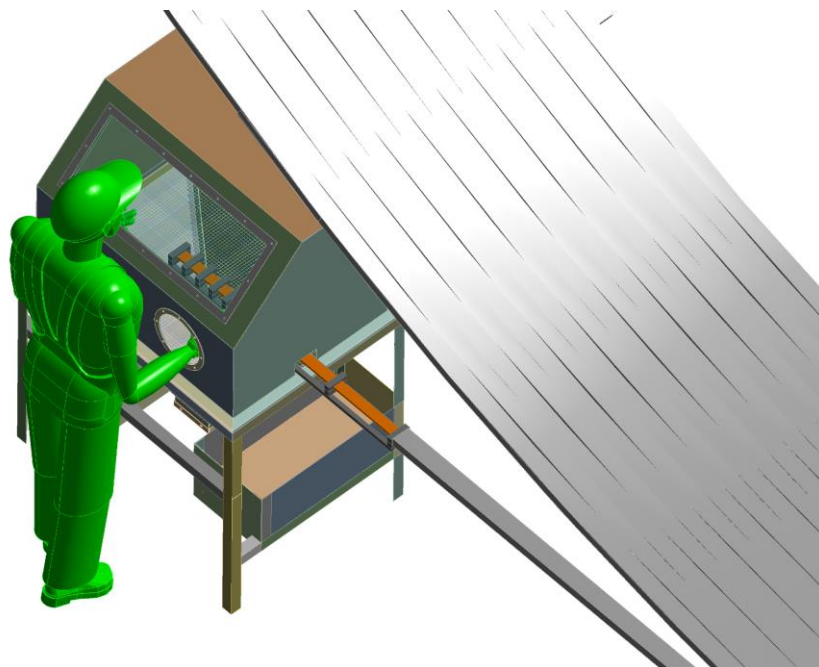
Figure 4.61 *Cabinet for the first stage of sandblasting and copper thermal spray.*
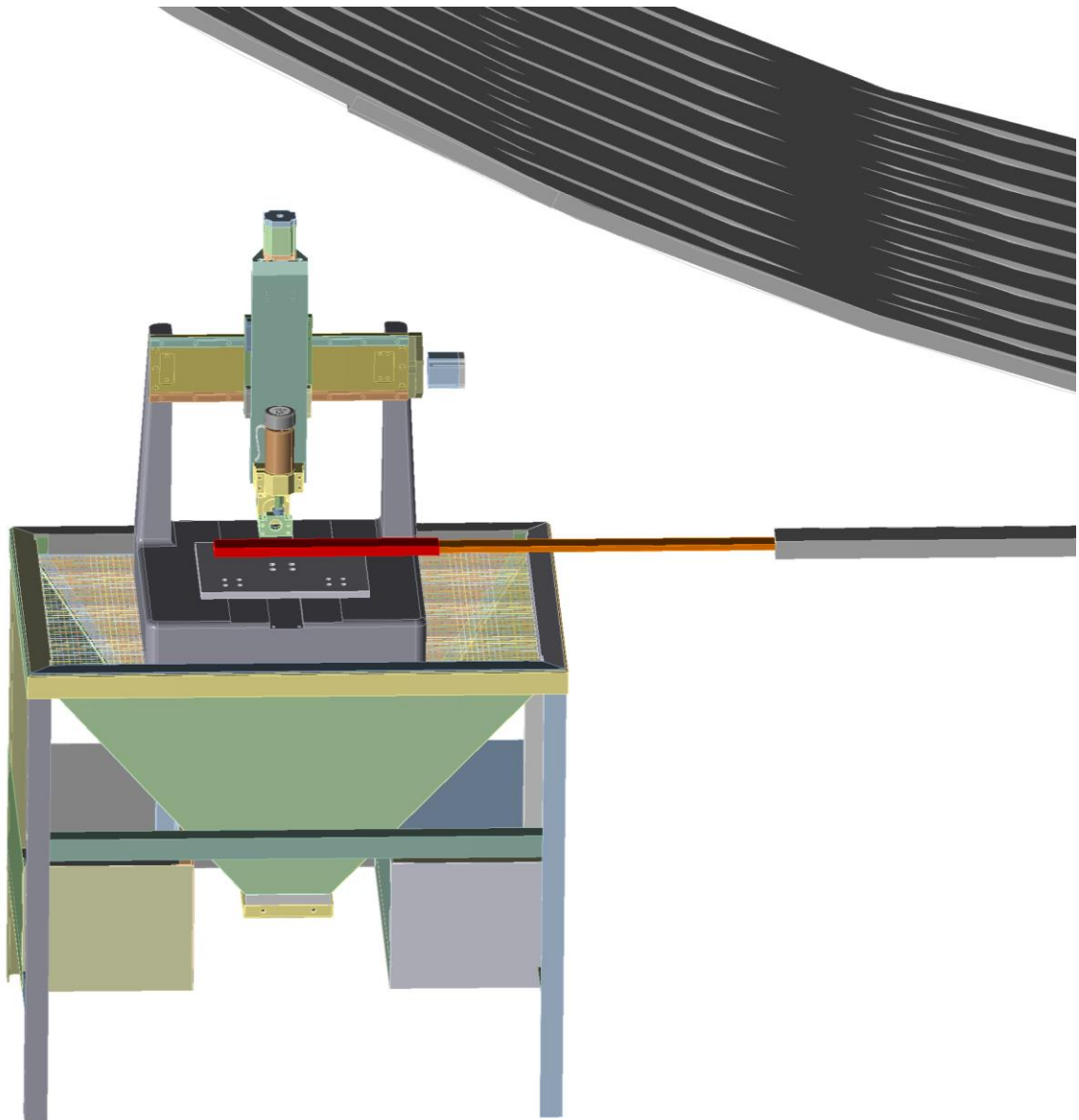
Figure 4.62 *Milling of the copper coating.*
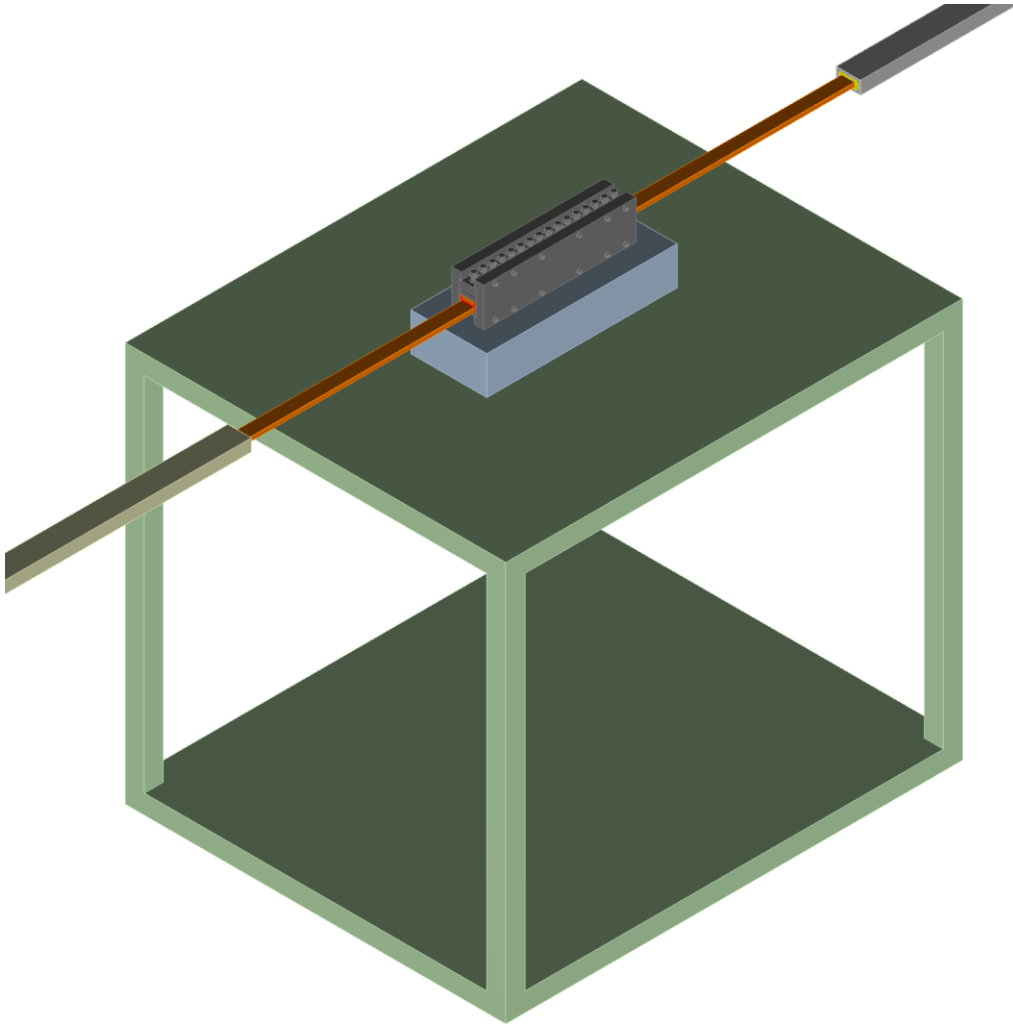
Figure 4.63 *Insertion of the cables into the diffusion-bonding clamp.*
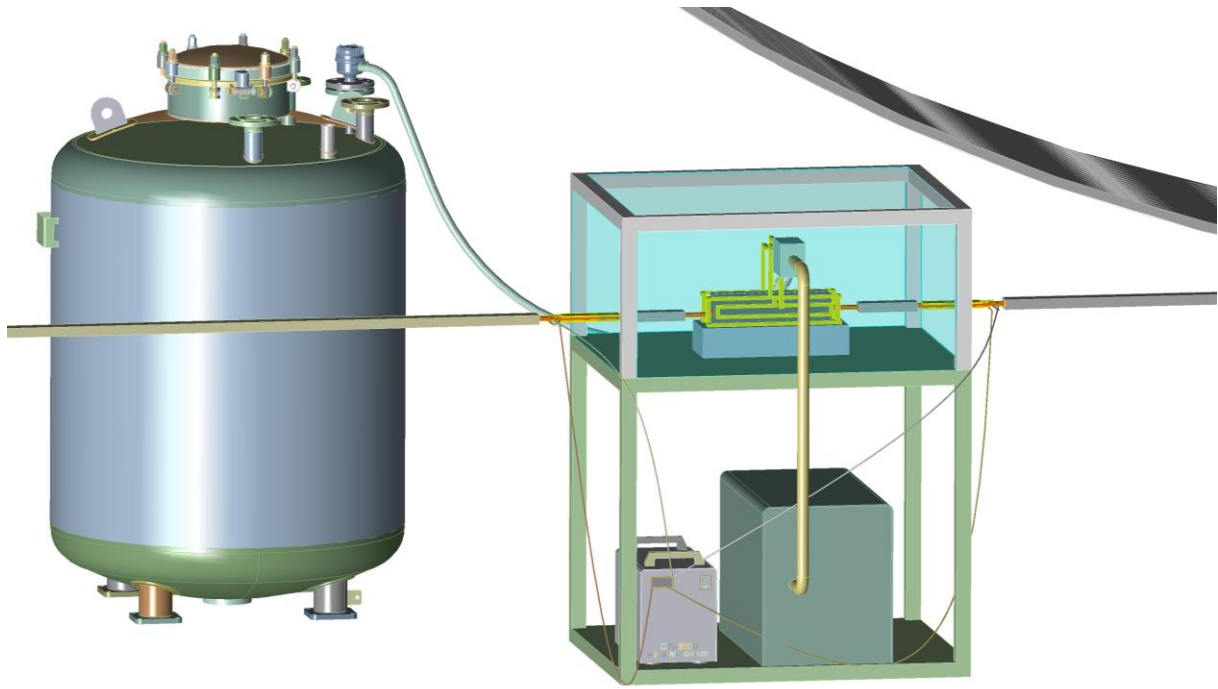
Figure 4.64 *Diffusion-bonding set-up: inductive oven, N₂ dewar for the inert atmosphere and chiller for the cool-down of the extremities of the conductor.*
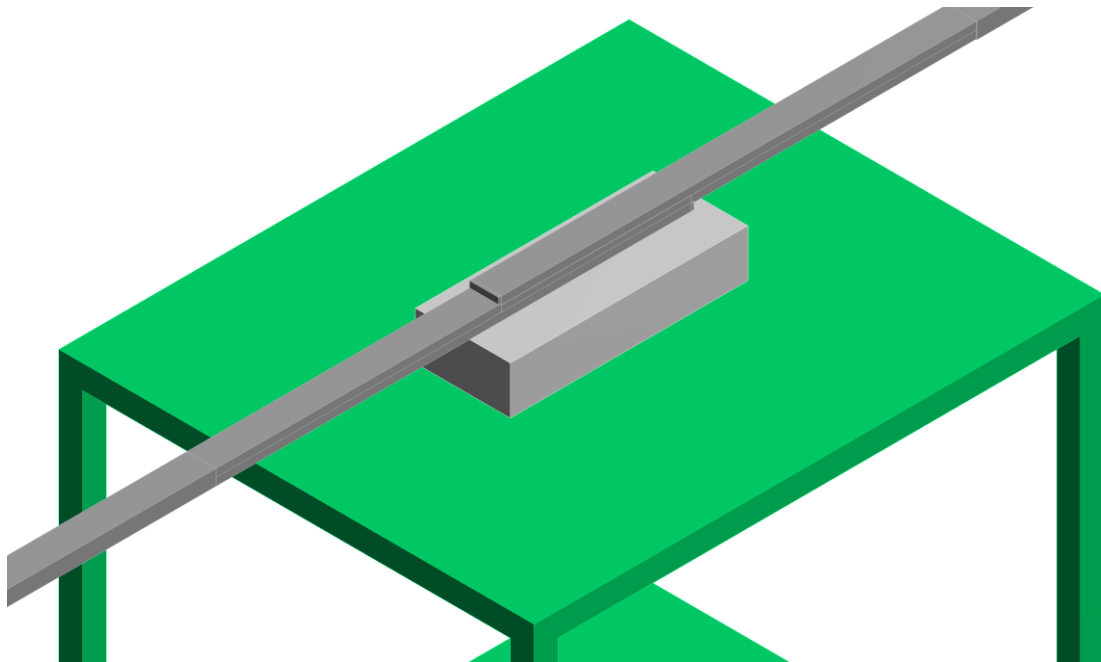
Figure 4.65 *Reassembly of segregated stabilizer, jacket and turn insulation.*

4.5 Summary and conclusions

A diffusion-bonded joint is proposed for building the electrical connections between the layers of the RW TF option for DEMO. With respect to classical soldered solutions, it is cleaner and has potentially a higher mechanical strength. The joints are built during the coil winding and are located at the surface of the winding pack, thus minimizing the space occupied and the amount of structural material involved. The interruption of the coil winding due to the single joint assembly can amount to about 2-3 business days. This includes the jacket and segregated

stabilizer removal from the section of the layers to join, the steps involved to splice the superconductor sections, and the reinstallation of the removed segregated stabilizer and jacket with the welding of the last one. This interruption must be multiplied times the number of joints, as winding and joint assembly proceed in series. The total time dedicated to the only joints assembly amounts to about one month for each TF, which has to be added to the assembly time of the magnet.

A joint prototype was developed taking into account the boundary conditions of the in-line winding: portable equipment, removable diffusion-bonding pressing clamp, local heating of the forming joint. The pressure is applied only at room temperature and its value at 650 °C depends on the thermal expansion coefficient of the materials, which were chosen to get a pressure gain with the temperature increase. Nevertheless, the actual pressure at diffusion-bonding temperature is unknown. An alternative way would be to provide an active system that adjusts the pressure. However, the fulfilment of the resistance requirements of the joint prototype demonstrates that this more complicated system is not essential.

The sample was electrically tested in SULTAN, demonstrating that the resistance is below 1 nΩ, namely R=0.48 nΩ before cyclic loading at the joint operating field and current (B=8 T and I=63.3 kA). The temperature is 5.1 K. This low resistance offers the magnet designer the possibility to implement a layer-by-layer grading because of the low dissipated power. In particular, the joint was tested at the same conditions in which the conductor was tested in previous experimental campaigns, i.e. 10.9 T and 63.3 kA, thus demonstrating its high range of operability without quench. The repetition of the resistance measurements after 1000 electromagnetic cycles at 8 T x 63.3 kA highlighted a light resistance degradation, namely +0.12 nΩ at B=8 T and I=63.3 kA, which is believed to occur at the transition between joint and conductor due to the sharp geometrical discontinuity in the mechanical support. This assumption is currently being verified at SPC by building a second joint prototype with modified jacket layout at the transition. Nevertheless, the number of mechanical cycles used in this test is still conservative with respect to the ones that a TF undergoes during its lifetime. Before this joint can be used in a CS coil, it must be checked if its degradation saturates with the number of mechanical cycles, as the expected one is 40'000 in a Tokamak like DEMO, thus much higher than the 1'000 cycles to which the sample prototype was exposed.

Other electrical tests involved the assessment of the AC losses, in which it was shown that the highest losses take place not in the joint but in the segregated stabilizer, whose design was already changed by SPC to decrease such power losses. In the end, a stability test with fast field rate showed that the joint is stable at the point that it should not suffer from the most rapid field rate that could occur in operating and accidental scenarios.

The measured electrical properties were linked to the metallographic characteristics of the joint, in particular to the strand-coating interface, the bulk of the copper coating and the coating-coating interface. Such copper coating is deposited by the arc spraying technique. The metallographic analyses highlight a series of imperfection and impurities, such as the inhomogeneity in the strand-coating contact, the oxidation of the coating and the inhomogeneity of the contact between the two diffusion-bonded surfaces. Nonetheless, the electric resistance remains low enough for the present application. However, there is still margin of improvement and, if a lower resistance should be needed in another application, it is suggested to either provide an inert atmosphere during the copper thermal spray procedure or to use a more sophisticated thermal spraying technique.

Such a joint will be subject to the electromagnetic forces to which a TF magnet is exposed and, in particular, to the local Lorentz force (pushing the conductor transversely) and the hoop force (pulling the conductor longitudinally). Through a static finite element analysis, it was shown that most of the forces are taken by the jacket and that the stresses could bring to the plasticization of the sprayed copper layer without reaching the ultimate strength. Nevertheless, the joint is a heterogeneous object whose mechanical properties are not fully known. In particular, the assessment of the strength of the strand-coating and coating-coating bonding go beyond the scope of this thesis. For the future, it is recommended to design and carry out mechanical tests specifically addressing the mechanical strength of such a joint concept.

5. Conclusion

The main objective of this thesis was twofold, namely the development of a high-field, high-current joint between Nb$_3$Sn cables for Wind&React high energy physics (HEP) magnets and React&Wind thermonuclear fusion coils of the next generation. For both, the target was achieved.

Regarding Wind&React HEP magnets, two types of splices to embed in the winding pack were designed and successfully tested in SULTAN. One of the types is based on diffusion-bonding, taking place during the cable heat treatment. A diffusion-bonding clamp fulfilling the requirements of holding the winding tension, integration into the head of the dipole magnet, and applying an adequate pressure distribution was presented. In particular, the test in SULTAN demonstrates that it is possible to obtain a low-resistance joint without an active system regulating the pressure, which is set at room temperature and let evolve at 650 °C, when most of the bonding takes place. This result, which exploits a combination of materials having different thermal expansion coefficient, is fundamental for the application in a coil, as this one is inaccessible during the reaction heat treatment. The resistance of the tested prototype is R=1.04 nΩ at B=10.9 T, T=5 K and I/I_c=0.63. The main challenge of this joint concept consists in its integration into the coil. In the framework of this thesis, the produced joint prototypes were tested as standalone. Therefore, before this splice can enter the industrial implementation phase, the manufacture and test of an insert coil with bent diffusion-bonded splice is recommended for the future R&D. In addition, it is recommended to assess the mechanical strength of such a joint concept, so that it can be checked against the splice stress foreseen in operating conditions in the magnet.

The second splice type for Wind&React HEP magnets is based on soldering, to be applied after the cable heat treatment. The issue of keeping the mechanical tension during winding is addressed by crimping the cable sections to splice with steel strips. The limited accessibility of the mated surfaces after heat treatment is addressed with the combination of flux and solder, Soldaflux K and Sn95Ag5 respectively, due to which the solder penetrates per capillarity and bonds with the two cable sections. With a reproducibility over six samples of ±0.09 nΩ, the resistance of the best prototype is R=0.58 nΩ at B=10.9 T, T=5 K and I/I_c=0.54. In view of the splice industrial implementation, it is recommended to investigate the minimum tightness of the crimping strips for holding the winding tension. As for the diffusion-bonded splice, a test aiming at assessing the splice strength is recommended, too.

The magnet designer has hence at least two splice options for a Nb$_3$Sn HEP coil with internal joints. Diffusion-bonding in bent geometry requires that the clamp is machined with particular precision to ensure that pressure is transmitted overall on the mated surfaces. For this reason, the clamp concept designed in the framework of this thesis might be more advisable for a block-

coil rather than for a cos-θ dipole magnet. In fact, the form of the dipole head of the latter requires a complicated shaping of the clamping fixture. The soldered splice option presented in this thesis foresees a "vertical" layout, i.e. both flux and solder are poured exploiting gravity. Therefore, we advise this technique for dipoles in which this soldering layout is possible.

Regarding React&Wind fusion magnets, a diffusion-bonded joint was designed and successfully tested in SULTAN. This time, diffusion-bonding takes place between reacted cables. Before mechanical cyclic loading, the resistance is R=0.48 nΩ at the joint operating field and current, namely B=8 T and I=63.3 kA. The temperature is 5.1 K. For a joint 400 mm long, its AC losses are about equal to twice those of the conductor. Beyond the low resistance at the joint nominal field, the test at full current and SULTAN highest field (I=63.3 kA and B=10.9 T) demonstrates that a possible degradation of the superconductor due to either the applied pressure on the fragile strands or the additional heat treatment of the conductor during diffusion-bonding is not an issue. Moreover, it was also proved that vacuum during diffusion-bonding is not essential for having a good bonding and that an inert atmosphere (N_2 in this thesis) is sufficient. Also in this case, an active system for the pressure control during diffusion-bonding is not required but, unlike in the case of Wind&React dipole magnets, it would be possible to implement it.

The joint showed a slight degradation upon cyclic loading, namely +0.12 nΩ at B=8 T and I=63.3 kA. In particular, 1'000 cycles at nominal current and field were carried out. This is acceptable, considering the cycles during the lifetime of a TF coil. The implementation of this joint in a CS coil, in which the amount of cycles is much higher, cannot be recommended yet. First, it should be checked if the observed degradation saturates with the number of cycles to an acceptable value. Moreover, a second joint prototype with modified jacket layout is being manufacture at SPC with the goal of mitigating this effect.

The objective related to the joint development was achieved and the procedure is ready for its industrial implementation. The developed splicing technique is proposed for the joints of the layer-wound DEMO TF designed by SPC. This allows the grading of the coil, by electrically connecting adjacent layers. More in general, the magnet designer can exploit the low ohmic losses and high operability range, in terms of current and magnetic field, of this joint also in other types of React&Wind magnets having rectangular conductor layout.

A. Appendix

A.1. Scaling law for superconductors

The critical surface of superconducting wires (or tapes, in case of HTS) is often described by scaling laws [108], which are a function of temperature T, magnetic field B and parameters that are determined by fitting experimental measurements. The critical field B_{c2} and the critical current I_c of the Nb$_3$Sn strand are reported in (A. 1).

$$B_{c2}(T) = B_{c20} \cdot (1 - t^{1.52})$$

$$I_c(T, B) = \frac{C_0}{B} \cdot (1 - t^{1.52})^\alpha \cdot (1 - t^2)^\alpha \cdot b^{0.5} \cdot (1 - b)^2$$

(A. 1)

Here, $t = T/T_c$ and $b = B/B_{c2}(T)$ are dimensionless constants, whereas B_{c20} [T], C_0 [A·T] and α [-] are fitting parameters.

For the SMC-11T cable used in Section 3.4.4, the strand critical current and the fitted parameters are reported in Figure A.5.1. They were measured and provided by CERN.
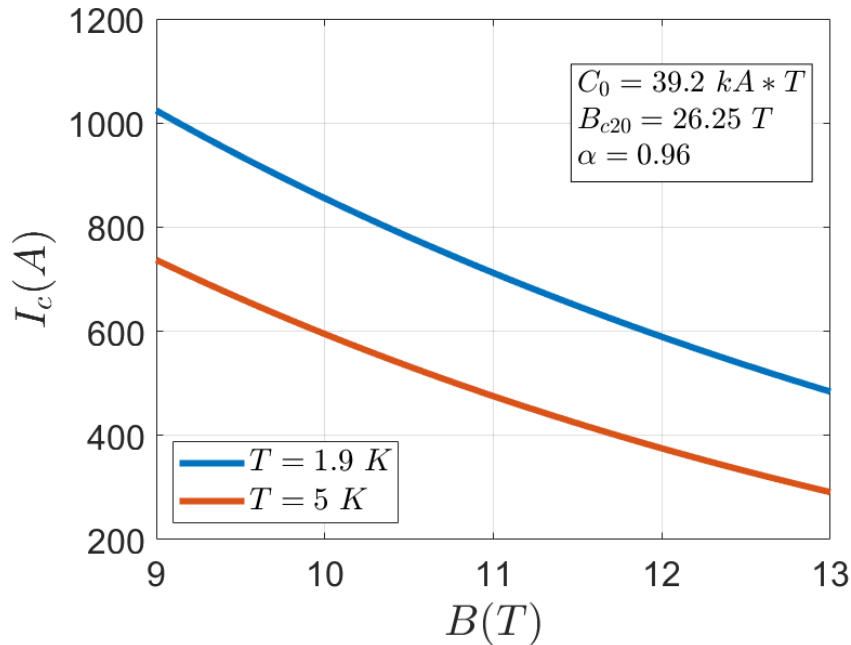
Figure A.5.1 *Strand critical current as a function of magnetic field.*

A.2. Elasticity equations in variational form

From the linear theory of elasticity, it is possible to derive the displacement differential equations (A. 5) at the base of the structural mechanics of solid bodies. These equations combine the equilibrium equations (A. 2), kinematic equations (A. 3) and material constitutive equations (A. 4). The reported equations are reported for solid bodies at constant temperature.

$$L^T \boldsymbol{\sigma} + \boldsymbol{f} = 0 \tag{A. 2}$$

$$\boldsymbol{\varepsilon} = \boldsymbol{L}\boldsymbol{u} \tag{A. 3}$$

$$\boldsymbol{\sigma} = \boldsymbol{C}\boldsymbol{\varepsilon} \tag{A. 4}$$

$$L^T \boldsymbol{C}\boldsymbol{L}\boldsymbol{u} + \boldsymbol{f} = 0 \tag{A. 5}$$

Here $\boldsymbol{\sigma}$ [Pa] is the stress state tensor, $\boldsymbol{\varepsilon}$ [-] the strain state tensor, $\boldsymbol{u}$ [m] the displacement vector, $\boldsymbol{f}$ [N/m^3] the body force vector, $\boldsymbol{L}$ the differential matrix and $\boldsymbol{C}$ the constitutive matrix of isotropic materials. These tensors are defined in (A. 6) and (A. 7). In particular, $\boldsymbol{C}$ contains the Young's modulus E [GPa] and the Poisson's coefficient v.

In the final element analysis, expression (A. 5) is not the one that is solved. It is instead used to express the minimum of the potential energy, which leads to the weak variational form of the elasticity problem [100] expressed in equation (A. 8), the one to approximate through the finite element method for deriving the approximated displacement field $\boldsymbol{u}$, the unknown of the problem. The stress tensor $\boldsymbol{\sigma}$ can be computed afterwards by approximating the derivatives contained in expressions (A. 3) and (A. 4).

$$\boldsymbol{\sigma} = \begin{bmatrix} \sigma_x \\ \sigma_y \\ \sigma_z \\ \tau_{yz} \\ \tau_{zx} \\ \tau_{xy} \end{bmatrix}, \boldsymbol{\varepsilon} = \begin{bmatrix} \varepsilon_x \\ \varepsilon_y \\ \varepsilon_z \\ \gamma_{yz} \\ \gamma_{zx} \\ \gamma_{xy} \end{bmatrix}, \boldsymbol{u} = \begin{bmatrix} u_x \\ u_y \\ u_z \end{bmatrix}, \boldsymbol{f} = \begin{bmatrix} f_x \\ f_y \\ f_z \end{bmatrix} \tag{A. 6}$$

$$
L^T = \begin{bmatrix} \dfrac{\partial}{\partial x} & 0 & 0 & 0 & \dfrac{\partial}{\partial z} & \dfrac{\partial}{\partial y} \\[2mm] 0 & \dfrac{\partial}{\partial y} & 0 & \dfrac{\partial}{\partial z} & 0 & \dfrac{\partial}{\partial x} \\[2mm] 0 & 0 & \dfrac{\partial}{\partial z} & \dfrac{\partial}{\partial y} & \dfrac{\partial}{\partial x} & 0 \end{bmatrix}
$$

$$
S = \begin{bmatrix} 1/E & -v/E & -v/E & 0 & 0 & 0 \\ -v/E & 1/E & -v/E & 0 & 0 & 0 \\ -v/E & -v/E & 1/E & 0 & 0 & 0 \\ 0 & 0 & 0 & \dfrac{2(1+v)}{E} & 0 & 0 \\ 0 & 0 & 0 & 0 & \dfrac{2(1+v)}{E} & 0 \\ 0 & 0 & 0 & 0 & 0 & \dfrac{2(1+v)}{E} \end{bmatrix}
\qquad \textbf{(A. 7)}
$$

$$
C = S^{-1}
$$

$$
\int_{\Omega} (\delta u^T L^T) C (Lu) d\Omega - \int_{\Omega} \delta u^T f d\Omega - \int_{\Sigma} \delta u^T \hat{\sigma} d\Sigma = 0
\qquad \textbf{(A. 8)}
$$

In expression (A. 8), δu represents a small variation of u, Ω is the volume domain, Σ the surface at the boundary of the domain, and $\hat{\sigma} = \begin{bmatrix} \hat{\sigma}_x \\ \hat{\sigma}_y \\ \hat{\sigma}_z \end{bmatrix}$ the stress vector on the surface. In particular, formulation (A. 8) is called weak because the requirement is that the unknown u is continuously differentiable once, opposed to expression (A. 5), in which the requirement is that u is continuously differentiable twice. Always with reference to expression (A. 8), the surface integral contains the boundary conditions of the problem.

The finite element method is at the base of the mechanical designs and analyses carried in Chapters 4 and 5 in this thesis.

A.3. The SULTAN facility

The superconductivity group of SPC in Villigen hosts SULTAN (SUpraLeiter TestANlage), the largest worldwide test facility for high current LTS and HTS forced flow conductors and joints. This facility is shown in Figure A.5.2, while its main parameters are summarized in Table A-1. The background magnetic field is provided by three concentric pairs of superconducting split coils cooled by forced flow supercritical helium. The facility has two types of access for the sample: a vertical one for sample cross-sections smaller than 92 mm x 142 mm (bore dimensions) and a horizontal one for bigger samples, up to a diameter

of 580 mm. While the horizontal test well shares the environment with the vacuum vessel in which the magnets are located, the vertical one has at disposal a separate one. The latter allows the insertion and extraction of samples in and out of the test well without having to break the vacuum and warm up the vessel of the SULTAN magnets. Therefore, the cool-down of a sample inserted in the vertical test well requires just a couple of days, whereas a sample in the horizontal access needs about one month to reach 4.5 K. For the samples of this thesis, the vertical access was employed.

A typical sample inserted in the vertical test well of SULTAN has two "legs", as already shown in Figure 4.30. Each leg contains either a conductor or a joint between conductors. The two legs are electrically connected each other through a bottom joint in praying hands layout.

In the vertical access configuration, the high current is provided by a superconducting transformer made of NbTi, whose primary winding can reach current values up to 200 A, whereas the secondary up to 100 kA [81]. The secondary winding is the one in electrical contact with the sample.

The temperature of the sample can be in the range 4.5-50 K. The upper extreme is of interest for the test of HTS conductors. If one wants to reach a temperature higher than 10 K, the sample is equipped with a HTS adapter for the electrical connection with the transformer, so that the heat flow to the LTS transformer is limited. Moreover, a counter-flow heat exchanger has to link the inlet with the outlet helium flow, so that the temperature of the coolant going back to the cryoplant is always below 10 K, the acceptable limit for this facility.

The maximum mass flow-rate in one sample leg is 10 g/s, while the maximum pressure is 10 bar. The helium mass flow rate and temperature can be regulated separately in each of the two legs.

In AC loss measurements, the AC field is provided by a set of two copper saddle coils (Figure A.5.3). The losses of the sample are assessed through a gas flow calorimetric method, i.e. from the enthalpy change of the helium mass flow rate passing through the sample. The saddle coils can also be fed by a bipolar pulse battery for transient stability tests. Through the discharge of such battery, a field rate up to 60 T/s can be reached with a discharged time of 128 ms.

Figure A.5.2 *The SULTAN test facility.*

the 2 legs of the sample holder

PULSED AC FIELD

SULTAN DC FIELD
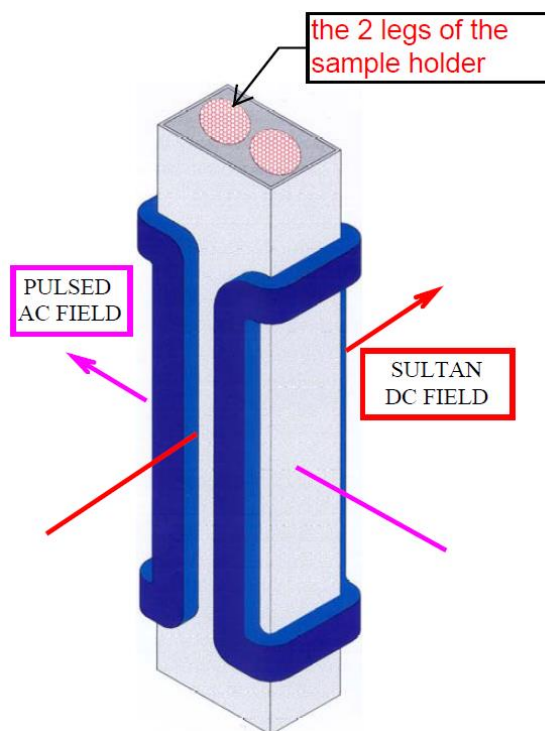
Figure A.5.3 *Sketch of the saddle coils.*

Table A-1 *The main characteristics of the SULTAN test facility.*

Parameter	Value
Peak field in the bore	10.9 T
Homogeneous field length (±2%)	410 mm
Vertical test well size	92 mm x 142 mm
Maximum sample current	100 kA
Test temperature	4.5-50 K
Maximum helium mass flow rate	20 g/s
AC field of pulsed coil	up to $\Delta B=\pm0.4$ T, f=0.01-6 Hz
AC field length	390 mm

Bibliography

[1]   A. D. C. Grassie, The superconducting state, Sussex University Press, 1975.

[2]   A. C. Rose-Innes and E. H. Rhoderick, Introduction to superconductivity, Pergamon Press, 1978.

[3]   M. N. Wilson, Superconducting Magnets, Clarendon Press Oxford, 1983.

[4]   L. Rossi, "The Large Hadron Collider and the Role of Superconductivity in One of the Largest Scientific Enterprises," *IEEE Transactions on Applied Superconductivity,* vol. 17, no. 2, 2007.

[5]   P. J. Bryant and K. Johnsen, The Principles of Circular Accelerators and Storage Rings, Cambridge University Press, 1993.

[6]   L. Bottura, "Superconducting technology for high energy physics and accelerators," in *Oxford Summer School*, 2018.

[7]   L. Rossi, "State-of-the-art Superconducting Accelerator Magnets," *IEEE Transactions on Applied Superconductivity,* vol. 12, no. 1, pp. 219-227, 2002.

[8]   L. Evans, The Large Hadron Collider: a marvel of technology, EPFL Press, 2018.

[9]   O. Brüning, H. Burkhardt and S. Myers, "The large hadron collider," *Progress in Particle and Nuclear Physics,* vol. 67, pp. 705-734, 2012.

[10]   L. Rossi, "Manufacturing and Testing of Accelerator Superconducting Magnets," in *CAS-CERN Accel. School: Course Supercond. Accel.*, Erice, Italy, 2013.

[11]   G. Arduini et al., "High Luminosity LHC: challenges and plans," *Journal of Instrumentation,* vol. 11, 2016.

[12]   M. Krammer, "The update of the European strategy for particle physics," *Physica Scripta,* vol. 2013, no. T158, 2013.

[13]   D. Schoerling et al., "The 16 T Dipole Development Program for FCC and HE-LHC," *IEEE Transactions on Applied Superconductivity,* vol. 29, no. 5, 2019.

[14]   J. Ongena et al., "Magnetic-confinement fusion," *Nature Physics,* vol. 12, pp. 398-410, 2016.

[15] C. Huang and L. Li, "Magnetic confinement fusion: a brief review," *Frontiers in Energy,* vol. 12, pp. 305-313, 2018.

[16] V. Smirnov, "Tokamak foundation in USSR/Russia 1950–1990," *Nuclear Fusion,* vol. 50, 2010.

[17] K. Lackner et al., "Fusion Physics," in *International Atomic Agency*, Vienna, 2012.

[18] "iter.org," [Online]. Available: https://www.iter.org/mag/9/65.

[19] J. P. Freidberg, Plasma Physics and Fusion Energy, Cambridge University Press, 2007.

[20] N. Mitchell and A. Devred, "The ITER magnet system: configuration and construction status," *Fusion Engineering and Design,* vol. 123, pp. 17-25, 2017.

[21] G. Federici et al., "DEMO design activity in Europe: Progress and updates," *Fusion Engineering and Design,* vol. 136, pp. 729-741, 2018.

[22] F. Romanelli, "Fusion Electricity, A roadmap to the realisation of fusion energy," EFDA, Garching, 2012.

[23] P. Bruzzone, "Superconductivity and fusion energy—the inseparable companions," *Superconductor Science and Technology,* vol. 28, 2015.

[24] B. T. Matthias et al., "Superconductivity of Nb_3Sn," *Physical Review,* vol. 95, no. 6, 1954.

[25] J. W. Ekin, "Strain Scaling Law and the Prediction of Uniaxial and Bending Strain Effects in Multifilamentary Superconductors," in *Filamentary A15 Superconductors*, Boston, Springer, 1980, pp. 187-203.

[26] J. W. Ekin, "Strain Effects in Superconducting Compounds," *Advances in Cryogenic Engineering Materials,* vol. 30, pp. 823-836, 1984.

[27] H. Müller and T. Schneider, "Heat treatment of Nb_3Sn conductors," *Cryogenics,* vol. 48, pp. 323-330, 2008.

[28] A. Godeke, Performance Boundaries in Nb_3Sn Superconductors, PhD Thesis, 2005.

[29] H. Rogalla and P. H. Kes, 100 years of superconductivity, CRC Press, Taylor & Francis Group, 2012.

[30] M. Suenaga, "Understanding Properties and Fabrication Processes of Superconducting Nb_3Sn Wires," in *Cryogenic Engineering. International Cryogenics Monograph Series*, New York, Springer, 2007, pp. 285-308.

[31] R. M. Scanlan, W. A. Fietz and E. F. Koch, "Flux pinning centers in superconducting Nb_3Sn," *Journal of Applied Physics,* vol. 46, no. 2244, 1975.

[32] M. O. Hoenig and D. Montgomery, "Dense supercritical-helium cooled superconductors for large high field stabilized magnets," *IEEE Transactions on Applied Superconductivity,* vol. 11, no. 2, 1975.

[33] "National High Magnetic Field Laboratory," [Online]. Available: https://nationalmaglab.org/magnet-development/applied-superconductivity-center/asc-image-gallery/nb3sn-image-gallery.

[34] H. Kanithi et al., "Trivalent Chrome Plating for ITER Strands," *IEEE Transactions on Applied Superconductivity,* vol. 22, no. 3, 2012.

[35] P. Bruzzone, K. Sedlak and B. Stepanov, "High current superconductors for DEMO," *Fusion Engineering and Design,* vol. 88, pp. 1564-1568, 2013.

[36] R. Gupta et al., "React and Wind Nb_3Sn Common Coil Dipole," *IEEE Transactions on Applied Superconductivity,* vol. 17, pp. 1130-1135, 2007.

[37] P. Bruzzone et al., "Upgrade of operating range for SULTAN test facility," *IEEE Transactions on Applied Superconductivity,* vol. 12, no. 1, pp. 520-523, 2002.

[38] M. Breschi, D. Macioce and A. Devred, "Performance analysis of the toroidal field ITER production conductors," *Superconductor Science and Technology,* vol. 30, 2017.

[39] C. Calzolaio and P. Bruzzone, "Analysis of the CICC Performance Through the Measurement of the Thermal Strain Distribution of the Nb_3Sn Filaments in the Cable Cross Section," *IEEE Transactions on Applied Superconductivity,* vol. 24, no. 3, 2014.

[40] C. Calzolaio, Irreversible Degradation in Nb_3Sn Cable in Conduit Conductors, PhD Thesis, 2013.

[41] C. Fiamozzi Zignani et al., "Strain distribution in the Nb_3Sn rectangular wind and react conductor of the European DEMO project, determined by inductive measurements," *Fusion Engineering and Design,* vol. 146, pp. 1539-1542, 2019.

[42] K. Sedlak et al., "DC Test Results of the DEMO TF React&Wind Conductor Prototype No. 2," *IEEE Transactions on Applied Superconductivity,* vol. 29, no. 5, 2019.

[43] N. N. Martovetsky, A. B. Berryhill and S. J. Kenney, "Qualification of the Joints for the ITER Central Solenoid," *IEEE Transactions on Applied Superconductivity,* vol. 22, no. 3, 2012.

[44] R. Valente et al., "Baseline Design of a 16 T cos θ Bending Dipole for the Future Circular Collider," *IEEE Trans. Appl. Supercond.,* vol. 29, no. 5, 2019.

[45] C. Lorin et al., "Design of a Nb_3Sn 16 T Block Dipole for the Future Circular Collider," *IEEE Transactions on Applied Superconductivity,* vol. 28, 2018.

[46] F. Toral, J. Munilla and T. Salmi, "Magnetic and Mechanical Design of a 16 T Common Coil Dipole for an FCC," *IEEE Transactions on Applied Superconductivity,* vol. 28, 2018.

[47] B. Auchmann et al., "Electromechanical Design of a 16-T CCT Twin-Aperture Dipole for FCC," *IEEE Transactions on Applied Superconductivity,* vol. 28, 2018.

[48] K. Sedlak et al., "Design and R&D for the DEMO Toroidal Field Coils Based on Nb_3Sn React and Wind Method," *IEEE Transactions on Applied Superconductivity,* vol. 27, no. 4, 2017.

[49] K. Sedlak et al., "Advance in the conceptual design of the European DEMO magnet system," *Superconductor Science and Technology,* vol. 33, 2020.

[50] P. Bruzzone et al., "EDIPO: The Test Facility for High-Current High-Field HTS Superconductors," *IEEE Transactions on Applied Superconductivity,* vol. 26, no. 2, 2016.

[51] X. Sarasola et al., "Progress in the Design of a Hybrid HTS-Nb_3Sn-NbTi Central Solenoid for the EU DEMO," *IEEE Transactions on Applied Superconductivity,* vol. 30, no. 4, 2020.

[52] B. Stepanov et al., "Twin-box ITER joints under electromagnetic transient loads," *Fusion Engineering and Design,* Vols. 98-99, pp. 1158-1162, 2015.

[53] A. Bonito-Oliva et al., "Completion and Test of the First ITER TF Coil Winding Pack by Europe," *IEEE Transactions on Applied Superconductivity,* vol. 28, no. 3, 2018.

[54] D. Ciazynski et al., "Test results on the first 50 kA NbTi full size sample for the International Thermonuclear Experimental Reactor," *Superconductor Science and Technology,* vol. 17, 2004.

[55] P. Decool et al., "Hydraulic characterization of twin-box joints for ITER magnets," *Fusion Engineering and Design,* vol. 146, pp. 543-546, 2019.

[56] Y. Ilyin et al., "Design and Qualification of Joints for ITER Magnet Busbar System," *IEEE Transactions on Applied Superconductivity,* vol. 26, no. 4, 2016.

[57] S. Davis et al., "JT-60SA Magnet System Status," *IEEE Transactions on Applied Superconductivity,* vol. 28, no. 3, 2018.

[58] N. N. Martovetsky, "Development of the Butt Joint for the ITER Central Solenoid," *IEEE Transactions on Applied Superconductivity,* vol. 17, no. 2, 2007.

[59] K. Kizu et al., "Development of Central Solenoid for JT-60SA," *IEEE Transactions on Applied Superconductivity,* vol. 23, no. 3, 2013.

[60] A. Di Zenobio et al., "Joint Design for the EDIPO," *IEEE Transactions on Applied Superconductivity,* vol. 18, no. 2, 2008.

[61] N. Martovetsky et al., "Performance of ITER CS Joints," in *MT 25*, Amsterdam, 2017.

[62] N. N. Martovetsky, "R&D effort for ITER Central Solenoid," in *26th Symposium on Fusion Engineering (SOFE)*, Austin, Texas, 2015.

[63] D. Schoerling and A. V. Zlobin, Nb_3Sn Accelerator Magnets, Springer International Publishing, 2019.

[64] G. Hartwig, "Low-Temperature Properties of Resins and Their Correlations," in *Advances in Cryogenic Engineering, vol 22*, Boston, MA, Springer, 1977, pp. 283-290.

[65] D. Schoerling et al., "Strategy for Superconducting Magnet Development for a Future Hadron-Hadron Circular Collider at CERN," in *The European Physical Society Conference on High Energy Physics 2015*, 2016.

[66] E. Neppiras, "Ultrasonic welding of metals," *Ultrasonics,* vol. 3, no. 3, pp. 128-135, 1965.

[67] H.-S. Shin et al., "Joining of REBCO Coated Conductor Tapes Using Ultrasonic Welding Method," *IEEE Transactions on Aplied Superconductivity,* vol. 25, no. 3, 2015.

[68] A. Jacquemod et al., "Qualification and Start of Production of the Ultrasonic Welding Machines for the LHC Interconnections," in *19th International Conference on Magnet Technology (MT19)*, Genova (Italy), 2006.

[69] N. F. Kazakov, Diffusion Bonding of Materials, Pergamon, 1985.

[70] J. W. Elmer et al, "Effect of surface condition and bonding pressure on quality of diffusion bonded high purity copper for linear collider accelerator structures," *Science and technology of welding and joining,* vol. 6, no. 5, pp. 268-272, 2001.

[71] B. Derby and W. E. R., "Diffusion bonds in copper," *Journal of Materials Science,* vol. 19, no. 10, pp. 3140-3148, 1984.

[72] I. T. Watkins et al., "Powder interlayer bonding of geometrically complex Ti-6Al-4V parts," *The International Journal of Advanced Manufacturing Technology,* vol. 106, pp. 3629-3639, 2019.

[73] L. Rossi, "Superconductivity: its role, its success and its setbacks in the Large Hadron Collider of CERN," *Superconducting Science and Technology,* vol. 23, no. 3, 2010.

[74] B. Bordini et al., "Witness samples results for Coil MQXF 105," European Organization for Nuclear Research, Geneva, 2016.

[75] E. Rochepault et al., "Dimensional Changes of Nb_3Sn Rutherford Cables During Heat Treatment," *IEEE Transaction on Applied Superconductivity,* vol. 26, no. 4, 2016.

[76] "MECASONIC Welding Plastic Solutions," Mecasonic, [Online]. Available: https://www.mecasonic.com/.

[77] P. Bauer, H. Rajainmaki and E. Salpietro, "EFDA Material Data Compilation for Superconductor Simulation," EFDA CSU, Garching, 2007.

[78] J. O. Almen and A. Laszlo, "The Uniform-Section Disk Spring," *Transactions of the American Society of Mechanical Engineers,* pp. 305-314, 1936.

[79] D. S. Easton et al., "A prediction of the stress state in Nb_3Sn superconducting composites," *Journal of Applied Physics,* vol. 51, pp. 2748-2757, 1980.

[80] V. D'Auria et al., "Progress on Tests on Splices Between Nb$_3$Sn Rutherford Cables for Graded High-Field Accelerator Magnets," *IEEE Transactions on Applied Superconductivity,* vol. 31, no. 5, 2021.

[81] G. Pasztor et al., "Design, fabrication and testing of a 100 kA superconducting transformer for the SULTAN Test Facility," in *15th International Conference on Magnet Technology*, Beijing, China, 1998.

[82] G. H. Morgan, "Eddy currents in flat metal-filled superconducting braids," *Journal of Applied Physics,* vol. 44, pp. 3319-3322, 1973.

[83] V. Sytnikov et al., "Coupling losses in superconducting transposed conductors located in changing magnetic fields," *Cryogenics,* vol. 29, no. 9, pp. 926-930, 1989.

[84] V. E. Sytnikov and I. B. Peshkov, "Application of the network method to superconducting cables," *Advances in Cryogenic Engineering Materials,* vol. 40, pp. 537-542, 1994.

[85] E. Niessen, "Continuum Electromagnetics of Composite Superconductors," PhD Thesis, 1993.

[86] A. P. Verweij, "CUDI: A model for calculation of electrodynamic and thermal behaviour of superconducting Rutherford cables," *Cryogenics,* vol. 46, pp. 619-626, 2006.

[87] A. P. Verweij, "Electrodynamics of Superconducting Cables in Accelerator Magnets," PhD Thesis, 1995.

[88] M. Schwartz, Soldering: Understanding the Basics, ASM Internationalyear, 2014.

[89] M. Kumar et al., "Preliminary tests of soldered and diffusion-bonded splices between Nb$_3$Sn Rutherford cables for graded high-field acceleratormagnets," *IEEE Trans. Appl. Supercond.,* vol. 29, no. 5, 2019.

[90] F. Heringhaus and T. Painter, "Magnetoresistance of selected Sn- and Pb-based solders at 4.2 K," *Materials Letters,* vol. 57, pp. 787-793, 2002.

[91] V. Corato et al., "The DEMO Magnet System – Status and Future Challenges," To be published.

[92] R. Wenninger, "DEMO2 Reference Design - 2015 May ("EU DEMO2 2015") - PROCESS Full Output (2MD7E6 v1.1)," 13 May 2015. [Online]. Available: https://idm.euro-fusion.org/default.aspx?uid=2MD7E6.

[93] R. Kembleton, "Phys_mag_PROCESS_baseline_July_18," August 2018. [Online]. Available: https://idm.euro-fusion.org/?uid=2N622S.

[94] L. Zani et al., "Overview of Progress on the EU DEMO Reactor Magnet System Design," *IEEE Transactions on Applied Superconductivity,* vol. 26, no. 4, 2016.

[95] P. Bruzzone et al., "A New Cabled Stabilizer for the Nb$_3$Sn React&Wind DEMO Conductor Prototype," *IEEE Transactions on Applied Superconductivity,* vol. 31, no. 5, 2021.

[96] C. Sanabria et al., "Evidence that filament fracture occurs in an ITER toroidal field conductor after cyclic Lorentz force loading in SULTAN," *Superconductor Science and Technology,* vol. 25, 2012.

[97] C. A. Swenson, "Properties of Indium and Thallium at Low Temperatures," *Physical Review,* vol. 100, no. 6, pp. 1607-1614, 1955.

[98] B. Stepanov, P. Bruzzone and K. Sedlak, "Inter-Layer Joint for the TF Coils of DEMO—Design and Test Results," *IEEE Transactions on Applied Superconductivity,* vol. 28, no. 3, 2018.

[99] "Bührer AG," [Online]. Available: https://www.buehrer-ag.ch/en/metal-spraying/.

[100] M. Amara and J. Thomas, "Equilibrium Finite Elements for the Linear Elastic Problem," *Numerische Mathematik,* vol. 33, pp. 367-383, 1979.

[101] Plustherm Point AG, [Online]. Available: https://www.plustherm.ch/.

[102] K. Sedlak et al., "AC Loss Measurement of the DEMO TF React&Wind Conductor Prototype No. 2," *IEEE Transactions on Applied Superconductivity,* vol. 30, no. 4, 2020.

[103] P. Bruzzone et al., "A new test method of AC loss assessment for fusion conductors," *Fusion Engineering and Design,* vol. 146, pp. 928-931, 2019.

[104] "CERN Engineering Department," [Online]. Available: https://en.web.cern.ch/group/mme.

[105] H. Berger et al., "Numerical and Analytical Approaches for Calculating the Effective Thermo-Mechanical Properties of Three-Phase Composites," *Journal of Thermal Stresses,* vol. 30, no. 8, pp. 801-817, 2007.

[106] F. Nunio, A. Panin and M. Biancolini, "Reference basis for mechanical & thermal analysis of TFC," https://ide.euro-fusion.org/?uid=2M7RKP, 2015.

[107] N. Mitchell, "Finite element simulations of elasto-plastic processes in Nb$_3$Sn strands," *Cryogenics,* vol. 45, pp. 501-515, 2005.

[108] J. W. Ekin et al., "Unified Scaling Law for flux pinning in practical superconductors: II. Parameter testing, scaling constants, and the Extrapolative Scaling Expression," *Superconductor Science and Technology,* vol. 29, no. 12, 2016.

List of Figures

145

149

151

List of Tables

153

Acknowledgements

I wish to express my gratitude to my thesis supervisors, Pierluigi Bruzzone and Ambrogio Fasoli. They showed not only high level of professionalism, but also care about the well-being of their students. This was especially evident in the lockdown period.

Many thanks go to the rest of the scientific staff of the superconductivity group: Kamil, Davide, Robert, Rainer, Hugues, Xabier, Federica, Roberto, Mithlesh, Chiara, Ortensia, Boris, Evgeny and Nikolay. The frequent conversations and exchange of information with them contributed to the development of this thesis.

I would like to thank the technical staff of the group: Marcel, Felix, Thomas, Franz, Roland, Andreas, Tobias, Markus, Christoph and Manuel. Everybody had a role in this project and demonstrated particular dedication and involvement.

Thanks to Viviana and Nadja for their precious administrative role.

I am grateful to my parents, Gennaro and Marianna, for their unfailing support. I know that they are there and always will be.

In the end, thanks to my girlfriend Luana, who accompanies me in my everyday life.

Vincenzo D'Auria

Bruggerstrasse 185, 5400 Baden, Switzerland

+41 76 748 60 77

vincenzo.dauria92@gmail.com

PERSONAL INFORMATION

- Date of birth: July 9, 1992
- Nationality: Italian
- LinkedIn profile: www.linkedin.com/in/vincenzo-dauria

SUMMARY

Diligent Research Assistant with background in Energy and Nuclear Engineering currently working towards the PhD in Physics in the framework of applied superconductivity (exam date 7th of December, 2021). Proficient in electrical and calorimetric measurements at cryogenic temperature, as well as physical modelling for design and analysis purposes.

SKILLS

- Designing experiments
- Preparing samples and specimens
- Analyzing and synthesizing data
- Analytical and numerical modeling
- Public presentations
- Manuscripts preparation for scientific journals
- Proficient in Microsoft Office, MatLab, FreeFem++, ANSYS, Origin, SolidWorks

EXPERIENCE

Research Assistant, 09/2017 - 12/2021
Superconductivity Group of Swiss Plasma Center, Villigen (Paul Scherrer Institut), Switzerland

- Designed and conducted experiments at cryogenic temperature, high current (60 kA), magnetic field (11 T) and mechanical load (660 kN/m).
- Maintained detailed records of experiments and outcomes.
- Prepared reports summarizing research results.
- Complemented the experimental results with thermo-mechanical and electromagnetic models.
- Shared research findings through publications and presentations at international conferences.
- Reviewed literature to remain current with new procedures and apply learnings to related research.

Apprentice, 03/2017 - 08/2017
U-Series, Bologna, Italy
- Nuclear tracks analysis at the microscope for Radon dosimetry.
- Creation of a computer code for the automatic detection at the microscope of nuclear tracks left by the decay of Radon, thus improving the detection reliability and the speed of the analysis.
- Assembly of Radon dosimeters.

EDUCATION

École Polytechnique Fédérale De Lausanne, *Lausanne, Switzerland, 12/2021*
Ph.D.: **Physics**
- Thesis in the framework of applied superconductivity: "Joints for Nb_3Sn Cables of High Magnetic Field Magnets"
- Supervision of Pierluigi Bruzzone, former head of the Superconductivity Group of Swiss Plasma Center

Politecnico Di Torino, *Turin, Italy, 10/2016*
Master of Science: **Energy and Nuclear Engineering**
- 110/110 and honors.
- Focus on nuclear technologies and applications.
- Master thesis: "Analysis and design of a Permeator Against Vacuum system for tritium extraction in fusion reactors".

Politecnico Di Torino, *Turin, Italy, 07/2014*
Bachelor of Science: **Energy Engineering**
- 110/110 and honors.

LANGUAGES

Italian: First Language

English: C1
Advanced

German: C1
Advanced

REFERENCES

- Pierluigi Bruzzone, former leader of the Superconductivity Group of Swiss Plasma Center. Mail: pierluigi.bruzzone@psi.ch. Phone: +41 56 310 43 63
- Ambrogio Fasoli, director of Swiss Plasma Center. Mail: ambrogio.fasoli@epfl.ch. Phone: +41 21 693 34 92

Publications

[1] V. D'Auria, S. Dulla, P. Ravetto, L. Savoldi, M. Utili, R. Zanino, "Tritium extraction from lithium-lead in the EU DEMO blanket using permeator against vacuum," *Fusion Science and Technology*, vol. 71, no. 4, 2017.

[2] V. D'Auria, S. Dulla, P. Ravetto, L. Savoldi, M. Utili, R. Zanino, "Design of a permeator-against-vacuum mock-up for the tritium extraction from PbLi at low speed," *Fusion Engineering and Design*, vol. 121, pp. 198-203, 2017.

[3] M. Kumar, V. D'Auria, D. Uglietti, P. Bruzzone, "Preliminary Tests of Soldered and Diffusion-Bonded Splices Between Nb_3Sn Rutherford Cables for Graded High-Field Accelerator Magnets," *IEEE Transactions on Applied Superconductivity*, vol. 29, no. 5, 2019.

[4] K. Sedlak, P. Bruzzone, B. Stepanov, R. Wesche, X. Sarasola, D. Uglietti, V. D'Auria, C. Vorpahl, L. Affinito, L. Muzzi, A. d. Corte, V. Corato, "DC Test Results of the DEMO TF React&Wind Conductor Prototype No. 2," *IEEE Transactions on Applied Superconductivity*, vol. 29, no. 5, 2019.

[5] V. D'Auria, B. Stepanov, K. Sedlak, P. Bruzzone, "Inter-Layer Joint of Nb_3Sn React&Wind Cables for Fusion Magnets," *IEEE Transactions on Applied Superconductivity*, vol. 30, no. 4, 2020.

[6] K. Sedlak, V.A. Anvar, N. Bagrets, M.E. Biancolini, R. Bonifetto, F. Bonne, D. Boso, A. Brighenti, P. Bruzzone, G. Celentano, A. Chiappa, V. D'Auria, M. Dan, P. Decool, A. Della Corte, A. Dembkowska, O. Dicuonzo, I. Duran, M. Eisterer, A. Ferro, C. Fiamozzi Zignani, W.H. Fietz, C. Frittitta, E. Gaio, L. Giannini, F. Giorgetti, F. Gömöry, X. Granados, R. Guarino, R. Heller, C. Hoa, I. Ivashov, G. Jiolat, M. Jirsa, B. Jose, R. Kembleton, M. Kumar, B. Lacroix, Q. Le Coz, M. Lewandowska, A. Maistrello, N. Misiara, L. Morici, L. Muzzi, S. Nicollet, A. Nijhuis, F. Nunio, C. Portafaix, G. Romanelli, X. Sarasola, L. Savoldi, B. Stepanov, I. Tiseanu, G. Tomassetti, A. Torre, S. Turtù, D. Uglietti, R. Vallcorba, L. Viererbl, M. Vojenciak, C. Vorpahl, K.P. Weiss, R. Wesche, M.J. Wolf, L. Zani, R. Zanino, A. Zappatore, V. Corato, "Advance in the conceptual design of the European DEMO magnet system," *Superconductor Science and Technology*, vol. 33, no. 4, 2020.

[7] V. D'Auria, M. Kumar, X. Sarasola, P. Bruzzone, "Progress on Tests on Splices Between Nb_3Sn Rutherford Cables for Graded High-Field Accelerator Magnets," *IEEE Transactions on Applied Superconductivity*, vol. 31, no. 5, 2021.

[8] P. Bruzzone, K. Sedlak, B. Stepanov, M. Kumar, V. D'Auria, "A New Cabled Stabilizer for the Nb_3Sn React&Wind DEMO Conductor Prototype," *IEEE Transactions on Applied Superconductivity*, vol. 31, no. 5, 2021.

[9] V. D'Auria, Nikolay Bykovskiy, Pierluigi Bruzzone and Kamil Sedlak, "Diffusion-bonding between strands and modeling of splices of Nb_3Sn Rutherford cables," to be published in *IEEE Transactions on Applied Superconductivity*.

[10] V. D'Auria, P. Bruzzone, M. S. Meyer, E. R. Castro and S. Sgobba, "Application of Copper Thermal Spraying for Electrical Joints between Superconducting Nb_3Sn Cables," Materials, vol. 15, no. 1: 125, 2022.

[11] V. Corato, C. Vorpahl, K. Sedlak, V.A. Anvar, J. Bennet, M.E. Biancolini, F. Bonne, R. Bonifetto, D.P. Boso, A. Brighenti, P. Bruzzone, G. Celentano, A. della Corte, G. De Marzi, V. D'Auria, F. Demattè, A. Dembkowska, O. Dicuonzo, C.

Fiamozzi Zignani, W.H. Fietz, C. Frittitta, L. Giannini, F. Giorgetti, R. Guarino, R. Heller, C. Hoa, M. Huguet, G. Jiolat, M. Kumar, B. Lacroix, M. Lewandowska, N. Misiara, L. Morici, L. Muzzi, D.S. Nickel, S. Nicollet, A. Nijhuis, F. Nunio, C. Portafaix, X. Sarasola, L. Savoldi, I. Tiseanu, G. Tomassetti, A. Torre, S. Turtù, D. Uglietti, R. Vallcorba, K.-P. Weiss, R. Wesche, M.J. Wolf, K. Yagotintsev, L. Zani, R. Zanino, A. Zappatore, "The DEMO magnet system – Status and future challenges," to be published in *Fusion Engineering and Design*.